DOTTORATO DI RICERCA IN PHYSICS AND NANOSCIENCES

CICLO XXXIII

Sede Amministrativa

Università degli studi di MODENA e REGGIO EMILIA

Tesi per il Conseguimento del Titolo di

Dottore di Ricerca

Computational spectroscopy of inhomogeneous materials by many-body perturbation theory: Method developments and applications

Candidato: Dario Alejandro León Valido

Relatori: Dr. Andrea Ferretti,
Prof. Elisa Molinari,
Dr. Daniele Varsano.

Coordinatore del dottorato
e Direttore della scuola: Prof. Stefano Frabboni

September, 2021

Abstract

In the framework of the GW approximation, the screened interaction W is a non-local and dynamical potential that may have a complex structure in its frequency dependence. A full description of such dependence in a large energy range is in many cases computationally prohibitive, and for this reason it is common practice to approximate it using a plasmon pole (PP) model. The PP approach may however fail for in-homogeneous systems, such as interfaces and defects, and also for some bulk materials, including e.g. metals.

In this thesis I develop and explore a multi-pole approach to provide an effective representation of the dynamical properties of W, and show that optimal sampling strategies of the polarizability in the complex plane can lead to an overall GW accuracy comparable to full-frequency methods at much lower cost. This method is then validated by calculating quasiparticle properties of relevant prototype systems.

The proposed developments are then exploited for the case of selected graphene-metal systems. The structural, electronic, and magnetic properties of these systems are first studied at the DFT level, and then by applying many body perturbation theory (GW). The work is done in tight collaboration with an experimental group performing spectroscopic measurements on the very same systems. Our GW calculations are then compared with angle-resolved photoemission data.

While doing this, I have also performed a detailed study of the structural, electronic, and magnetic properties of the aforementioned graphene-metal interfaces. Among others, I have addressed the effect of oxygen intercalation under graphene in modifying the magnetic properties of the Gr/Co/Ir(111) metallic heterostructure. I have also studied the magnetic and electronic properties of Gr/Fe/Ir(111) and Gr/FeCo/Ir(111) systems, together with the prototype case of Gr/Co(0001). Here the transition metal film is made of one or a few atomic layers intercalated under graphene on Ir(111). The comparison with experiments covers a number of different techniques, ranging from XPS, NEXAFS and XMCD to (angle resolved) photoemission spectroscopy (AR-PES) and inverse photoemission (IPES). In this respect, the proposed methodology for the calculation of GW corrections proves to be an important tool in applying MBPT to complex systems such as those studied in the present thesis.

Acknowledgements

First I would like to thank my supervisor, Elisa Molinari, for offering me the opportunity to come to Modena to do the PhD, and Gabriel Gil, my senior companion from Cuba, for encouraging and helping me through the application process, and introducing me to the people of the institute. I am also thankful with the selection committee for their patience during the interview, especially due to connection problems and the blackout caused by the hurricane that was approaching Cuba at the time.

I'm extremely grateful to all my supervisors, Andrea Ferretti, Daniele Varsano and Elisa Molinari, for welcoming to their group and introducing me to this great international science ecosystem around the MaX Center of Excellence. But mostly for presenting me interesting problems, guiding and encouraging me to address them and also allowing and giving me their confidence for developing many ideas of my own. I very much appreciate all the conversations during car trips with Andrea, many of them became fundamental discussions for the work.

I'm deeply indebted to Claudia Cardoso for helping me in many manners as a coworker in the group, but also for listening to me and advising me on all my thoughts and for creating a very pleasant work environment. This thesis would not be possible without her invaluable contributions.

I would also like to extend my gratitude to the people from the University of Modena and Reggio Emilia and the S3 CNR Institute, who have assisted me throughout this time.

I am profoundly grateful to Profs. Maurizia Palummo and Myrta Grüning for accepting to serve as reviewers of my thesis, for their thorough review of it and their very nice comments. Thanks should also go to the Yambo community, specially the group of developers, for the nice environment and for welcoming the implementations done in the present thesis.

I would like to send special thanks to my good friend Federico Grasselli and Alice, Luigi and Cristina, for offering me a home in Reggio Emilia and warmly welcome me and my girlfriend Emely to Italy, even before we met.

I had great pleasure of working alongside all the companions that have passed through the office along all these years and the other guys from the institute with whom we have had very good times having lunch together, especially in Claudia's pizza

days: Michael Atambo, M. Celeste Maschio, Luigi Cigarini, Jacopo Fregoni, Giacomo Sesti, Alberto Guandalini, Miki Bonacci, Sutapa Dutta, Simone Vacondio, Matteo Zanfrognini, Stefan Peeters, Giulia Righi, Giulio Fatti and everyone else I've interacted with.

I am very happy and thankful for the small Cuban community of students that we have created in Modena, of which I am the 3th after Alain Delgado and Gabriel Gill, and I glad to coincide with two more persons at the same time, Frank Quintela and Michael Hernandez and all the help among us. We hope the relationships in Modena continue to prosper and other Cuban students manage to enroll as well.

Many thanks to my GW fellows: Michael Atambo, Giacomo Sesti, Alberto Guandalini, Miki Bonacci, Simone Vacondio, Matteo Zanfrognini and also Tommaso Chiarotti, especially the group meeting team to whom I dedicate these words:

"Abbiamo vissuto insieme tante avventure in eventi e incontri, ricordi che porterò sempre con me. Viaggi all'ICTP; l'evento a Losanna con Miki, la visita al lago e il ritorno in prima classe nel trenino della panna cotta; le traversate per Cagliari, la spiaggia e il percorso con Alberto e molti altri viaggi. Grazie mille per la buona compagnia e speriamo di ritrovarci presto".

I wish to thank all the unconditional support of my family and old friends during all this time that managed to overcome many adversities, including hurricanes, a ultra rare tornado in Cuba and the global pandemic of coronavirus; specially from my parents, my little sister, my cousin Tomás and my girlfriend Emely, to whom I dedicate the present thesis and these words:

"No importa cuan lejos las circunstancias nos hagan estar, su apoyo me seguira fortaleciendo y lograremos seguir adelante en busca de nuestras metas. Los quiero mucho."

Preamble

In the present Thesis I have studied the structural, electronic, magnetic, and spectroscopic properties of Gr-metal interfaces. This was achieved by using first principle electronic structure methods as based on density functional theory and many-body perturbation theory. In the latter case, besides being a user, I also spent a significant amount of time in developing a dedicated theoretical framework and approach.

Before describing the content of the Thesis in detail, let me acknowledge the context. The theoretical study that I have performed has run in parallel with the experimental measurements performed by the group of Prof. Maria Grazia Betti and Carlo Mariani, at University of Roma1 La Sapienza, with whom we have established a longstanding collaboration. Moreover, the calculations and methodological developments presented here take advantage and contribute to the software developments done within the MaX – Materials design at the exascale – centre of excellence (`http://www.max-centre.eu/`), focused on the development and exploitation of electronic structure community codes in a high performance computing (HPC) environment.

This Thesis's work can be divided into two main parts. In the first part, I have provided original contributions to a joint experimental/theoretical study of structural, electronic, and magnetic properties of graphene-metal junctions. Specifically, I have performed density functional theory calculations on large scale magnetic interfaces. The computational data, while relevant per se, have also been used to complement and clarify experimental measurements, including XPS, NEXFAS, XMCD, and ARPES data. In particular, I have studied the Fe and FeCo intercalation on Gr@Ir(111) and the results have been published in two articles that include both the DFT calculations and experimental measurements [1, 2]. I have also studied the adsorption of oxygen on Co(0001) and Co/Ir(111) surfaces, focusing on the energetics of the O adsorption sites and on the effect of O intercalation as a way to control the Gr/metal coupling. The results are presented in an paper now under revision.

In a second part of my Thesis, I aimed at providing an accurate interpretation of existing ARPES experiments on Gr/Co interfaces. To this end, state-of-the-art approaches typically employ many-body perturbation theory (MBPT) methods to calculate quasi-particle corrections and band structures at the GW level. Nevertheless, current implementations of the GW method present several limitations that make difficult its application to systems as complex as the magnetic Gr-metal interfaces that I have studied. This comes both from the computational cost and from the inadequacy of commonly used approximations. Driven by this, a large part of the Thesis work focused on revisiting a widely studied but still open problem: the frequency description of the operators entering in the GW formalism. This description can be done either by making use of an approximation (the plasmon pole model) that is not accurate enough for the systems under study, or making use of full frequency procedures that however have a prohibitive computational cost. These limitations motivated the development of a new and original approach for the description of the frequency dependence of the polarizability, that we call here *multipole approximation (MPA)*, an accurate alternative to the widely used plasmon-pole approximation (PPA), with a similar computational cost.

The development of the multipole approximation is the most extensive and challenging part of this Thesis. It is also important to remark that such development ranged from the paper and pencil derivation of the equations, to their numerical implementation and HPC optimization (MPI, OpenMP, and GPU acceleration), to the validation on selected systems, and the application to cases of interest.

In particular, I have developed a new type of interpolation for the polarizability based on a coarse sampling in the complex frequency plane, optimized the frequency sampling, and implemented this new algorithm in the many-body perturbation theory (MBPT) code Yambo [3, 4]. Then, I have benchmarked and validated this approach by addressing simple systems including bulk semiconductors, molecules, and metals. Finally I have used the developed method to calculate the electronic band structure of the Gr/Co interface, one of the Gr-metal interfaces that I have studied at the DFT level. In addition to the calculation of quasi-particles within MPA, I also implemented the numerical tool required to evaluate the self-energy as a function of the frequency for both PPA and MPA. Overall, this new approach goes beyond the present applications and soon will be included in a public release of the Yambo code, and will become available to its whole, wide community of users.

The description of the MPA method and its validation are presented in a published article [5], while its application to metallic systems are presented in a separate manuscript, now in preparation. Other potential applications, such as a dedicated multipole approach for the self-energy or the Bethe-Salpeter equation, or the use of convergence accelerators within MPA for **k**-grids and sum-over-states, are left for future developments.

The thesis is organized in 6 chapters. Chapter 1, *Introduction to the systems under study*, draws the motivations to study graphene-metal interfaces and describe their structural, magnetic, and electronic properties. I also discuss the trends and experiments currently carried out by the scientific community active in the field. Chapter 2, *Theoret-*

ical frameworks, describes the main theoretical tools that we employ in our calculations at the DFT level, and introduces the key concepts of the many-body framework at the base of the methodological developments presented in the next chapters. In Chapter 3, *The Multipole Approximation (MPA)*, a detailed description of the MPA technique developed during this PhD Thesis is presented, while Chapter 4, *Validation of MPA on prototypical materials*, presents the validation of the newly developed approach looking at bulk semiconductors, molecules, and metals. Chapter 5, *Applications*, is devoted to the description of the DFT results concerning the study of oxygen adsorption on Co and Co/Ir intercalated underneath graphene and the Co and FeCo intercalation on Gr/Ir surfaces. In this chapter we also discuss the application of the MPA technique to the Gr/Co interface. In Chapter 6, *Conclusions*, we summarize the main results of the present work.

Contents

Abstract i

Acknowledgements ii

Preamble iv

1 Introduction to the systems under study 1

- 1.1 Metal intercalation in graphene/Ir interfaces 1
  - 1.1.1 Co, Fe and FeCo intercalation 2
  - 1.1.2 Oxygen adsorption 4
- 1.2 Experimental characterization of the systems under study 5
  - 1.2.1 Structural measurements 5
  - 1.2.2 Electronic properties accessed by ARPES 10
  - 1.2.3 Near Edge X-ray Absorption Spectroscopy 13
  - 1.2.4 Magnetic properties through X-ray magnetic circular dichroism . 16

2 Theoretical frameworks 20

- 2.1 Density Functional Theory (DFT) 20
  - 2.1.1 Exchange-correlation functionals and pseudo-potentials 22
  - 2.1.2 Basis set and supercell techniques 22
  - 2.1.3 Band unfolding 23
  - 2.1.4 Magnetism 24
  - 2.1.5 Van der Walls interactions 25
- 2.2 Many-body perturbation theory 26
  - 2.2.1 The one-body Green's function 26
  - 2.2.2 From Hedin's equation to the GW approximation 27
  - 2.2.3 Quasi-particle GW calculations in practice 29
- 2.3 Frequency integration methods in GW 31
  - 2.3.1 The plasmon-pole model 32
  - 2.3.2 Full frequency on the real axis 34
  - 2.3.3 Full frequency contour deformation 36

3 The multipole Approximation (MPA) 38
3.1 The multipole scheme . . . 38
3.2 Interpolation procedures . . . 40
3.2.1 Linear solver . . . 40
3.2.2 Padé/Thiele solver . . . 43
3.3 Connecting the GN- and HL- plasmon pole models . . . 45
3.4 Comparison of different samplings on a test function . . . 46
3.4.1 Perturbing the GN sampling . . . 47
3.4.2 Samplings along the real axis . . . 48
3.4.3 Form of the factors . . . 49
3.5 Samplings strategies . . . 50
3.5.1 The polarizability in the complex plane . . . 50
3.5.2 Analysis of one-pole solutions . . . 51
3.5.3 Double parallel sampling . . . 52
3.5.4 Parallel vs. double parallel sampling . . . 54
3.6 Physical constraints with optimal representability . . . 55
3.6.1 Failure condition . . . 55
3.6.2 Representability measurements . . . 56

4 Validation of MPA on prototypical materials 58
4.1 MPA applied to semiconductors . . . 58
4.1.1 The polarizability matrix . . . 59
4.1.2 Convergence of quasiparticles . . . 61
4.1.3 Self-energy and spectral functions . . . 63
4.2 MPA applied to molecules . . . 65
4.2.1 The GW100 set . . . 66
4.2.2 MPA on F2 . . . 68
4.3 MPA applied to metals . . . 71
4.3.1 Particular issues of the GW approximation on metals . . . 71
4.3.2 The polarizability of Cu . . . 72
4.3.3 MPA on Cu . . . 75

5 Applications 79
5.1 Oxygen adsorption on Co, Co/Ir, and Gr/Co interfaces . . . 79
5.1.1 Methods . . . 80
5.1.2 Oxygen adsorption energies on Co and Co/Ir surfaces . . . 82
5.1.3 Electronic and magnetic properties . . . 84
5.1.4 Graphene on Co: decoupling through O intercalation . . . 87
5.1.5 Technicalities . . . 89

5.1.6 Summary . . . 95
5.2 Fe intercalation on Gr/Ir(111) . . . 96
5.2.1 Methods . . . 96
5.2.2 Electronic structure . . . 98
5.2.3 Magnetic properties of the Fe layer . . . 100
5.3 FeCo intercalation on Gr/Ir(111) . . . 102
5.3.1 Methods . . . 102
5.3.2 Narrowing of d bands . . . 103
5.3.3 Parameters for the DFT+U scheme . . . 106
5.3.4 Comparison of pDOS for different transition metals . . . 108
5.4 GW/MPA calculations for the Gr/Co interface (preliminary results) . . . 111
5.4.1 Summary of experimental results . . . 111
5.4.2 Summary of DFT results . . . 112
5.4.3 Challenges of GW calculations . . . 113
5.4.4 Setup and preliminary results . . . 114
5.4.5 Partial conclusions . . . 118

6 Conclusions **120**
6.1 Gr/metal interfaces . . . 120
6.2 Development of the MPA method . . . 121
6.3 Future perspectives . . . 122

7 List of publications **124**

Chapter 1

Introduction to the systems under study

1.1 Metal intercalation in graphene/Ir interfaces

Intercalation of metals underneath graphene (Gr) grown on a substrate has proven to efficiently lead to the formation of atomically smooth metallic layer(s) [1, 6–16] in a layer-by-layer growth mode [17], where the graphene cover acts as a protective membrane of the confined epitaxial metallic layer(s) [18–21]. The method has been extensively explored in the past decade for fundamental and applied physics, in part driven by the interest in creating magnetic systems with tunable properties [10, 12, 22–25]. The main outcomes of the metal intercalation are the modulation of the Gr electronic structure near the Dirac cone [26–28], the enhancement of the interfacial moiré pattern and surface corrugation [8, 29–32], and the stabilization and protection against oxidation of magnetic thin films, thanks to Gr's chemical stability [18, 19, 27, 33, 34].

Graphene is also a very promising material for spintronics owing to its long spin-diffusion lengths of several micrometers [35], gate-tunable carrier concentration, and high electronic mobility [36]. The coupling of Gr with ferromagnetic systems opens new perspectives when efficient injection of spin-polarized electrons can be achieved, as observed for a graphene membrane on Co(0001) [37]. It is well-known that nearly flat epitaxial graphene of high structural quality can be formed on several magnetic $3d$ metal substrates, like the lattice-matched Ni(111) [13, 38–40] and Co(0001) [8–10, 37] surfaces. It has been shown that a tiny magnetic moment arises on the carbon atoms, induced by the strong hybridization of graphene π-orbitals with Ni or Co $3d$-states [8, 11, 37, 41]. The combination of graphene corrugation together with the magnetic substrate has permitted to obtain advanced organic spin-interface architecture with magnetic remanence at room temperature, constituted by metal phthalocyanine molecules magnetically coupled with Co layer(s), mediated by graphene. A practical realization of this structure has been recently achieved by adsorbing TM-phthalocyanine molecules on Gr@/CoIr [15, 22].

The electronic properties of epitaxial Gr significantly depend on the supporting substrate and on the interface. For instance, Gr grown on Ir(111) presents a rippled moiré superstructure, with a weak interaction with the metallic substrate, and preserving the peculiar spectroscopic features of the Gr band-structure, such as the Dirac cone [42, 43]. Conversely, the growth of Gr onto transition metal (TM) surfaces such as Ni(111) or Co(0001) generally results in a better lattice matching at the expenses of a significantly perturbed band structure [44], as shown by angle-resolved photoemission spectroscopy (AR-PES) [9, 13].

In the present thesis we will focus on the intercalation of Co, Fe and FeCo under Gr in Gr/Ir(111) interfaces.

1.1.1 Co, Fe and FeCo intercalation

Bulk cobalt has a hexagonal-closed-package (hcp) periodicity and iridium is face-centred-cubic (fcc), with the (111) plane with the hexagonal geometry. Graphene and Co lattice parameters differ by only 0.05 Å, being in practice lattice matched. In fact, Gr grown on Co lies flat on the surface, with a small interplanar distance. The electronic properties of graphene are affected by the strong interaction with the Co layer. On the other hand, graphene and Ir lattice parameters differ by 0.25 Å. Graphene grown on Ir forms a moiré pattern corresponding to a 10×10 graphene supercell, over a 9×9 Co cell, however the electronic properties of graphene are only slightly altered because of the small hybridization between the two systems. Although Co(0001) and Ir(111) have different in-plane lattice parameter, when a single Co(0001) layer is intercalated underneath Gr grown on top of an Ir(111) it assumes the lattice parameter of iridium [8]. The graphene layer has an important role in the stabilization the Co single layer on the Ir surface in avoiding Co clusters formation [9]. When a larger number of Co are added Co recovers its bulk structure [9]. Depending on the number of intercalated Co layers, Gr either corrugates and forms a moiré pattern with the Co single layer or lies flat due to the lattice match with multi layer Co, as already studied in Refs. [15, 22].

Although iron is the most widespread transition metal, and the technology of passivated Fe films with a graphene membrane can be appealing for several reasons, only a few experimental results for graphene grown on Fe surfaces are available [45–47]. Fe would permit a considerable price reduction in comparison with other transition metal substrates and, most importantly, a strong magnetic response. The main hurdle for the formation of graphene on top of Fe surfaces is related to the rich Fe-C phase diagram [48]. In fact, the high carbon diffusion coefficient and solubility in iron are detrimental for chemical vapor deposition processes, where a high annealing temperature is necessary to ensure high quality graphene on top of the metal surfaces. Thus, the epitaxial growth of a graphene membrane on a Fe film/single crystal is made difficult because of the formation of iron carbide, which is thermodynamically favored [48]. The epitaxial growth of graphene on Fe is also prevented because none of the bcc-Fe facets is lattice-matched with graphene, at variance with close-packed surfaces of other $3d$ metals, like Co and Ni. Recently, a detailed structural study has demonstrated that the Fe(110) face, with its distorted hexagonal symmetry, can be a good candidate, because of a partial match with the graphene lattice [45, 46]. A more challenging strategy has been proposed exploiting Fe intercalation beneath graphene [49] as a viable route to overcome the hurdles to realize a direct growth on Fe surfaces. Recently, a scanning tunnelling microscopy (STM) experiment demonstrates that successful Fe intercalation under graphene grown on Ir(111) can be obtained with the substrate temperature in the range between 450 K and 550 K [21], giving rise to a smooth Fe layer pseudomorphic with Ir(111) and a highly corrugated graphene membrane on top. We address the Fe intercalation on Gr/Ir in Section 5.2. We have studied well-defined smooth Fe layers intercalated between Gr and Ir(111), without any alloying and Fe-C intermixing. By means of Density Functional Theory, we gain a detailed insight into the physical properties of the iron-intercalated Gr/Ir(111) heterostructure. The sandwiched Fe layers present a redistribution of the minority and majority electronic density of states triggered by the spatial confinement and by the peculiar strained structural configurations, as predicted by first principles spin resolved electronic structure calculations and experimentally confirmed by angular resolved photoemission and X-Ray magnetic dichroism.

Ferromagnetic metals (FMs) and their alloys can be finely manipulated by changing their chemical composition [50], structural configuration [51], and by reducing their dimensionality [52, 53]. Modified symmetry and scaled dimension, indeed, may induce in FMs higher magnetic moments and larger uniaxial magnetic anisotropy energy (MAE) with respect to their 3D counterparts [12, 53–56]. The enhanced magnetism in nanostructures, can be used e.g, for engineering spintronic devices [57], high-density magnetic storage [58], and permanent magnets [59].

Among all iron-based alloys, including also pure iron, equiatomic FeCo exhibits the highest Curie temperature and magnetic moment driven by an almost filled Fe majority spin band [60–63]. On the other hand, due to its cubic symmetry, the FeCo alloy shows also a low MAE [64]. Indeed, modifying dimensionality or symmetry has been shown to be a viable route in order to improve the magnetic response of FeCo alloys [12, 65], although clustering and granularity may hinder a controlled growth of artificial systems [66]. Although several metals have been intercalated under Gr, the combined intercalation of Fe and Co, to form an equiatomic alloy is more challenging, as segregation without intermixing may be dominant [21]. Recently, the growth of homogeneous and smooth Fe_xCo_{1-x} layers underneath Gr/Ir(111) was reported [12], by co-depositing Fe and Co at the same evaporation rate and keeping the substrate temperature at about 500 K, to avoid any Fe-Ir and Co-Ir alloying formation and clustering. X-ray magnetic circular dichroism (XMCD) measurements show that Fe and Co are well intermixed and magnetically coupled underneath Gr, leading to an enhancement of the magnetic moments with respect to pure Fe and Co films, and exhibiting a strong ferromagnetic exchange coupling between the two species [12]. We address the FeCo intercalation on Gr/Ir in Section 5.3. We investigate the electronic and structural properties of the equiatomic FeCo layers grown epitaxially on Ir(111) underneath a Gr cover, by means of Density Functional Theory (DFT). We show that the reduced dimensionality in the artificially confined system leads to a narrowing and a redistribution of majority and minority $3d$ states with respect to the pure species, enhancing also the splitting between Fe $3d$-up and Fe $3d$-down spin bands. Our description of the electronic structure in equiatomic FeCo layers sheds light on the enhanced magnetism previously demonstrated by XMCD [12] and provides a useful insight in the engineering of low dimensional FM alloys.

1.1.2 Oxygen adsorption

It is known that oxygen intercalation constitutes an effective way to decouple graphene from certain metal substrates [34, 67–69]. Indeed, scanning tunneling spectroscopy data (STS) and density functional theory (DFT) results have shown that a graphene layer in the Gr/O/Ru(0001) interface is electronically decoupled from the substrate and graphene-derived π-states become p-doped [67]. Moreover, scanning tunneling microscopy (STM) experiments have also shown [67] that the degree of corrugation observed upon O intercalation is smaller than for the pristine Gr/Ru(00001). Oxygen intercalation also decouples effectively graphene from Ni(111) [68], quenching the strong substrate-adsorbate interaction with the formation of a thin Ni oxide layer at the interface. Angle-resolved photoemission spectroscopy (ARPES) measurements on pristine Gr/Ni(111) show [68] that the graphene π-band is shifted towards higher binding energy by about 2.5 eV with respect to the position of free-standing graphene, and the Dirac cone dissolves into the metal $3d$ bands. Upon oxygen intercalation the hybridization with Ni $3d$ states is removed and the characteristic shape of the Dirac cone is restored and identifiable near the Fermi level.

When Co is exposed to oxygen both physical adsorption and oxidative processes may occur [70, 71]. While low exposures result in chemisorbed oxygen coupled ferromagnetically with the substrate [72, 73], when the oxygen exposure increases, cobalt oxide may form in two different stoichiometries: CoO or, in smaller proportion, Co_3O_4. A theoretical study [71], investigating the surface and subsurface oxygen adsorption on

Co(0001) over a wide coverage range from 0.11 to 2.0 ML, shows that the coverage with the highest adsorption energies is 0.25 ML, whereby the O atoms are adsorbed on the surface. For larger exposures, O begins to penetrate into the surface. In the same study, the energetics of O adsorption and the structural and electronic properties of the surface are discussed in detail. On the other hand, the Gr@Co interfaces can adsorb oxygen under Gr in a stable way [34, 69, 70, 74]; however, the mechanisms and structural details of O adsorption on Co depend sensitively upon the experimental parameters [70, 74], on the epitaxial relation between graphene and the substrate and on the concentration of holes (carbidic islands) in the graphene layer [34]. In the case of epitaxially oriented graphene, the holes in the layer act as intercalation centers.

Recent studies based on X-ray photoemission spectroscopy (XPS), photoemission electron microscopy (PEEM) and ARPES measurements on graphene epitaxialy grown on Co(0001) [34, 69] show that, upon O intercalation, there is an electronic decoupling between graphene and Co. For an O coverage of 0.5 ML the graphene C_{1s} peak shifts by 1.1 eV to lower binding energies and valence band mapping reveals that the graphene band structure acquires a nearly free-standing character with a small p-doping. It has also been shown that the O adsorption can be reversed upon annealing [34].

The mechanisms and structural details of the adsorbed O and the structural and electronic effects of its intercalation in Gr/Co and Gr/CoIr systems are the matter of study of Section 5.1. We start by using DFT calculations to study the effect of O adsorption on Gr/Co and GrCoIr and then address the effect of Co and Fe intercalation on the structural and electronic properties of the Gr/Ir interface. We finally go beyond the DFT level and apply the GW/MPA approach, presented in Section 5.4, to the calculation of the band structure of the Gr/Co interface, of which we present only preliminary results.

1.2 Experimental characterization of the systems under study

In this section we will summarize some of the structural and electronic properties of the Gr/Ir(111) interfaces and the effects of Co and Fe intercalation. We will focus mostly on the experimental results that were obtained in parallel with the theoretical results that are the topic of this thesis, and were then published together, though we also make extensive reference to other results in the literature.

1.2.1 Structural measurements

As mentioned before, the structure of the Gr-metal interfaces depends on the relation between lattice parameter of graphene and that of the substrate. For the case of the

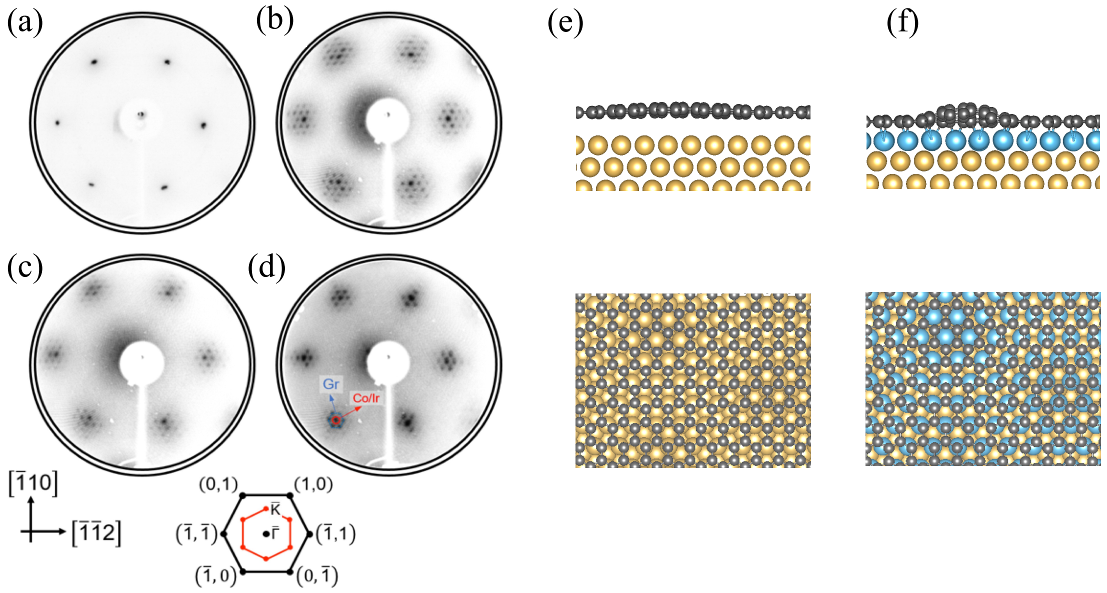

Figure 1.1: Low energy electron diffraction (LEED) images taken at a beam energy of 140 eV: (a) Ir(111), (b) Gr/Ir(111), (c) as deposited 1ML-Co/Gr/Ir(111) and (d) after Co intercalation by annealing at 670 K [*i.e.* Gr/1ML-Co/Ir(111)]. At the bottom: sketch of the diffraction pattern of Ir(111) surface. The surface Brillouin Zone (SBZ) is shown in red. Middle panels: (e) side and top view of the corrugation and moiré pattern of Gr/Ir(111) and (f) of Gr/1ML-Co/Ir(111), as determined by DFT in Ref. [75].

systems studied here, the structural characterization was done using low-energy electron diffraction (LEED). In the LEED technique, single-crystalline materials are bombarded with a collimated beam of low-energy electrons (30–200 eV), that are diffracted and spotted on a fluorescent screen. The diffraction pattern is recorded and the analysis of the spot positions gives information on the symmetry of the surface structure. In the presence of an adsorbate the qualitative analysis may reveal information about the size and rotational alignment of the adsorbate unit cell with respect to the substrate unit cell. In many of the systems under study, LEED measurements reveal the moiré structure of the Gr-metal interface.

Let's start by analysing the effect of the graphene deposition on top of the Ir(111) surface and Co intercalation. The Ir(111) LEED (Fig. 1.1a) shows bright hexagonal spots and after Gr growth (Fig. 1.1b), a larger hexagonal pattern surrounded by hexagonal satellites (up to third order diffraction features), consistent with the smaller Gr lattice parameter, and a moiré superstructure caused by the lattice mismatch between Gr and Ir [76]. After Co deposition (Fig. 1.3c), the surface shows an unaltered pattern, only slightly attenuated after the Co addition, while the number of satellite spots is reduced when the Co layer is intercalated underneath Gr (Fig. 1.1d). The intercalation of a single layer of cobalt, sandwiched between the Ir(111) surface and Gr, results in a corrugated Gr layer with a moiré superstructure superimposed to the hexagonal lattice

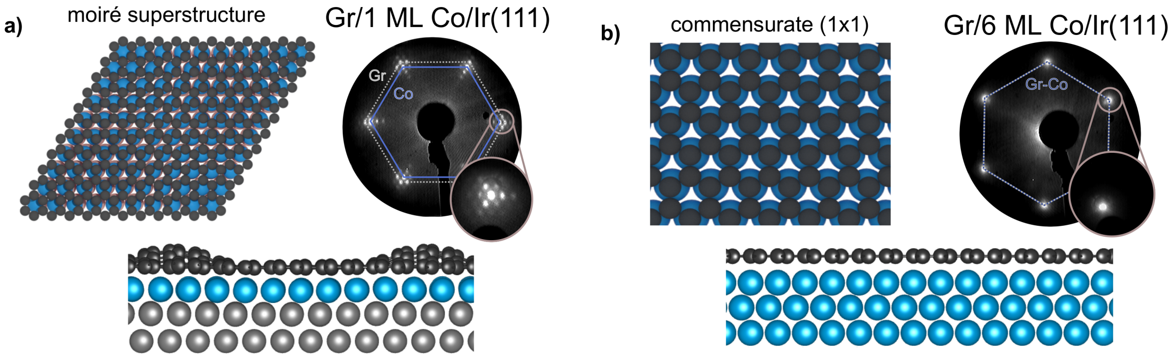

Figure 1.2: Moiré superstructure of Gr on Ir(111) upon intercalation of 1 ML Co (a) and flat and commensurate Gr/Ir upon 6 ML Co intercalation (b), as deduced by ab initio DFT calculation at the LDA level and confirmed by the LEED patterns in Ref. [22].

of Gr, as deduced from the LEED patterns reported in the left panels of Fig. 1.1. These differences are likely correlated with the changes in the Gr morphology in the presence of the Co intercalation [8].

The Co-C interaction in the moiré superstructure depends on the C site, with the result of increasing the corrugation of the Gr layer. The interaction with Gr is stronger in top-hollow and bridge sites, while van der Waals-like interaction is reported for other sites (showing fcc/hcp stacking) [9], as confirmed by DFT structural models [15, 22, 77]. The increase of the Gr corrugation upon Co intercalation and the structural details of the moiré structures, as computed in our DFT calculations, are illustrated in Figs. 1.1(e) and (f).

The structural evolution of the Gr sheet upon intercalation from 1 to 6 ML of Co shown in Fig. 1.2 is consistent with what reported in Refs. [8, 9], giving a picture confirmed by the theoretical predictions. When a single layer is intercalated, the Co atoms arrange pseudo-morphically to the Ir(111) surface, without altering the periodicity and symmetry of the Gr moiré superstructure while its corrugation is enhanced. Further Co intercalation induces the relaxation of the lattice mismatch and the Co film recovers the bulk Co(0001) arrangement, almost commensurate with the Gr lattice, as sketched in Fig. 1.2b. The 1×1 hexagonal pattern confirms that the Gr is commensurate and flat on the Co film.

Similarly to Co, a single layer of Fe, intercalated under Gr grown on Ir(111), induces a corrugation of the Gr membrane and preserves the periodicity of the moiré superstructure, superimposed to the hexagonal Gr lattice, as unraveled by the LEED patterns reported in Fig. 1.3(a,b). The diffraction pattern of Gr/Ir(111) (Fig. 1.3a) shows bright spots in a hexagonal pattern surrounded by satellites, consistent with the moiré superstructure caused by the lattice mismatch between Gr and Ir [32, 76]. After Fe intercalation, the pattern is only slightly attenuated (Fig. 1.3b), thus the first Fe layer appears commensurate to the Ir(111) surface lattice. This evidence is corroborated by

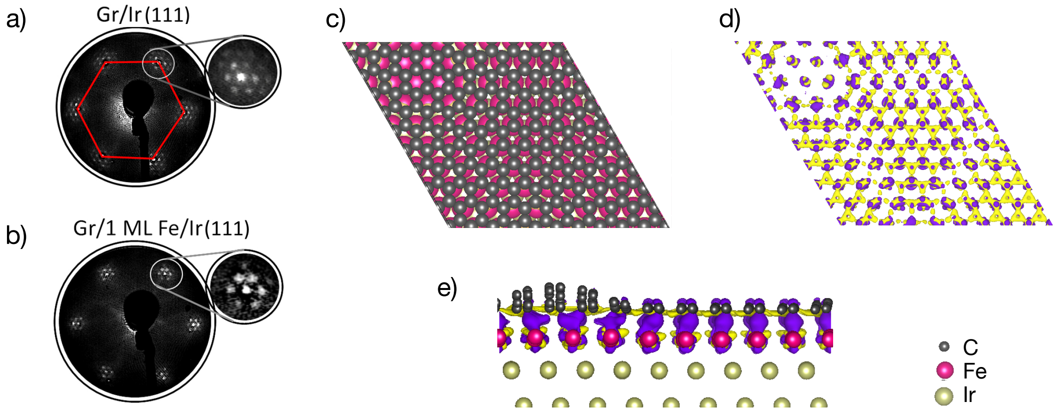

Figure 1.3: Low energy electron diffraction (LEED) patterns (electron beam energy 140 eV) for (a) Gr/Ir(111) and (b) Gr/1 ML Fe/Ir(111); (c) atomic structure as deduced by DFT, top view of the moiré pattern of Gr/Fe/Ir(111) with C atoms represented in gray, Fe in red and Ir in cream; (d-e) charge difference with respect to the free standing Gr and the pristine Fe/Ir(111) slab, computed with DFT in Ref. [1]: (d) top view of the charge difference isosurfaces (positive shown in purple, negative in yellow) and (e) side view of the Gr/Fe/Ir(111) structure showing the graphene corrugation and charge difference isosurfaces, using the same colors described for the previous panels.

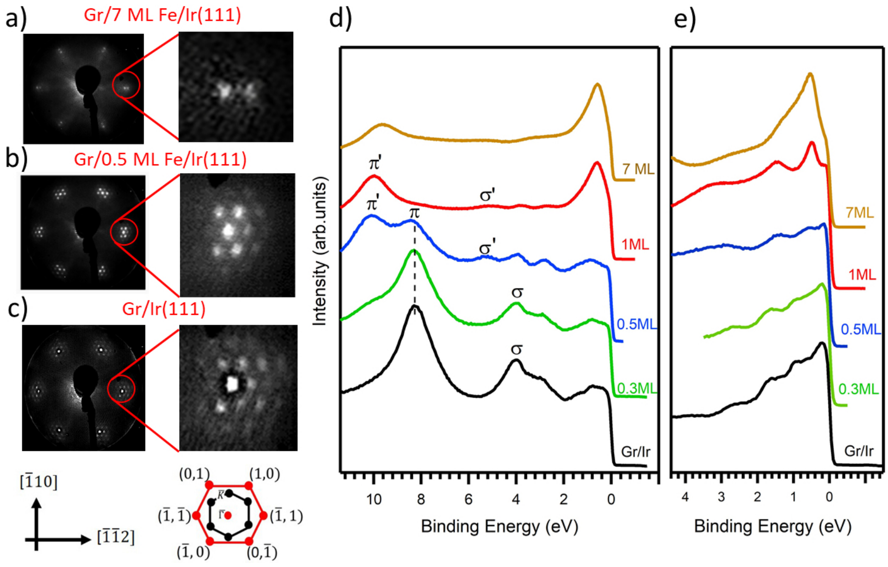

Figure 1.4: LEED patterns (electron beam energy 140 eV) and zoomed pattern around the (10) diffraction spot for Gr/7ML Fe/Ir(111) obtained in Ref. [1]: (a), Gr/0.5ML Fe/Ir(111) (b) and Gr/Ir(111) (c); below: sketch of the main symmetry directions and of the diffraction pattern of the Ir(111) surface (red dots); the Surface Brillouin Zone (SBZ) is shown in black. Photoemission Energy Distribution curves (EDC) taken at 40.814 eV (He II$_\alpha$); angular integrated spectra around Γ (d) and K (e) points of the SBZ for different thickness of the intercalated Fe layer between Gr and Ir.

a recent work [11] where STM measurements show that a few monolayers (ML) of Fe intercalated under graphene arrange in registry with the hexagonal Ir(111) surface, with a corrugation of 1.3 Å, larger than the one measured for Gr/Ir(111) [78].

The topography of the Gr/Fe/Ir(111) heterostructure is similar to the corrugated moiré superstructure observed for the Gr/Co/Ir(111) system [22], but very different from the structure reported for Gr directly grown on bcc-Fe(110) [45]. Previous STM measurements and DFT calculations performed at the LDA level, for Gr/bcc-Fe(110) point out the formation of a periodic corrugated pattern of the graphene layer parallel to the [001] direction of the substrate, consisting in a supercell of 7×17 graphene hexagons with a smaller corrugation of 0.6/0.9 Å, and only a small fraction of the C atoms considerably elevated over the Fe surface, thus making the entire graphene membrane strongly interacting with the metal substrate.

The corrugation of the Gr membrane discussed so far is attenuated when the number of Fe intercalated layers increases above a few ML, with a reduction of the brightness of the superstructure LEED spots, as reported in Fig. 1.4(a-c). At 7 ML, we observe the formation of a Fe film with a lattice constant smaller than Ir(111) and therefore closer to the graphene structural parameters. However, even when the strain induced by the Ir(111) surface is released, the Fe film remains slightly incommensurate with graphene, as shown in Fig. 1.4(a). This is in contrast with the case of Co intercalation beneath graphene on Ir(111): when the Co film is formed, it recovers its hpc lattice constant and becomes commensurate with the graphene layer [9, 15]. Indeed, while the hcp Co(0001) surface lattice parameter (2.50 Å), is comparable with the 2.46 Å of Gr, none of the bcc-Fe faces is lattice-matched with graphene. In fact, graphene directly grown on bcc-Fe(110) presents a distorted hexagonal symmetry with only a partial match with the graphene lattice, as deduced by STM [45]. In our case, the Fe intercalated multilayer has a novel strained structural configuration with a 8% mismatch with respect to the graphene lattice constant.

Importantly, the magnetic response of Fe films is extremely sensitive to tiny variations of the structural configuration [79], and the strained lattice of the Fe film intercalated under graphene can give rise to an altered distribution of the electronic majority and minority states and to different spin and orbital configurations with respect to the bulk reference [53].

Figure 1.5 shows the LEED patterns of Gr/Ir(111), taken with primary energy of about 90 eV, before (a) and after (b) the intercalation of nominal 3ML of FeCo. The moiré superstructure characteristic of the corrugated Gr/Ir(111) system is maintained after FeCo intercalation, attesting that the equiatomic FeCo layers arrange pseudomorphycally on the hexagonal Ir(111) surface. The moiré pattern is only slightly smeared out at increasing amount of intercalated atoms, with an intensity reduction of the extra spots. The persistence of multiple reflection spots suggests that the thickness of the in-

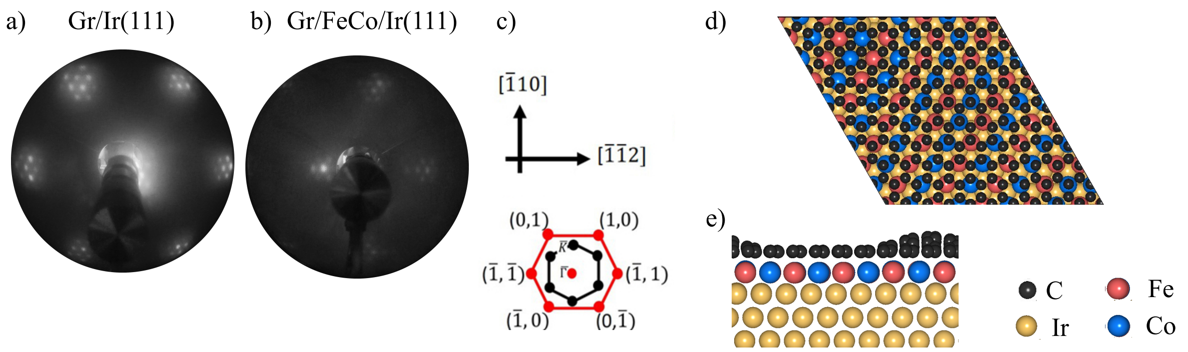

Figure 1.5: Low energy electron diffraction (LEED) patterns (electron beam energy 90 eV) of (a) Gr/Ir(111) and (b) Gr/FeCo/Ir(111), taken slightly off-normal, as obtained in Ref. [2]. In the middle: sketch of the diffraction pattern and Brillouin Zone (BZ) of Ir(111), referred to (a-b) panels. (c) Atomic structure as deduced by DFT, top view of the moiré pattern of Gr/FeCo/Ir(111) with C atoms represented in gray, Fe in red, Co in blue and Ir in cream; (d) side view of the Gr/FeCo/Ir(111) structure showing the Gr corrugation, using the same colors described in the previous panel.

tercalated FeCo layer is within 1 and 2 ML, as deduced by comparison with the LEED patterns of pure Co [9] and Fe [1] intercalated systems.

1.2.2 Electronic properties accessed by ARPES

Angle-resolved photoemission spectroscopy is a technique for revealing the band structure of materials by measuring the electrons ejected from initial energy and (quasi)-momentum states into vacuum [80]. The energy difference corresponds to the energy of the photon used to excite the solid. In the process, the electron momentum remains virtually intact, except for its component perpendicular to the material's surface. The band structure is thus translated from energies at which the electrons are bound within the material, to energies that free them from the crystal binding and enable their detection outside of the material.

As mentioned above, the band structure of graphene grown on Ir(111) is similar to the free standing graphene bands (left panel of Fig. 1.6). Upon Co intercalation, the band structure as measured by ARPES [9] is closer to the Gr/Co(0001) band structure [39]. The interaction of graphene with the substrate shifts the π band to higher binding energies as compared to freestanding graphene which results in an upward dispersion into the second Brillouin zone and no visible band gap the K point. The Dirac-point of graphene on the Co surface is located at 2.82 eV. Due to the Co large magnetic exchange splitting the π states of graphene are also expected to become spin polarized.

The photoemission spectral density as a function of Fe intercalation thickness is reported in Fig. 1.4 (d) and (e), at the Γ and K points of the surface Brillouin zone

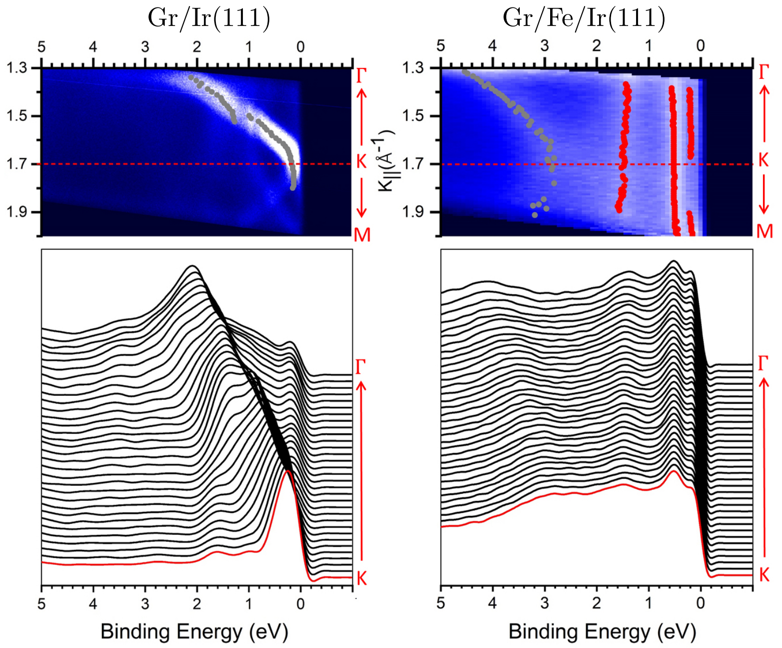

Figure 1.6: Angular resolved photoelectron spectroscopy hν=40.814 eV spectra of Gr/Ir(111) (left panels) and Gr/1 ML Fe/Ir(111) (right panels), around the K point of the SBZ. Electronic band structure vs. $k_{//}$ as intensity plot (upper panels); spectral density plotted as sequential EDC curves from the K point towards Γ (bottom panels), as obtained in Ref. [1].

(SBZ), respectively. The Gr/Ir(111) valence band at the Γ and K points presents the expected electronic spectral density [42, 81] whereas the intercalated system shows three new features can be observed when comparing the intercalated system with the bare Gr/Ir : (*i*) the appearance of a peak at 10 eV and the disappearance of the one related to the π- bands of bare Gr/Ir(111) at 8 eV at the Γ point; (*ii*) the quenching of the intensity from the Ir surface states close to the Fermi level; and (*iii*) the emergence of extra spectral density in the low binding energy region.

Concerning (*i*), the intensity of the peak at 8 eV BE at Γ, corresponding to the bottom of the π-band for bare Gr/Ir(111), decreases with increasing Fe thickness. The peak emerging at 10.0 eV BE can be associated to the shifted π-band, due to the interaction of Gr with the intercalated Fe layer. An interacting π-band has also been observed for Co and Ni layers sandwiched between Gr and Ir [9, 10, 13, 40]. The presence of two features associated with the π-bands, with opposite intensity behavior before the completion of the first Fe ML, demonstrates the coexistence of bare Gr/Ir regions and regions of intercalated Fe atoms, up to the formation of a smooth Fe single layer, when the peak at 8 eV (bare Gr/Ir) is eventually quenched.

Furthermore, (*ii*) the progressive intensity lowering of the Ir(111) surface states in the energy region 0-3 eV BE, upon Fe intercalation, without any energy shift, suggests the absence of Fe-Ir intermixing observed at higher intercalation temperatures [21, 82]. The emergence of a spectral density (*iii*) at low binding energy close to the Fermi level can be ascribed to electronic states mainly localized in the Fe layer, since their intensity definitely raises at increasing Fe thickness, as can be clearly observed in the spectral density of 7 ML Fe intercalated under graphene (orange curve in Fig. 1.4e).

A clearer assignment of the electronic states due to the Fe-Gr interaction process can be derived from the electronic state dispersion. The ARPES data around the K point of the SBZ for Gr/Ir(111) and Gr/1 ML Fe/Ir(111), are shown in Fig. 1.6 (left and right panels, respectively). Considering the energy region closer to the Fermi level, three localized Fe states can be identified at about 0.2 eV, 0.5 eV and 1.5 eV BE, and found to be only slightly dispersing over the whole SBZ (Fig. 1.6 right panel), as expected for a confined Fe film. Inspecting the spectra at higher binding energies, other Fe-related states are observed in the energy region of 3-4 eV BE, resonant with the graphene π-band states. Besides the presence of these localized Fe states close to the Fermi level, the most evident consequence of Fe intercalation under graphene is the downshift of the Dirac cone at the K point of the SBZ, similarly to the case of Gr/Co/Ir [9]. In fact, the π-band, as deduced by the EDCs (Fig. 1.6), is broadened and less defined after intercalation and there is a coexistence of other Fe related states in this energy region (3-4 eV). The position of the Dirac cone vertex (at K) is downshifted by 3 eV, while the bottom of the π band is less shifted at Γ. It is worth noting that the Dirac cone is shifted by 2 eV towards higher binding energy also for graphene directly grown on Fe(110) [47], suggesting a weaker interaction in that case.

Figure 1.7(a) shows ARPES results of Gr/FeCo/Ir(111) taken along $\bar{\Gamma}$-$\bar{\mathrm{K}}$. The effect of Fe and Co states on the π and σ bands of Gr can be discussed by comparing the system under study with pure Gr/Co and Gr/Fe (either supported on Ir(111) or not), as reported in the literature [1, 9, 37, 39, 82]. At the $\bar{\Gamma}$-point (Fig. 1.7a) the bottom of the π band and the top of the σ bands are shifted to about 10.2 eV and 5.4 eV of binding energy (BE), respectively, in agreement with previous results for pure Fe and Co intercalated systems [1, 9]. Moreover, ARPES data extracted along the direction perpendicular to $\bar{\Gamma}$-$\bar{\mathrm{K}}$ (Fig. 1.7b) shows the maximum of the Gr π band at about 2.1 eV of BE. Other pure Gr/FM systems exhibit a π band maximum between 2.5 and 3.0 eV, depending both on the metal and on the number of intercalated layers [1, 9, 37, 39, 40, 82]. The Gr/Co system, e.g., leads to a crossing point between π bands located at 2.8 eV of BE [9]. For Gr/FeCo/Ir, the lower BE value of the π band maximum suggests a reduced width of the FeCo-d states and thus a reduced hybridization with the π band.

The region in proximity of the $\bar{\mathrm{K}}$-point exhibits several features directly related to the mixed Fe-Co interface with Gr. Specifically, in Fig. 1.7(a) we highlight with red dashed lines three slightly dispersing states, crossing the $\bar{\mathrm{K}}$-point at about -1.8 eV, -0.6 eV and at the Fermi level (E_{F}). It is worth noticing that the appearance of these well-defined localized bands within $\sim$2 eV from E_{F} and their dispersive behavior provide further evidence of a uniform FeCo alloy. The bands at about 4 eV of BE, less dispersive

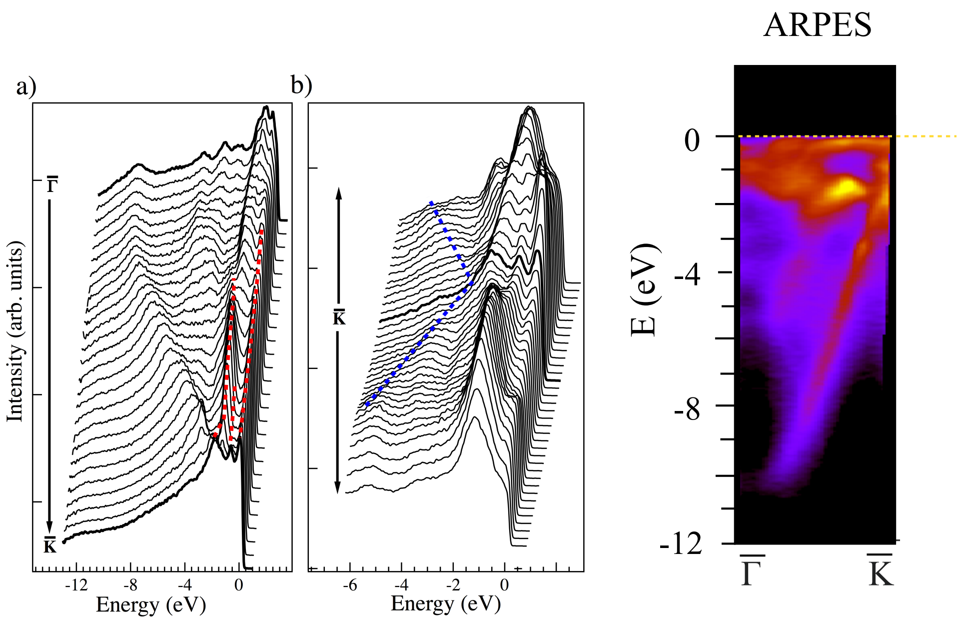

Figure 1.7: (a) Selected EDCs of Gr/FeCo/Ir(111), extracted from data of Fig. 5.14(a), acquired with photon energy of 86 eV and taken along the $\bar{\Gamma}$-$\bar{\mathrm{K}}$ direction. Red dashed lines highlight states originating from the FeCo interface. (b) Selected EDCs taken along the direction perpendicular to $\bar{\Gamma}$-$\bar{\mathrm{K}}$. Blue dashed lines highlight the π band of Gr. The $\bar{\mathrm{K}}$-point has been extracted at electron kinetic energy of about 80 eV. Figures, as obtained in Ref. [2].

towards the $\bar{\mathrm{K}}$ point and resonant with the π band of Gr, can be attributed to the FeCo interlayer. As discussed in the following, these states are due to the majority $3d$ states of both Co and Fe atoms, while the states close to E_{F} can be associated to the Fe and Co $3d$ spin minority bands.

1.2.3 Near Edge X-ray Absorption Spectroscopy

X-ray absorption fine structure (NEXAFS) is a kind of absorption spectroscopy based on the analysis of the photoabsorption cross section for electronic transitions from an atomic core level to final states in the near conduction energy region, where the wavelength of the photoelectron is larger than the interatomic distance between the absorbing atom and its first neighbour atoms. The measurements give information of on the local structure and on the unoccupied local electronic states.

The C K absorption spectra (NEXAFS) for Gr/Ir(111) and Gr/1ML-Co/Ir(111), published in Ref. [75], is reported in panels (a,b) of Fig. 1.8. The electric field oriented almost normal (70° with respect to the surface plane) allows the enhancement of the signal from the π^* states, even though this setup does not completely quench the σ^* states contribution. Concerning Gr/Ir(111), the main peak at 285.5 eV is associated with the π^* conduction states. Moreover, a shoulder located at about 284.2 eV can be seen in Fig. 1.8(a). This feature observed for single layer Gr on metals, graphene

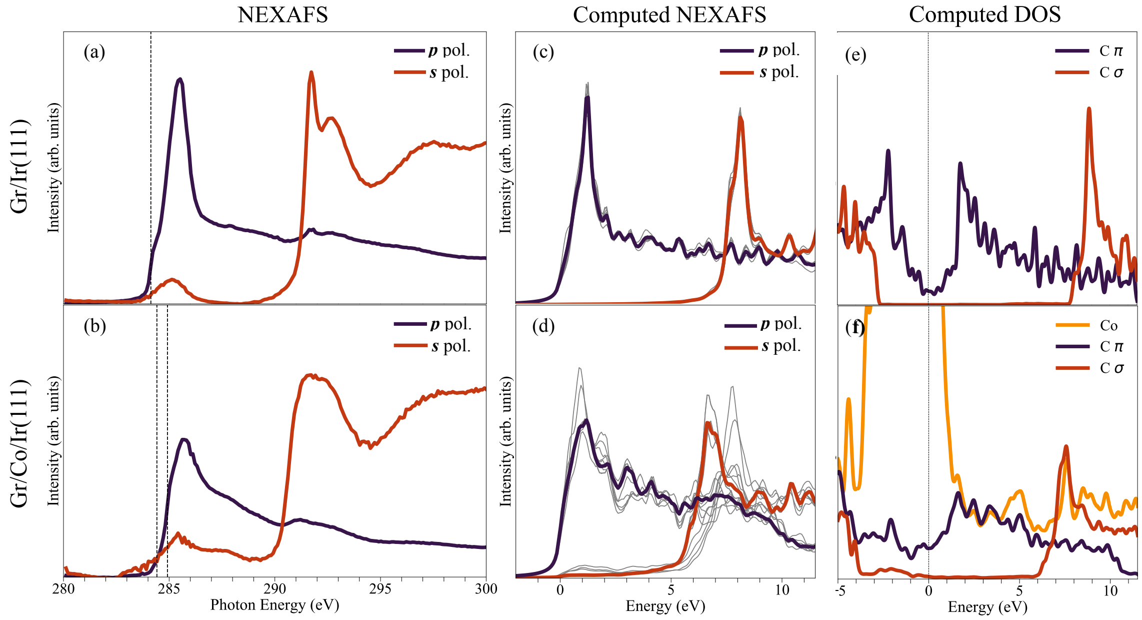

Figure 1.8: Measured NEXAFS (a,b), computed NEXAFS (c,d), and DOS data (e,f) for Gr/Ir(111) (upper panels) and Gr/1ML-Co/Ir(111) (lower panels), respectively. Purple and red lines correspond to C 1s levels excited by out-of-plane and in-plane polarized photons. Vertical dashed lines correspond to the Fermi level reference, as deduced by the energy position of the C 1s core levels (284.13 eV for Gr/Ir; 284.92 eV and 284.42 for Gr/Co/Ir). Central panels: simulated NEXAFS spectra averaged over different positions of the half core-hole (see supplementary information of Ref. [75]). The grey lines represent the spectra computed for different core-holes, and give an idea of the initial-state induced broadening of the spectra. Right panels: computed DOS projected on Co and Gr σ (C s+p_x+p_y) and π (C p_z) orbitals for the same systems. The zero of the energy scale corresponds to the Fermi level.

flakes [83, 84] and nano-graphite grains [85], was attributed to edge-derived electronic states. However, in the present case, the highly ordered corrugated Gr structure with large single domains, cannot justify a contribution from edge defects to the pre-edge feature. On the other hand, a small p-doping observed for Gr/Ir(111) [86] can induce a tiny density of empty states below the Dirac cone apex available for the excited core electrons. This is supported by DFT simulations [75] where the comparison between the DOS computed for free standing Gr and Gr on Ir reveals a small p-doping corresponding to an excess charge of about 1.1×10^{-3} electrons per C atom. The higher energy features are due to transitions towards higher-lying states resonant with contributions coming from the σ^* conduction states, thus more visible in s configuration (red curve).

The measured C K absorption edge of Gr/1ML-Co/Ir(111) is reported in Fig. 1.8(b). Three main signatures diversify the NEXAFS spectra before and after the Co intercalation (*i*) the disappearance of the pre-edge feature due to the small p-doping observed for Gr/Ir(111) (*ii*) a broadening of the spectral features related to the π^* and σ^* transitions, and (*iii*) an energy shift of the absorption onset larger for the σ^* transitions than for the π^* ones.

The quenching of the pre-edge can be ascribed to removal of p-doping due to a shift of the Dirac cone, as discussed later in Section 5.4. As far as it concerns the π^* transitions, the main peak, centered at 285.7 eV appears weaker and broadened. Moreover, in the energy region above the onset, between 287-290 eV, a wide shoulder appears in both p and s configurations, as observed also for Gr grown on highly interacting substrates like Gr/Ru(0001), Gr/Rh(111) or Gr/Ni(111) [41]. The origin of the smearing of these features can be due both to initial state effects, and hybridization of the out-of-plane C-π and Co-d final states. The initial state effect is due to the spatially modulated adsorption potential of C upon Co-intercalation, which stems from the moiré structure of Gr/Ir(111), reflected in different binding energies of the C 1s Gr core levels. After intercalation, the C 1s core level photoemission presents a multi-component line-shape with two main features, at 284.42 and 284.92 eV [9, 15], assigned to C atoms in the Gr layer weakly and strongly bound to the intercalated Co layer, respectively.

The presence of these features induces a convolution of multi-edge onset, however they cannot fully explain the large broadening of the spectral density in the energy range 285-290 eV, where the contribution from the hybridized Co-C states dominates. As supported by the DFT calculations (Fig. 1.8f), a contribution to the π^* transitions spectral density can be certainly ascribed to the hybridization of C-π and Co states induced by the intercalation. Such contribution is further evidenced by changing the light polarization from p to s. In fact, in-plane σ^* states present an onset at about 291 eV for Gr/Ir(111) with two well-defined structures, while for Gr/1ML-Co/Ir(111) the absorption from the σ^* states is observed also at a lower photon energies (285-290 eV), with slightly smeared structures. This is consistent with a broken symmetry of the

π^*-conduction states as mixed with the Co d states, resulting in a non-negligible signal with s-polarization.

Simulated the NEXAFS spectra for the in-plane and out-of-plane polarizations using DFT and including core-hole effects help interpret the experimental results. Results are reported in Fig. 1.8(c,d) for Gr/Ir(111) and Gr/1ML-Co/Ir(111), respectively. In both figures we show the spectra computed considering the half core-hole located on different carbon atoms, sampling moiré valleys, hills, and intermediate regions (grey lines) and the final spectra obtained by performing a weighted average (blue and red lines) that takes into account the C-metal distance. The comparison of the averaged spectra clearly shows a broadening of the peaks for Gr/1ML-Co/Ir(111) when compared with Gr/Ir(111), in agreement with experiments.

In order to further clarify the differences seen in the NEXAFS spectra after Co intercalation we report in Fig. 1.8(e,f) the computed projected density of states (where no core-hole is considered) of the two systems, focusing on the Gr π^*- and σ^*-projections. A less structured and more broadened DOS is clearly evident for the case of Gr in Gr/1ML-Co/Ir(111), confirming the idea of a contribution from the change of the final-state eigenpairs to the experimentally observed broadening of the NEXAFS spectrum. The σ^* states located at 8.9 eV for Gr/Ir(111) are also shifted towards lower energies, at 7.6 eV, for Gr/1ML-Co/Ir(111). Such a shift allows for the superposition of the Gr σ^* and Co peaks and is in agreement with the downshift of the σ^* peaks seen for Gr/1ML-Co/Ir(111), in the measured and computed NEXAFS spectra.

Besides the broadening of the spectra, a shift in the energy position of the σ^* and π^* main peaks of Gr/1ML-Co/Ir(111) with respect to Gr/Ir(111) is observed. In agreement with experiments, where a shift of about 0.8 V is measured, the main σ^* peak is found in calculations [75] 1.1 eV lower in energy for Gr/1ML-Co/Ir(111) than for Gr/Ir(111). This means that, the weaker the Gr-metal interaction [Gr/Ir(111) compared to Gr/1ML-Co/Ir(111), but also C atoms further away from the surface in the moiré structure of Gr/1ML-Co/Ir(111)], the higher the energy of the main σ^* peak in the NEXAFS spectra. A downshift in energy of the electronic σ^* bands calculated for Gr/Co with respect the Gr layer is reported in Section 5.4, confirming the observed shift of the onset of σ^* transition in the C K edge and the influence of the Co layer under graphene even on the empty states far from the Fermi energy.

1.2.4 Magnetic properties through X-ray magnetic circular dichroism

X-ray magnetic circular dichroism (XMCD) is the spectrum resulting from the difference of two X-ray absorption spectra (XAS) in the presence of a magnetic field, measured respectively with left and right circularly polarized light. The small differences in the

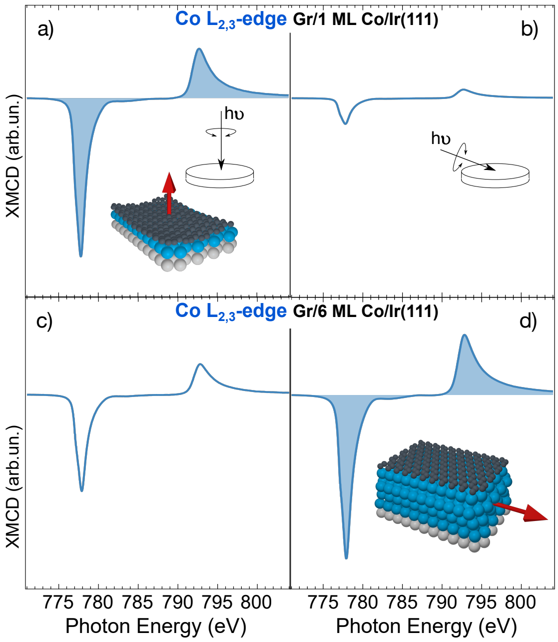

Figure 1.9: XMCD spectra of Co $L_{2,3}$ absorption edges for Gr/1 ML (a) and b)) Co and Gr/6 ML (d) and d)) Co acquired in remanence at RT in normal and grazing incidence geometries. Magnetic anisotropy switches from perpendicular (Gr/1 ML Co, a) to parallel (Gr/6 ML Co, d) to the surface plane. Figure adapted from Ref. [22].

XMCD spectrum are directly related to the magnetic properties of the atom considered (selected by the corresponding energy edges) and allow one to obtain, for instance, its spin and orbital magnetic moments.

The absorption spectra for XMCD are usually measured at the L-edge for transition metals like Fe, Co and Ni. In the case of Fe, the process corresponds to an excited electron from a 2p to the 3d state by an X-ray of about 700 eV. The spectra contain information on the magnetic properties through the 3d states that originate them.

Turning to the magnetic properties, the XMCD spectra at the Co $L_{2,3}$ edge for a single Co layer and a Co film intercalated under the Gr sheet, obtained as the difference between the absorption edges acquired with left- and right-circularly polarized radiation, are reported in remanence condition, i.e. with no applied external field, at room temperature in the right panels of Fig. 1.9. The higher dichroic response with photon impinging at normal incidence (NI) unravels the out-of-plane magnetic anisotropy of the Co layer in the incommensurate configuration with a stretched Co-Co distance, Fig. 1.2b, in agreement with Refs.[8, 10]. Conversely, the higher dichroic response for Co $L_{2,3}$ XMCD at grazing incidence (GI) for the thicker intercalated Co film, reveals a magnetic state with the Co bulk in-plane easy magnetization axis. The Gr/Co heterostructures, exhibiting a tunable easy magnetization axis direction, are ideal templates to test the magnetic coupling of paramagnetic flat-lying FePc and CuPc molecules. [25]

The strong ferromagnetic behavior of GrFeIr is confirmed by the X ray absorption

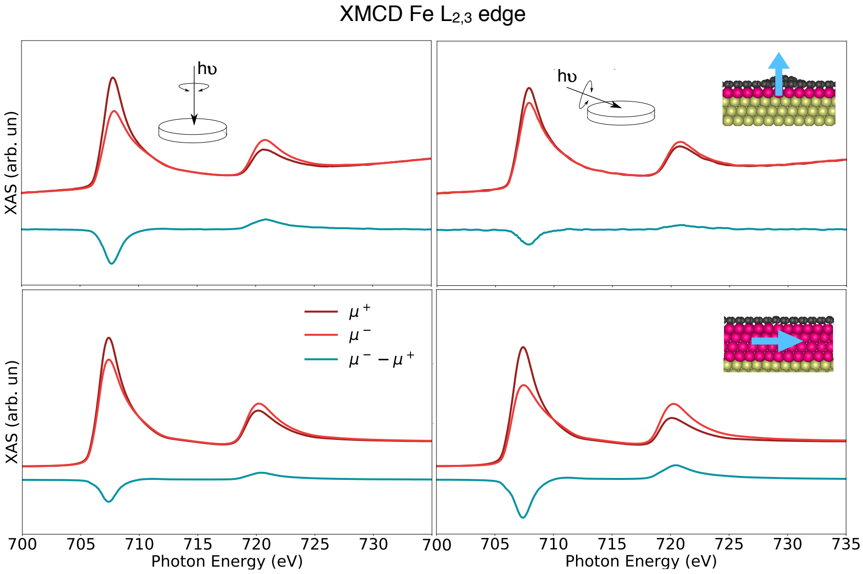

Figure 1.10: XMCD spectra of Fe $L_{2,3}$ absorption edges for Gr/1.4 ML Fe/Ir(111) (top) and Gr/7ML Fe/Ir(111) (bottom) acquired in remanence at RT in normal (left) and grazing (right) incidence geometries (see sketches for the experimental geometry). The easy magnetization direction switching from perpendicular (top) to parallel (bottom) to the surface plane is indicated by the blue arrows.

spectra and the XMCD at the $L_{2,3}$ edges for 1.4 ML and 7 ML of Fe sandwiched between Gr and Ir(111), shown in Fig. 1.10. XAS are acquired in remanence conditions with circularly polarized radiation and with photons impinging normal (left panel) and grazing (right panel) to the surface. The XMCD spectra are obtained as the difference between the absorption edges acquired with left- and right-circularly polarized radiation. The higher dichroic response with photon impinging at normal incidence (left panel) reveals an out-of-plane magnetic anisotropy of the Fe layer when it is pseudomorphic to the Ir(111) surface, with a stretched Fe-Fe distance with respect the bulk bcc(110) or (111) surfaces. The higher dichroic response for Fe $L_{2,3}$ XMCD at grazing incidence (right panel) for the thicker intercalated Fe film, unveils a switch of the easy magnetization axis from perpendicular to the surface to in-plane. This is consistent with the magnetic response of heterostructures of single Co or Fe_xCo_{1-x} layers on Ir(111) covered with a Gr membrane [12, 22].

The spin and the orbital moments at the Fe site, as deduced via XMCD sum rules, show a doubled L/S_{eff} ratio ($S_{eff} = S+7D$ and D is the dipolar moment [87, 88]), with respect to the bulk element (0.11±0.01 for a Fe single layer and 0.09 ±0.01 for the 7 ML). These experimental results, related only to the intensity of the dichroic signal and independent on the number of $3d$ holes, suggest an enhanced magnetic response due to the redistribution of the majority spin states in the conduction Fe bands. The evaluated average total moment is 2.1±0.2 μ_B/atom for 7 ML of Fe intercalated under Gr, in fair agreement with 2.2 μ_B/atom (spin moment), as deduced by the DFT predictions. The orbital and spin moment for a single layer of Fe, where interface effects can play a role, shows a comparable magnetic response, as deduced by the similar dichroic signals reported in Fig. 1.10. As mentioned above, the pseudomorphic hexagonal Fe single layer grown directly on Ir(111) presents a complex magnetic structure with skyrmionic spin spiral textures stabilized by the $3d - 5d$ hybridization between Fe and Ir [89–92]. On the other hand, other magnetic materials like Europium have been successfully intercalated underneath graphene on the same Ir(111) surface [93] and, depending on its coverage, Eu displays either a paramagnetic or a ferromagnetic behavior [94]. The clear magnetic dichroism response of the single Fe layer intercalated under graphene suggests a different spin configuration. Furthermore, this confined single Fe intercalated layer, with stretched Fe-Fe distances, presents spin and orbital configurations similar to that of the thin Fe intercalated film, where the influence of the Fe-Ir interface is completely released.

Chapter 2

Theoretical frameworks

2.1 Density Functional Theory (DFT)

Density functional theory (DFT) is one of the most successful approaches to treat the many-body problem of electronic systems from an *ab initio* or first principles perspective, especially when it comes to finding properties of the ground state represented by the wavefunction Ψ_0, like the total energy E_0 of a system:

$$E_0 = \langle \Psi_0 | H | \Psi_0 \rangle = \min_{\Psi} \langle \Psi | H | \Psi \rangle \tag{2.1}$$

where H is the electronic Hamiltonian and the minimization is performed over all possible solutions of the Schrödinger equation.

In mean field theories one considers non-interacting electrons in a effective potential by writing Ψ as a product of one-electron orbitals like in Hartree [95], or by introducing particle exchange in the form of a Slater determinant like in Hartree-Fock [96]. DFT proposes an alternative way to avoid the complications of dealing with N-particle wave functions $\Psi(\mathbf{r_1}, ..., \mathbf{r_N})$. Following the earlier ideas by L. H. Thomas [97] and E. Fermi [98], the fundamental quantity in DFT is the ground-state electronic density:

$$\rho_0(\mathbf{r}) = N \int d\mathbf{r_2}...d\mathbf{r_N} \, |\Psi_0(\mathbf{r}, \mathbf{r_2}, ..., \mathbf{r_N})|^2 \tag{2.2}$$

from which it is possible in principle to compute any property of the many-particle system by minimizing a corresponding functional, whose existence is guaranteed by Hohenberg and Kohn's mathematical proofs [99] of the following properties:

- For any system of interacting particles there is a one-to-one mapping up to a constant value between the space of external potentials, v_{ext}, and the space of the ground-state densities, ρ.
- Since the Hamiltonian is thus fully determined, except for the constant shift of the energy, it follows that the many-body wave functions for all states are determined.

- The ground state energy is the variational global minimum of the total energy functional, $E[\rho]$, of all possible densities describing the system: $E_0 = E[\rho_0] \leq E[\rho]$ for any ρ.

The properties resulting from the Hohenberg–Kohn theorems are apparently very simple considering the many-body problem. However, they leave the challenge of how to reformulate the many-body theory in terms of functionals of the density, for which the Hohenberg–Kohn theorems do not provide any recipe. We know however that, due to the electronic correlation, the unknown functionals of the density in DFT must be nonlocal, depending simultaneously on $\rho(\mathbf{r})$ at different $\mathbf{r}$ positions. Since the total energy is a functional of the density, it is possible to isolate some parts that are obviously density-functionals:

$$E[\rho] = \langle \Psi_0 | T | \Psi_0 \rangle + \frac{1}{2} \int d\mathbf{r} d\mathbf{r}' \frac{\rho(\mathbf{r})\rho(\mathbf{r}')}{|\mathbf{r} - \mathbf{r}'|} + \int d\mathbf{r} \rho(\mathbf{r}) v_{ext}(\mathbf{r}) + E_{xc}[\rho], \qquad (2.3)$$

where $v_{ext}(\mathbf{r})$ is a given local external potential. The remainder will still be a functional of the density and is called the exchange-correlation energy, $E_{xc}[\rho]$. The form of the kinetic energy term given by the expectation value of the kinetic energy operator, T, is also unknown.

Hohenberg–Kohn theorems allow for the possibility of different wavefunctions having the same density, since ρ carries much less information than Ψ. Then, the problem of knowing whether or not a certain density function is the ground-state density of a local potential is called v-representability. In order to provide a simple way of approximating the unknown parts of the functional $E[\rho]$, Kohn and Sham [100] formulated an efficient strategy in which they introduce a fictitious system of non-interacting electrons in an effective external potential, v^{KS}. Given that any interacting v-representable density has a non-interacting v-representable density arbitrarily close to it [101], the Kohn-Sham potential, v^{KS}, is built in order to reproduce the same density as the real interacting system:

$$v^{KS}(\mathbf{r}) = v_{ext}(\mathbf{r}) + \int d\mathbf{r}' \frac{\rho(\mathbf{r}')}{|\mathbf{r} - \mathbf{r}'|} + v_{xc}[\rho](\mathbf{r}) \qquad (2.4)$$

The energy functional of the interacting system is then written in terms of the non-interacting (Kohn-Sham) orbitals, $\phi_i(\mathbf{r})$, that minimize the non-interacting electronic kinetic energy, $\langle T^{KS} \rangle$, under the fixed density constrain. The many-body problem is then simplified to an independent particle system of equation:

$$\left(-\frac{\nabla^2}{2} + v^{KS}(\mathbf{r}) \right) \phi_i(\mathbf{r}) = \epsilon_i \phi_i(\mathbf{r}), \qquad \rho(\mathbf{r}) = \sum_i^N |\phi_i(\mathbf{r})|^2. \qquad (2.5)$$

Therefore, the problem reduces to obtaining an adequate approximation for v_{xc}, within the framework of the fictitious non-interacting system.

2.1.1 Exchange-correlation functionals and pseudo-potentials

The exchange–correlation potential, v_{xc}, is determined by the combination of the repulsive electron-electron Coulomb interaction and the Pauli exclusion principle. Its corresponding exchange–correlation energy, $E_{xc}[\rho]$, can be reasonably approximated by a local (or semilocal) functional in a large number of materials. The first practical realization of the so-called *local density approximation* (LDA) was introduced by Kohn and Sham [100], in which the exchange-correlation energy density at each point $\mathbf{r}$ in space is computed by means of a homogeneous electron gas model, for which the exact exchange-correlation energy density $\epsilon_{xc}^{\mathrm{HEG}}$ is available [102] as a function the gas density. Practically, this leads to the following expression:

$$E_{xc}^{\mathrm{LDA}} = \int d\mathbf{r}\rho(\mathbf{r})\epsilon_{xc}^{\mathrm{HEG}}(\rho(\mathbf{r})). \tag{2.6}$$

Other approximations are intended to improve the locality of dependency on the density in LDA by means of a semilocal generalized gradient approximation (GGA), meta-GGA or by including a weighted contribution of the exact exchange potential (hybrid functionals). More detailed descriptions can be found in dedicated reviews and code implementations, e.g. [103–105].

In order to make DFT calculations feasible with delocalized basis sets like plane-waves, it is common to resort to a pseudopotential approximation, which reduces the number of electrons involved in the calculation and the number of plane waves required to achieve converged results. To this aim, the density ρ is partitioned in valence and core electronic contribution. Since core electrons in a solid do not participate in chemical bonding, they are assumed to occupy the same orbitals as in atoms (frozen-core approximation). Therefore in the calculations only valence electrons are explicitly considered. The attractive interaction between the nuclei and the valence electrons is screened by the core electrons giving rise to a weaker (and smoother to represent in plane-waves) effective potential: the pseudopotential. The effective interaction between the ionic cores and the valence electrons are described by pseudo-wavefunctions. There are several different recipes to construct atomic pseudopotentials from first principles, complying for instance with norm conservation. During the presentation of this Thesis we mention the specific pseudopotentials used in each set of calculations.

2.1.2 Basis set and supercell techniques

A fundamental initial choice in DFT is the basis set employed in the calculations. Multiple choices are possible and available, ranging from very localized to very delocalized bases. Depending on the system, the choice will determine how fast the results will converge with respect to the number of basis functions included in the calculations. Plane-waves (PWs) constitute one of the most common options to study extended systems (such as bulk materials or surfaces), also empowered by mathematical simplicity and orthonormality properties. In fact, PWs are especially suitable for periodic crystals, where they provide intuitive phenomenological understanding. Moreover, thanks to fast Fourier transforms (FFT), many general methodologies for solving differential equations, including the Schrödinger and Poisson equations, are based in plane-waves and spacial and energy grids [106].

Furthermore, the spatial description of the eigenfunctions that satisfy the Schrödinger equation in a system with periodic boundary conditions can be simplified by means of the Bloch theorem, according to which the solution has the form of a plane wave modulated by a periodic function with the same periodicity of the system. Due to the translational symmetry, for the description of the properties of the system in the reciprocal space it is enough to consider the first Brillouin zone, that is the most compact possible primitive cell. However, sometimes a supercell construction, that is compose by a set of neighbouring primitive cells repeated along one or more directions, is used in order to locally relax the symmetry of the system. A supercell approach, for instance, can be used for describing defects in a bulk material or low dimensional materials as surfaces, polymers and molecules, where an artificial vacuum region is included along the non-periodic directions of the supercell in order to reduce the intensity of the interactions with their replicas.

A computational methodology should be flexible enough to compute different kind of materials, be they finite or infinite, in order, for example, to combine them into an hybrid system as in the case of the systems under study in the present thesis. Even if mixtures of localized and non-localized basis sets do exist, in many cases the simplicity of plane-waves is preferred to describe, for instance, organic molecules adsorbed on complex Gr/metal interfaces [22]. In this thesis we adopt the suppercell technique for most of the calculations through the implementations in the Quantum ESPRESSO [107, 108] and Yambo [3, 4] packages.

2.1.3 Band unfolding

The analysis of the band structure is one of the most basic and useful tools for interpreting the calculated electronic properties of simple crystals. The plot of allowed electronic energy levels in a solid, corresponding to the energy of the Bloch orbitals as a function of their crystal momentum in the primitive Brillouin zone, tells us by simple inspection, e.g., whether a material is a metal or a semiconductor. In a heterogeneous material, a deeper analysis may reveal the main features of the bonding interactions. However, if we consider a supercell, even if it corresponds exactly to the repetition of several unit cells, we will get a much more complex (folded) band structure. As the size of the cell in real space increases, the first Brillouin zone in reciprocal space shrinks and more lines populate the band structure, due to the folding of the bands into the smaller Brillouin zone. This situation makes difficult its analysis and the comparison with experiments. By using the properties of the Bloch functions, it is possible, using band unfolding techniques [109–112] to restore the picture within the primitive cell, even in difficult cases such as those with actually broken translational symmetry.

In our supercell calculations, we adopted the method proposed in Ref. [110], as implemented in the `unfold-x` [113] code, interfaced with Quantum ESPRESSO. This approach has been further extended by our group in order to include atomic projections on Lödwin orthogonalized atomic orbitals, as computed by the Quantum ESPRESSO tool `projwfc.x` [107, 108].

2.1.4 Magnetism

One of the first extensions made to DFT consists in the inclusion of the spin degrees of freedom, thanks to the development of the spin-density-functional theory [114, 115]. Since the original works, spin-polarized DFT calculations have been vastly used in order to theoretical compute the spin magnetic moments at zero temperature and understand the basic mechanisms that lead to the occurrence of magnetism in materials. The realization of a magnetic ground state is determined by a competition between exchange and kinetic energy effects. Most solid state materials are non-magnetic, since the gain in exchange energy is dominated by the loss in kinetic energy, which arises from the delocalization of the valence electrons in a solid, except for cases where the electrons are sufficiently localized like in elemental metals (Fe, Co, ..), where magnetism occurs. Magnetism is also enhanced in lower-dimensional systems like metallic surfaces and interfaces.

Further developments of DFT include the description of relativistic effects, including, in particular, the spin–orbit interaction (SOC). It has been shown that the SOC term can be described using a scalar relativistic approach and solving the non-relativistic Schrödinger equation or solving the fully relativistic Dirac equation considering spinors. Since the relevance of the spin-orbit corrections increases for heavier atoms, for the systems studied in the present thesis, the spin-orbit interaction is small enough to be disregarded.

A challenging class of systems in standard DFT are correlated materials, whose electronic properties are not correctly described by the theory. Local and semilocal approximations to DFT exchance-correlation functionals tend to over-delocalize valence electrons and to over-stabilize metallic ground states [116]. An extension to the theory, called DFT+U, is formulated to improve the description of the ground state of correlated systems. The DFT+U method is inspired by the Hubbard model [116, 117] and simply adds an Hubbard-like term with a tuned numerical parameter U to the local or semilocal density functionals, LDA+U or GGA+U, without requiring a significant extra computational cost. The role of the U term is to treat the strong on-site Coulomb interaction of localized states like d and f orbitals by adding an energy penalty for states that are partially occupied. The value of the U parameter can be extracted from ab-initio calculations using linear-response theory [118], but it is also common practice to obtain them semi-empirically.

In the present thesis, when studying transition metal surfaces, we have adopted a DFT+U scheme [117], with a Hubbard U parameter of 2 eV for Fe and 4 eV for Co. The choice of the values is explained in detail in the Section 5.3.3.

2.1.5 Van der Walls interactions

There are many types of bonding interactions that contribute to the bonding of a real material. For example, besides strong covalent and ionic intra-molecular or intra-layer bonds, van der Waals interactions and other weak bonding between the molecules or layers of a given material also play a crucial role. Contrarily to ionic or covalent bonds, the locality of standard DFT approaches fails to describe interaction that do not result from a chemical electronic bond. One example is given by van der Waals interactions, which are due to correlated fluctuations of dipoles on different atoms or molecules. Despite being comparatively weaker, the attractive forces resulting from van der Waals (vdW) interactions are responsible for many physical phenomena. In particular, the stacking of layers corresponding to different materials gives rise to the so-called van der Waals heterostructures. Even if the layers are weakly bonded, vdW interactions may permit to stabilize the stack and form a new material.

There are several recipes for including van der Waals interactions in the DFT framework, ranging from dispersion-corrected potentials, nonlocal van der Waals functionals, and more empirical correction schemes, extensively reviewed for example in Refs. [119, 120]. In the present thesis we have included van der Waals interactions in the calculation of specific systems for which those interactions were identified as relevant. We adopted the DFT+D3 [121] version of the Grimme's empirical approach, in which the self-consistent Kohn-Sham energy is corrected by a London dispersion term that incorporates atom-pairwise specific coefficients and cutoff radii computed from first principles.

2.2 Many-body perturbation theory

The formalism of many-body perturbation theory (MBPT) is based on the diagrammatic language adapted from quantum field theory, and relies on the Gell-Mann-Low theorem for the case of adiabatically switched on many-body interactions [122, 123]. The processes described within the theory involve the transfer of particles to/from the initial unperturbed system, described by the creation-annihilation operators of second quantization and the Heisenberg and interaction pictures of quantum mechanics. The Hilbert space is then extended in order to allow for many-body states with different number of particle, giving rise to the Fock space which includes a complete basis set for each possible number of particles, from zero (the vacuum state) to infinity. The basis states of the Fock space in case of electrons (Fermions) can be written as antisymmetrized time-ordered products of one-body wave functions. The time evolution of any operator is then given by a Dyson series in the interaction picture. Thanks to Wick's theorem [124], each time-ordered product in the Dyson series can be systematically rewritten in sums of normal ordered products of pairs of these operators, being these expansions usually represented by Feynman diagrams. On the other hand, the mathematical machinery to compute the many-body properties of the system is founded on Green's function theory [125].

In the next paragraphs we present a brief description of some of the fundamental concepts used in the present thesis. A more detailed description can be found in specialized textbooks [126–128].

2.2.1 The one-body Green's function

In a many-body system, the time-ordered one-particle Green's function $G(1,2)$ at equilibrium and zero temperature, is defined as

$$\begin{aligned} iG(1,2) &= \langle N|T[\hat{\psi}(1)\hat{\psi}^{\dagger}(2)]|N\rangle = \\ &= \theta(t_1-t_2)\langle N|\hat{\psi}(1)\hat{\psi}^{\dagger}(2)|N\rangle - \theta(t_2-t_1)\langle N|\hat{\psi}^{\dagger}(2)\hat{\psi}(1)|N\rangle \end{aligned} \tag{2.7}$$

where $|N\rangle$ is the normalized N particle wavefunction of the ground-state of the many-body system and the time ordering introduced by the time-ordering operator, T, is explicitly written in the right part of the equation. Second quantization field operators are in the Heisenberg representation. Physically, the Green's function gives the probability amplitude for the propagation of an added or removed electron from an initial state $(\mathbf{r_1}\sigma_1, t_1)$ to a final state $(\mathbf{r_2}\sigma_2, t_2)$, labeled in a simplified notation as 1 and 2 respectively.

The Green's function defined in Eq. (2.7) contains less information than the full

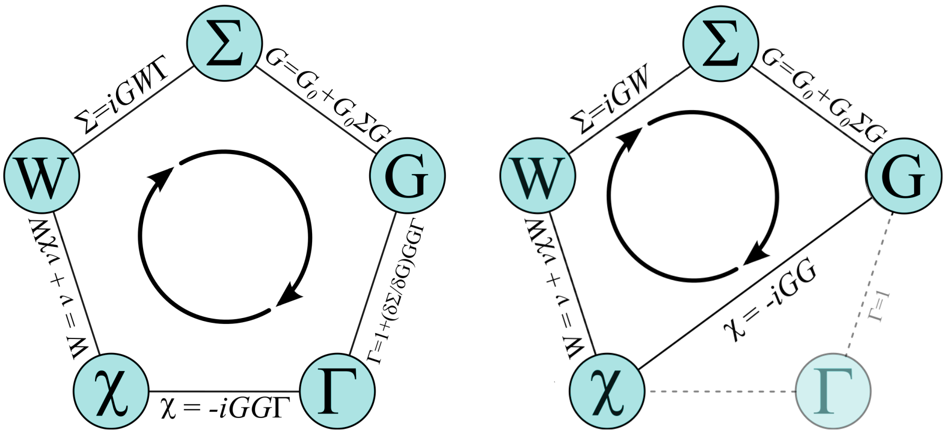

Figure 2.1: (Left) representation of Hedin's cyclic pentagon of equations. (Right) representation of the GW approximation to Hedin's equations.

many-body wavefunction, but the relevant quantities for describing charged excitations can be extracted from it. The quantities include the ground-state energy of the system obtained through the Galitskii-Migdal formula [129], the expectation value of any single-particle operator in the ground-state, and the charged excitation spectrum of the system.

From the equation of motion in the Heisenberg picture, there is a hierarchy of equation of motions (EOMs) for the Green's function corresponding to any number of particles starting from the one-particle Green's function. The EOM for $G(1,2)$ depends on the two-particle Green's function $G(1,2;1',2')$, which describes the propagation of coupled pairs of particles. Each Green's function can be computed from the knowledge of its next higher order Green's function. By defining a non-local, non-Hermitean and time-dependent potential called the self-energy, it is possible to formulate a single equation of motion for the one-particle Green's function without solving the system of equations. This is knows as the Dyson equation, and reads:

$$G(1,2) = G_0(1,2) + \int G_0(1,3)\Sigma(3,4)G(4,2)d34, \tag{2.8}$$

where a connection between the non-interacting Green's function, G_0, and the fully interacting one, G, is establish through the self-energy operator, Σ. In the form of Eq. (2.8) the problem of calculating $G(1,2)$ is reduced to the calculation of the self-energy.

2.2.2 From Hedin's equation to the GW approximation

As shown by Hedin [130] and also obtained later by means of Schwinger functional derivatives techniques [128], the exact self-energy of the many-body system can be obtained self-consistently from a hierarchy of coupled integro-differential equations involving five key quantities including the self-energy, Σ, the Green function, G, the irreducible polarizability, χ, the dynamically screened Coulomb potential, W, and a irreducible vertex function, Γ. The set of equations are sketched in the left panel of Fig. 2.1. χ describes the response of the system to the total classical (Hartree + external) perturbation and renormalizes the bare interaction resulting in the screened potential W, which is linearly related to the bare Coulomb interaction and the inverse dielectric function, while Γ describes the interactions between virtual hole and electron excitations.

Solving Hedin's equations is an extremely challenging task, in particular the evaluation of the vertex Γ, since it introduces higher order multi-particle interactions through the creation of electron–hole pairs. However, the system of equations can be simplified by introducing approximations. One of the most common considers the vertex function as a local and instantaneous function, i.e. neglects vertex contributions beyond the independent-particle level (for both Σ and the irreducible polarizability χ). This simplification gives rise to the so-called GW approximation of the electron-electron self-energy. As illustrated in fig. 2.1 (right panel), Σ reduces to a simple product of G and W in the space-time domain, that becomes a convolution when expressed in frequency-space and gives the name to the approximation:

$$\Sigma^{GW}(\omega) = \frac{i}{2\pi}\int_{-\infty}^{+\infty} d\omega'\, e^{-i\omega'\eta}\, G(\omega-\omega')W(\omega'), \tag{2.9}$$

which can be seen as the first order in a perturbation expansion involving W instead of the bare interaction v. By expressing the independent particle irreducible polarizability, from now on denoted by X_0, as

$$X_0(\omega) = -\frac{i}{2\pi}\int_{-\infty}^{+\infty} d\omega' G(\omega+\omega')G(\omega'), \tag{2.10}$$

the screened Coulomb interaction W and the dressed polarizability X can be obtained from the following Dyson equation:

$$\begin{aligned} X(\omega) &= X_0(\omega) + X_0(\omega)vX(\omega), \\ W(\omega) &= \varepsilon^{-1}(\omega)v = v + vX(\omega)v. \end{aligned} \tag{2.11}$$

In the above expressions, v is the bare Coulomb potential and ε is the dielectric function. Importantly, the frequency dependence of W comes from its correlation term $W_c = W - v = vXv$, in turn leading to the correlation part of the self-energy, Σ_c, according to Eq. (2.9).

2.2.3 Quasi-particle GW calculations in practice

In the context of condensed matter physics or quantum chemistry, many body perturbation theory (MBPT) provides accurate methods to study spectroscopic properties of matter from an *ab initio* perspective [104, 128, 131]. The calculations often adopt the so-called *GW* approximation [128, 130, 132–134] for the evaluation of the self-energy.

Since its first implementations, the *GW* approach has been successfully applied to a wide range of systems [133, 134] for the description of quasi-particle (QP) energies and bands as measured by ARPES experiments [80, 135–138], including spectral functions [138, 139], electronic satellites [140–142], and QP lifetimes [143, 144]. Importantly, *GW* quasi-particle energies are also routinely used as input for absorption spectroscopy calculations within the Bethe-Salpeter approach [131, 145]. Reflecting its wide adoption, the GW method has been implemented within multiple numerical schemes [105], ranging from localized basis sets [146–149], to plane waves and pseudopotentials or PAW [3, 150–153], to all-electron approaches using LAPW [154–157], also allowing for cross validation and verification [153, 158].

Here we list some examples of the numerous systems studied within GW, that range from bulk materials [150, 153, 157, 159–161], to surfaces and interfaces [162–165], two-dimensional [166–168] and topological materials [169, 170], low dimensional systems [171–174], molecules and atoms [146, 158, 175].

As already mentioned, the GW approximation is based on the perturbational series expansion of Σ in terms of the interacting one-particle Green function G and the dynamic screened interaction potential W, leading to a convolution in the frequency domain as it is illustrated in Eq. (2.9).

Usually, a non-interacting Green's function G_0 is taken as initial guess and the GW self-energy is evaluated without performing further self-consistent iterations (one-shot G_0W_0), and G_0 is typically chosen as the Green's function of the Kohn-Sham system. Moreover, treating the self-energy as a first order perturbation to the KS problem, one can then compute the quasi-particle (QP) energies, ϵ_m^{QP}, either by numerically solving the exact QP equation,

$$\epsilon_m^{\mathrm{QP}} = \epsilon_m^{\mathrm{KS}} + \langle \psi_m^{\mathrm{KS}} | \Sigma(\epsilon_m^{\mathrm{QP}}) - v_{xc}^{\mathrm{KS}} | \psi_m^{\mathrm{KS}} \rangle \tag{2.12}$$

or its linearized form:

$$\epsilon_m^{\mathrm{QP}} \approx \epsilon_m^{\mathrm{KS}} + Z_m \langle \psi^{\mathrm{KS}} | \Sigma(\epsilon_m^{\mathrm{KS}}) - v_{xc}^{\mathrm{KS}} | \psi_m^{\mathrm{KS}} \rangle. \tag{2.13}$$

In the latter expression the renormalization factor Z_m is computed from the first term of the Taylor expansion of the self energy, Σ:

$$Z_m = \left[1 - \langle \psi_m^{\mathrm{KS}} | \frac{\partial \Sigma(\omega)}{\partial \omega} |_{\omega = \epsilon_m^{\mathrm{KS}}} | \psi_m^{\mathrm{KS}} \rangle \right]^{-1} . \tag{2.14}$$

In practice, in order to build the self-energy and compute quasi-particle corrections at the $G_0 W_0$ level, as a first step one needs to construct the polarizability X_0 from the knowledge of G_0 according to Eq. (2.10). The former is then used for the calculation of W. The Lehmann representation for the bare Green's function G_0, computed using the KS states is written in a compact form as:

$$G_0(\omega) = \sum_m^{N_B} P_m \left[\frac{f_m}{\omega - E_m} + \frac{(1 - f_m)}{\omega - E_m^*} \right], \tag{2.15}$$

where $E_m = \epsilon_m^{\mathrm{KS}} + i\eta$, $|\psi_m\rangle$ and ϵ_m^{KS} are KS eigenpairs, f_m their occupations, $P_m = |\psi_m\rangle\langle\psi_m|$ their projectors, and the sum-over-states is usually truncated at a maximum number of bands N_B. Eventually, the limit $\eta \to 0^+$ is taken. By using G_0 in Eq. (2.10), the irreducible polarizability can be expressed as:

$$X_0(\omega) = \sum_n^{N_T} \frac{2\Omega_n^{KS} R_n^{KS}}{\omega^2 - (\Omega_n^{KS})^2}, \tag{2.16}$$

where n runs over single particle transitions, possibly truncated to N_T according to the number of bands included in the calculation. Note, however, that methods avoiding the explicit sums over empty states have been developed and made available [176–178]. In Eq. (2.16), R_n^{KS} are the transition amplitudes computed from the Kohn-Sham states, while the poles Ω_n^{KS} are defined as

$$\Omega_n^{\mathrm{KS}} = \Delta\epsilon_n^{\mathrm{KS}} - i\delta, \tag{2.17}$$

where $\Delta\epsilon_n^{KS} \geq 0$ and $\delta \to 0^+$ is a damping parameter that ensures the time ordering, similarly to η in the case of G_0.

Here, for the sake of simplicity, we have kept all spatial degrees of freedom implicit and have not highlighted quantum numbers such as $\mathbf{k}$ and $\mathbf{q}$ deriving from a possible translational symmetry of the system. In this respect, and using a plane-wave basis set of $\mathbf{G}$ vectors, $X_0(\omega)$ and R_n^{KS} in Eq. (2.16) would depend on the extra indexes $\mathbf{qGG'}$, while the index n labels transitions between states $\mathbf{k}, i$ and $\mathbf{k} - \mathbf{q}, j$.

2.3 Frequency integration methods in GW

In principle, the screened interaction $W(\omega)$ needs to be computed, as the solution of Eq. (2.11), for all the frequencies needed to evaluate the GW self-energy according to Eq. (2.9). Nevertheless, the frequency dependence of W may be quite complex, making the evaluation of the correlation part of the GW self-energy not straightforward and computationally time consuming.

Crucial to the deployment of the GW method, the frequency integration in the evaluation of the self-energy has also been addressed in different ways. Early approaches [159, 179–182] adopted the so-called plasmon-pole model, originally proposed with explicitly real poles neglecting any spectral broadening. The simplification of the structure of X, and also of W according to Eq. (2.11), that the model provides is called the plasmon-pole approximation (PPA) [159, 183]. The PPA has mainly two variants, one proposed by Godby and Needs (GN) [180], and the other by Hybertsen and Louie (HL) [159] (though more parametrizations and refinements exist [179], for example the von der Linden-Horsch [181], or Engel-Farid [182] models).

In a full frequency real-axis (FF-RA) approach, the polarizability is evaluated considering a dense frequency grid on the real axis and the integral for the self energy evaluation is then computed numerically [161, 184, 185]. Such approach requires the use of a finite damping that broadens the structure of the polarizability [161], and a large number of frequency sampling points is typically required to converge the integral. Other numerical integration techniques for the evaluation of the response function or the GW self-energy make use of quadrature rules [186, 187], spectral representations of the polarizability [150, 188], or resort to Fourier transform to imaginary time to perform frequency convolutions [149, 189–191].

Other procedures make use of imaginary-path axis integral methods in order to transform the integration on the real axis in the self-energy into an integral over an imaginary axis [155, 186, 192]. A similar approach resorts to a contour deformation (CD) defined in the first and third quadrants of the complex plane [193], in order to obtain a convenient frequency path that avoids all the poles of W and encompasses only the poles of G. The integration on the real axis is then replaced by a sum of the residues of the poles in the contour plus an integral on the imaginary axis. This integral can be addressed either numerically [194, 195] or with the help of multi-pole forms [196, 197] or Padé approximants [134, 158]. Taking advantage of the time-reversal symmetry of W, it is possible to reduce the frequency range in which W is evaluated for the self-energy integration, either on the real or the imaginary axis [155, 186, 192].

Other dedicated approaches are also available. A many-pole model for the self-energy has been developed for the calculation of inelastic losses in X-ray spectroscopy [198, 199]. Full-frequency GW has also been reformulated as a frequency-independent eigenvalue problem [200]. Similarly, a spectral representation of propagators in the form of a generalized sum-over-poles combined with an algorithmic inversion technique has been recently developed and applied to the homogeneous electron gas [201]. The FF-CD has been recently used jointly with analytic-continuation techniques in an all electrons scheme that adopts a sampling along both, the imaginary axis and parallel to the real axis [195].

Since main purpose of this study is the development of a new method for the description of the frequency dependence of the polarizability within the GW approximation (Chapter 3), it is specially relevant to describe in detail some of the most common approaches presently used.

2.3.1 The plasmon-pole model

The plasmon pole model (PPM) has its origins in the study of electronic correlation effects in simple metals, which can be modeled by an electron gas. Individual test charges or electrons embedded in a degenerate electron gas experience two types of excitation for a given wave-vector transfer $\mathbf{q}$: one-electron excitations and plasmonic (collective) excitations. The latter are more relevant for small $\mathbf{q}$, where the imaginary part of the screened potential, W, is characterized by a strong peak corresponding to a plasmon excitation at the plasmon frequency, with zero width in the long wavelength limit $\mathbf{q} \to 0$. The plasmon pole model approximates all the spectral weight of W, including the contributions from finite $\mathbf{q}$'s, by a single plasmon excitation, that corresponds to a delta-like peak in the time-ordered inverse dielectric function [202, 203]:

$$\mathrm{Im}[\varepsilon^{-1}(\mathbf{q},\omega)] = A_{\mathbf{q}}[\delta(\omega - \Omega_{\mathbf{q}}) + \delta(\omega + \Omega_{\mathbf{q}})]. \tag{2.18}$$

The real part of the dielectric function, ε, and W are then accessible through the use of Kramers-Kronig relations. The parameters of the model, $A_{\mathbf{q}}$ and $\Omega_{\mathbf{q}}$ are obtained by imposing the static limit of ε^{-1} (Kramers-Kronig transform) and compliance with the corresponding f-sum rule. The model has been successfully applied to the description of the main longitudinal plasmon mode observed in electron loss spectroscopy experiments, as shown in Table 2.1 for a set of materials. There are, however, many elements and compounds with less simple electron energy loss spectra, for instance, a large list of examples is reported in Ref. [204]. In particular, even if the PPM was fist conceived for homogeneous metals, it is not applicable to transitional metals like Ni, Co, and Cu.

The PPM has been also generalized for semiconductors and insulators [159], for which the screening is qualitatively different and more complex than in the homogeneous electron gas, requiring the use of a full dielectric matrix $\varepsilon^{-1}_{\mathbf{GG}'}(\mathbf{q})$. Within this generalization, each element of the matrix in reciprocal space is modeled by a pole that

ω_p (Ha)	model	experiment
Diamond	1.14	1.25
Si	0.61	0.61
Al	0.58	0.55
Mg	0.40	0.38
Li	0.29	0.26
Na	0.22	0.21
K	0.16	0.14
Ag	-	0.14
Au	-	0.11
Cu	-	0.10

Table 2.1: Comparison of the plasmon energy predicted by the PPM and the corresponding experimental measurements for a set of crystals. The values are extracted from Ref. [204], in addition to Cu [205], and converted to Ha.

disperses with $\mathbf{q}$:

$$\mathrm{Im}[\varepsilon^{-1}_{\mathbf{GG}'}(\mathbf{q},\omega)] = A_{\mathbf{qGG}'}[\delta(\omega - \Omega_{\mathbf{qGG}'}) + \delta(\omega + \Omega_{\mathbf{qGG}'})]. \tag{2.19}$$

This description is less accurate for large values of $\mathbf{q}$, since in contrast with the electron gas, the spectrum of excitation energies, at lower energies, already contains particle–hole excitations that eventually merges with the plasmon excitation with increasing $\mathbf{q}$ [132]. However, since the diagonal elements $\mathrm{Im}[W_{\mathbf{GG}}(\mathbf{q})]$ are given by the loss function, $-\mathrm{Im}[\varepsilon^{-1}_{\mathbf{GG}}(\mathbf{q})]$, multiplied by $v_c(\mathbf{q}) = 4\pi/|\mathbf{q}|^2$, i.e. $W = \varepsilon^{-1}v_c$, the screened Coulomb interaction is dominated by small values of $|\mathbf{q}+\mathbf{G}|$ [128].

In many materials, the experimental absorption spectrum, $-\mathrm{Im}[\varepsilon^{-1}_{\mathbf{GG}}(0)]$, is given approximately by one well-defined plasmon peak, justifying the use of a PP model. Moreover, the self-energy spectral function is also characterized by a series of separated poles. The fact that, in many cases, these poles are located far from the Fermi level, as supported by GW calculations beyond the PPA, explains the success of this approximation.

The PPM was originally proposed with an explicit real pole, i.e. neglecting any spectral broadening, and the simplification of the structure of W that the model provides is called the plasmon-pole approximation (PPA) [159, 183]. It is also possible to write the analytic continuation of the polarizability within the PPA encompassing both, real and imaginary parts:

$$X^{\mathrm{PP}}(z) = \frac{2\Omega^{\mathrm{PP}}R^{\mathrm{PP}}}{z^2 - (\Omega^{\mathrm{PP}})^2}, \tag{2.20}$$

where for simplicity we have omitted the spacial indexes ($\mathbf{qGG}'$) and Ω^{PP} is defined according to $\mathrm{Re}[\Omega^{\mathrm{PP}}] > 0$ and $\mathrm{Im}[\Omega^{\mathrm{PP}}] = 0^{-}$. Nowadays there are several flavours of the model, that are compared for instance in Refs. [164, 183], but two of them are more commonly used, one due to Hybertsen and Louie [159] (HL), and the other due to Godby and Needs [192] (GN). In the Hybertsen and Louie (HL) approach, two physical constraints are imposed: (1) compliance with the Kramers-Kronig relations in the limit of small frequencies, and (2) compliance with the f-sum rule. The Kramers-Kronig relations for X^{HL} provide:

$$\begin{aligned} X^{\mathrm{HL}}(0) &= \frac{2}{\pi}\mathcal{P}\int_0^\infty d\omega\,\omega^{-1}\mathrm{Im}[X^{\mathrm{HL}}(\omega)] \\ &= \frac{2}{\pi}\mathcal{P}\int_0^\infty d\omega\,\omega^{-1}\mathrm{Im}[X(\omega)] = X(0), \end{aligned} \tag{2.21}$$

whereas the f-sum rule is enforced by the condition:

$$\frac{2}{\pi}\int_0^\infty d\omega\,\omega\,\mathrm{Im}[X^{\mathrm{HL}}(\omega)] = \frac{2}{\pi}\int_0^\infty d\omega\,\omega\,\mathrm{Im}[X(\omega)] = S, \tag{2.22}$$

where X is the computed dressed polarizability. In the above equation, the result of the integral (S) can be expressed in terms of some of the components of the electronic density and Coulomb interaction. On a plane-wave basis, it reads:

$$\begin{aligned} S_{\mathbf{GG}'}(\mathbf{q}) &= -\frac{\omega_p^2}{v(\mathbf{q}+\mathbf{G})}\,\frac{\rho(\mathbf{G}-\mathbf{G}')}{\rho(0)}\,\frac{(\mathbf{q}+\mathbf{G})\cdot(\mathbf{q}+\mathbf{G}')}{|\mathbf{q}+\mathbf{G}|^2} \\ &= \rho(\mathbf{G}-\mathbf{G}')\,\left[(\mathbf{q}+\mathbf{G})\cdot(\mathbf{q}+\mathbf{G}')\right], \end{aligned} \tag{2.23}$$

where ρ is the electronic density and the plasma frequency, ω_p, is computed as $\omega_p = \sqrt{4\pi\rho(0)}$.

In the Godby and Needs (GN) approach, the polarizability is evaluated at two different frequencies located along the imaginary axis of the frequency plane: $z = 0$ and $z = i\varpi_p$, being ϖ_p comparable with the plasma frequency of the material.

$$(R^{\mathrm{GN}}, \Omega^{\mathrm{GN}}) : \begin{cases} X^{\mathrm{GN}}(0) = X(0) \\ X^{\mathrm{GN}}(i\varpi_p) = X(i\varpi_p). \end{cases} \tag{2.24}$$

Other versions of the PPA are based on the above recipes aiming at improving the description of the off-diagonal matrix elements of the polarizability [181, 182, 206].

2.3.2 Full frequency on the real axis

The integral of the self-energy in eq. (2.9) can be separated in several contributions corresponding to each pole of the Green function, particularizing between occupied and unoccupied states:

$$\Sigma^{GW}(\omega) = \frac{i}{2\pi} \sum_m P_m \left[f_m \int_{-\infty}^{+\infty} d\omega' \frac{W(\omega')}{\omega - \omega' - E_m} + (1 - f_m) \int_{-\infty}^{+\infty} d\omega' \frac{W(\omega')}{\omega - \omega' - E_m^*} \right]. \tag{2.25}$$

The idea of the full-frequency on the real axis is then to compute numerically each of this integrals (Hilbert transforms of W) in a finite frequency interval, for instance by means of a linear tetrahedron method [184]. Note that the denominators in Eq. (2.25) are smooth functions of the frequency ω', while $W(\omega')$ changes more rapidly due to its frequency structure, which is taken into account in the numerical integration. The interval of the integrals is determined by the smaller and the larger energy transitions computed from the bands included in the calculation of the polarizability matrix, X, and thus in W, which is partitioned in sub-intervals according to the number of frequency points included in the calculation of X.

The calculation of X in a finite grid is the first step of the FF approach. However, a finite damping parameter, δ, must be included in the calculation of X_0 in Eq. (2.16) before entering in the Dyson equation, Eq. (2.11) in order to smooth out the function and make the numerical calculation possible. Once computed W in a sufficiently dense frequency grid of N_f points, in the numerical integration of Eq. (2.25) the frequency dependence of $W(\omega)$ in each ith sub-interval ($i = 1, ..., N_f - 1$) is linearly approximated by a sort of trapezoidal Riemann sum of the form:

$$W(\omega_i < \omega < \omega_{i+1}) \approx a_i \omega_i + b_i, \qquad \text{where} \tag{2.26}$$

$$a_i = \frac{W(\omega_i) - W(\omega_{i+1})}{\omega_i - \omega_{i+1}} \tag{2.27}$$

$$b_i = W(\omega_i) - a_i \omega_i. \tag{2.28}$$

The solution of the integrals in Eq. (2.25) are then computed analytically in each sub-interval:

$$\int_{\omega_i}^{\omega_{i+1}} d\omega' \frac{a_i \omega' + b_i}{\omega - \omega' - E_m} = -a_i(\omega_{i+1} - \omega_i) - [a_i(\omega - E_m) + b_i] \log\left(\frac{\omega - \omega_{i+1} - E_m}{\omega - \omega_i - E_m} \right). \tag{2.29}$$

The integrals corresponding to unoccupied states are analogous.

In practice it is common to make an homogeneous partition of the frequency interval, so that the difference $(\omega_{i+1} - \omega_i)$ for any interval i is constant. The integral in Eq. (2.25), that leads to the quasi-particle solutions, converges faster than the structure of X with respect to the number of frequencies considered in the energy interval, due to the smoothness introduced by the convolution with the Green function. The convergence is achieved typically for sub-intervals of around 0.5 eV. The computational cost, that is proportional to number of frequency points, is then more dependent on the size of the whole interval, determined by the number of bands included in the calculation of X, rather than on the small changes of the density of points, since the convolution with G_0 removes the local oscillations in the structure of X.

By taking advantage of the symmetry $W(\omega) = W(-\omega)$, that comes from the time ordering and Kramers-Kronig relations for the polarizability, it is possible to reduce the integration interval:

$$\int_{-\infty}^{+\infty} d\omega' \frac{W(\omega')}{\omega - \omega' - E_m} = \int_{0}^{+\infty} d\omega' W(\omega') \left[\frac{1}{\omega + \omega' - E_m} + \frac{1}{\omega - \omega' - E_m} \right]. \tag{2.30}$$

More details on the full frequency on the real axis method can be found in the PhD thesis of Andrea Marini [207].

2.3.3 Full frequency contour deformation

One of the first methods addressing the pole structure of the time-ordered Green function and screened potential in the complex plane in order to properly compute the correlation part of the self-energy in the GW approximation, featured an imaginary-path axis integral with a contour deformation technique [192]. The idea is to choose a convenient trajectory of integration in the complex plane in order to avoid as much as possible the poles of G and W, for instance with any of the two variants displayed in Fig. 2.2. From both contours the same results for the integration along the real axis can be derived. On one hand, the contour in Fig. 2.2 left panel encloses the same poles as a contour in the upper semi-plane and the application of the residue theorem in each situation establishes a relation between the integration along the real and the imaginary axes. On the other hand, the residue theorem applied to the contour in Fig. 2.2 (right panel) already links the integration along both, real and imaginary axes. The same expression is then obtained:

$$\begin{aligned}\Sigma^{GW}(\omega) &= \frac{i}{2\pi} \int_{-\infty}^{+\infty} d\omega' e^{-i\omega'\eta} G(\omega - \omega') W(\omega') \qquad (2.31)\\ &= \frac{i}{2\pi} \int_{-i\infty}^{+i\infty} d\omega' e^{-i\omega'\eta} G(\omega - \omega') W(\omega') - \sum_j \mathrm{Res}[G(\omega - z) W(z), z = z_j],\end{aligned}$$

where z_j are the poles surrounded in the contours.

There are several strategies for calculating numerically the integral along the imaginary axis in Eq. (2.31). Similarly to Eq. (2.30), it is possible to take advantage of Kramers-Kronig relations, which results in the symmetry $W(i\omega) = W(-i\omega)$ for $\omega \neq 0$, in order to rewrite the integral only for positive frequencies along the imaginary axis, and therefore minimize the frequency range in which the polarizability is evaluated. As

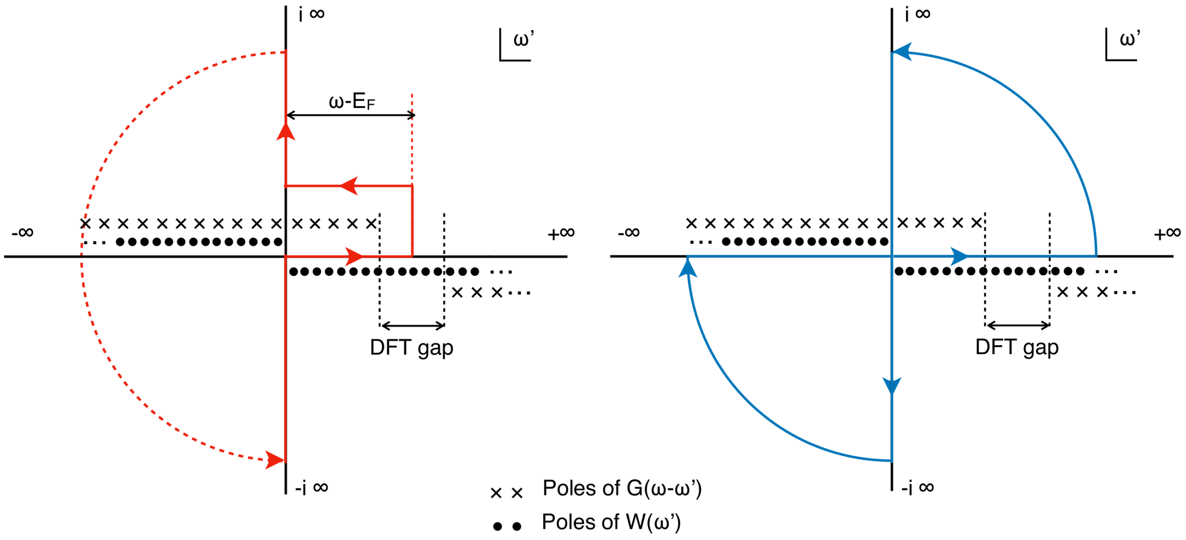

Figure 2.2: Examples of contours for the integration of the self-energy. (Left) In red, the illustration of an integration path along the imaginary axis with a Keldysh contour around the poles in the first quadrant. The dashed half circumference represents the closure of the contour that encompasses the same poles of a semicircular contour in the positive semi-plane. (Right) In blue, a contour that encompasses only poles in the first quadrant, including integrals on both real and imaginary axes.

mentioned before, the integral can then be addressed either numerically, in a similar way that the integration along the real axis in Section 2.3.2, or through Padé approximants or multipole models. The use of analytical forms are very useful for reducing the number of needed frequency evaluations of X, i.e. the computational cost of the method. The convergence is typically achieved with very sparse grids due to the smoothness of the polarizability along the imaginary axis. The analytical forms also help to evaluate the residues in Eq. (2.31), which contribute to the total number of evaluations of X needed in its analytic continuation. This kind of approach is very effective, although the computational cost is unbalanced for different quasi-particles due to the different number of poles entering in the contour in Fig. 2.2, which increases as we consider states far from the Fermi level.

Chapter 3

The multipole Approximation (MPA)

As discussed in Section 2.3, the PPA method has the computational advantage of greatly simplifying the self-energy evaluation, but on the other hand its accuracy may be compromised especially for systems displaying a complex frequency structure in the screened potential. On the other hand, full-frequency approaches are typically accurate in terms of integration, but they may turn out computationally demanding or somehow limited in accuracy by the analytic continuation (AC) methods [134, 158, 189, 191, 196, 197] required by some of them.

The main part of this Thesis project has dealt with the development of a computationally effective treatment of the frequency dependence of the polarizability, in the context of many-body perturbation theory, to evaluate the GW self-energy. The present chapter describes the multipole approximation (MPA) method, covering from the formal definition to the computational approach, and to its implementation within the Yambo code. The MPA technique naturally bridges from the PPA to a full-frequency treatment of the GW self-energy.

3.1 The multipole scheme

Our multipole scheme is based on the Lehmann representation of the dressed polarizability X [127, 128, 208, 209], which consists in expressing the polarizability as a sum of poles. It is important to emphasise that, contrarily to standard PPA implementations, we consider complex poles and that, in the proposed model, the computed poles do not correspond to single particle transitions (poles of X_0), but are rather intended to represent plasmon excitations. Each plasmonic pole describes the envelope of a set of transitions, with a finite imaginary part corresponding to the width of the excitation.

To represent and exploit the analytic properties of the polarizability X, we define a complex frequency $z \equiv \omega + i\varpi$, and write $X(z)$ as the sum of a finite (and small) number n_p of poles:

$$X^{\mathrm{MP}}(z) = \sum_{n}^{n_p} \frac{2\Omega_n R_n}{z^2 - \Omega_n^2}. \tag{3.1}$$

Then, we determine the parameters Ω_n and R_n by interpolating the polarizability $X(z)$ computed numerically on a number of frequencies that is twice the number of poles (in order to match the unknowns). This leads to a non-linear system of $2n_p$ equations and variables:

$$\sum_{n=1}^{n_p} \frac{2\Omega_n R_n}{z_j^2 - \Omega_n^2} = X(z_j), \qquad j = 1, ..., 2n_p. \tag{3.2}$$

The expression in Eq. (3.1) is at the core of the MPA approach. In fact, once the solution of the system is known, we obtain an analytical representation of $X(z)$ over the whole complex plane, suitable to evaluate Σ^{GW}. Indeed, by exploiting the Lehmann representation of the Green's function, Eq. (2.15), and making use of Eq. (3.1) to evaluate W_c, it is possible to compute the correlation part of the GW self-energy as

$$\Sigma_c(\omega) = \sum_{m}^{N_B} \sum_{n}^{n_p} P_m v R_n \left[\frac{f_m}{\omega - E_m + \Omega_n} + \frac{(1 - f_m)}{\omega - E_m^* - \Omega_n} \right]. \tag{3.3}$$

This expression generalizes the PPA solution to the case of a multipole expansion for $X(z)$, and bridges to an exact full-frequency approach when the number of poles in X is increased to convergence.

Concerning the solution of the non-linear system in Eq. (3.2), several approaches are possible. While the system can be solved analytically for a small number of poles, in general the exact solution can be accessed numerically either by mapping the non-linear problem into an equivalent system that is linear with respect to the parameters R_n and Ω_n, or through the Padé/Thiele procedure [210–212]. A detailed description of our implementations of these approaches is provided in next section.

For the one pole case, the analytical solution of the interpolation with 2 complex frequencies is easily obtained:

$$\begin{cases} \Omega^2 = \dfrac{X(z_1)z_1^2 - X(z_2)z_2^2}{X(z_1) - X(z_2)} \\ 2\Omega R = -(z_1^2 - z_2^2)\dfrac{X(z_1)X(z_2)}{X(z_1) - X(z_2)}. \end{cases} \tag{3.4}$$

We have also derived the analytical solution for the case of 2 and 3 poles, which are much more complex and not reported here for simplicity (they are nevertheless encoded in the Yambo solver).

3.2 Interpolation procedures

3.2.1 Linear solver

The non-linearity of the system of equations given in Eq. (3.2) depends only on inverse factors involving the variables Ω_n, since the system is otherwise linear in R_n. It is possible to separate these two behaviours by following the procedure described below. We start by splitting the sampled points $\{z_j, X(z_j)\}$ in two sets, for example:

$$\begin{aligned} s_1 &: \ j = 1, ..., n_p, \\ s_2 &: \ j = n_p + 1, ..., 2n_p. \end{aligned} \tag{3.5}$$

The first set defines a matrix $\mathbf{A_1}$ and vector $\mathbf{x_1}$ as follows:

$$\begin{aligned} \mathbf{A_1}_{mn} &= \frac{2\Omega_n}{z_m^2 - \Omega_n^2}, \\ \mathbf{x_1}_m &= X(z_m), \qquad n, m = 1, ..., n_p \end{aligned} \tag{3.6}$$

such that we can write a linear system for the vector $\mathbf{r} = (R_1, R_2, ..., R_{n_p})$:

$$\mathbf{A_1 r} = \mathbf{x_1}. \tag{3.7}$$

We can do the same with the other half of the data, by defining the matrix $\mathbf{A_2}$ and the vector $\mathbf{x_2}$ as:

$$\begin{aligned} \mathbf{A_2}_{mn} &= \frac{2\Omega_n}{z_{n_p+m}^2 - \Omega_n^2}, \\ \mathbf{x_2}_m &= X(z_{n_p+m}), \qquad n, m = n_p + 1, ..., 2n_p \end{aligned} \tag{3.8}$$

leading to

$$\mathbf{A_2 r} = \mathbf{x_2}. \tag{3.9}$$

Either Eq. (3.7) or (3.9) can be used to compute the residues if the positions of the poles are known. Furthermore, from these two equations it is possible to obtain a complete set of n_p equations for Ω_n:

$$\mathbf{r} = (\mathbf{A_1})^{-1}\mathbf{x_1} = (\mathbf{A_2})^{-1}\mathbf{x_2}. \tag{3.10}$$

Here we explore in depth this idea using a different formulation that maps the problem into an equivalent linear system that can be easily solved with standard linear algebra tools.

Within the multipole model, $X(z)$ can be written in the form of a particular Padé approximant, i.e. as a fraction of two polynomials $N(z^2)$ and $D(z^2)$ of degree $n_p - 1$ and n_p, respectively:

$$X(z) = \frac{N_{n_p-1}(z^2)}{D_{n_p}(z^2)} = \frac{a_1 + a_2 z^2 + ... + a_{n_p} z^{2(n_p-1)}}{b_1 + b_2 z^2 + ... + b_{n_p} z^{2(n_p-1)} + z^{2n_p}}, \tag{3.11}$$

where the factorization of $D_{np}(z^2)$ gives the position of all the poles:

$$D_{n_p}(z^2) = \prod_{n=1}^{n_p} (z^2 - \Omega_n^2). \tag{3.12}$$

On the other hand, the coefficients a_n in the numerator involve combinations of poles and residues. From the point of view of the system of equations, we are changing the unknown variables $\{R_n, \Omega_n\}$ into $\{a_n, b_n\}$. If we consider a vector constructed from the progression of powers of z: $\mathbf{Z}(z) = (1, z^2, ..., z^{2(n_p-1)})$, and vectors $\mathbf{a}$ and $\mathbf{b}$ constructed from the coefficients of $N(z^2)$ and $D(z^2)$: $\mathbf{a} = (a_1, a_2, ..., a_{n_p})$ and $\mathbf{b} = (b_1, b_2, ..., b_{n_p})$, we can write Eq. (3.11) in a more compact way and then make it linear with respect to the new variables:

$$X(z) = \frac{\mathbf{Z}(z) \cdot \mathbf{a}}{\mathbf{Z}(z) \cdot \mathbf{b} + z^{2n_p}} \tag{3.13}$$

$$X(z) z^{2n_p} + X(z)\, \mathbf{Z}(z) \cdot \mathbf{b} = \mathbf{Z}(z) \cdot \mathbf{a}. \tag{3.14}$$

By using the first set of points of Eq. (3.5) we can define the following vector and matrices:

$$\mathbf{v_1} = \begin{bmatrix} X(z_1) z_1^{2n_p} \\ X(z_2) z_2^{2n_p} \\ \vdots \\ X(z_{n_p}) {z_{n_p}}^{2n_p} \end{bmatrix} \tag{3.15}$$

$$\mathbf{Z_1} = \begin{bmatrix} 1 & z_1^2 & ... & z_1^{2(n_p-1)} \\ 1 & z_2^2 & ... & z_2^{2(n_p-1)} \\ \vdots & \vdots & & \vdots \\ 1 & z_{n_p}^2 & ... & z_{n_p}^{2(n_p-1)} \end{bmatrix} \tag{3.16}$$

$$\mathbf{M_1} = \begin{bmatrix} X(z_1) & X(z_1) z_1^2 & ... & X(z_1) z_1^{2(n_p-1)} \\ X(z_2) & X(z_2) z_2^2 & ... & X(z_2) z_2^{2(n_p-1)} \\ . & . & & . \\ . & . & & . \\ . & . & & . \\ X(z_{n_p}) & X(z_{n_p}) z_{np}^2 & ... & X(z_{n_p}) z_{n_p}^{2(n_p-1)} \end{bmatrix} \tag{3.17}$$

$\mathbf{Z_1}$ is known as a square Vandermonde matrix [213] and it is always invertible as far as all the sampling points are different [214]. Then we can write Eq. (3.14) in matrix form:

$$\mathbf{v_1} + \mathbf{M_1}\mathbf{b} = \mathbf{Z_1}\mathbf{a}, \tag{3.18}$$

while an analog equation is obtained with the second set of points:

$$\mathbf{v_2} + \mathbf{M_2}\mathbf{b} = \mathbf{Z_2}\mathbf{a}. \tag{3.19}$$

By combining Eq. (3.18) and (3.19) to remove vector $\mathbf{a}$ we obtain a linear system for $\mathbf{b}$:

$$\begin{aligned} \mathbf{M}\mathbf{b} &= \mathbf{v} & (3.20)\\ \mathbf{M} &= \mathbf{Z_1}^{-1}\mathbf{M_1} - \mathbf{Z_2}^{-1}\mathbf{M_2} & (3.21)\\ \mathbf{v} &= -\mathbf{Z_1}^{-1}\mathbf{v_1} + \mathbf{Z_2}^{-1}\mathbf{v_2}. \end{aligned}$$

In terms of the number of matrix inversions to be performed, Eqs. (3.20)-(3.21) can be recast into the following more practical form:

$$\left[\mathbf{Z_2}\mathbf{Z_1}^{-1}\mathbf{M_1} - \mathbf{M_2}\right]\mathbf{b} = -\mathbf{Z_2}\mathbf{Z_1}^{-1}\mathbf{v_1} + \mathbf{v_2}. \tag{3.22}$$

Before we proceed, in order to the reduce numerical instabilities of the algorithm, it is convenient to carry out a normalization

$$\begin{aligned} z_j &= y_j z_{\max}, & (3.23)\\ z_{\max} &= \max(|z_n|), \qquad n = 1, .., n_p, \end{aligned}$$

where, i.e., $z_{\max}$ is the largest frequency modulus in the sampling set involved with the matrix we need to invert, $\mathbf{Z_1}$.

The proposed normalization balances the large differences among the matrix elements that emerge when increasing the number of poles, due to the range of the sampling and the increasing powers. Rescaled unknowns can then be defined as:

$$\begin{cases} a'_n = a_n (z_{\max})^{n-1} \\ b'_n = b_n (z_{\max})^{n-1}. \end{cases} \tag{3.24}$$

Likewise, we also define the $\mathbf{Y_{1,2}}$ and $\mathbf{M'_{1,2}}$ matrices similarly to $\mathbf{Z_{1,2}}$ and $\mathbf{M_{1,2}}$, Eqs. (3.16) and (3.17) respectively, by using y_n instead of z_n. Eventually, Eqs. (3.20)-(3.21) can be re-written as a linear system for $\mathbf{b}'$:

$$\left[\mathbf{Y_2}\mathbf{Y_1}^{-1}\mathbf{M}'_\mathbf{1} - \mathbf{M}'_\mathbf{2}\right]\mathbf{b}' = -\mathbf{Y_2}\mathbf{Y_1}^{-1}\mathbf{v_1} + \mathbf{v_2}. \tag{3.25}$$

Once we have computed $\mathbf{b}'$, and in turn $\mathbf{b}$ via Eq. (3.24), we need to obtain the poles Ω_n, which are the variables with physical meaning and those required in the evaluation of the self-energy integral. As mentioned above, this is equivalent to find the zeros of the polynomial $D_{n_p}(z^2)$ in Eq. (3.12), and a powerful method to perform this task is the diagonalization of the corresponding companion matrix:

$$\mathbf{C} = \begin{bmatrix} 0 & 0 & \dots & 0 & -b_1 \\ 1 & 0 & \dots & 0 & -b_2 \\ 0 & 1 & \dots & 0 & -b_3 \\ \vdots & \vdots & \ddots & \vdots & \vdots \\ 0 & 0 & \dots & 1 & -b_{n_p} \end{bmatrix} \tag{3.26}$$

The eigenvalues of $\mathbf{C}$ correspond to the squares of the position of the poles, Ω_n^2.

As mentioned before, in case all the poles are different, the residues may be computed with either Eq. (3.7) or (3.9). Alternatively we can use all the $2n_p$ points to fit R_n with a linear least squares method:

$$\min_{\mathbf{r}} ||\mathbf{A}\mathbf{r} - \mathbf{x}||, \tag{3.27}$$

where, for each $n = 1, ..., n_p$, and $j = 1, ..., 2n_p$, one has

$$\mathbf{A}_{jn} = \frac{2\Omega_n}{z_j^2 - \Omega_n^2}, \qquad \mathbf{x}_j = X(z_j). \tag{3.28}$$

A similar least-square approach was also recently adopted in the definition of the sum-over-poles approach [201], and applied to the case of the homogeneous electron gas.

3.2.2 Padé/Thiele solver

An alternative way to the method described above consists in solving at the same time both polynomials, numerator and denominator, in the Padé interpolant (3.11) by means of the Thiele's interpolation formula, witch expresses the interpolant as a continued fraction of the reciprocal differences [210]. The number of required steps corresponds to the number of points to be interpolated, that is $2n_p$ in our case:

$$\frac{N(z^2)}{D(z^2)} = \frac{c_1}{1+}\frac{c_2(z^2 - z_1^2)}{1+}\dots\frac{c_{2n_p}(z^2 - z_{2n_p-1}^2)}{1 + (z^2 - z_{2n_p-1}^2)g_{2n_p}(z)}, \tag{3.29}$$

where the coefficients c_s and functions $g_s(z)$ are given by the following recursion relations:

$$c_s = g_s(z_s), \tag{3.30}$$

$$g_s(z) = \begin{cases} X(z_s),\ s=1 \\ \dfrac{g_{s-1}(z_{s-1}) - g_{s-1}(z)}{(z-z_{s-1})g_{s-1}(z)},\ s \geq 2 \end{cases} \tag{3.31}$$

where index $s = 1, .., 2n_p$ represents both, the iteration step and the index of the corresponding point in the given set.

The polynomials $N(z^2)$ and $D(z^2)$ and their coefficients can then be computed recursively. Note that in Thiele's relation the definitions of each polynomial differ from the one in Eq. (3.11) by a multiplicative constant that, however, does not affect the zeros of the polynomials, and moreover cancel out in the fraction. As in the case of the linear solver, with the Thiele's procedure we are interested in computing only the monomial coefficients of the denominator, since we can always obtain the residues by means of Eq. (3.7) or (3.27). The recipe [210] for the polynomial in the denominator is:

$$D_s(z) = \begin{cases} 1, & s = 0,1 \\ D_{s-1}(z) - c_s(z-z_{s-1})D_{s-2}(z), & s \geq 2 \end{cases} \tag{3.32}$$

The desired polynomial of degree n_p is obtained in the last step, $s = 2n_p$. Notice that in this notation the index s does not reflect anymore the degree of the polynomial. In each iteration the degree of the polynomial $D_s(z)$ is $(s-1)/2$ for odd integers and $s/2$ for even numbers.

We can write a vector of the coefficients of the final polynomial, $\mathbf{d} = (d_1, ..., d_{n_p}, d_{n_p+1})$. It has an extra dimension comparing to vector $\mathbf{b}$ in Eq. (3.14) due to the multiplicative constant mentioned before that goes to the higher order monomial of D in Eq. (3.11). The recursion of the polynomial in Eq. (3.32) can be easily translate into a recursion of the vector $\mathbf{d}$:

$$\mathbf{d^s} : \begin{cases} (1,0,..,0), & s = 0,1 \\ d_i^s = d_i^{s-1} + c_s z_s d_{i+1}^{s-2} - c_s z_{s-1} d_i^{s-2}, & s \geq 2 \end{cases} \tag{3.33}$$

where the second term of the sum on the right member of (3.33) is computed just for $i = 1, ..., n_p$, while the other two includes also the last dimension, $i = n_p + 1$.

The recursion of the c_s coefficients can also be recast in vectorial form, by considering in each iteration, s, a $2n_p$ dimensional vector, $\mathbf{c}$:

$$\mathbf{c^s} : \begin{cases} (X(z_1), .., X(z_{2n_p})),\ s = 1 \\ c_j^s = \dfrac{c_{j-1}^{s-1} - c_j^{s-1}}{(z_j - z_{j-1})c_j^{s-1}},\ s \geq 2 \end{cases} \tag{3.34}$$

where now the iterations are represented by index s in the upper position, and the vector coordinates and point identifiers are represented by index j in the lower position. Notice however that only one particular component of vector $\mathbf{c}^s$ enters in Eq. (3.33) at each iteration, i.e. $c_s \equiv c_s^s$, other components are worth only to update the vector.

Once computed $\mathbf{d}$, the relation with the coefficient of vector $\mathbf{b}$ is as simple as $b_n = d_n/d_{n+1}$, that recovers the unitary coefficient accompanying the higher order monomial of the polynomial. The position of the poles can then be computed with the companion matrix, Eq. (3.26) likewise in the case of the linear solver.

3.3 Connecting the GN- and HL- plasmon pole models

The most common way of simplify the structure of the polarizability is by an analytical model with a single pole, as discussed in Section 2.3.1. The main two recipes, one due to Godby and Needs [180] (GN), and the other due to Hybertsen and Louie [159] (HL), seems different before hand. However, the idea of interpolating the two parameters $(R^{\text{PP}}, \Omega^{\text{PP}})$ of the plasmon-pole model starting from X evaluated at two different frequencies, used by the GN-PPM, is very flexible, and multiple sampling options can be adopted. Nevertheless, using different pairs of sampling frequencies typically leads to different parametrization of the resulting PPM. With this in mind, we search for the pair of frequency points to be used in Eq. (3.4) that would correspond to the conditions imposed by the HL scheme. The equations for the GN-PPM are:

$$\begin{aligned} X(0) &= -\frac{2R^{\text{GN}}}{\Omega^{\text{GN}}}, \\ \Omega^{\text{GN}} &= \varpi_p \,\text{Re}\left[\frac{X(i\varpi_p)}{X(0)-X(i\varpi_p)}\right]^{\frac{1}{2}}, \end{aligned} \tag{3.35}$$

while those for the HL-PPM are:

$$\begin{aligned} X(0) &= -\frac{2R^{\text{HL}}}{\Omega^{\text{HL}}} \\ 2\Omega^{\text{HL}} R^{\text{HL}} &= S. \end{aligned} \tag{3.36}$$

We note that Eq. (2.21) in the HL formulation, connected to the Kramers-Kronig relation, implies the first condition (equality of X and X^{HL} at $\omega = 0$) imposed in the GN recipe, Eq. (2.24), as also evident in comparing Eqs. (3.36) and (3.35).

If we consider the exact polarizability X, written in the Lehmann representation similar to the multipole model given in Eq. (3.1), but with all the N_T addends and with

$\mathrm{Im}[\Omega_n] \to 0^-$, and solve the integral in the f-sum rule we get:

$$\frac{2}{\pi}\int_0^\infty d\omega\, \omega\, \mathrm{Im}[X(\omega)] = 2\sum_n \Omega_n R_n. \tag{3.37}$$

Then, the condition imposed by HL in the plasmon-pole model is

$$2\Omega^{\mathrm{HL}} R^{\mathrm{HL}} = 2\sum_n \Omega_n R_n. \tag{3.38}$$

This relation imposes the equality of the $1/z^2$ coefficient (leading order) of the asymptotic behaviour of the polarizabilities, making explicit the known fact that sum rules describe properties at infinity [215]:

$$\lim_{\omega\to\infty} X^{\mathrm{HL}}(\omega)/X(\omega) = 1. \tag{3.39}$$

This means that in the long frequency range, $\omega \gg \max\limits_n |\Omega_n|$, X behaves as a one-pole function with the exact same asymptotic decay of X^{HL}. Thus, we can think of the HL representation as a limiting case of GN-PPM recipe when the second frequency goes to infinity:

$$(R^{\mathrm{HL}}, \Omega^{\mathrm{HL}}) : \begin{cases} X^{\mathrm{HL}}(0) = X(0) \\ X^{\mathrm{HL}}(\infty) = X(\infty), \end{cases} \tag{3.40}$$

where the evaluation of the infinite frequency in the second equation is taken as the limit of the X^{HL}/X ratio, according to Eq. (3.39).

3.4 Comparison of different samplings on a test function

In order to get an analytical understanding of the intrinsic differences among diverse types of samplings, we have explored and extended the analysis made in the previous section to a simple test function that models a polarizability with two pairs of poles. The utility, reasoning and main conclusions of this procedure are highlight in further Section 3.5.

The test function is written as

$$y(z) = x_1(z) + x_2(z) \equiv \frac{2\Omega_1 R_1}{z^2 - \Omega_1^2} + \frac{2\Omega_2 R_2}{z^2 - \Omega_2^2}. \tag{3.41}$$

In the following, we study how different sampling options affect the solution of the fitting procedure when using a model with one pole.

3.4.1 Perturbing the GN sampling

Let us define the reference GN sampling with an imaginary frequency of modulus ϖ_0:

$$s^{GN}: \begin{cases} z_1 = 0 \\ z_2 = i\varpi_0 \end{cases} \tag{3.42}$$

and those we want to compare with, starting with a perturbation on z_1:

$$s^{0}: \begin{cases} z_1 = \omega \\ z_2 = i\varpi_0, \end{cases} \tag{3.43}$$

$$s^{i0}: \begin{cases} z_1 = i\varpi \\ z_2 = i\varpi_0, \end{cases} \tag{3.44}$$

where $\varpi < \varpi_0$. When ω and ϖ are small, we have a similar behaviour with the same parameters:

$$\begin{cases} \Omega^0 = \Omega^{GN}\left(1 - \dfrac{f_1^0}{\varpi_0^2}\omega^2 + O[\omega^3]\right) \\ R^0 = R^{GN}\left(1 - \dfrac{c_1^0 f_1^0}{\varpi_0^2}\omega^2 + O[\omega^3]\right), \end{cases} \tag{3.45}$$

$$\begin{cases} \Omega^{i0} = \Omega^{GN}\left(1 + \dfrac{f_1^0}{\varpi_0^2}\varpi^2 + O[\varpi^3]\right) \\ R^{i0} = R^{GN}\left(1 + \dfrac{c_1^0 f_1^0}{\varpi_0^2}\varpi^2 + O[\varpi^3]\right). \end{cases} \tag{3.46}$$

We also consider a perturbation on z_2 as:

$$s^{\varpi_0}: \begin{cases} z_1 = 0 \\ z_2 = i(\varpi_0 + \varpi). \end{cases} \tag{3.47}$$

When ϖ is small in this case, we have:

$$\begin{cases} \Omega^{\varpi_0} = \Omega^{GN}\left(1 + \dfrac{f_0^{\varpi_0}}{\varpi_0}\varpi + O[\varpi^2]\right) \\ R^{\varpi_0} = R^{GN}\left(1 + \dfrac{f_0^{\varpi_0}}{\varpi_0}\varpi + O[\varpi^2]\right). \end{cases} \tag{3.48}$$

When $\varpi \gg \varpi_0$ in Eq. (3.47), we have:

$$\begin{cases} \Omega^{\varpi_0} = \Omega^{GN} L_{\varpi_0}\left(1 - \dfrac{f_\infty^{\varpi_0}\varpi_0^2}{\varpi^2} + O[\varpi^{-3}]\right) \\ R^{\varpi_0} = R^{GN} L_{\varpi_0}\left(1 - \dfrac{f_\infty^{\varpi_0}\varpi_0^2}{\varpi^2} + O[\varpi^{-3}]\right). \end{cases} \tag{3.49}$$

The HL approach can be included in this regime and from this equation we can understand why the HL solution overestimates Ω and R with respect to GN, since it is given by the asymptotes:

$$\begin{cases} \Omega^{HL} = \Omega^{GN} L_{\varpi_0} \\ R^{HL} = R^{GN} L_{\varpi_0}. \end{cases} \tag{3.50}$$

Moreover, it is possible to merge both behaviours of Eq. (3.48) and (3.49) into a single a function that goes continuously from one solution to the other:

$$\begin{cases} \Omega^{\varpi_0}(\varpi) = \dfrac{\Omega^{GN}\varpi_0^2 + \Omega^{HL}\varpi^2}{\varpi_0^2 + \varpi^2} - \dfrac{\varpi\varpi_0^2}{\frac{\varpi^3}{\Omega^{HL} f_\infty^{\varpi_0}} - \frac{\varpi_0^3}{\Omega^{GN} f_0^{\varpi_0}}} \\ R^{\varpi_0}(\varpi) = \dfrac{R^{GN}\varpi_0^2 + R^{HL}\varpi^2}{\varpi_0^2 + \varpi^2} - \dfrac{\varpi\varpi_0^2}{\frac{\varpi^3}{R^{HL} f_\infty^{\varpi_0}} - \frac{\varpi_0^3}{R^{GN} f_0^{\varpi_0}}}. \end{cases} \tag{3.51}$$

3.4.2 Samplings along the real axis

Lets start by defining samplings, for now still with two frequencies, but that represent samplings along a line either parallel P or tilted, with a positive A^+ or negative A^- angle, with respect to the real axis (RA).

$$s^{RA} : \begin{cases} z_1 = 0 \\ z_2 = \omega_0, \end{cases} \tag{3.52}$$

$$s^{P} : \begin{cases} z_1 = i\varpi \\ z_2 = \omega_0 + i\varpi, \end{cases} \tag{3.53}$$

$$s^{A+} : \begin{cases} z_1 = 0 \\ z_2 = \omega_0 + i\varpi, \end{cases} \tag{3.54}$$

$$s^{A-} : \begin{cases} z_1 = i\varpi \\ z_2 = \omega_0. \end{cases} \tag{3.55}$$

When ϖ is small, we have:

$$\begin{cases} \Omega^{P} = \Omega^{A+} = \Omega^{RA}\left(1 - i\dfrac{f_0^{\omega_0}}{\omega_0}\varpi + O[\varpi^2]\right) \\ R^{P} = R^{A+} = R^{RA}\left(1 - i\dfrac{f_0^{\omega_0}}{\omega_0}\varpi + O[\varpi^2]\right), \end{cases} \tag{3.56}$$

which shows that a parallel sampling close to the real axis affects the parameters by a quantity that is proportional to the shift ϖ.

When ϖ is large, we have:

$$\begin{cases} \Omega^{A+} = \Omega^{HL}\left(1 - \dfrac{f_\infty^{\omega_0}\omega_0^2}{\varpi^2} + O[\varpi^{-3}]\right) \\ R^{A+} = R^{HL}\left(1 - \dfrac{f_\infty^{\omega_0}\omega_0^2}{\varpi^2} + O[\varpi^{-3}]\right). \end{cases} \tag{3.57}$$

3.4.3 Form of the factors

In order to get a general picture from the coefficients of the series expansions presented in the previous sections, we write them in a compact way by defining simply recognizable averaged quantities that may be weighted by particular elements. We use a notation, $\overline{\Omega^e}_w$, in which Ω represent the average quantity, the position of a pole in this case, while e is an exponent and w the weighting function:

$$f_\infty^{\omega_0} = \frac{1}{2\omega_0^2}\frac{(\Omega_1^2-\Omega_2^2)^2}{\overline{\Omega}_R\overline{\Omega}_{R^{-1}}}, \tag{3.58}$$

$$f_\infty^{\varpi_0} = \frac{1}{2\varpi_0^2}\frac{(\Omega_1^2-\Omega_2^2)^2}{\overline{\Omega}_R\overline{\Omega}_{R^{-1}}}, \tag{3.59}$$

$$f_1^0 = \frac{(\Omega_1^2-\Omega_2^2)^2}{2\Omega_1^2\Omega_2^2}\frac{\varpi_0^2}{\overline{\Omega^2}_{x^{-1}}(i\varpi_0),} \tag{3.60}$$

$$f_0^{\varpi_0} = \frac{(\Omega_1^2-\Omega_2^2)^2}{(\varpi_0^2+\Omega_1^2)(\varpi_0^2+\Omega_2^2)}\frac{\varpi_0^2}{\overline{\Omega^2}_{x^{-1}}(i\varpi_0)}, \tag{3.61}$$

$$f_0^{\omega_0} = \frac{(\Omega_1^2-\Omega_2^2)^2}{(\omega_0^2-\Omega_1^2)(\omega_0^2-\Omega_2^2)}\frac{\omega_0^2}{\overline{\Omega^2}_{x^{-1}}(\omega_0)}, \tag{3.62}$$

$$L_{\varpi_0} = \frac{\sqrt{\overline{\Omega^{-2}}_x(i\varpi_0)}}{\overline{\Omega^{-1}}_R}, \tag{3.63}$$

$$\begin{cases} R_{HL} = R_1 + R_2 \\ \Omega_{HL} = \dfrac{1}{\overline{\Omega^{-1}}_R}, \end{cases} \tag{3.64}$$

$$c_1^0 = -\overline{x(\varpi_0)/x(i\varpi_0)}_{R/\Omega}; \tag{3.65}$$

where:

$$\overline{\Omega}_R \equiv \frac{R_1\Omega_1 + R_2\Omega_2}{R_1+R_2}, \tag{3.66}$$

$$\overline{\Omega}_{R^{-1}} \equiv \left(\frac{\Omega_1}{R_1} + \frac{\Omega_2}{R_2}\right)(R_1+R_2), \tag{3.67}$$

$$\overline{\Omega^{-1}}_R \equiv \frac{R_1\Omega_1^{-1} + R_2\Omega_2^{-1}}{R_1 + R_2}, \tag{3.68}$$

$$\overline{\Omega^{-2}}_x(i\varpi_0) \equiv \frac{\Omega_1^{-2}x_1(i\varpi_0) + \Omega_2^{-2}x_2(i\varpi_0)}{y(i\varpi_0)}, \tag{3.69}$$

$$\overline{\Omega^2}_{x^{-1}}(\omega_0) \equiv y(\omega_0)[\Omega_1^2 x_1^{-1}(\omega_0) + \Omega_2^2 x_2^{-1}(\omega_0)], \tag{3.70}$$

$$\overline{x(\varpi_0)/x(i\varpi_0)}_{R/\Omega} \equiv \frac{\frac{R_1}{\Omega_1}\frac{x_1(\varpi_0)}{x_1(i\varpi_0)} + \frac{R_2}{\Omega_2}\frac{x_2(\varpi_0)}{x_2(i\varpi_0)}}{\frac{R_1}{\Omega_1} + \frac{R_2}{\Omega_2}}. \tag{3.71}$$

3.5 Samplings strategies

An interpolation in the form of Eq. (3.1) is independent of the chosen sampling frequencies as far as they are all different, and the number of poles in the model, n_p, equals the total number of poles of the target polarizability, N_T. Nevertheless, in the present approach we intent to describe $X(z)$ using a number of poles much smaller than N_T, and therefore the representation is not unique. We then need to understand the possible choices for the points to be used in the interpolation of X. In the following, we discuss how a shift of the frequency sampling from the real axis affects the structure of the polarizability together with alternative sampling strategies. Eventually we show that the sampling plays a fundamental role in achieving a good approximation of $X(z)$ with a reduced number of poles.

3.5.1 The polarizability in the complex plane

According to the Lehmann representation, the poles of the time-ordered dressed polarizability X, are distributed above/below the real axis (at an infinitesimal distance), in an energy range determined by the corresponding transitions. X presents a very complex structure along the real axis, while at increasing distance from the real axis the analytic continuation of X becomes smoother. As discussed in Sec. 2.3, existing approaches typically sample $X(z)$ at frequencies either along the real or the imaginary axis. As an alternative we have studied samplings with components on both axes.

Let's consider at first a sampling of X along a line parallel to the real axis, but at a distance ϖ. From the point of view of the distance from the poles, this sampling effectively balances the contribution of different poles, in particular those located at large (real) frequencies. Moreover, the constant shift from the real axis smooths out the frequency dependence of the polarizability and can be understood as a filter effect resulting from the convolution between the imaginary part of the polarizability computed on the real axis, $-\text{Im}[X(\omega)]\text{sgn}(\omega)$, and the function $1/\pi(\omega + i\varpi)$ with a pole in the complex frequency plane, which is a kind of Hilbert transform:

$$X(z) = -\frac{1}{\pi}\int_{-\infty}^{+\infty} \frac{\text{Im}[X(\omega')]\text{sgn}(\omega')}{\omega - \omega' + i\varpi} d\omega'. \tag{3.72}$$

The larger the value of the shift, ϖ, the smoother the function in the convolution and the sampled polarizability $X(z)$, and therefore the fewer the poles required to model it, as also depicted in Fig. 3.1. It is interesting to note that the FF-RA method described in Sec. 2.3.2 makes typically use of a finite damping to obtain a similar simplification of the structure of X. In this respect, the multipole interpolation method presented here has the advantage that, once the parameters R_n and Ω_n are obtained, it is then possible to perform a sort of deconvolution towards the real-axis, by evaluating there the polarizability when performing the integral of the self-energy. This allows us to get rid of (or at least reduce) the effect of the artificial smoothing of $X(z)$, which is not possible in the FF-RA scheme.

3.5.2 Analysis of one-pole solutions

Before presenting our numerical results for different sampling strategies, we discuss some analytical results useful to guide our analysis.

As shown in Section 3.3, the two most used versions of the PPA can be mapped into a X interpolated on two different frequency samplings. In fact, in the Godby-Needs (GN) scheme the parameters of the plasmon pole model (PPM) are obtained by computing $X(z)$ at $z_1 = 0$ and $z_2 = i\varpi_p$, being ϖ_p comparable with the experimental plasma frequency of the material, while the conditions imposed by the Hybertsen-Louie (HL) scheme are shown in Section 3.3 to be equivalent to sampling X at $z_1 = 0$ and $z_2 = \infty$ (meaning that X and X^{HL} have the same leading order coefficient in the $1/z^2$ term for $z \to \infty$). In practice, the two methods give slightly different results: the HL-PPM tends to overestimate the position of the pole with respect to GN-PPM [183, 216], and GN-PPM reproduces better the polarizability with respect to full frequency calculations [183]. Mathematically, this can be understood by considering that the interpolation of a function $X(z)$ with a structure is more effective when the sampling is done in a region of meaningful variation of the function, as done in the GN-PPM case. It is therefore reasonable to expect that the choice of the sampled frequency points affects the interpolated X.

In Section 3.4 we applied Eq. (3.4) to a test function with two poles, Eq. (3.41), and computed a series expansions of the parameters, Ω and R for a perturbation on a reference sampling. This allows us to investigate the dependency of the MPA fit parameters on the sampling. We conclude that it is possible to write equations for Ω

and R capturing the behaviour of both the GN- and HL-PPM schemes at the same time, and going from one to the other with a continuous function. The same analysis also shows that a sampling close and parallel to the real axis (see Fig. 3.1, orange line except for the first point) introduces an error in Ω and R that is proportional to the distance from the real axis, when comparing to the solution obtained when performing a sampling on the real axis. This means that, with X sampled parallel and close to the real axis, it is convenient to stay as close to the real axis as possible, as in the case of the FF-RA, where the damping needs to be sufficiently small in order to avoid the introduction of a systematic error. As shown in the next Section 3.5.3, this is not the case when using a double parallel sampling.

In Section 3.4.3, we define and report the f-factors in the expansions of Ω and R, and show that the test function behaves as a one-pole polarizability when $R_2/R_1 \to 0$ (one pole dominates) or $Q_2 \to Q_1$ (the two poles tend to coalesce). In these cases the solutions do not depend on the sampling, which supports the idea of obtaining a simplified description of the polarizability with a reduced number of poles in cases where some of the poles are close to each other or some of the residues are much larger than others. The sensitivity of the MPA method to the sampling will depend on the ratio of the residues and on the distance between the poles of X. While we have not analytically investigated more complicated test polarizability functions or fitting models (including a larger number of poles), we have performed numerical analyses (e.g. a 3 pole function fitted on a 2 pole model) which tend to confirm the findings discussed above.

3.5.3 Double parallel sampling

After testing several sampling strategies (samplings parallel to the real axis, tilted with a positive or negative angle with respect to it, etc), our results led to the choice of a sampling along two lines parallel to the real axis, that we will call double parallel sampling:

$$s^{\mathrm{DP}} = \begin{cases} \mathbf{z^1}\colon\ z_n^1 = \omega_n + i\varpi_1 \\ \mathbf{z^2}\colon\ z_n^2 = \omega_n + i\varpi_2, \end{cases} \qquad n = 1, .., n_p \tag{3.73}$$

where one of the two branches is a line close to the real axis while the other is located further away, e.g. $\varpi_1 < \varpi_2$. The sampling is illustrated in Fig. 3.1, by the orange and green lines, while in gray we represent the isolines of a toy polarizability function with poles close to the real axis. From the isolines it is possible to see that, at some distance of the real axis, individual poles that are close enough are no longer distinguishable and contribute to a collective excitation. In a simplified view, X sampled along the first line, in orange, preserves some of the structure of X in the region of the poles and X sampled along the second line, in blue, is simple enough to be described with a small number of poles, and accounts for the overall structure of X. The two branches should not be too close in order to avoid numerical instabilities, since a superposition would indeterminate the system of equations.

This sampling has proved to converge faster with respect to the number of poles and to be less sensitive to the distance of the first line from the real axis (ϖ_1) than the others we tried. This can be understood from the analysis of a small perturbation to $z_1 = 0$ applied to the GN-PPM sampling (at fixed z_2), i.e. to the simplest one-pole double parallel sampling. The linear term in the perturbation of Ω and R (see Eqs. (3.46) and (3.45)) cancels and the first perturbative term is quadratic on ϖ, at variance with perturbations on z_2 where the linear term is present (Eq. (3.48)). Moreover, considering different sampling strategies, Ω and R change in the same way, when passing from a real axis sampling to a parallel or tilted sampling ($z_1 = 0$ only in the latter), further stressing that overall behaviour is governed by z_2 and that a perturbation to z_1 has negligible impact.

We still have to chose a distribution of the frequencies along the real axis, $\{\omega_n\}$, that again favours the convergence with respect to the number of poles. Differently from the homogeneous grid used in Ref. [195], we propose a partition that simply adds new frequency points when increasing the number of poles, reducing in this way oscillations in the results. Here we write a semi-homogeneous partition in powers of 2:

$$\{\omega_n\} : \left\{ \begin{array}{r} (0)\,,\, n_p = 1 \\ (0,1) \times \omega_m,\, n_p = 2 \\ \left(0, \frac{1}{2}, 1\right) \times \omega_m,\, n_p = 3 \\ \left(0, \frac{1}{4}, \frac{1}{2}, 1\right) \times \omega_m,\, n_p = 4 \\ \left(0, \frac{1}{8}, \frac{1}{4}, \frac{1}{2}, 1\right) \times \omega_m,\, n_p = 5 \\ \left(0, \frac{1}{8}, \frac{1}{4}, \frac{1}{2}, \frac{3}{4}, 1\right) \times \omega_m,\, n_p = 6 \\ \left(0, \frac{1}{8}, \frac{1}{4}, \frac{3}{8}, \frac{1}{2}, \frac{3}{4}, 1\right) \times \omega_m,\, n_p = 7 \\ \dots \end{array} \right. \tag{3.74}$$

where ω_m is the extreme of the interval. We choose to use a finite value of ω_m since X tends to zero for large enough frequency values, and is enough to describe its tail. Also supporting this option is the fact that the fulfillment of the f-sum rule, the condition used in the HL-PPM that is equivalent to taking $z_2 = \infty$ in the GN-PPM recipe (Appendix 3.3), is not critical for obtaining an accurate description of polarizability matrix elements within FF methods [217]. The maximum value of ω_m corresponds to the largest energy transition according to the number of empty states included in the

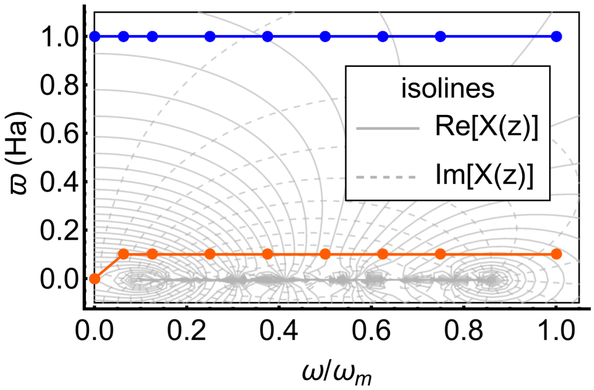

Figure 3.1: An illustration of the double parallel sampling with a 9 points semi-homogeneous grid along the real axis with $\varpi_2 = 1\ Ha$, similar to the the imaginary frequency used in the GN PPM and $\varpi_1 = 0.1\ Ha$, except for the origin of coordinates. The isolines in the background correspond to a toy polarizability function with 200 poles on the real axis.

calculation of X. Alternatively, one can simply use a frequency with a sufficiently large real part so that it is located in the tail of the polarizability and use the other sampling points to describe its structure closer to the imaginary axis.

In practice, we use the value ϖ_2 used in the GN approach described in Section 2.3.1, in order to have the same sampling on the imaginary axis when using only one pole and a straightforward extension along the real axis when using more poles. Regarding ϖ_1, in case of one pole we take a null value consistently with PP models, while a (small but) finite value is considered for additional sampling points along the real axis in order to avoid numerical noise. Based on the experience and results obtained using the FF real axis method, and the analytical results discussed above (Eq. (3.46)) we increase ϖ_1 up to 0.1 Ha. This is also similar the values proposed for molecules in Ref. [195].

3.5.4 Parallel vs. double parallel sampling

A possible drawback of the double parallel sampling is the fact that it reduces by half the capability to explore the landscape of the polarizability along the real axis. A criterion for when to start to consider a parallel sampling over a double parallel sampling comes from the simple observation that Eqs. (3.45) and (3.46) are equivalent if one replaces the shift along the real axis, ω, by a shift along the imaginary axis, $i\varpi$. If one then has a grid of $2n_p$ points in the parallel sampling they would be separated by an average distance of $\omega_m/(2n_p-1)$, that can be compared with the shift ϖ_1 in the double parallel sampling. The criterion can be written as

$$\frac{1}{2n_p-1} \lesssim \frac{\varpi_1}{\omega_m}. \tag{3.75}$$

3.6 Physical constraints with optimal representability

3.6.1 Failure condition

Sometimes, when considering only a small number of poles, the interpolation gives rise to poles that are either not physical or not reasonable, posing representability problems. This is usually solved by reassigning the values of the poles. An example is given by the treatment of the so-called "unfulfilled modes" that plays an important role in different PPM schemes [153]. Here we discuss the case of the GN-PPM approach as implemented in Yambo [3, 153, 180, 193]. The condition used to identify unfulfilled modes in the GN-PPM is the following:

$$\mathrm{Re}\left[\frac{X_{\mathbf{GG'}}(\mathbf{q},0)}{X_{\mathbf{GG'}}(\mathbf{q},i\varpi_p)}-1\right]<0 \;\rightarrow\; \Omega^{\mathrm{GN}}=1\ \mathrm{Ha}, \tag{3.76}$$

where the position of the pole is set to $\Omega^{GN}=1$ Ha in case of failure. This condition is related to the estimate of Ω^{GN} according to Eq. (3.35). For diagonal elements ($\mathbf{G}=\mathbf{G'}$), the polarizability evaluated on the imaginary axis is real, making the term in the square-root of Eq. (3.35) also real. Unfulfilled modes are then those for which the radicand is negative and the resulting pole imaginary. The same condition is also used for off-diagonal matrix elements in order to ensure that the pole Ω^{GN}, which is anyway taken real, mainly derives from the real part of the radicand in Eq. (3.35).

Setting the pole for unfulfilled modes at $\Omega^{\mathrm{GN}}=1$ Ha usually works well for semiconductors [153], even if it may have a (usually small) impact on the quasi-particle corrections. However, in more complex systems the reliability of the PPA may be compromised either by the large number of matrix elements for which the pole is corrected or simply by the inadequacy of such a simple model correction.

In the case of MPA we propose a slightly different strategy. The condition in Eq. (3.76), used in the PP approach, applies to a sampling on the imaginary axis but can be generalized as:

$$\Omega_n=\begin{cases}\sqrt{\Omega_n^2}, & \mathrm{Re}\left[\Omega_n^2\right]\geq 0\\ \sqrt{-(\Omega_n^2)^*}, & \mathrm{Re}\left[\Omega_n^2\right]<0\end{cases} \tag{3.77}$$

avoiding in this way, in case of failure, the use of a replacement constant value. The second line in Eq. (3.77), when applied, is equivalent to exchange the real and imaginary parts of Ω_n. In addition, since we consider complex poles, if needed we also impose time ordering, i.e. while $\mathrm{Re}[\Omega_n]\geq 0$ because of Eq. (3.77) we may force $\mathrm{Im}[\Omega_n]<0$. Note this procedure is applied to all n_p poles in MPA.

We now analyze the evaluation of the residues when at least one of the poles of the multipole interpolation is modified by the failure condition above. We start by considering a model with a single pole, for which the residue R can be calculated using the information of either the sampling point z_1, first equation in Eq. (3.35) within the GN model, or z_2 as

$$R = \frac{X_2(z_2^2 - \Omega^2)}{2\Omega}. \tag{3.78}$$

When the pole is not corrected, the computed residue is independent of the choice between z_1 and z_2. However that is not the case if the failure condition is used. In order to improve the representation with respect to considering only one of the given solutions depending on z_1 or z_2, we propose to use Eq. (3.27) to fit R. When using more than one pole, in addition to Eq. (3.77) we have added an extra condition: in case a pole is close to another or its position is out of the sampling range, its residue is replaced by zero and the fit of Eq. (3.27) is applied only to the remaining residues.

3.6.2 Representability measurements

In order to quantify the representability error of the model with respect to the sampled points when correcting the position of the poles with Eq. (3.76) and (3.77), we compute the mean number of corrected matrix elements, $\langle N_F \rangle$, and an average relative standard deviation, $\langle RSD \rangle$. The analysis presented in the following can be done for each $\mathbf{q}$-point, if translational symmetry is present. For one pole, the average number of failures is simply:

$$\langle N_F \rangle_{n_p=1} = \frac{1}{N_g} \sum_{g=\mathbf{GG}'}^{N_g} \Theta(\Omega^{\mathrm{MP}}_{n=1,g}), \tag{3.79}$$

where Θ is a Heaviside-like step function that verify the condition:

$$\Theta(\Omega) = \begin{cases} 0, & \mathrm{Re}\left[\Omega^2\right] \geq 0 \\ 1, & \mathrm{Re}\left[\Omega^2\right] < 0. \end{cases} \tag{3.80}$$

Regarding the error measurement, we use a modified version of the relative standard deviation, also known as coefficient of variation, that is then averaged over all the matrix elements. Since we model all the matrix elements with the same number of poles, the average deviation gathers, in a single estimate, the representability error. The estimator was modified by replacing in the normalization factor the mean value of the sampled values of X by their maximum value. Namely, for each matrix element $g = \mathbf{GG}'$ (within a given $\mathbf{q}$ block, not labelled explicitly here), we define

$$M_g = \max_j |X_{\mathbf{GG}'}(z_j)|. \tag{3.81}$$

This is justified by the fact that X is close to zero for a large region of frequencies, together with its average when it is computed with several points, which may results in an inadequate use of the coefficient of variation. The error estimators then read:

$$\langle RSD\rangle_{n_p=1} = \frac{1}{N_g}\sum_{g=\mathbf{GG}'}^{N_g}\frac{1}{M_g}\sqrt{\sum_{j=1}^{2}|X_{jg}^{\mathrm{MP}} - X_{jg}|^2} \tag{3.82}$$

$$\langle RSD\rangle_{\mathrm{PPA}} = \frac{1}{N_g}\sum_{g=\mathbf{GG}'}^{N_g}\frac{\Theta(\Omega_{ng}^{\mathrm{PP}})}{M_g}\sqrt{\sum_{j=1}^{2}|X_{jg}^{\mathrm{PP}} - X_{jg}|^2}. \tag{3.83}$$

In case of the PPA we compute the error just for the matrix elements that fail the condition in order to favour the comparison with MPA, since there may be a deviation already due to the fact of discarding the imaginary part of the poles in the PPA (MPA is based on an interpolation, while PPA is not).

In the general multipole case we define:

$$\langle N_F\rangle = \frac{1}{N_g}\sum_{g=\mathbf{GG}'}^{N_g}\frac{\sum_n^{n_p}\Theta(\Omega_{ng}^{\mathrm{MP}})|R_{ng}^{\mathrm{MP}}|}{\sum_n^{n_p}|R_{ng}^{\mathrm{MP}}|} \tag{3.84}$$

$$\langle RSD\rangle = \frac{1}{N_g}\sum_{g=\mathbf{GG}'}^{N_g}\frac{1}{M_g}\sqrt{\frac{1}{2n_p-1}\sum_{j=1}^{2n_p}|X_{jg}^{\mathrm{MP}} - X_{jg}|^2}, \tag{3.85}$$

where we have introduced a normalization by the residues of each pole in the counter of the failure condition $\langle N_F\rangle$, in order to differentiate the contribution of each pole.

Chapter 4

Validation of MPA on prototypical materials

4.1 MPA applied to semiconductors

We have validated the MPA method in three different bulk materials: Si, a prototype semiconductor, hBN with AA and AA' staking, and rutile TiO_2, a mid band-gap semiconductor oxide. We compare the MPA approach described above with PPA and FF calculations and with the existing literature. In particular, we compare our results for Si with Refs. [153, 218], hBN with Refs. [219, 220], and TiO_2 with Ref. [153].

DFT calculations were performed using the Quantum ESPRESSO package [107, 108]. We employed the LDA exchange-correlation functional for Si and hBN, while GGA-PBE for TiO_2, with norm-conserving pseudopotentials in all cases. For Si, we use a grid of $12 \times 12 \times 12$ $\mathbf{k}$-points, a kinetic energy cutoff of 20 Ry and 300 KS states to perform sums-over-states. In case of hBN, we used $\mathbf{k}$-points meshes of $18 \times 18 \times 9$ and $18 \times 18 \times 6$, corresponding to AA and AA' stacking respectively, with an energy cutoff of 60 Ry and 400 KS states. For rutile TiO_2, we use a shifted $\mathbf{k}$-grid of $4 \times 4 \times 6$ $\mathbf{k}$-points, a kinetic energy cutoff of 70 Ry for the wavefunctions, and 600 KS states.

GW calculations were performed with the Yambo code [3, 4]. We use a standard Monte Carlo stochastic scheme called Random Integration Method (RIM) [3, 221] to treat integrals over the Brillouin zone with Coulomb divergence.The RIM technique is used in order to accelerate convergences with respect to the $\mathbf{k}$-point mesh in case of hBN and TiO_2, but not for Si simply to illustrate that the MPA works well independently of this choice. The size of the polarizability matrix is set to 25, 10 and 15 Ry for Si, hBN and TiO_2, respectively. In the case of hBN, the value of 10 Ry is not sufficient to converge quasi-particle corrections, and a more suitable value is 25 Ry. Due to the high computational cost of FF real-axis calculations, we decided to perform the comparison of PPA, MPA, and FF methods for hBN with a X matrix cutoff of 10 Ry, while the

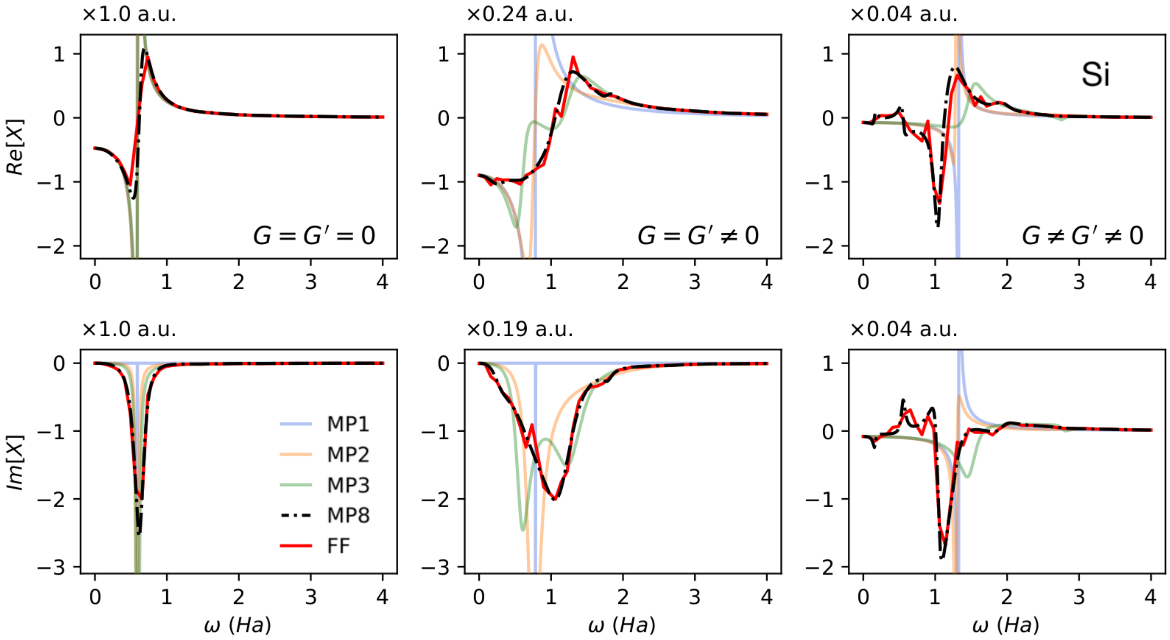

Figure 4.1: Selected Si X matrix elements computed within MPA with 1, 2, 3 and 8 poles and compared with the corresponding FF results. Although the real and imaginary parts of the function are plotted using different arbitrary units, the different matrix elements can be compared since their scale is consistent and indicated in each plot.

results obtained with 25 Ry (quasi-particle energies in the case of PPA and MPA) are given in Table 4.1. Regarding the self-energy evaluation, in the bare Green function we use a damping parameter $\eta = 0.1$ eV for all calculations.

4.1.1 The polarizability matrix

In Figs. 4.1, 4.2 and 4.3 we plot a set of diagonal and off-diagonal matrix elements of the polarizability for three different bulk materials: Si, hBN, and TiO_2 rutile, respectively. Each plot shows the real and imaginary parts of the polarizability computed within MPA using a different number of poles, compared with the corresponding FF real-axis results. The same number of poles is used for all the matrix elements. In fact, on the one hand the multiple peak structures of X is more complex for large **G**-vectors, while on the other hand their maximum amplitude, and therefore their weight in the integration of the self-energy, decreases with **G**. This means that a more simplistic description of the structure of these elements will not affect much the computed Σ. For reasons of computational convenience, besides the number of poles, the array of sampled frequencies is also the same for all the matrix elements. Of course, the complexity of X depends on the material under study. In silicon, for instance, the most important matrix elements have an almost single-peak structure that favours the use of a single pole, while for TiO_2 the first element, $\mathbf{G} = \mathbf{G}' = 0$, already shows several peaks and a

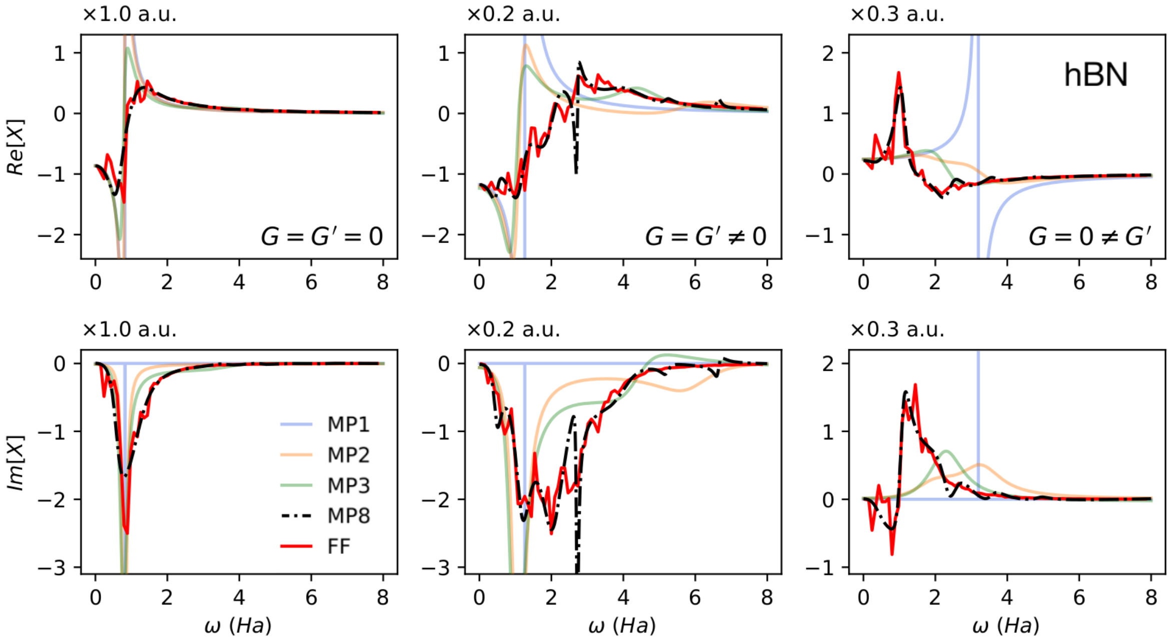

Figure 4.2: Selected hBN X matrix elements computed within MPA with 1, 2, 3 and 8 poles and compared with the corresponding FF results. The same scheme from Fig. 4.1 is used for the units.

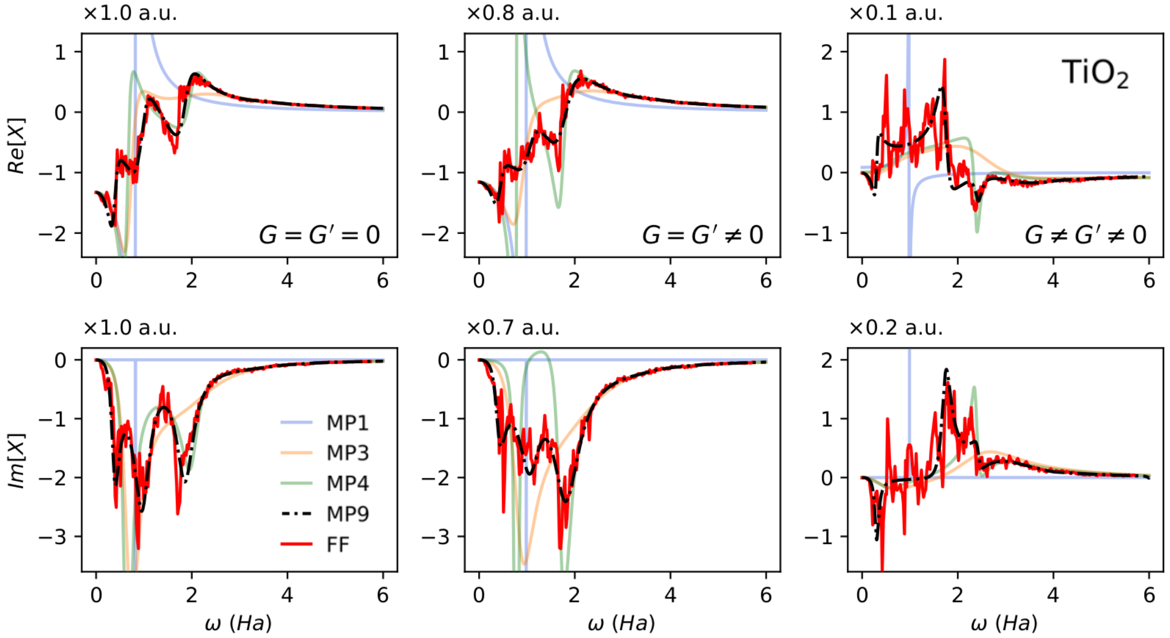

Figure 4.3: Selected TiO_2 X matrix elements computed within MPA with 1, 3, 4 and 9 poles and compared with the corresponding FF results. The same scheme from Fig. 4.1 is used for the units.

slower decay of the maximum amplitude with respect to $\mathbf{G}$.

The imaginary part of diagonal elements of X describes the spectral properties of the polarizability, and therefore is always negative with peaks around the real part of the poles and widths given by their imaginary part. A model with a single pole describes approximately the envelop of the real part of diagonal elements, but is unable to describe the width of the main peak, since the small value of the imaginary part of the pole obtained from the interpolation is translated into a delta-like peak. The use of a complex pole is not that different from a real one obtained by neglecting its imaginary part, as in the PPA case. The inclusion of a second pole however, may improve the description of the imaginary part of the diagonal elements of X even if there are no significant improvements in the real part. On the other hand, the off-diagonal matrix elements of X show a mixture of their real and imaginary parts, since the residues of the poles in Eq. (2.16) have an imaginary part depending on their $\mathbf{G}$ and $\mathbf{G}'$ components. Off-diagonal matrix elements are more likely to fail the PP condition of Eq. (3.76) and even a single but complex pole and the generalized failure condition of Eq. (3.77) may lead to considerable improvements on the description of X, as shown in the right panels of Fig. 4.1.

In general the description of the polarizability improves quickly as the number of poles increases, as demonstrated by the representability measurements $\langle N_F \rangle$ and $\langle RSD \rangle$ plotted in Fig. 4.4. Already with one pole, the error of the generalized condition is lower than the one obtained with the PPM and then both $\langle N_F \rangle$ and $\langle RSD \rangle$ rapidly decrease with increasing number of poles.

4.1.2 Convergence of quasiparticles

In Fig. 4.5 we report the convergence of the GW correction to the band gap with respect to the number of poles used in the MPA for the three systems under study. The same frequency sampling was used in the three cases, namely a double parallel sampling, Eq. (3.73) with the grid given by Eq. (3.74) along the real axis and shifts $\varpi_1 = 0.1$ Ha and $\varpi_2 = 1$ Ha. For TiO_2, which has a more structured polarizability, the quasi-particle corrections are more sensitive to the sampling. With a single pole model using different values of ϖ_2 the results can differ by as much as ~ 100 meV. In the multipole case the difference decreases to 6 meV when comparing results obtained with $\varpi_2 = 0.5$ and 1.0 Ha. Even if we expect the highest value to lead to a slightly simpler X, the convergence is reached with the same number of poles in both cases.

Interestingly, the same convergence behaviour is found for the three systems: between 8 and 11 poles the quasi-particle corrections differ by less than 1 meV from the FF results. The number of poles needed to obtain convergence is much more homogeneous than the number of frequencies in FF real axis calculations (300 for Si, 400 for hBN

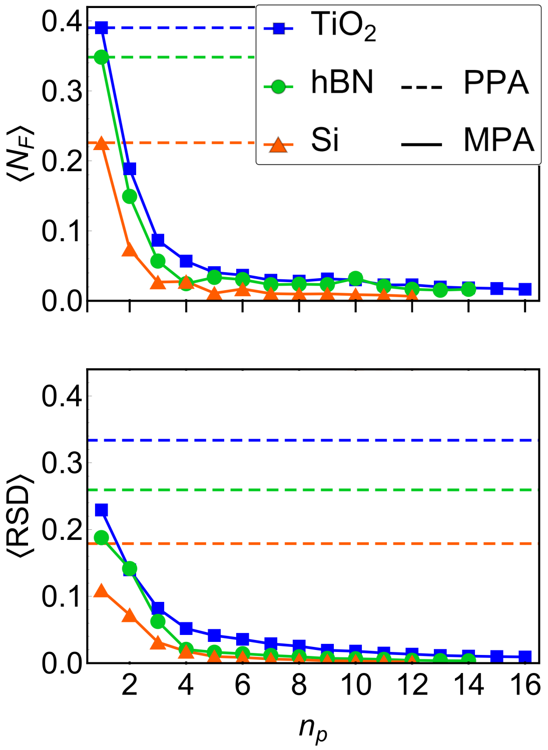

Figure 4.4: (Top) $\langle N_F \rangle$, mean number of matrix elements for which the position of the poles was corrected according to Eq. (3.77) for MPA and Eq. (3.76) for PPA, and (bottom) $\langle RSD \rangle$, average deviation as defined in Eq. (3.85), as a function of the number of poles used in the MPA approach. Due to the high computational cost of the FF calculations, in case of hBN the comparison is made with a non fully converged dimension of the polarizability matrix, of 10 Ry. The plots correspond to the AA stacking, but similar values are seen also for the AA' stacking with 10 Ry of X matrix.

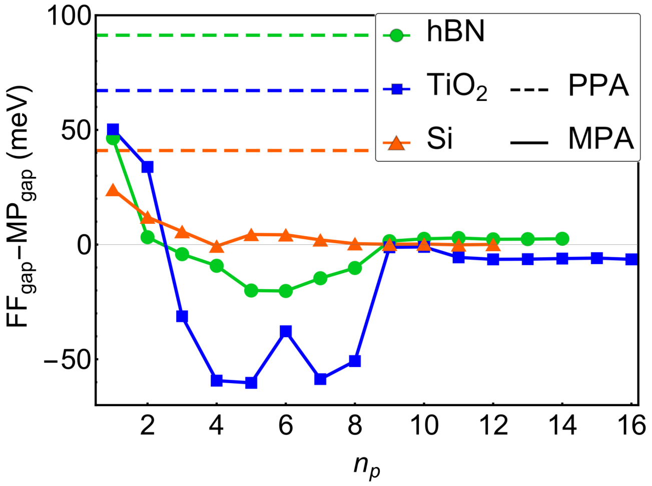

Figure 4.5: Deviations of the fundamental gap calculated via the MPA with respect to FF results as a function of number of poles for Si, hBN and TiO$_2$. As in Fig. 4.4, in case of hBN we use 10 Ry of X matrix and plot only the results of the AA stacking.

System	QP(eV)	PPA	MPA	FF
Si	$\Gamma_c \rightarrow \Gamma_v$	3.28	3.30	3.30
	$K_c \rightarrow \Gamma_v$	1.26	1.30	1.30
hBN$_{AA}$	$M_c \rightarrow K_v$	7.35	7.47	7.46 [7.25]
	$K_c \rightarrow K_v$	7.02	7.16	7.16 [6.91]
	$H_c \rightarrow K_v$	5.33	5.50	5.50 [5.23]
	$L_c \rightarrow K_v$	5.26	5.42	5.42 [5.17]
hBN$_{AA'}$	$L_c \rightarrow K_v$	6.21	6.24	6.24 [6.20]
	$K_c \rightarrow K_v$	6.17	6.20	6.20 [6.17]
	$H_c \rightarrow K_v$	6.02	6.05	6.05 [6.01]
	$M_c \rightarrow K_v$	5.93	5.98	5.98 [5.92]
TiO$_2$	$\Gamma_c \rightarrow \Gamma_v$	3.20	3.27	3.26

Table 4.1: Quasi-particle (QP) transitions computed with the linearized QP Eq. (2.13) on top of PP, MPA and FF. In case of hBN, FF calculations are performed using a 10 Ry cut-off for the X matrix (results in square brackets) and then extrapolated to 25 Ry, using the MPA results as reference. All other calculations are directly performed with a 25 Ry cutoff.

and 1500 for TiO2), since the shifts ϖ in the double parallel sampling determine the structure of the polarizability and therefore the number of poles required to model it.

We report our final QP results in Table 4.1. In the case of hBN, the difference between the PPA and FF-RA values changes with respect to the size of the polarizability matrix. At 10 Ry we found similar differences for stacking AA and AA' with a maximum value of 0.10 eV. At 25 Ry the difference increases up to a maximum value of 0.17 eV for the stacking AA and decreases up to a maximum value of 0.05 eV for the stacking AA', the plasmon-pole approximation being more accurate in the AA' configuration.

4.1.3 Self-energy and spectral functions

The present MPA method targets the dynamical dependence of the dressed polarizability, in turn directly related to W, in order to perform the frequency integral in the self-energy and finally to compute the quasiparticle corrections to the independent particle states. For this purpose, we need a good description of $\Sigma(\omega)$ in a frequency region around the solution of the quasiparticle equation, Eq. (2.12). However, the description of the self energy in a larger range of frequencies is interesting by itself, since $\Sigma(\omega)$ contains, besides the quasiparticle energies, information about many-body features like satellites and quasiparticle lifetimes. These properties are computed by solving the cor-

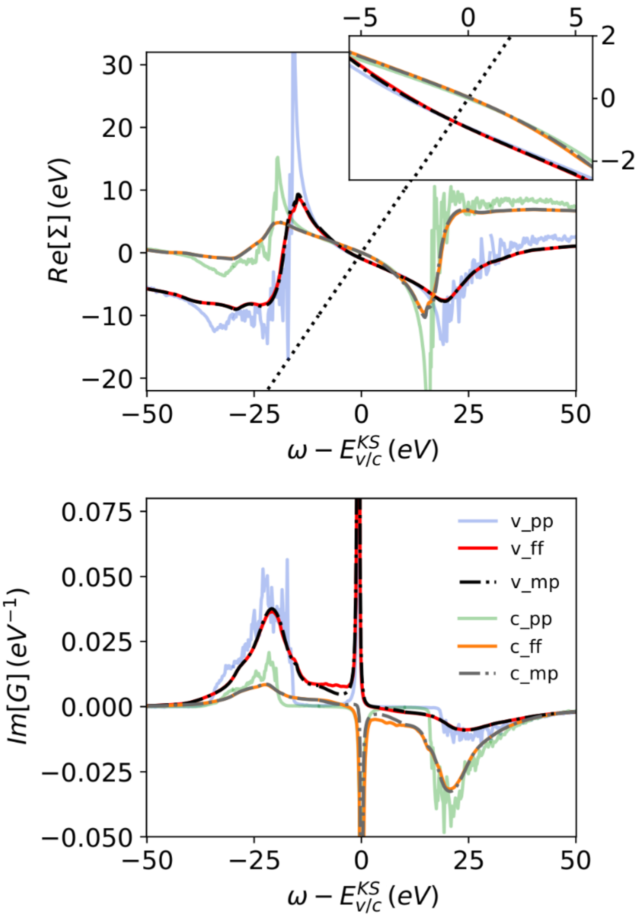

Figure 4.6: Frequency dependence of the Si valence (v) and conduction (c) real part of the self-energy (top) and spectral function (bottom) of the quasiparticles involved in the fundamental gap computed with PPA, MPA and FF.

responding Dyson equation for the Green function, $G = G_0 + G_0 \Sigma G$. Through Eq. (3.3), the MPA method provides a description for the frequency dependence of the self-energy, that we assess in this Section.

In Fig. 4.6 we compare the Si self energy (top) and spectral function (bottom), obtained as the imaginary part of the dressed Green's function, Im $[G]$, computed within PPA, MPA, and FF-RA. The self-energy presents a typical two-pole structure [189, 196] corresponding to the contributions of the empty and occupied states. The picture can be better understood taking Eq. (3.3) into account: occupied states contribute to the self-energy at energies around the value $-\Omega$ plus their own KS energies (negative), different from the empty states that contribute at $+\Omega$ plus a positive term from the KS energies further separating the two contributions of the main plasmon at $\pm\Omega$.

The PPA gives a good description of the tail of the main peaks, especially including the region around the solution of the quasiparticle equation, and the overall behaviour of Σ. However, intrinsic representability problems appear due to the inability of PPA in describing the imaginary part of W. The result is a very noisy Σ, particularly around its peaks, giving rise to noisy satellite peaks in the spectral function. In contrast, the MPA self energy (computed with 8 poles, i.e. the number required to obtained converged quasiparticle energies) reproduces quite well the FF-RA results in the whole energy range. In fact, there is a reversal on the level of complexity of the polarizability with respect to the self-energy: X is smooth when computed within PPA, and very structured in FF-RA and MPA, whereas Σ is very spiky within PPA and smooth for FF-RA and MPA.

This result can be understood by analysing the effect of the Dyson equation for W, Eq. (2.11), on the polarizability matrix elements $X_{\mathbf{GG'}}(\mathbf{q},\omega)$. At the independent particle level, X_0 presents a large number of peaks described by Eq. (2.16). When applying the Dyson equation, the poles from different matrix elements of X_0 are combined, resulting in a dressed polarizability X with broader peaks corresponding to plasmonic excitations, as shown in Figs 4.1, 4.2 and 4.3. Thanks to this feature, it is possible to use few (complex) poles in the MPA modeling (then approximated with 1 real pole in PPA) of each matrix element $X_{\mathbf{GG'}}(\mathbf{q},\omega)$. However, there is a further pole superposition of the matrix elements in the integral of the self-energy (Eq. (3.3)), whose accurate description in a full frequency range needs a proper modeling of the imaginary part of X. This superposition in PPA is partially remedied by the finite η damping of the Green function, while the presence of finite imaginary parts in the MPA poles naturally improves the PPA description. In Silicon, the proximity of the several electronic states and the number of additional low intensity plasmon-excitations result in a noisy behaviour of the PPA self-energy around the main peaks. In contrast, the FF and MPA methods properly describe the superposition of all the excitations, and the resulting $\Sigma(\omega)$ function is smooth.

This picture may be different for less screened systems like e.g. molecules [158, 222], where the energy levels are scattered, the plasmonic excitations are far apart, and the plasmon-pole model may lead to a self-energy that presents a simpler structure than a FF treatment. On the other hand, the nonexistence of a gap in metallic systems may lead to a self-energy with a single main peak [223] also noisy within PPA. However, the special cases of metals with small plasmon energies or strongly correlated materials are particularly challenging for simple models like the PPA, since the quasi-particle solutions lie in a zone of multiple plasmonic excitations, as shown in Ref. [224] for $SrVO_3$. The applicability of the PPA on such systems has been discussed in the literature [132, 161] and the advantages in the use of the MPA for a metallic case are addressed in Section 4.3.

4.2 MPA applied to molecules

The multipole scheme was developed for describing efficiently the frequency dependence of the polarizability and making the integration of the self-energy in the GW approximation accurate and less expensive from a computational point of view. MPA is in principle independent of the spatial properties of the system, since we applied the same methodology to each spatial matrix element $\mathbf{qGG'}$ of the Brillouin zone. Therefore it should be straightforward applicable to low dimensional materials.

4.2.1 The GW100 set

In order to validate the MPA in low dimensional materials we have chosen as a reference the GW100 benchmark set [158], where GW calculations with different methodologies are performed on a set of 100 molecules with several independent codes, including e.g. TURBOMOLE [225], FHI-aims [226], and BerkeleyGW [152]. The comparison is interesting for several reasons: for instance the generality of the level of theory (the GW approximation) is validated against practical parameters like the type of basis set used in the calculations, plane waves versus local orbitals, or the approximations within each method, PPA methods versus FF or others. We have listed in Table 4.2 the ionization potential computed for a subset of molecules with different frequency treatments in GW: the generalized plasmon-pole (GPP) model [159] and FF approaches. We see large deviations already among the results of the Hybertsen and Louie plasmon-pole model and the full-frequency implemented in BerkeleyGW, with differences as large as 2.51 eV between the GPP and FF for the molecule BN. The data from BerkeleyGW is suitable for a comparison with our calculations since both BerkeleyGW (BGW) and Yambo are plane-wave codes, and both have implemented the plasmon-pole model and a FF method, even if Yambo uses the version by Godby and Needs of the PPA. We have selected the F_2 molecule as a representative case of the subset of molecules since it presents difference of 0.86 eV between BGW-GPP and BGW-FF results.

Finite systems such as molecules are demanding to compute with a plane-wave basis set and periodic boundary conditions, since one needs to construct a supercell with a large amount of vacuum around the molecule in order to avoid the interaction with the replicas. At the DFT level, the Martyna-Tuckerman approach [227] helps to reduce the interactions, as well as Coulomb cutoff techniques for supercell calculation in Yambo [221]. Nevertheless, typical sizes of the spherical cutoff uses radius already large, around 20 Å. Furthermore, an accurate calculation of quasi-particle energies beyond the independent particle picture in poorly correlated materials like molecules, requires the inclusion of a very large number of empty states, since the interaction with the vacuum level is fundamental. The typical number of bands included in the calculations of the GW100 test reaches values of some thousands.

IP(eV)	BGW-GPP	BGW-FF	GW-FF(AIMS&TURBOMOLE)
N_2	15.43	14.72	14.81 to 14.89
F_2	15.59	14.73	14.85 to 14.96
CH_4	14.28	13.80	13.86 to 13.93
C_2H_6	12.63	12.22	12.30 to 12.37
C_2H_4	10.68	10.30	10.17 to 10.33
C_2H_2	11.35	10.97	10.93 to 11.02
C_2H_3F	10.80	10.14	10.08 to 10.20
LiH	7.85	6.67	6.51 to 7.09
F_2Mg	13.73	12.44	12.26 to 12.72
BN	12.19	9.68	11.00 to 11.19
H_2NNH_2	9.78	9.10	9.23 to 9.28
C_2H_4O	10.16	9.43	9.48 to 9.59
HOOH	11.58	10.82	10.90 to 10.99
H_2O	12.75	11.68	11.89 to 11.97
CO_2	13.81	13.17	13.04 to 13.25
OCS	11.49	11.02	10.73 to 10.91
O_3	13.05	12.00	11.36 to 11.91
BeO	10.66	9.68	8.58 to 9.35
MgO	8.51	7.08	6.66 to 7.03

Table 4.2: Ionization potential of a subset of molecules of the GW100 set where full frequency GW results are available with the different software packages.

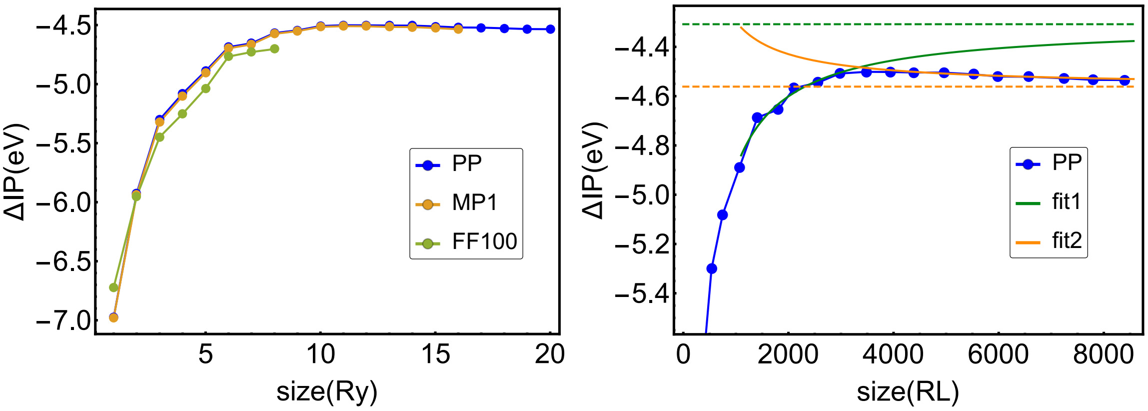

Figure 4.7: (Left) Convergence of the correction to the Ionization Potential in PPA, MPA with one pole and the FF scheme with respect to the dimension of the X matrix for the F2 molecule. We have fixed the number of bands to 4000. (Right) different extrapolations in the form ($\frac{a}{\dim(RL)} + b$) of the PPA results before and after 2565 RL (9 Ry).

4.2.2 MPA on F_2

For the DFT starting point we use scalar-relativistic Optimized Norm-Conservinng Vanderbilt Pseudopotential [228] with kinetic energy cutoff of 84 Ry. We use face centered cubic supercells, in order to minimize the vacuum around the molecule, with 20 Å of vacuum and the Martyna-Tuckerman scheme to treat the long-range Coulomb interaction. Then we converge the ionization potential (IP) of F_2 with PPA and FF up to the limit of our computational resources. The calculations were performed in a node of a local cluster of the CNR-NANO institute at Modena, equipped with a Intel Xeon 6230 processor with 40 cores and 384 Gb of memory/node. We found that in addition to the large number of bands, also the dimension of the polarizability matrix must be considerably large to obtain converged results. In Fig. 4.7, left panel, we plotted the IP convergence with respect to the dimension of the polarizability matrix in Ry computed with 4000 bands. Our computational resources limited us to the use of 100 frequencies and we filled the available memory when considering 8 Ry for the X matrix size, that unfortunately is not enough to obtain converged results in the FF scheme. Within the PPA scheme we were able to use 20 Ry for the X matrix dimension and we see that already for 15 Ry the IP values change less than 7 meV. We also plotted the convergence of the MPA approach with one pole. The differences wit respect to the PPA results are about 30 meV, with a similar convergence behaviour.

It is a common practice to extrapolate GW results with respect to the different numerical parameters when convergence is out of reach like in this case. For the extrapolation with respect to the dimension of the X matrix of the MPA results we use the total number of matrix elements denoted in Yambo as reciprocal lattice (RL) instead of the dimension approximated in Ry, since this number is written in the Yambo output files with less accuracy. As illustrated in the right panel of Fig. 4.7, the extrapolation must be done with some care. Even if the results seem to converge already around 9 Ry, there is a subtle change of slope that can lead to a wrong extrapolation when it is performed before the slope change. The computational cost of the FF calculations does not allow one to perform a similar extrapolation for this scheme.

Next we compute the MPA corrections to the IP with a larger number of poles while increasing the number of bands from 4000 to 8000 but keeping a fixed dimension of the X matrix of 10 Ry. The results are shown in Fig. 4.8, where we can see that with 6 poles the quasi-particles change less than 8 meV with respect to more accurate values with 10 poles, which corresponds to a similar number of poles as the ones required to converge the bulk systems discussed in Section 4.1. The comparison between the curves in Fig. 4.8 computed with different number of bands shows more negative corrections for the calculations done with more bands, as the negative slope of the second fit in fig. 4.7 right decreases with respect to the number of bands and a dimension larger that

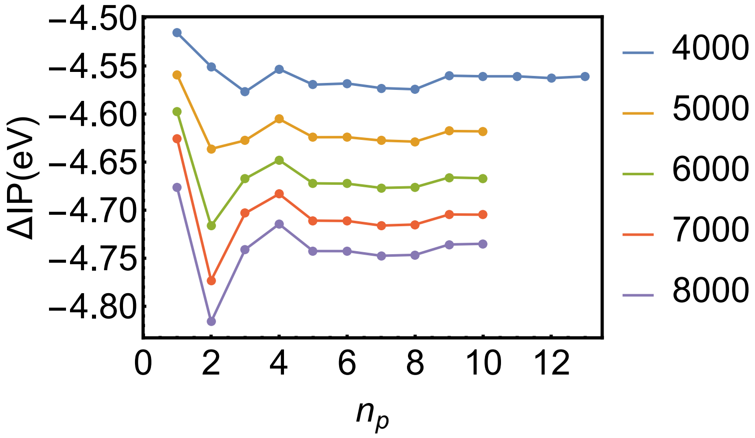

Figure 4.8: MPA convergence with respect to the number of poles of the corrections to the Ionization Potential of the F2 molecule. Where we have fixed the size of the X matrix to 10 Ry and each curve was computed with a number of bands that ranges from 4000 to 8000.

20 Ry might be also required to obtain converged results.

We have repeated the convergence study with respect to the number of poles, with a X matrix dimension of 15 Ry, but we were able to do it only up to 6 poles. The results are similar those discussed above. In Fig. 4.9 we show the IP values computed with 1 and 6 poles with different number of bands and extrapolate the results for an infinite number of bands. The difference between the value computed with 8000 bands and the extrapolation is 0.15 and 0.21 eV for 1 and 6 poles respectively, showing that the present results are still far from convergence. The difference between the extrapolated IP computed with 1 and 6 poles is 0.17 eV, showing that with this level of accuracy the F_2 molecule can be approximately described by a plasmon-pole model.

In a further step, we use the extrapolated values of Fig. 4.9 computed from 15 to 20 Ry and extrapolated the IP values for an infinite dimension of X. The values corresponding to 15, 20 Ry and their extrapolation in the case of PPA and MPA with 6 poles are shown in Table 4.3. Despite the limited accuracy of our extrapolations, our results underestimate the BGW-FF results in Table 4.2 by 0.36 and 0.13 eV with PPA and MPA respectively. Furthermore, assuming that the extrapolated value computed with MPA with 6 poles is accurate and can therefore be used as a reference for the full-frequency results computed with Yambo, the difference between PPA and FF would be smaller than 0.25 eV. This suggest that the GN version of the plasmon-pole is closer than the HL one to the full-frequency results, at least in the case of the F_2 molecule. As shown in Table 4.2, HL-GPP systematically overestimate the FF results ranging from 0.38 to 2.51 eV, by 0.86 eV in the case of the F_2 molecule.

As shown in the results reported in Ref. [158], the GW100 set is a suitable collection of systems for which GW without empty states methods [229], or with accelerators with respect to the summation over the total number of bands [229, 230], give good

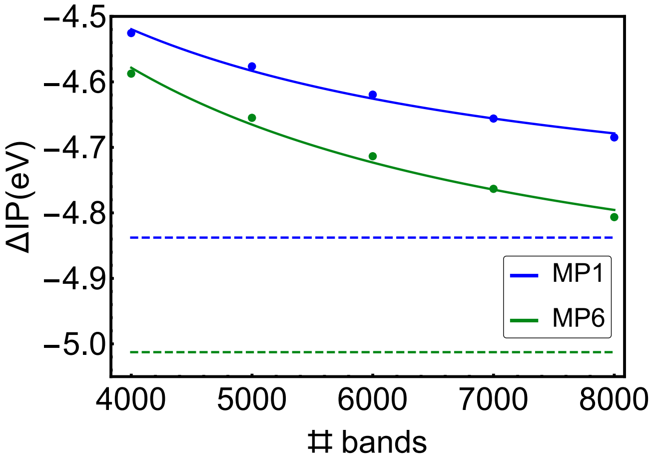

Figure 4.9: Extrapolation in the form $(\frac{a}{\#bands}+b)$ of the convergence with respect to the number of bands of the GW correction to the Ionization Potential of the F2 molecule computed with MPA with 1 and 6 poles. Where we have fixed the size of the X matrix to 15 Ry. The dashed lines represent the asymptotic values.

IP(eV)	DFT	MPA(15 Ry)	MPA(20 Ry)	extrapolation
GN-PP	9.42	14.22	14.27	14.37
MP6	9.42	14.43	14.49	14.60

Table 4.3: Extrapolated results for the ionization potential of the F_2 molecule.

agreements with respect to the more standard and computationally costly approaches. The MPA scheme can also be combined with convergence accelerators like the one already implemented in Yambo for the sum-over-bands convergence of the PPA self-energy [230], in order to speedup the convergences and avoid as much as possible the use of extrapolations. This however requires further developments and is beyond the scope of the present thesis.

4.3 MPA applied to metals

4.3.1 Particular issues of the GW approximation on metals

The plasmon pole model described in Section 2.3.1 has been successfully applied to the homogeneous electron gas [202] and simple metals as Al and Ni [223]. In contrast, metals with small plasmon energies, such as Cu and Co, are particularly challenging for simple models like the PPA, since non-free-electron metals present strong screening effects resulting in multiple plasmonic excitations [231]. The applicability of the PPA and the approximation of the band structure of transition and noble metals by that of a jellium model has been discussed in the literature [132, 161], highlighting the role played by valence electrons of d orbitals.

From the point of view of the calculations, another difficulty of metals is that even at zero temperature and contrarily to non-doped semiconductors, metallic systems present a non-vanishing probability that an electron is excited within the same band, in case the band is only partially filled. These transitions give rise to the so-called “intraband” contribution to the dielectric function:

$$X^{0}_{\mathbf{GG}'}(\mathbf{q},\omega) = X^{\text{inter}}_{\mathbf{GG}'}(\mathbf{q},\omega) + X^{\text{intra}}_{\mathbf{GG}'}(\mathbf{q},\omega). \tag{4.1}$$

In principle, at finite $\mathbf{q}$ the intra-band contribution, $X^{\text{intra}}_{\mathbf{GG}'}(\mathbf{q},\omega)$, can be computed explicitly by Eq. (2.16) as in the case of the inter-band term, $X^{\text{inter}}_{\mathbf{GG}'}(\mathbf{q},\omega)$, with the sum running over the semi-filled states, although, better alternative methods are proposed in the literature [232, 233]. On the other hand, the long-wavelength limit, $\mathbf{q} \to 0$, is usually treated by a Drude term [207] that for the dielectric function takes the form

$$\varepsilon^{\text{intra}}(\omega) = 1 - \frac{\omega_D^2}{\omega^2} + O[q^2], \tag{4.2}$$

where the Drude frequency, ω_D, is a parameter difficult to estimate with *ab initio* calculations, since it may require very fine $\mathbf{k}$-points grids [207]. The intra-band term plays an important role for noble metals [207, 234].

QP(eV)	LDA [161]	PBE [191]	GW [161]	GW [237]	GW [191]	Exp [235]
Γ_{12}	-2.27	-2.05	-2.81	-2.36	-1.92 to -2.11	-2.78
X_5	-1.40	-1.33	-2.04	-1.63	-1.45 to -1.22	-2.01
L_3	-1.63	-1.47	-2.24	-1.78	-1.58 to -1.36	-2.25
Γ_1	-9.79	-9.29	-9.24	-9.35	-9.14 to -9.20	-8.60
$L_{2'}$	-1.12	-0.92	-0.57	-0.92	-0.98 to -1.02	-0.85
L gap	5.40	4.80	4.76	4.78	4.98 to 5.09	4.95

Table 4.4: DFT and GW quasi-particles of Cu computed with different methodologies by different groups and compared with the experimental values. All the GW calculations correspond to FF approaches ran on top of LDA [161], PBE [191] and full-potential LMTO [237].

4.3.2 The polarizability of Cu

The electronic structure of Copper has been studied, both experimentally [235, 236] and theoretically [161, 191, 237]. Yet, from the theoretical point of view the results are very sensitive to the choice of the exchange and correlation functional and large differences are found within the GW approximation, being particularly sensitive to the DFT starting point as shown in Table 4.4. For this reason, Copper is a very challenging test case for the application of MPA and allow us to better understand the failure of the PPA and validate our approach.

We performed DFT calculations at the PBE level using scalar-relativistic Optimized Norm-Conserving Vanderbilt Pseudopotentials [228] and a kinetic energy cutoff of 100 Ry. Our DFT results are in good agreement with the previous results with the same method [191], being slightly different from the LDA results reported in [161]. The GW calculations were done using a $12 \times 12 \times 12$ **k**-points grid and a total of 200 occupied plus unoccupied states. The FF calculations on the real axis were done considering frequency grids from 500 to 2000 frequency points.

We then performed GW calculations starting by the plasmon pole method. When applying the PPA we found that 48% of the polarizability matrix elements fail the plasmon pole condition (3.76) and, as explained in Section 3.6.1, in this situation the position of the pole is set to 1 Ha. This results have an averaged relative deviation defined in (3.85) of $\langle RSD \rangle = 0.42$. These values are extremely high and lead to quasi-particle solutions very different from FF, worsening the DFT results summarized in Table 4.4.

In order to avoid the same problem in the MPA, we have slightly modified the double parallel sampling described in Section 3.5.3 by introducing a shift, $\varpi_1 = 0.1Ha$, also at the X sampling point at origin of the coordinates. Despite presenting a larger percentage of corrected poles, the MPA with only one pole and the modified sampling considerably improves the representability when compared with the PPA, lowering the average deviation to $\langle RSD \rangle = 0.35$ and suggesting that the method we introduced to correct the unphysical poles works well. Let's start by considering that X is well described in a small number of matrix elements within the plasmon pole model (frequency sampling at zero). Since the others matrix elements diverge at $\omega = 0$, the pole would then comply with the plasmon pole condition only by chance, amounting to a total number of failures slightly below 50% as actually happens. By introducing a shift in the frequency sampling previously done at zero, the number of times the pole condition is not met within MPA increases but is also more realistic, since it is not given by a random number, but due to the complex structure of the polarizability of Cu. The representability significantly improves already with 2 poles, considerably changing the number of failures and the relative deviation, as shown in Fig. 4.11. This suggests that the main issue with the plasmon pole model description of the envelop structure of the polarizability is both the method used to determine its parameters and an insufficient number of poles. In fact, a larger number of poles does improve the X representability. In Fig. 4.11 we illustrate the evolution of the number of failures and $\langle RSD \rangle$ for an increasing number of poles. Both quantities decrease very rapidly with increasing number of poles.

We get more insights by analysing the full frequency polarizability computed with a frequency grid of 1000 points and plotted in Fig. 4.12. The overall structure is not much different from those of Si, hBN and TiO_2 plotted in figs. 4.1, 4.2 and 4.3, in the sense that they seem simple enough to be approximated by a multipole model with a few poles. The main differences consist in the position of the most intense plasmon, that in the case of Cu has a very low energy, and the presence of several secondary excitations results in a very noisy polarizability. The first issue makes difficult the estimation of the plasmon pole parameters, since the sampling at $\omega = 0$ lies in a noisy region of many poles. This is probably related to the large number of X matrix elements that do not comply with the failure condition in the PPA, (3.76). The correction of the pole with an inadequate value is the main cause of the large errors.

Before addressing the converged results, we compare the polarizability computed within MPA with the PPA and FF results. In Fig. 4.12 we show selected X matrix elements computed with 1 and 12 poles. As already seen in the previous section for TiO_2, and taking the FF calculation as a reference, Cu polarizability has a complex structure that cannot be captured by a single pole solution. Increasing the number of poles the agreement between X computed with MPA and FF improves significantly, however the FF polarizability presents a level of noise that cannot be reproduced unless the number of poles considered is of the order of magnitude of half the number of points in the FF grid and the X sampling is done much closer to the real axis. For example, the

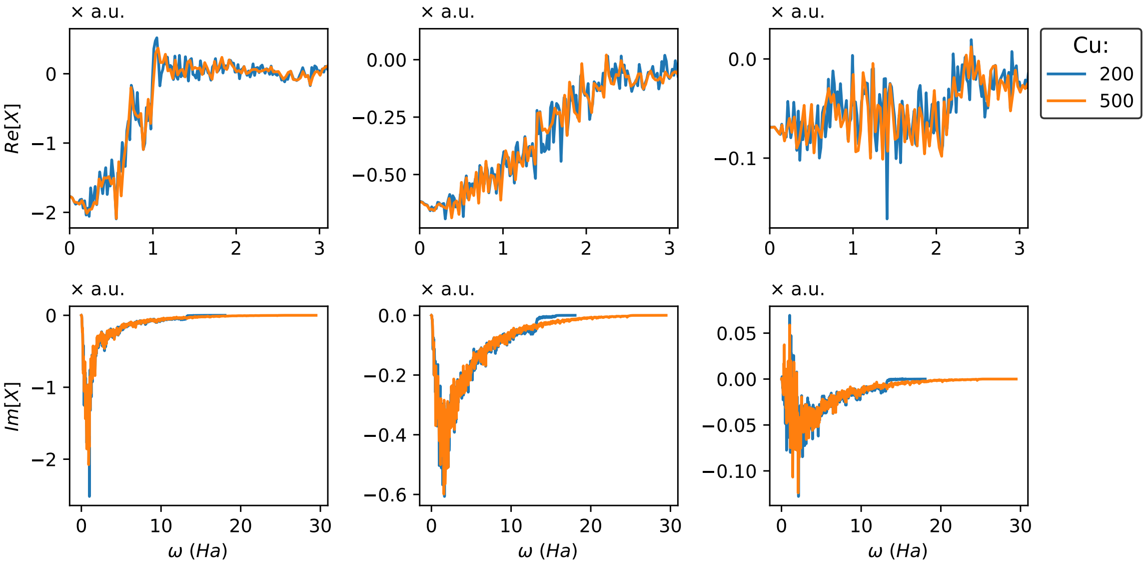

Figure 4.10: Selected Cu X matrix elements computed within FF with different number of bands (200 and 500). In order to show both, the overall and the detailed behavior of the polarizability, we plotted the imaginary part of X in the bottom panels in the full frequency interval determined by the number of bands, while the real part of X are plotted in the top panels in a zoomed region. A similar scheme from Fig. 4.1 is used for the units of X, where we omitted the specific scales in order to avoid confusion with the zoomed plots.

polarizability computed with multipole model using 12 poles gives the overall frequency-dependency of the full frequency results, while the X is much smoother.

The origin of the noise is related to the topology of the bands of Cu, similarly to the case of Ni [238]. The general starting point of the GW calculations is an independent particle polarizability, X_0, defined in Eq. (2.16), whose structure has many peaks, each of them corresponding to a single particle transition. The X_0 matrix then enters in the Dyson equation, Eq. (2.11), that superimposes all the poles coming from different matrix elements and gives rise to the dressed polarizability X. As already discussed in Sections 4.1.1 and 4.1.3, this screening process results in a progressively simpler structure of X as we enlarge the size of X_0 and therefore of the X matrices. In many materials, the head of X, i.e. the matrix element corresponding to $\mathbf{G} = \mathbf{G}' = 0$ and also the most relevant, shows a very simple structure, suitable to be approximated by a plasmon-pole model. In Cu we obtain an overall simplified X as well, but there are many secondary transitions close in energy that are not well overlapped and contribute to the noise. Those many secondary transitions originate from the almost flat d-bands of Cu [161]. As shown in Fig. 4.10, the convergence of the fine structure of X is very difficult and depends on many parameters.

Despite the instability of the fine structure of X in the full frequency approach, the final quasi-particle corrections are not significantly affected when computed with

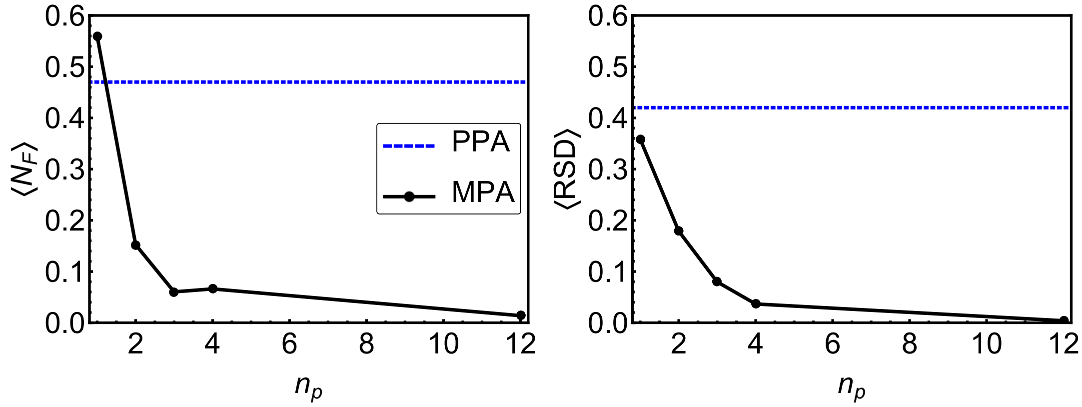

Figure 4.11: Values calculated for Cu of (left) the mean number of matrix elements, $\langle N_F \rangle$, for which the position of the poles was corrected according to Eq. (3.77) for MPA and Eq. (3.76) for PPA, and (right) $\langle RSD \rangle$, average deviation as defined in Eq. (3.85), as a function of the number of poles used in the MPA approach.

sufficiently large frequency grids, of the order of thousands points. This explains why the MPA quasi-particles approximate well the FF results, within 0.1 eV, even if only the main contributions of the excitations remain in the multipole polarizability, due to the simplifications introduced by the double parallel sampling shifted from the real axis by $\varpi_2 = 1$ Ha and the limited number of poles.

4.3.3 MPA on Cu

Now we will focus on the application of the MPA method to the band structure of Cu. We start by converging the number of poles required to achieve an accuracy similar to the FF method.

We found that the accurate description of different quasi-particles requires a different number of poles. In order to understand this behaviour we have computed the frequency dependence of the self energy for two selected quasi-particles of Table 4.4, Γ_{12} and Γ_1 and compare with the corresponding PPA and full frequency results. The results are shown in Fig. 4.13. We can see how the MPA with one pole improves the PPA description of the tail of the self energy close to the solution without solving the general problems of the plasmon pole model discussed in Section 4.1.3. In particular the poor overlapping of the poles of the self-energy that results in spurious solutions of the quasi-particle equation. In particular, the states close to the Fermi energy, as Γ_{12} shown in Fig 4.13, have a large number of possible solutions.

Figure 4.13 shows that the self-energy computed with the FF approach presents a more complex structure that the one of the systems studied so far, for example of Si shown in Fig. 4.6. The convergence of this structure is very challenging, since an accurate quasiparticle solution requires an accurate description of the tail of the self-energy and therefore a very large number of frequencies in the computation of the

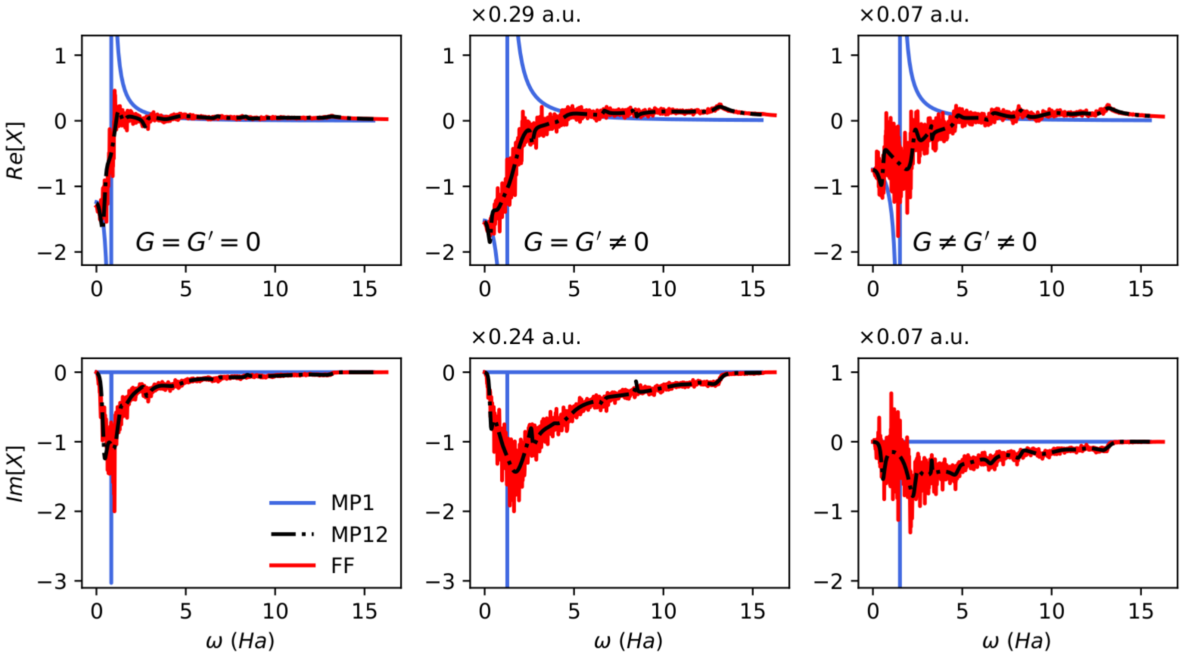

Figure 4.12: Selected Cu X matrix elements computed within MPA with 1 and 12 poles compared with the corresponding FF results. The same scheme from Fig. 4.1 is used for the units.

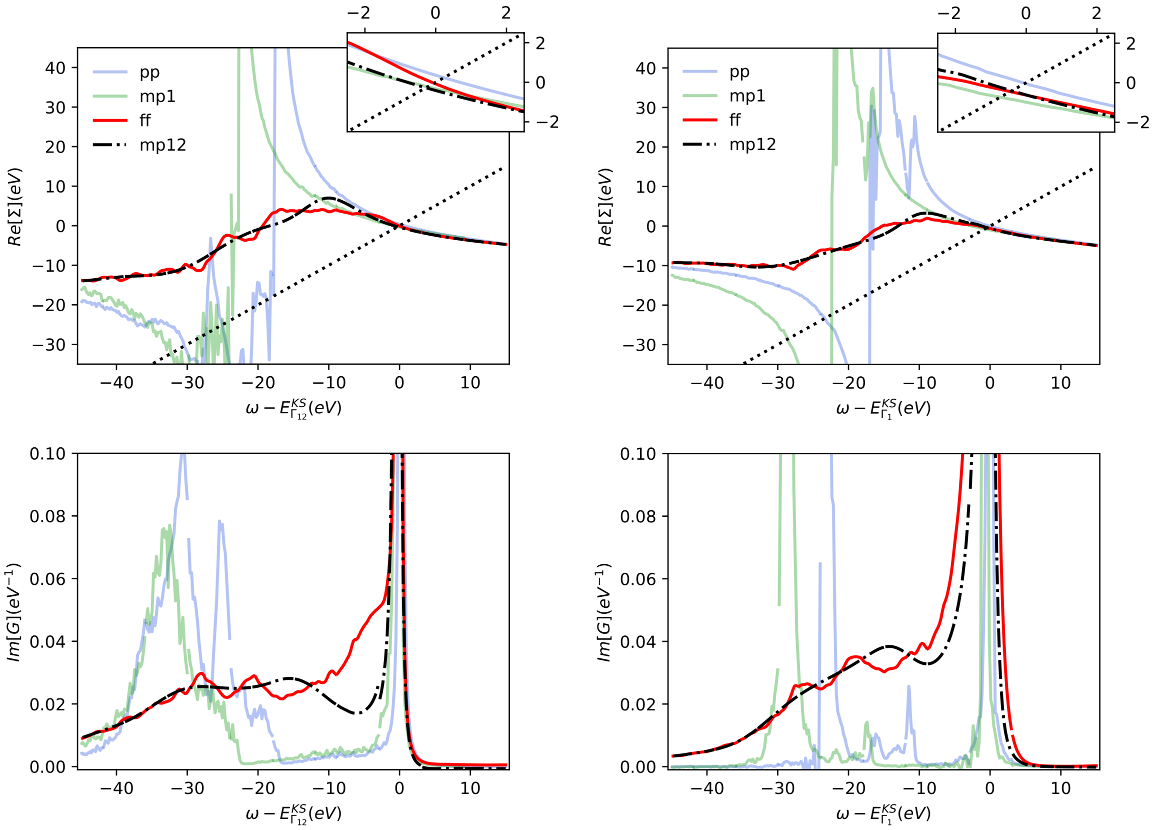

Figure 4.13: Frequency dependence of the real part of the self-energy (top) and spectral function (bottom) of the Γ_{12} (left) and Γ_1 (right) quasi-particles of Cu computed with PPA, MPA and FF.

polarizability within the full frequency approach. The calculations done with 500, 1000 and 2000 frequency points still present changes. This is in part due to the large frequency range along the real axis, which is determined by the number of bands included in the calculation of X: around 20 Ha with 200 bands and reaching around 30 Ha with 500.

The effects of secondary plasmonic excitations on the self-energy of Cu are more relevant for the correction of Γ_{12} than for Γ_1. This feature is also observed for other quasi-particles at intermediate energies, suggesting that the effects are stronger for higher states closed to the Fermi level. As shown in the bottom panels of Fig. 4.13, secondary plasmons modify the shape of the satellite structure in the spectral function, which have several peaks in both cases. Moreover, in the case of Γ_{12} the fine structure in the tail of the self-energy derive in a shoulder shape close to the quasi-particle peak in the spectral function, that is not captured by the multipole model with 12 poles.

In general, the quasi-particle solution is sensible to the small peaks in the tail of the self-energy, that are difficult to convergence with respect to almost all the parameters, specially the number of frequency/poles and the number of bands, and may explain part of the divergences of the results available in literature and the sensibility to the starting DFT point. The MPA model with 12 poles reproduces the overall frequency dependence of the self-energy, but does not describe well the fine structure of the secondary plasmons and in many cases results in quasi-particle corrections that are still different from the FF results. The quasi-particle correction improve significantly with respect to the FF results for the model with 17 poles and not much more up to 20 poles. This can be understood not only by the increase of the number of poles but rather by an increase in the number of poles in the region close to zero frequency. The distribution along the real axis of the frequency sampling, described in Section 3.5.3 adds a new point closer to $\omega = 0$ in powers of 2: when the number of poles is $n_p = n^2 + 1$, being n an integer which, for a number of poles larger than 12, happens exactly for $n_p = 17$. This leads to conclude that the sampling of X around $\omega = 0$ is fundamental in systems with low energy plasmons such as Cu, in order to determine the fine structure of the peaks of the tail of the self-energy and thus an accurate quasi-particle solution.

After having determined a suitable number of poles and checked other parameters of sampling, we had analysed in detail other parameters of convergence, e.g. the **k**-points grid and the number of bands. In Table 4.5 we compare with results obtained with a $12 \times 12 \times 12$ and a $24 \times 24 \times 24$ **k**-points grid computed with 200 bands. It is interesting to notice that despite the DFT values obtained with the two **k**-grids having differences of the order of 100 meV the GW quasi-particle energies present differences of the order of 10 meV. In the case of Γ_{12}, GW corrections actually change sign.

In a further step we have checked the convergence with the number of bands up to 500, as shown in Table 4.6. Even with 500 bands results are not converged, since the results change slowly, therefore we have performed and extrapolation illustrated in

grid:	$12 \times 12 \times 12$		$24 \times 24 \times 24$	
QP(eV)	DFT	MPA17	DFT	MPA17
Γ_{12}	-2.08	-2.14	-2.18	-2.15
Γ_1	-9.17	-9.38	-9.27	-9.39

Table 4.5: Quasi-particles of Cu for two different **k**-points grids.

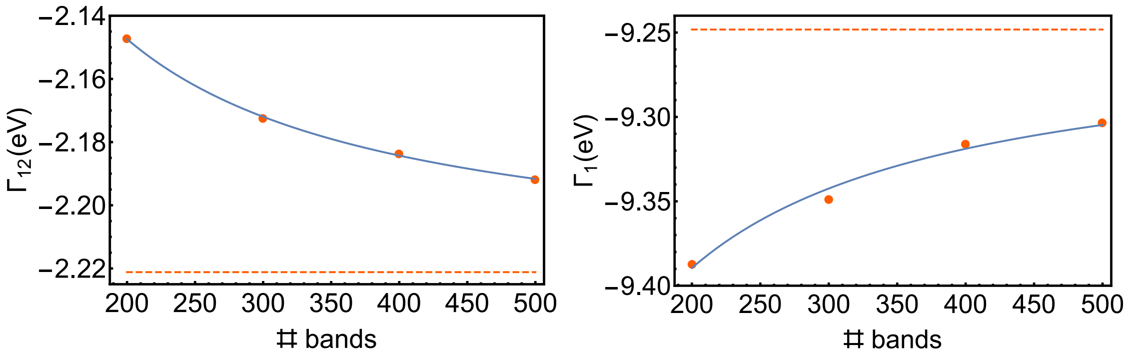

Figure 4.14: Extrapolation in the form $(\frac{a}{\#bands} + b)$ of the convergence with respect to the number of bands of the Γ_{12} (left) and Γ_1 (right) quasi-particles of Cu. Where we have fixed the **k**-points grid to 24 × 24 × 24 points and the size of the X matrix to 20 Ry. The dashed lines represent the asymptotic values.

Fig. 4.14, which results are also included in Table 4.6. Despite not including the intraband term in any of our calculations, due to a limitation in the current implementations in the Yambo code, we see that the extrapolated results improves the PBE results with respect to the experiments for all the quasi-particles, showing non trivial corrections that cannot be achieved by a rigid shift, as already commented in Ref. [161]. We also expect that the inclusion of the Drude term will reduce the remaining differences with the experimental values.

# bands:	200	300	400	500	extrapolation
Γ_{12}	-2.15	-2.17	-2.18	-2.19	-2.22
Γ_1	-9.39	-9.35	-9.32	-9.30	-9.25

Table 4.6: Convergence with respect to the number of bands of the Γ_{12} and Γ_1 quasi-particles of Cu. The data and its extrapolation correspond to the values of Fig. 4.14.

Chapter 5

Applications

In this chapter we describe the results of the study Gr/Ir(111) interfaces done by means of first-principals calculations. We start by using DFT calculations to study the effect of O adsorption on Gr/Co and GrCoIr. We then address the effect of Co and Fe intercalation on the structural and electronic properties of the Gr/Ir interface. We finally go beyond the DFT level and apply the GW/MPA approach in the calculation of the band structure of the Gr/Co interface, of which we present only preliminary results.

5.1 Oxygen adsorption on Co, Co/Ir, and Gr/Co interfaces

Graphene (Gr) grown on different transition metal (TM) substrates presents distinct structural characteristics and various alterations of its electronic properties depending on the lattice mismatch and degree of hybridization [1, 8–10, 13, 15, 18, 19, 22, 33, 37–40]. In particular, when grown on non-commensurate surfaces, it can corrugate and form a moiré pattern [8, 9, 15, 22]. The magnitude of the corrugation depends on the metal underneath and can be used e.g. as a template for the adsorption of molecules [15, 22, 239–242] of which TM-phthalocyanine molecules deposited on Gr/Co/Ir are an example [15, 22].

Bulk cobalt has a hexagonal-closed-packed (*hcp*) periodicity while bulk iridium is face-centred-cubic (*fcc*), with the (111) plane displaying hexagonal geometry. The lattice parameters of graphene and Co differ by only 0.05 Å [78, 243–245], being in practice lattice matched. In fact, Gr grown on Co lies flat on the surface, with a small interplanar distance [37]. The electronic properties of graphene are anyway significantly altered by the strong interaction with the Co layer [9, 22, 39]. On the other hand, graphene and Ir lattice parameters differ by 0.25 Å [78, 245, 246] and Gr grown on Ir forms a moiré pattern corresponding to a 10×10 graphene supercell, over a 9×9 Ir cell. However the electronic properties of graphene are only slightly altered by the weak interaction with the substrate present in Gr/Ir(111).

Although Co(0001) and Ir(111) have different in-plane lattice parameter, when a single Co layer is intercalated underneath Gr grown on top of an Ir(111) layer, it assumes the lattice parameter of iridium [8, 9]. Here, the graphene layer has an important role in stabilising the Co single layer on the Ir surface against, e.g., the formation of Co clusters [9]. When a larger number of Co layers are intercalated, Co recovers its bulk structure [9]. Depending on the number of intercalated Co layers, Gr either corrugates and forms a moiré pattern with the Co single layer or lies flat due to the lattice matching when in the presence of multi layer Co [15, 22].

The aim of the present Section is to investigate, by means of first principles calculations, how the Gr/Co hybridization, and therefore, graphene electronic properties, can be tuned by oxygen intercalation and how changes in the structure of the Co surface, such as Ir-induced strain, can influence the O binding energies. In order to evaluate the effects of a strained Co surface on the adsorption of O, we considered the Co intercalation on Gr/Ir(111) as a mean to obtain an electronically identical system to Gr/Co(0001) but with different structural properties, in particular a lattice mismatch with Gr inducing a moiré pattern and Gr corrugation. We performed DFT calculations to compute the structural, electronic, and magnetic properties of O adsorbed on these two surfaces, Co(0001) and Co/Ir(111).

Then we study the mechanisms of the O intercalation under graphene in a Gr/Co(0001) interface, focusing on the effect on the Gr-Co hybridization. In particular, we compute the band structure of a Gr/Co(0001) supercell before and after O adsorption and compare the results with the reported experiments, that is then unfolded into the graphene unit cell in order to compare the results with recent ARPES and PEEM measurements [34, 69]. In particular, our *ab-initio* calculations on the electronic properties of the Gr/Co(0001) interface in the presence of adsorbed O have been found to be in very good agreement with experiments, and shed light on how oxygen intercalation modifies the Gr-Co hybridization.

5.1.1 Methods

We have performed DFT calculations on Co(0001) and Co/Ir(111) slabs, with and without adsorbed oxygen, as well as on the Gr/O/Co(0001) interface. Co and Ir bulk systems were also computed for completeness. All calculations were performed using the plane wave and pseudopotential implementation of DFT provided by the Quantum ESPRESSO package [107, 108]. We employed the GGA-PBE [247] exchange-correlation functional and we used ultrasoft (US) pseudopotentials to describe electron-ion interactions. The kinetic energy cutoff was set to 30 Ry for the wavefunctions and 330 Ry for the charge density.

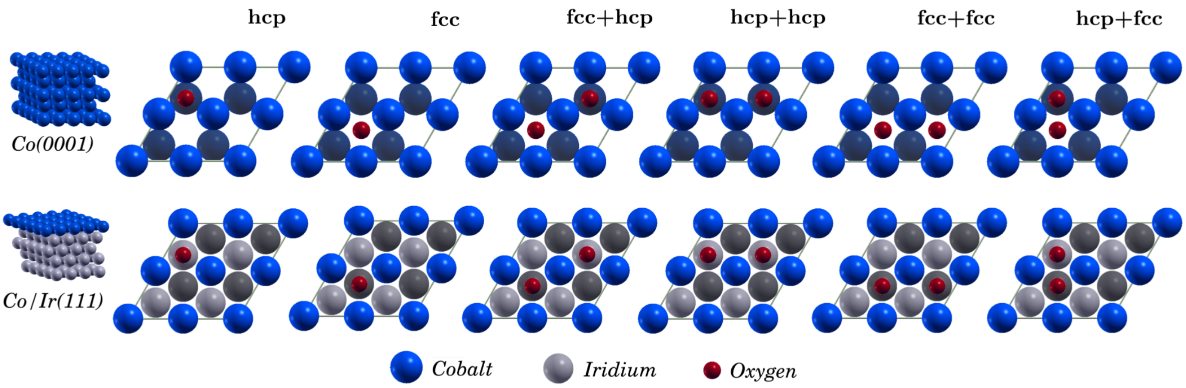

Figure 5.1: Top view of the different O adsorption sites considered in the calculations, for the Co (top) and Co/Ir surfaces (bottom), for 0.25 and 0.5 ML O concentrations. The labeling of the different configurations follows the notation used in Ref. [71]. The notation refers to surface adsorption sites. The case where an O occupies an fcc position below the first Co layer is labeled hcp+fcc (octa) in the text.

The Brillouin zone was sampled by using **k**-points meshes of 16 × 16 × 16 for cobalt and iridium bulk, 16 × 16 × 1 for Co(0001) and Co/Ir(111) surfaces, and 8 × 8 × 1 for surfaces with adsorbed oxygen. The projected density of states for Gr/O/Co(0001) was computed with a 40 × 40 × 1 grid. In all the calculations we use thresholds of 1.5×10^{-5} Ry for the total energy convergence. The metallic substrates were modelled by considering slabs of 5 atomic layers with a vacuum layer of 10 Å in order to prevent spurious interactions between the replica. An additional 2 Å of vacuum was introduced in the modelling of the surfaces in the presence of oxygen. The slab thickness of 5 layers was validated by calculating adsorption energies considering up to 9 layers as reported in Section 5.1.5.

We have considered low oxygen concentration, 0.25 and 0.5 ML, i.e. below the values required to form CoO and for which the oxygen atoms remain chemisorbed on the surfaces, according to Ref. [71]. In order to model these oxygen concentrations we have used supercells made of $p(2\times2)-O$ and $p(2\times2)-2O$ surface unit cells. The initial positions for the oxygen atoms within the supercell were chosen according to the most stable configurations reported in Ref. [71] and are shown in Fig. 5.1. We have labelled the O sites following the notation of Ref. [71]. All the atomic positions (O, Co and Ir) were then optimised until the forces acting in the atoms were smaller than 1.0×10^{-4} Ry/Bohr.

The adsorption energy per oxygen atom on Co(0001) and Co/Ir(111) surfaces, E^{O}_{Co} and $E^{O}_{\mathrm{Co/Ir}}$, are defined as the difference between the total energy of the target system with the adatoms and the energy of the clean surface plus the energy of the isolated atom:

$$E^{O}_{\mathrm{Co}} = -\frac{1}{N_{\mathrm{O}}}\left(E_{\mathrm{O/Co}} - E_{\mathrm{Co}} - N_{\mathrm{O}}E_{\mathrm{O}}\right) \tag{5.1}$$

$$E^{O}_{\mathrm{Co/Ir}} = -\frac{1}{N_{\mathrm{O}}}\left(E_{\mathrm{O/Co/Ir}} - E_{\mathrm{Co/Ir}} - N_{\mathrm{O}}E_{\mathrm{O}}\right), \tag{5.2}$$

where N_{O}, $E_{\mathrm{O/Co}}$, E_{Co} and E_{O} are the number of oxygen atoms in the supercell, the total energy of the adsorbate+substrate system, of the pristine surface, and of free oxygen atom, respectively. In principle, O adsorption energies could also be referred to the energy of the isolated O_2 molecule, resulting in an overall renormalization of the absorption energies without altering the trends [71].

5.1.2 Oxygen adsorption energies on Co and Co/Ir surfaces

We compute the adsorption energies for oxygen adsorbed on a 5 layers Co slab ($\mathrm{Co(0001)_5}$) and on a slab with a layer of Co on top of a 4 Ir layers ($\mathrm{Co_1/Ir(111)_4}$), for both 0.25 and 0.5 ML coverage, corresponding to one or two O atoms per cell, respectively. We consider different possible adsorption sites as illustrated in Fig. 5.1, and the corresponding calculated adsorption energies are reported in Table. 5.1.

For the lowest oxygen coverage on $\mathrm{Co(0001)_5}$, 0.25 ML, we find very similar adsorption energies for the two possible adsorption sites, fcc (5.43 eV) and *hcp* (5.47 eV), The adsorption energy drops to values around 5.0 eV for the 0.5 ML coverage, indicating a repulsive interaction between O adatoms. The most favourable adsorption configuration is the one labelled $hcp + hcp$, differing by less than 0.01 eV from the $fcc + hcp$ configuration (see Fig. 5.1), although such a small energy difference is at the verge of the precision of the DFT method and both sites can be considered energetically equivalent (more details in Section 5.1.5). Overall, the present results compare well with the values previously reported in Ref. [71], with both the adsorption energy and the energy differences between different configurations decreasing when increasing O concentration.

In the case of $\mathrm{Co_1/Ir(111)_4}$, for 0.25 ML, the configuration with the lowest energy corresponds to the O atom adsorbed on a fcc site. The adsorption energy is 5.76 eV, 0.04 eV larger then for the *hcp* configuration. As in the case of the Co surface, the adsorption energy decreases with increasing O content, and the preferred sites are also the same. The most favourable configuration is then the $fcc + fcc$, followed by the $fcc + hcp$ configuration, with an absorption energy of 5.51 and 5.42 eV, respectively. In general, the most favourable site for oxygen adsorption on cobalt is the *hcp* one, whereas it becomes the fcc site when oxygen is adsorbed on Co/Ir. Comparing the two surfaces, we find that the adsorption energies of oxygen for both 0.25 ML and 0.5 ML are respectively 0.29 eV and 0.45 eV larger on Co/Ir than on Co.

The computed distances between the oxygen adatoms and the surface are reported

O coverage	O site	$Co(0001)_5$	$Co_1/Ir(111)_4$
0.25 ML	hcp	5.47 [5.56]	5.72
	fcc	5.43 [5.55]	5.76
0.5 ML	fcc+hcp	5.05 [5.02]	5.42
	hcp+hcp	5.06 [4.98]	5.40
	fcc+fcc	5.00 [4.86]	5.51
	hcp+fcc	4.65 [-]	5.09

Table 5.1: Adsorption energies in eV/O computed for $Co(0001)_5$ and $Co_1/Ir(111)_4$, where the indexes 1, 4 and 5 refer to the number of layers of each element. We show in brackets the result for Co from Ref. [71].

in Table 5.2 as d_O. For the 0.25 ML configurations, the higher the adsorption energy the closer the oxygen atoms are to the surface. The two configurations of adsorbed O on Co(0001) show, anyway similar O-surface distances, that differ in less than 0.06 Å. Instead, the configurations of O adsorbed on Co/Ir show a larger difference, 0.14 Å, even if their adsorption energies are similar. For 0.5 ML, the O-surface distances, for both $Co(0001)_5$ and $Co_1/Ir(111)_4$, have a larger dependence on the absorption site. In contrast with what happens to the 0.25 ML coverage, there is no apparent correlation between the O-surface distances with the adsorption energies, probably due to the O-O interaction. On the other hand, the O-surface distance for each specific O atom geometry presents a similar behaviour for both concentrations: O_{fcc} are closer than O_{hcp} to the surface when adsorbed on Co/Ir surfaces, and the opposite happens when adsorbed on the Co surface. For the most favourable configurations, the oxygen atoms are closer to the surface on Co/Ir than on Co possibly due to the larger lattice parameter of Co/Ir when compared to Co(0001).

The first interlayer distance, d_{z1}, on both $Co(0001)_5$ and $Co_1/Ir(111)_4$ (shown in Tab. 5.2), increase with the O concentration. If we compare the most favourable oxygen configurations, the increase is 2.4% for Co and 4.2% for Co/Ir in the case of 0.25 oxygen ML, while for 0.5 ML is about 5.4% for Co and 7.6% for Co/Ir. The second interlayer distance, d_{z2}, is less sensitive to the presence of O, varying less than 1.4% for Co and 2.5% for Co/Ir.

Several geometries were also relaxed using as a starting configuration a slab with the oxygen atoms below the first Co layer. Contrary to what is reported in Ref. [71], for both $Co(0001)_5$ and $Co_1/Ir(111)_4$, and for both O concentrations considered, we always observe a relaxed geometry where the added O migrates to the surface. This can be due to the different methods used to perform the structural relaxation. In Ref. [71], in addition to oxygen, only the atomic positions of the atoms in the 3 top layers of a slab of 5 were relaxed, whereas we have relaxed the whole slab. Moreover, we also considered

O coverage	O site	Co(0001)$_5$ d$_O$	Co(0001)$_5$ d_{z1}	Co(0001)$_5$ d_{z2}	Co$_1$/Ir(111)$_4$ d$_O$	Co$_1$/Ir(111)$_4$ d_{z1}	Co$_1$/Ir(111)$_4$ d_{z2}
pristine	-	-	3.69	3.83	-	3.82	4.33
0.25 ML	hcp	2.12	3.75	3.80	1.98	3.89	4.31
	fcc	2.18	3.78	3.78	1.84	3.90	4.30
0.5 ML	fcc+hcp	2.24	3.86	3.76	1.92	3.95	4.29
	hcp+hcp	2.07	3.82	3.78	1.90	3.94	4.30
	fcc+fcc	2.06	3.87	3.75	1.80	3.97	4.29
	hcp+fcc	2.22	3.90	3.78	1.88	3.97	4.29

Table 5.2: Distances between the deposited oxygen and the substrates, d_O, and first and second interlayer distances, d_{z1} and d_{z2} respectively. For the Co(0001)$_5$ surfaces the interlayer distances correspond to the distances between Co neighboring layers. For the Co$_1$/Ir(111)$_4$ surfaces, the first interlayer distance corresponds to the distance between the Co layer and the next Ir layer, the second corresponds to an Ir-Ir layer distance. All the reported distances are in Å and were computed considering the difference between the average vertical coordinate of each atomic layer.

a configuration with O occupying an fcc site below the 2^{nd} layer. This corresponds to a Co layer for the case of the Co slab, and to an Ir layer for the case of Co/Ir. The latter is the only configuration for which the adsorption energy is larger for Co(0001)$_5$ than for Co$_1$/Ir(111)$_4$. The subsurface configuration has a considerably higher energy than the configurations with O adsorbed on the surface. In fact, subsurface O adsorption is expected to occur only for O contents larger than 1 ML [71]. We report more details about the geometry optimisations performed starting from the configurations with subsurface O in Section 5.1.5.

5.1.3 Electronic and magnetic properties

In order to understand the influence of O on the Co electronic properties, we report in Fig. 5.2 the density of states projected on the O and the top layer Co atoms. Majority and minority spin bands are shown for 0.25 and 0.5 ML coverage, for both Co(0001)$_5$ and Co$_1$/Ir(111)$_4$, and compared with the pristine systems (shown in grey). The DOS computed for the pristine systems show the Co 3d states localised around the Fermi energy, with a spin split of about 2 eV, that results in a magnetic moment of 1.68 μ_B/Co for Co(0001)$_5$ and 2.02 μ_B/Co for Co$_1$/Ir(111)$_4$. The majority spin d-states are completely occupied below the Fermi level, whereas the minority DOS cuts through the Fermi level, with peaks above and below, and a valley at Fermi for both systems.

The Co$_1$/Ir(111)$_4$ shows a narrower DOS than Co(0001)$_5$, leading to larger magnetic

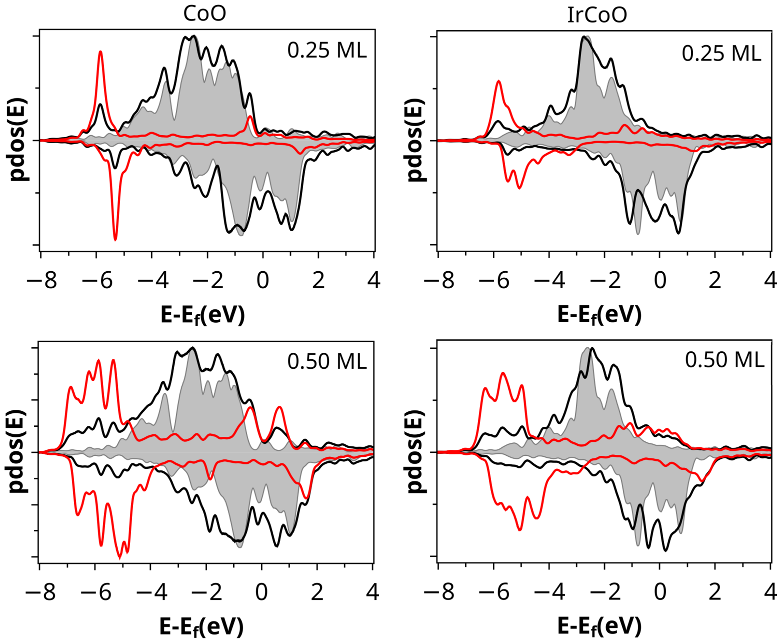

Figure 5.2: Density of states computed for O@Co (left panels) and O@Co/Ir (right panels), for 0.25 (top panels) and 0.5 ML (bottom panels). The density of states is projected on the atomic orbitals of O (red lines) and Co on the top layer (black lines). The Co top layer DOS for the pristine surface is shown is grey.

moments. This enhancement of the magnetic moment is related with the reduction of dimensionality when going from a Co slab to a single layer [22] as well as to the stretched lattice parameter of Co 1ML due to the presence of Ir(111). The same narrowing of the DOS leading to large magnetic moments was reported for the Gr/Fe/Ir [1] and Gr/FeCo/Ir [2] interfaces, both from experiment and DFT calculations. It is worth noticing though, that these calculations were performed within DFT+U [117] and that the choice for the Hubbard U parameter affects the computed magnetic moment, as described in detail in the Supplementary material of Ref. [2].

In the presence of O there is a clear overlap between Co and O states, that induces in a spin-split of the latter. The O $2p$ states hybridise with the lowest edge of the Co $3d$ bands, resulting in a peak around 5.5 eV below the Fermi level. Next, we observe an anti-bonding state, with the majority spin located just below the Fermi (E_F) level and the minority spin about 1.5 eV above E_F in the case of the 0.25 ML, more pronounced for Co(0001)$_5$ than in Co$_1$/Ir(111)$_4$. For the 0.5 ML, the O band energy distribution becomes wider and shifts slightly downward (i.e. towards larger binding energies) reaching to 6.8 eV, due to the O-O repulsive interaction. This is in agreement with Ref. [71], where it is shown that, for a larger range of O concentrations, the surface d-band broadens and monotonously shifts to lower energies. Comparing the Co(0001)$_5$ and Co$_1$/Ir(111)$_4$ surfaces, there are evidences of a larger hybridisation of the O atom with Co states in the case of Co$_1$/Ir(111)$_4$, for which the O pDOS peaks

		$Co(0001)_5$			$Co_1/Ir(111)_4$		
O coverage	O site	m_{tot}	m_{Co}	m_O	m_{tot}	m_{Co}	m_O
pristine		1.68	1.76	-	2.02	1.92	-
0.25 ML	hcp	1.68	1.69	0.23	2.07	1.89	0.37
	fcc	1.70	1.72	0.26	2.06	1.85	0.31
0.5 ML	fcc+hcp	1.61	1.24	0.08	2.02	1.73	0.37
	hcp+hcp	1.67	1.49	0.18	2.12	1.80	0.33
	fcc+fcc	1.68	1.53	0.19	1.94	1.68	0.26
	hcp+fcc	1.71	1.64	0.27	2.29	1.93	0.43

Table 5.3: Total magnetization in Bohr magnetons per cobalt atom (μ_B/Co), average magnetic moment for the Co atoms in the first layer and average O magnetic moments, computed for O adsorbed on $Co(0001)_5$ and $Co_1/Ir(111)_4$, for both the 0.25 and 0.5 ML coverages.

are broader. This is in agreement with the larger O adsorption energies computed for $Co_1/Ir(111)_4$.

In Table 5.3 we show a summary of the magnetization obtained for O adsorbed on $Co(0001)_5$ and $Co_1/Ir(111)_4$ slabs. In all configurations the O moment is aligned ferromagnetically with Co. For the pristine systems, the magnetic moment of the top layer Co atoms is larger for $Co_1/Ir(111)_4$ than for the $Co(0001)_5$ slab, 1.92 and 1.76 μ_B/Co respectively, reflecting the narrower DOS structure of $Co_1/Ir(111)_4$. After oxygen adsorption a small magnetic moment is found on the O atom, ranging from 0.08 to 0.27 μ_B when O is adsorbed on $Co(0001)_5$, and slightly larger, 0.26 to 0.43 μ_B, when adsorbed on $Co_1/Ir(111)_4$, depending on the oxygen concentration. Chemisorbed oxygen atoms have a very small impact on the total magnetization of the Co and Co/Ir slabs ($\lesssim$ 4% and $\lesssim$ 13% respectively). $Co_1/Ir(111)_4$ has only one magnetic layer, the intercalated Co, then the variations are slightly larger, since they are not compensated by the bulk-like deeper Co layers as in the $Co(0001)_5$ slab. Among the most energetically stable configurations, the variations are smaller than 5%. In fact, while the $hcp + fcc$ configuration has a 13% increase on the magnetization, it should be noticed that it is energetically much less favourable. The moments of the Co atoms in the first layer, (m_{Co} in Table 5.3), except in one Co/Ir case, decrease with respect to the pristine systems. The larger variation for $Co(0001)_5$ occurs for the $fcc{+}hcp$ configuration with a 30% decrease of the surface Co magnetization, while in the case of $Co_1/Ir(111)_4$, it happens for the $fcc + fcc$ configuration with a decrease of 14%. The smaller variations in this case are again related to the number of magnetic layers in the slabs.

Cobalt oxide bulk (CoO) is known to have an antiferromagnetic (AF) order, that has

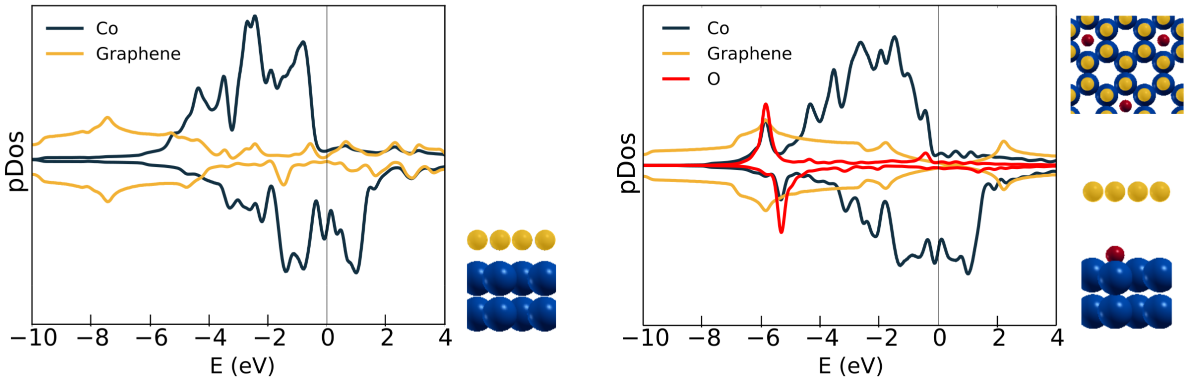

Figure 5.3: Density of states computed for Gr@Co (left panel) and Gr@O/Co (right panel) and projected on the C, on the first layer Co and O atomic orbitals. Next to each plot, a scheme with the atomic structure, illustrating the difference in the Gr-Co distance for the two systems and, for the case of Gr@O/Co, a top view showing the O distribution.

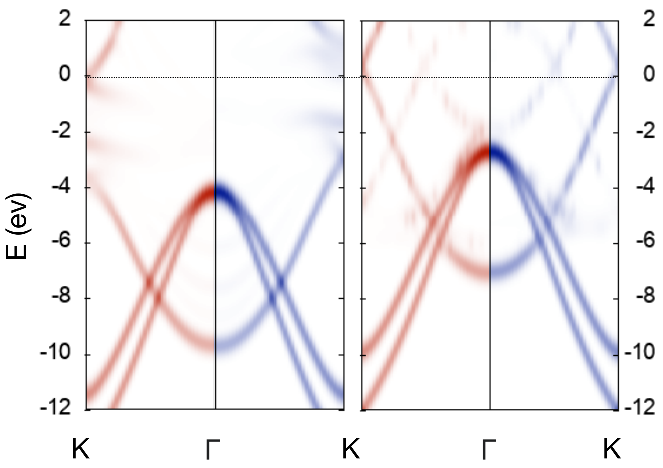

Figure 5.4: Bands projected on the atomic orbital of graphene, computed for Gr@Co and Gr@OCo and unfolded in the graphene unit cell. The red and blue colors correspond to the spin up and spin down states.

been well-described at the DFT+U level in Refs. [248–252]. This motivated the search for possible antiferromagnetic configurations for adsorbed O on the two Co surfaces considered here. Anyway, we find AF solutions only for Co/Ir with $hcp + hcp$ and $fcc + fcc$ oxygen configurations, but with a total energy 0.3 eV/O higher than the ferromagnetic configuration, thereby significantly less stable. More details are provided in Section 5.1.5.

5.1.4 Graphene on Co: decoupling through O intercalation

XPS, PEEM and ARPES measurements on Gr/Co(0001) show that, upon O intercalation there is an electronic decoupling between graphene and Co and graphene band structure acquires a nearly free-standing character except for a small p-doping [34, 69].

In order to assess the effect of oxygen intercalation under Gr, we have performed calculations for graphene on Co(0001)$_5$, with and without O adsorbed under graphene. We consider a 0.25 ML oxygen coverage on a 2×2 Gr@Co unit cell. Van der Waals interactions were taken into account through the Grimme-D3 scheme [121]. We observe that oxygen adsorption has a large impact on the structure of the Gr/Co interface yielding a dramatic increase in the graphene-Co distance, that changes from 2.1 in the pristine case to 4.7 Å upon O adsorption. In absence of the oxygen, a clear hybridisation between Co *d* electrons and C states close to the Fermi level can be seen from the projected density of states of Gr@Co as shown in Fig. 5.3 (left panel), as already observed in Refs. [9, 39, 75]. In presence of adsorbed oxygen, the density of states projected on C atomic orbitals is similar to that of freestanding graphene, as expected in view of the larger distance between the Co and Gr layers.

Such decoupling is even clearer when looking at the band structure for the two interfaces. In Fig. 5.4 the bands computed for the 2×2 Gr@Co unit cell are mapped into the Gr 1×1 Brillouin zone by using the `unfold-x` code [113]. This procedure allows us to visualise an effective band structure corresponding to the graphene unit cell in the presence of substrates and adatoms. Similarly to what found in Refs. [1, 2] for the GrCoIr interface in a 10×10 Gr supercell, the Dirac cone is disrupted by the hybridisation of Gr with the Co *d* states and the C states show a spin split induced by the spin-polarised Co states. This results in a shift of the apex of the cone of about -3.7 and -2.9 eV for the majority and minority spin channels, respectively (left panel of Fig. 5.4).

At variance with the Gr@Co case, for Gr@O/Co the graphene states are preserved, including the Dirac cone, without any spin splitting (right panel of Fig. 5.4). In this case, it can be seen that the Dirac point is located slightly above the Fermi level, at about 0.4 eV, indicating a small doping of graphene, in excellent agreement with value of the 0.3 eV recently measured with ARPES [69], and the 0.4 eV value from the PEEM momentum map reported in Ref. [34]. The same type of doping is also seen for Gr@Ir [75, 86] or on Gr/Ru(0001) upon O intercalation [67], with the Dirac cones at +0.21 and +0.5 eV respectively.

The O adsorption also changes the magnetic moments of the interface. Without O, the average magnetic moment of Co is 1.7 μ_B, but the hybridisation with graphene decreases the moment of the Co top layer. In fact, the average magnetic moment increases from 1.6 to 1.8 μ_B/Co when going from the top to the fourth Co layer, is good agreement with the values estimated from X-ray Magnetic Circular Dichroism, $\mu_s = 1.47\mu_B$ [34]. Concerning graphene, there is a small magnetic moment induced in the two nonequivalent C atoms, -0.08 and 0.05 μ_B. Upon O adsorption the Co magnetic moment is more uniform across the layers, 1.7 μ_B/Co and there is no significant moment on graphene. The adsorbed O atom has a magnetic moment of 0.2 μ_B, in the same range

	Exp. [71, 246]	**DFT NC [71]**	**DFT US**	**DFT NC**
Co, a(Å)	2.507	2.52	2.515	2.497
Co, c/a	1.623	1.62	1.617	1.618
Ir a(Å)	3.839	-	3.896	3.870
d_{O-O} (Å)	1.21	1.23	1.229	1.230
$E_O - \frac{1}{2}E_{O_2}$ (eV)	2.56	2.89	2.867	2.878

Table 5.4: Comparison of structural parameters and formation energy with experiments, and previous DFT PBE calculations Ref. [71]. Calculations using ultra-soft (US) and norm conserving (NC) pseudopotentials are also reported.

of the ones computed without the graphene layer.

5.1.5 Technicalities

In order to validate the computational method described in the main text, we started by calculating the structural parameters for Co, Ir and the oxygen molecule, using both ultra-soft (US) and norm conserving (NC) pseudopotentials. The results are summarized in Table. 5.4, and compared with values previously reported, both experimental [253] and computed with a similar level of theory [71, 254]. The computed lattice parameter of *hcp* cobalt bulk is $a = 2.515$ Å and $c/a = 1.617$, which differs from the experimental values by less than 0.4%. For the fcc iridium bulk we obtain a lattice parameter of $a = 3.896$ Å, which differs by less than 1.5% from the experimental one.

In case of the oxygen molecule, we obtained for the bound length 1.229 Å, which differs by less than 1.7% from the experimental value, while the binding energy, 2.867 eV/O, differs by less than 12%. This typical overestimation is well-known [71, 254] and due to the sensitivity of molecular bindings on the details of the pseudopotential. All our calculations are in very good agreement with the existent literature, such small differences are comparable with the level of accuracy of DFT.

The differences in the structural parameters that we obtained in Table 5.4 when using NC and US pseudopotentials are very small. Nevertheless, as reported in Table 5.5, we checked also the differences in the adsorption energies of few cases of O adsorbed on Co and Co@Ir respectively. The results of NC and US pseudopotentials are very consistent with each other. In the case of the 50% oxygen coverage, the fcc+hcp and the hcp+hcp configurations are very closed in energy but the small difference results in a different ground state when using different pseudopotentials.

The Co(0001) and Co/Ir(111) surfaces were modelled using periodic boundary conditions, considering slabs surrounded by a vacuum layer, thick enough to prevent spurious interactions between the replica. In Table 5.6 we present the dependence of the adsorption energy of oxygen in slabs of 5 layers of Co and Co/Ir on the vacuum thickness. The

O	adsorption	Co			Co/Ir	
(ML)	site	NC [71]	US	NC	US	NC
0.25	**hcp**	5.56	5.47	5.51	5.72	
	fcc	5.55	5.43		5.76	5.81
0.5	**fcc+hcp**	5.02	5.05	5.10	5.42	
	hcp+hcp	4.98	5.06	5.08	5.40	
	fcc+fcc	4.86	5.00		5.51	
	hcp+fcc	-	4.65		5.09	
0.5	**hcp+fcc(octa)**	2.95				
	hcp+fcc(octa')	-	4.16		3.22	

Table 5.5: Comparison of the adsorption energies for Co and Co@Ir obtained with ultra soft and nor conserving pseudopotentials.

difference in the adsorption energy when using 10 to 12 Å is below 0.001 eV for all the systems, and therefore we used a 1212 Å vacuum layer in the calculations presented in the main text.

The Co(0001) and Co/Ir(111) surfaces were modelled using considering slabs with a limited number of atomic layers. In order to converge the results with respect to the slab thickness, we performed calculations of the adsorption energy with respect to the number of atomic layers. In Fig. 5.5 we show the values for 4 to 9 layers at 0.25 ML, the most reactive oxygen coverage, for Co and Co/Ir. When increasing the number of layers, the adsorption energy shows some fluctuations, that are of about 0.02 eV for Co/Ir and much larger for Co, about 0.1 eV. The difference is probably due to the increase of the total magnetization of the Co slab when adding a new layer. The observed fluctuations seem to follow the vertical periodicity of the Co stacks: Co has an A-B stacking, with a periodicity of two layers. For Co/Ir, an extra Ir layer does not change the magnetization and the adsorption energy does not change beyond 7 layers. Despite the fluctuations, the order of the configuration with respect to the adsorption energy does not change, being larger for O_{fcc}@Co/Ir and O_{hcp}@Co/Ir than for O@Co.

In Fig. 5.6 is shown the computed distance between the oxygen and the surface, for slabs with the different number of layers. The values are very stable with fluctuations of 0.01 Å for the oxygen-surface distances. During the energy minimization we observed that the code sometimes arrives to an energy local minima, without finding the global minimum. To solve the problem start by performing calculations fixing the total magnetization and computing the total energy curve as a function of the magnetization value, as it is shown in Fig. 5.7. Choosing then the magnetic configuration with the lower energy, we release the constraint on the magnetization and perform the structural relaxation. To reach the minimum, we often need to perform non-collinear

		E_{ad} (eV)		
O (ML)	adsorption site	10 Å	12 Å	15 Å
0.25 @Co_5	**hcp**	5.470	5.470	
	fcc	5.428	5.429	
0.5 @Co_5	**fcc+hcp**	5.052	5.051	
	hcp+hcp	5.060	5.060	
	fcc+fcc	5.003	5.002	
	hcp+fcc	4.647	4.646	
0.25 @Co/Ir_4	**hcp**	5.717	5.717	5.717
	fcc	5.756	5.756	5.756

Table 5.6: Adsorption energies computed for different amounts of vacuum for O adsorbed on Co_5 and Co/Ir_4 slabs.

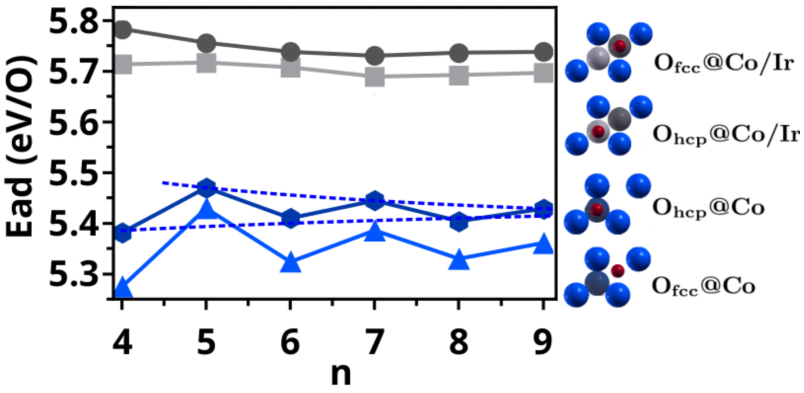

Figure 5.5: Adsorption energy for an oxygen coverage of 25 ML on Co_n (grey lines) and Co/Ir_{n-1} (blue lines) slabs for the configurations shown on the right side of the plot. The A-B periodicity of the Co stacks is fitted with dashed lines in one of the cases in order to illustrated the convergence with the number of layers.

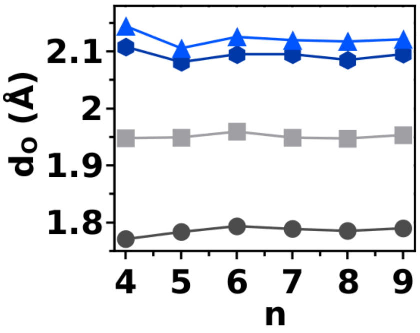

Figure 5.6: Distance of O to the surface for the same systems in Fig. 5.5 (same color code), computed for on Co_n and Co/Ir_{n-1}.

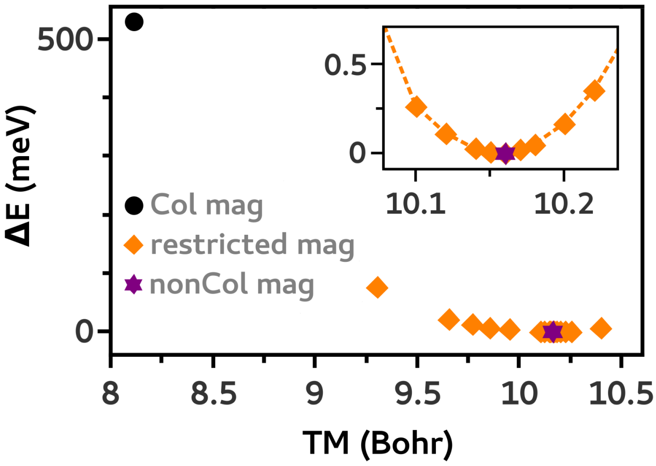

Figure 5.7: Convergence of the ground state by sampling its total magnetization (TM).

O (ML)	adsorption site	Co	Co/Ir
0.5	**hcp+fcc(octa)**	2.95 [71]	
	hcp+fcc(octa')	4.16	3.22

Table 5.7: Comparison of the adsorption energies for Co and Co@Ir obtained considering O penetration. As it is explained in the text, we did not find any *hcp+fcc(octa)* solution, instead we find a configuration where the O atoms in the position *fcc* are located under the second layer of the substrates.

magnetization calculations, even if the final results only show magnetization on the axis perpendicular to the surfaces.

We have considered several starting configuration with oxygen atoms below the first Co layer. For both Co and Co/Ir surfaces, and for both O concentrations considered, upon geometry optimization the O migrated to the surface. We were not able to find any solution corresponding to the configuration $hcp + fcc(octa)$ as is define in Ref. [71]. This can be due to the different methods used to perform the structural relaxation. For example, in Ref. [71], in addition to oxygen, only the atomic positions of the atoms in the 3 top layers of a slab of 5 were relaxed, whereas we have relaxed the whole slab. Instead we were able to compute a configuration with O occupying an *fcc* site below the 2^{nd} layer. This corresponds to a Co layer for the case of the Co slab, but to an Ir layer for the case of Co/Ir and is the only configuration for which the adsorption energy is larger for Co than for Co/Ir. This configuration is, anyhow, less stable then the surface sites and in fact the interlayer positions are expected to occur only for O contents larger than 1 ML [71].

The dependence of the magnetic properties with the slab thickness for 0.25 oxygen ML is showed in Fig. 5.9. The total magnetization of cobalt systems with and without O converges to the bulk value, while the magnetization of Co/Ir systems varies between 1.8 and 2.3 μ_B/Co. When O occupies the *fcc* position, the magnetization is similar

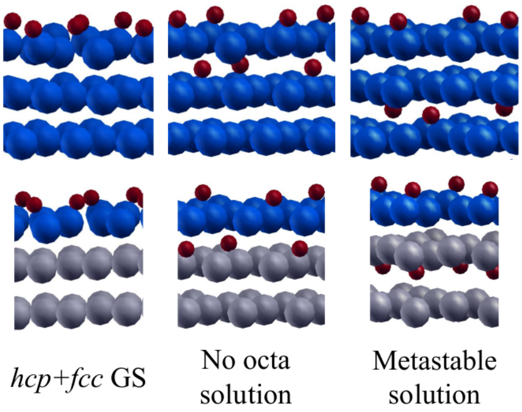

Figure 5.8: Scheme illustrating the atomic structure corresponding to a) the ground state configuration with no subsurface O, b) the configuration found in Ref. [71], called 'hcp+fcc(octa)', and the only metastable solution with subsurface O (below the second layer) found in the present work.

to one of the pristine surface, whereas when it occupies the *hcp*, the magnetization is higher by 0.1 μ_B/Co.

CoO is know to have an antiferromagnetic order, that has been well described at the DFT level in Ref. [248–252]. This motivated the search for possible antiferromagnetic configurations for adsorbed O on the two Co surfaces considered previously.

We chose, among the configurations with higher O content, closer to the CoO stoichiometry, the ones with higher adsorption energies, labeled $fcc + fcc$ and $hcp + hcp$. In CoO, the antiferromagnetic pattern is formed by adjacent cobalt layers that are separated by an oxygen layer. In the present case, and since O is adsorbed on the surface, the only possibility for O to mediate an AF interaction is to consider configurations with in/plane AF coupling, as shown in Figure 5.10, although Co forms a triangular lattice that will present frustration in the other Co atoms of the supercell. The Co rows along x are coupled antiferromagneticaly, following the distribution of the O atoms. The results are summarized in Table 5.8.

We find AF solutions only for Co/Ir. In case of Co no such configuration is found, since the strong ferromagnetic interaction in the slab imposes to the oxidized layer. In any cases the total energy of the AF configurations found for O@Co/Ir are 0.3 eV/O higher than the ferromagnetic solution.

In AF O@Co/Ir, the two rows of Co atoms closer to O show AF order. The other rows of Co atoms present zero magnetic moment as was expected. This is due to the fact that these atoms are surrounded by four Co atoms with different magnetic moment orientations, leading to magnetic frustration. It is possibly this frustration that makes this configurations so high in energy. The magnetization pattern of Co extends to the iridium layers: the Ir atoms close to magnetized Co planes are AF coupled, while the others have zero magnetic moment, resulting in a completely antiferromagnetic solution.

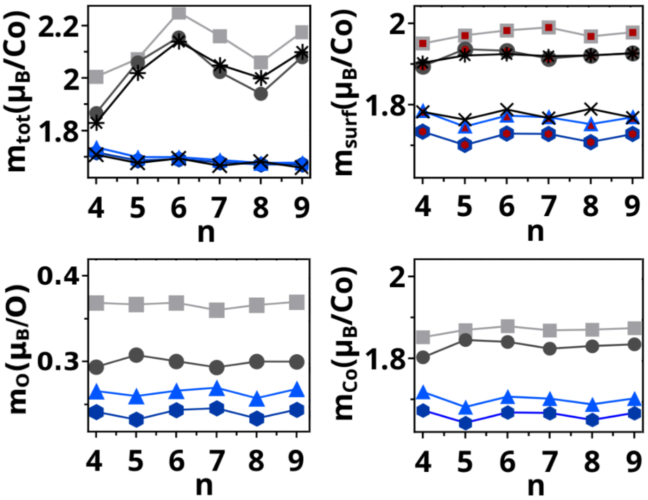

Figure 5.9: Total slab magnetization (top-left) and oxygen (bottom-right), cobalt (bottom-right) and total (top-right) surface magnetization for Co@Ir and Co systems with 25 ML oxygen coverage computed for slabs with different number of layers. Colors are set according to Fig.5.5, where we have filled the points with a smaller red zone to represent the sum in the total surface magnetization, m_{Co} + m_O. In the cases of the total slab and surface magnetization, the values for the pristine surface (black) are also shown. All the data is normalized to the number of Co atoms or to the number of O atoms for the oxygen magnetization.

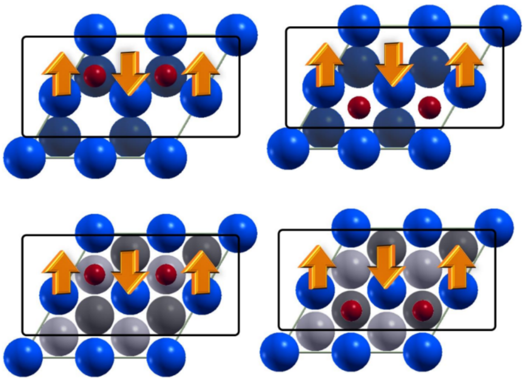

Figure 5.10: Illustration of the different O adsorption sites (red dots) for a 0.5 ML concentration, with respect to the antiferromagnetic configuration imposed on the Co lattice (orange arrows). The upper panels represent O@Co and the bottom panels O@Co/Ir. Only half of the Co atoms present a non zero magnetic moment, and are arrange along a line in the x direction.

	hcp+hcp	fcc+fcc
$E_{AF} - E_{FM}$ (eV/O)	0.31	0.32
m_{tot} (abs)	0.00 (5.07)	0.00 (4.45)
m_{Co}	±1.70/0.00	±1.57/0.00
m_{O}	±0.08/0.00	±0.07/0.00
m_{Ir}	±0.10/0.00	±0.06/0.00

Table 5.8: Summary of the energy differences and magnetic moments corresponding to the AF configurations illustrated in fig. 5.10. The reported energy correspond to the difference with respect to the ground state ferromagnetic configuration. All the values of magnetization are given in μ_B per Co, O or Ir atom correspondingly.

5.1.6 Summary

We have shown, by means of DFT calculations, how O intercalation can be used to control the electronic properties of the Gr/Co(0001) and how the structurural properties of the Co surface influence the O adsortion.

Starting from the effects of strain on the adsorption of O on Co surfaces, we studied two different surfaces: Co(0001) and a single layer of Co deposited on of Ir(111), taking into account that in the latter case the single Co layer assumes the lattice parameter of iridium [8, 9], and therefore has a lattice parameter 0.25 Å larger than Co(0001) surface. The adsorption energies are about 0.3 eV larger for Co/Ir(111) than for the Co(0001) surface and in both structures, the adsorption energies decrease with increasing O content. We show that the most favourable surface positions for adsorption are the *hcp* sites on Co and fcc on Ir/Co. According to our results, for the studied O contents, subsurface sites are not stable.

We then looked at the influence of O on the Co electronic properties by computing the DOS for O adsorbed on Co and Co/Ir. We have seen that the clear overlap between O and Co states induces a spin polarization of the O states with a larger hybridisation in the case of Co/Ir(111), for which the O pDOS peaks are broader. The larger magnetic moment of the Co single when deposited on Ir, a consequence of its strained lattice, also results on a slightly larger O magnetic moment. For increasing O coverage, the O-O repulsion widens the DOS and shifts it slightly downwards in energy.

Finally, we have studied the effect of O intercalation in the graphene@Co(0001) interface, clearly showing that the presence of O results in an increased graphene-Co distance, effectively reducing the electronic interaction with the Gr layer, confirming the experimental data [34, 69]. The graphene Dirac cone, disrupted by the hybridisation with the Co states around the Fermi energy, is restored upon O intercalation. Graphene bands recover their free-standing character except for a small p doping of graphene since its Dirac cone is now located slightly above the Fermi energy, in perfect agreement with reported ARPES [69] and PEEM [34] measurements.

This resuts support the idea that O intercalation on Gr/Co interfaces, shown experimentaly to be a reversible process, could be used in the tuning if the Gr-Co hybridization, and possibly, in the case of the Gr/Co/Ir(111), in the control of the moiré pattern and graphene corrugation.

5.2 Fe intercalation on Gr/Ir(111)

Following the successful strategy for Fe growth, we have studied well-defined smooth Fe layers intercalated between Gr and Ir(111), without any alloying and Fe-C intermixing. By means of a combined experimental and theoretical approach, we gain a detailed insight into the physical properties of the iron-intercalated Gr/Ir(111) heterostructure. The sandwiched Fe layers present a redistribution of the minority and majority electronic density of states triggered by the spatial confinement and by the peculiar strained structural configurations, as predicted by first principles spin resolved electronic structure calculations and experimentally confirmed by angular resolved photoemission and X-Ray magnetic dichroism.

5.2.1 Methods

Density functional theory (DFT) simulations were carried out using the QUANTUM ESPRESSO package [107, 108] where wavefunctions are expanded in plane-waves and pseudopotentials are used to account for the electron-ion interaction. We used the local density approximation (LDA) for the exchange-correlation potential, according to the Perdew-Zunger parametrization [255]. Similarly to previous works [22, 75] carried out by the same experimental and theoretical groups, we simulated the Gr/1ML-Fe/Ir(111) interface considering the complete moiré induced periodicity by using a 9×9 supercell of Ir(111), corresponding to a 10×10 supercell of pristine Gr. The lattice parameters were obtained by relaxing Ir bulk at the LDA level using ultrasoft pseudopotentials (USPP), resulting in a Ir–Ir bond distance of 2.7048 Å (corresponding to a hexagonal cell of 46.001 Bohr radius for the moiré structure). In all the calculation we included four metallic layers (3 Ir plus one Fe layer or 4 Ir layers). In order to make the two sides of the slab inequivalent we added a layer of H atoms in one of the two sides. Atomic positions were then fully relaxed (except for the two bottom Ir layers and the H saturation layer) until ionic forces were smaller than 0.001 Ry/Bohr. For all the self-consistent calculations we used a 2×2 grid of **k**-points, ultra soft pseudopotentials to model the electron-ion interaction and a kinetic energy cutoff of 30 and 300 Ry to represent Kohn-Sham wavefunctions and density, respectively.

Since LDA is known to underestimate the values of the orbital magnetic moments in transition metals [103], we have adopted a DFT+U scheme [117], with a Hubbard U parameter of 2 eV. In order to compare calculated band structures with ARPES data, we applied an unfolding procedure [110, 113] to the computed bands of Gr/Fe/Ir and Gr/Ir. With this procedure, the band structure computed for the 10×10 supercell is mapped into the graphene 1×1 Brillouin zone by using the `unfold-x` code [113]. In this way we obtain an effective band structure corresponding to the graphene unit cell. In this picture, the $\mathbf{k}$-dispersion is broadened by the break of the 1×1 translational symmetry induced by the 10×10 moiré pattern.

A single layer of iron, intercalated under Gr grown on Ir(111), induces a corrugation of the Gr membrane and preserves the periodicity of the moiré superstructure, superimposed to the hexagonal Gr lattice, as described in Section 1.2.1. After Fe intercalation, the pattern is only slightly attenuated (Fig. 1.3b), thus the first Fe layer appears commensurate to the Ir(111) surface lattice.

We have further investigated the structural properties of this system by means of DFT at the LDA+U level. The calculations confirm the large corrugation of the graphene layer (1.44 Å), with a minimum graphene-Fe interplanar distance of 1.85 Å and a maximum of 3.29 Å on the crests of the hills, as shown in Fig. 1.3(c). Previous DFT calculations [11] done at the PBE level including van der Waals interactions by using the DFT–D2 method [256, 257] found a similar scenario, with slightly larger Gr-Fe distances (2.05 and 3.33 Å for valleys and hills, respectively).

The topography of the Gr/Fe/Ir(111) heterostructure is similar to the corrugated moiré superstructure observed for the Gr/Co/Ir(111) system [22], but very different from the structure reported for Gr directly grown on bcc-Fe(110) [45]. Previous STM measurements and DFT calculations performed at the LDA level, for Gr/bcc-Fe(110) point out the formation of a periodic corrugated pattern of the graphene layer parallel to the [001] direction of the substrate, consisting in a supercell of 7×17 graphene hexagons with a smaller corrugation of 0.6/0.9 Å, and only a small fraction of the C atoms considerably elevated over the Fe surface, thus making the entire graphene membrane strongly interacting with the metal substrate.

In the present case, the larger graphene corrugation modulates the Gr/Fe interaction. This is illustrated by the charge difference computed for Gr/Fe/Ir(111) shown in Fig. 1.3(d,e). The excess of negative charge (yellow isosurface) is accumulated in the graphene membrane, donated by the Fe intercalated layer. The redistribution of charge is more pronounced in the valley regions and milder in the areas corresponding to the crests of the hills, corroborating a different strength of hybridization between graphene and Fe going from the valleys to the crests due to the increasing graphene–Fe distance. The periodicity of strongly and weakly bound regions in which covalent and van der Waals bonding dominate, respectively, induces a different balance in the charge transfer determined also by the registry with respect to the underlying Fe atoms.

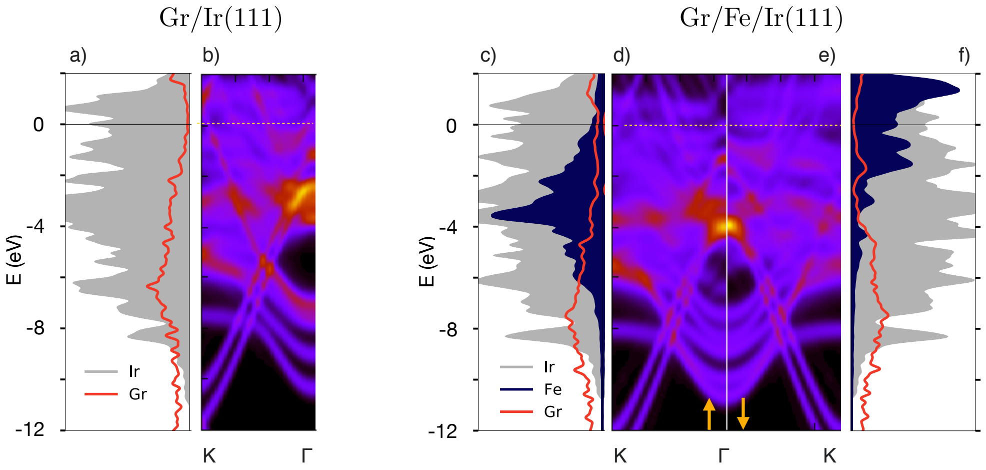

Figure 5.11: Band Structure and projected Density of States (pDOS) computed within DFT for Gr/Ir(111) and Gr/1 ML Fe/ Ir(111): a) Gr/Ir DOS projected on C and Ir atomic orbitals and b) Gr/Ir band structure, unfolded on the 1×1 graphene unit cell as described in the main text; c) Gr/Fe/Ir majority spin DOS projected on C, Fe and Ir atomic orbitals; d) majority and e) minority spin band structure, unfolded on the 1×1 graphene unit cell; f) Gr/Fe/Ir minority spin pDOS.

Importantly, the magnetic response of Fe films is extremely sensitive to tiny variations of the structural configuration [79], and the strained lattice of the Fe film intercalated under graphene can give rise to an altered distribution of the electronic majority and minority states and to different spin and orbital configurations with respect to the bulk reference [53].

5.2.2 Electronic structure

A deeper insight into the interaction between Gr and the Fe intercalated layer(s) can be unveiled by the spectral density deduced by angular resolved photoelectron spectroscopy of the Gr/Fe/Ir(111) heterostructure, described in Section 1.2.2, compared with ab initio theoretical predictions of the electronic density of states (DOS) and band structure calculated by DFT.

The measured ARPES data are complemented by DFT calculations, as shown in Fig. 5.11, where the electronic structures computed for Gr/Ir(111) and Gr/Fe/Ir(111) are unfolded and mapped into the 1×1 graphene Brillouin zone along the $\Gamma - K$ direction, as described in Sec. 5.2.1. Projected DOS (and projected bands in Fig. 5.12) are also provided to complement the band information. The bands obtained for Gr/Ir(111) are in good agreement with existing literature, as from e.g. Ref. [258]. Concerning the Fe intercalated system, as also observed in the experiments, the Gr π- and σ-bands are shifted to higher binding energies by the effect of Fe intercalation (i). While for Gr/Ir(111) the π bands are clearly recognizable, in the case of Gr/Fe/Ir(111) they are strongly hybridized with Fe states above -6 eV and the upper part of the cone is iden-

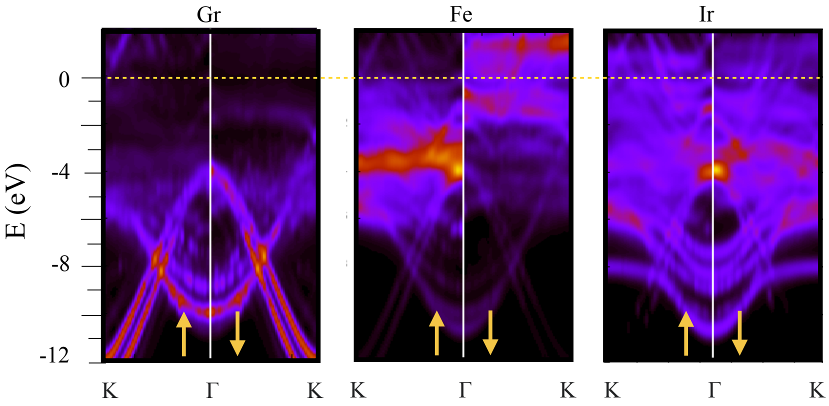

Figure 5.12: Bands computed for the Gr/1ML-Fe/Ir(111) unfolded on the Graphene 1×1 cell and projected on C (graphene), Fe, and Ir.

tifiable only for the minority spin states. The bottom of the π bands at Γ moves from about -7.5 eV in Gr/Ir to about -10.0 eV in Gr/Fe/Ir (see Fig. 5.12), with an overall downshift of ∼2.5 eV, in quite good agreement with the experimental findings. Similarly, the σ bands of graphene undergo a downshift by about -1.5 eV at both Γ (going from -2.5 to -4 eV) and K (from -10.5 eV to -12 eV). While the experimental offset of these features is found at larger binding energies (namely 4.0 eV and 5.5 eV as marked by σ and σ' in Fig. 1.4d), the downshift is quite consistent with the calculations [259].

In order to identify Fe-related states, we consider the projected DOS, shown in Fig. 5.11(c,f), where a strong spin splitting of the Fe components is observed (see discussion below). For instance, a large peak of the Fe pDOS is found in the energy region of 3-4 eV BE, in good agreement with the experimental data, and mainly located in the majority spin channel. Such peak then overlaps with the π bands of Gr disrupting the Dirac cone for majority states. In contrast, the Dirac cone is still faintly visible in the minority spin bands at about 2.5-3 eV. In both spin channels the pDOS reveals overlapping peaks due to Fe and graphene states, suggesting that the shadowing of the vertex of the Dirac cone observed in the experimental photoemission data is clearly induced by the hybridization of the graphene π-states with the Fe d majority states. Furthermore, the spin resolved DOS in the energy region closer to the Fermi level shows that the main Fe-related peak of the minority spin states lies above the Fermi level, with smaller peaks between -2 eV and the Fermi energy, in good agreement with the experimental observation (*iii*). Overall, this picture is further confirmed by the projected unfolded bands provided in Fig. 5.12.

In order to better compare with Gr/Ir and to support the identification and assignment of the electronic structure features, in Fig. 5.12 we plot the unfolded bands of GrFeIr projected on C, Fe, and Ir atoms. In particular, this allows one to better appreciate the downshift of graphene-related states, the position of Fe-related states in the majority and minority channels, and the role of Iridium states.

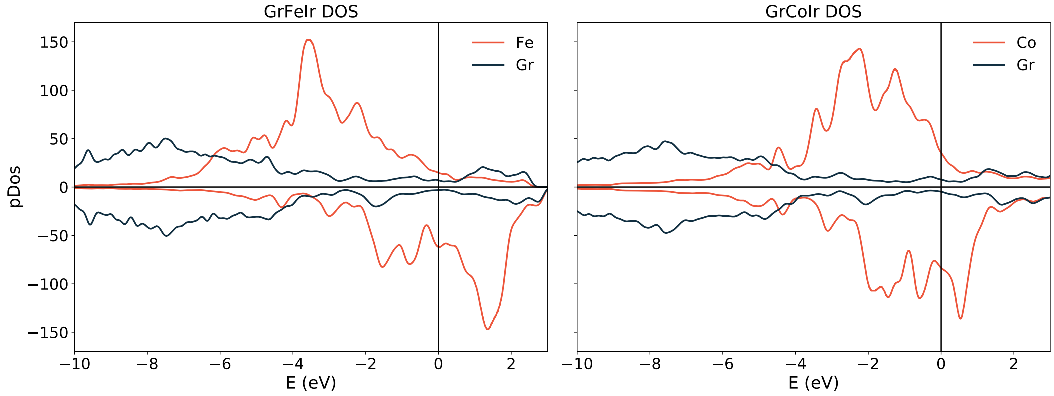

Figure 5.13: Comparison of the Density of states projected on graphene and Fe or Co, computed for the Gr/1ML-Fe/Ir(111) and Gr/1ML-Co/Ir(111)

In order to compare with the case of GrCoIr, in Fig. 5.13 we present the Density of States, projected onto C, Fe and Co orbitals, computed within DFT for Gr/Fe/Ir(111) and Gr/Co/Ir(111), including the complete moiré induced periodicity by using a 9×9 supercell of Ir(111), corresponding to a 10×10 supercell of pristine Gr. As discussed in the main text, LDA+U with U=2 is used for GrFeIr, while U is not included for GrCoIr. The main differences between the two systems are seen in the Fe and Co pDOs. The first presents a larger spin split, with the majority *d* states almost fully occupied, and less occupied minority states, when compered with Co. Fe also shows a pronounced peak around 4 eV below the Fermi energy. These Fe *d* states are resonant hybridized with the graphene π states.

5.2.3 Magnetic properties of the Fe layer

In contrast with Fe grown on Ir(111), for which the loss of inversion symmetry at the interface of the magnetic layer and substrate stabilizes different skyrmion lattices depending on the Fe/Ir stacking [89–92, 260], when a Fe monolayer is intercalated between Gr and Ir(111), the heterostructure exhibits a ferromagnetic order with an out-of-plane easy magnetization axis [11]. For this reason, and based on the experimental evidence described below, in the present DFT calculations we have considered only collinear magnetic configurations, excluding in this way skyrmions or spin spiral textures.

The pDOS computed for the Gr/Fe/Ir(111) heterostructure shows a large spin split of the Fe states, with the maxima of the two spin pDOS almost 5 eV apart. In particular, the majority spin states are almost fully occupied while the largest peak of the minority spin states is empty, which results in an average Fe-magnetic moment of 2.2 μ_B/atom. The computed ground state magnetic configuration is ferromagnetic even if the Fe magnetic moment shows a modulation over different sites ranging from 2.0 to 2.7 μ_B/atom, in good agreement with previous calculation [261]. The modulations is determined by the graphene layer, with the Fe atoms located below the graphene crests, i.e. with larger Fe-C distances, having the largest values. Concerning graphene, the C magnetic moments are non-zero but quite small (at the LDA+U level ranging from -0.02 to 0.01 μ_B/atom), similarly to what reported for Gr/Co/Ir(111) [10, 22], with a distance- and sublattice-dependent modulation.

Overall, we find that the Fe monolayer displays a clear spin splitting, as an effect of the band narrowing and subsequent increased number of majority electrons. This is confirmed by the strong localization of the Fe-induced electronic states observed in the photoemission spectral density. It is interesting to point out that a different scenario is found for the Gr/Co/Ir(111) interface [10] where Co spectral weight in the minority channel is shifted at lower energies leading to a spin split significantly smaller than in the present case.

The strong ferromagnetic behavior is confirmed by the X ray absorption spectra and the XMCD at the $L_{2,3}$ edges for 1.4 ML and 7 ML of Fe sandwiched between Gr and Ir(111), shown in Fig. 1.10. The evaluated average total moment is 2.1±0.2 μ_B/atom for 7 ML of Fe intercalated under Gr, in fair agreement with 2.2 μ_B/atom (spin moment), as deduced by the DFT predictions.

The strategy to sandwich the Fe layer beneath the graphene membrane with an intercalation process at moderate temperature (500 K), prevents any alloying, and the absence of any hallmark of Fe-Ir and Fe-C intermixing proves the formation of a well-defined homogeneous Fe layer in registry with the Ir(111) surface. Such single layer of Fe, protected by the graphene membrane, induces a downshift in energy and a symmetry breaking of the Dirac cone due to the interaction between Gr and Fe majority states resonant in the energy region of the vertex of the cone. The redistribution of the spin resolved Fe pDOS with a narrowing of the Fe bands and a larger spin splitting between majority (fully occupied) and minority states (almost empty) of the Fe states associated with increased total Fe magnetic moment influences the magnetic response of the Fe intercalated layer(s).

In contrast to the case of direct growth of Fe on Ir(111), where, despite the large Fe magnetic moment, a non-collinear magnetic order has been observed [89–91, 260], the Fe layer with graphene on top reveals a ferromagnetic long range order with spin and orbital moments that are higher than the ones found for the bulk phases. The graphene top layer acts not only as a protective membrane, but also allows for a stable ferromagnetic configuration, counteracting the effect of Ir substrate. The concomitant dimensionality reduction with a narrowing of the d bands and a reduced superimposition between the spin-split majority and minority Fe bands, further contribute to the transition of a single Fe layer (or few layers of Fe), from weak to strong ferromagnet, when intercalated beneath graphene. These $3d$ confined layers protected by a graphene membrane with a novel structural configuration with respect to the bulk lattice arrangement offer a powerful playground to tune their electronic structure and magnetic state for magnetic/spintronic devices.

5.3 FeCo intercalation on Gr/Ir(111)

Ferromagnetic metals (FMs) and their alloys can be finely manipulated by changing their chemical composition [50], structural configuration [51], and by reducing the dimensionality [52, 53]. Modified symmetry and scaled dimension, indeed, may induce in FMs higher magnetic moments and larger uniaxial magnetic anisotropy energy (MAE) with respect to their 3D counterparts [12, 53–56]. The enhanced magnetism in nanostructures, can be used e.g, for engineering spintronic devices [57], high-density magnetic storage [58], and permanent magnets [59].

In this section, we investigate the electronic and structural properties of the equiatomic FeCo layers grown epitaxially on Ir(111) underneath a Gr cover, by means of Density Functional Theory (DFT). We show that the reduced dimensionality in the artificially confined system leads to a narrowing and a redistribution of majority and minority $3d$ states with respect to the pure species, enhancing also the splitting between Fe $3d$-up and Fe $3d$-down spin bands. Our description of the electronic structure in equiatomic FeCo layers sheds light on the enhanced magnetism previously demonstrated by XMCD [12] and provides a useful insight in the engineering of low dimensional FM alloys.

5.3.1 Methods

Density functional theory (DFT) simulations were carried out using the plane wave implementation of the Quantum ESPRESSO [107, 108] distribution. We used the local density approximation (LDA) for the exchange-correlation potential, according to the Perdew-Zunger parametrization [255]. Since LDA is known to underestimate the values of the orbital magnetic moments in transition metals [103], we have adopted a DFT+U scheme [117], with a Hubbard U parameter of 2 eV for Fe and 4 eV for Co. The choice of the values is explained in detail in the Section 5.3.3. Similarly to our previous works [1, 22, 75], we simulated the Gr/1ML-FeCo/Ir(111) interface considering the complete moiré induced periodicity by using a 9×9 supercell of Ir(111), corresponding to a 10×10 supercell of pristine Gr. The lattice parameters were obtained by performing a relaxation of the Ir bulk in the LDA approximation using ultrasoft pseudopotentials (USPP), resulting in a Ir–Ir bond distance of 2.7048 Å (corresponding to a hexagonal cell of 46.001 Bohr radius for the moiré structure). In all the calculations we included four metallic layers (3 Ir plus one FeCo layer). The two sides of the slab were made non-equivalent by adding a layer of H atoms in one of the two sides. Atomic positions

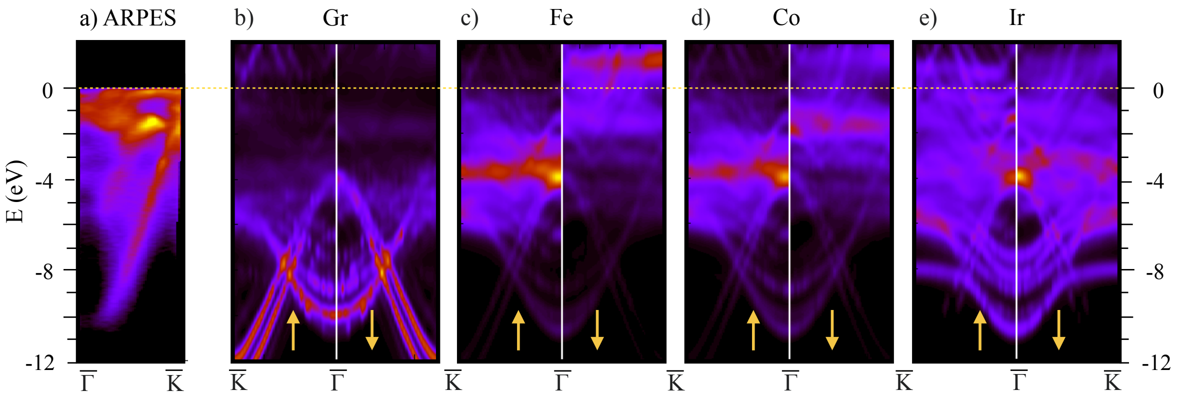

Figure 5.14: Comparison between ARPES measurements of Gr/FeCo/Ir(111) taken along the $\bar{\Gamma}$-$\bar{K}$ direction (a), and the band structure computed for the 10×10 supercell of Gr/1ML-FeCo/Ir(111), mapped into the graphene 1×1 BZ and projected into the atomic orbitals of the different atomic species (b-e).

were then fully relaxed (except for the two bottom Ir layers and the H saturation layer) until ionic forces were smaller than 0.001 Ry/Bohr. All the self-consistent calculations were performed using a 2×2 **k**-point grid, USPP to model the electron-ion interaction and a kinetic energy cutoff of 30 and 240 Ry to represent Kohn-Sham wavefunctions and density, respectively.

In order to obtain a simpler representation of the Gr/FeCo/Ir(111) band structure, we have applied an unfolding procedure [110, 113] in which the band structure computed for the 10×10 supercell is mapped into the Gr 1×1 Brillouin Zone (BZ) by using the `unfold-x` code [113]. This approach has been further extended to include atomic projections on Lödwin orthogonalized atomic orbitals as provided by the QUANTUM ESPRESSO package [107, 108].

5.3.2 Narrowing of d bands

The Gr/FeCo/Ir(111) interface was modeled at the DFT level as described previously. The calculations indicate a large corrugation of the Gr layer (1.40 Å), with a Gr-FeCo interplanar distance of 1.90 Å and 3.30 Å at valleys and hills, respectively, as shown in Fig. 1.5(c-d). The corrugation of the Gr/FeCo/Ir(111) and the energy landscape of the stable structural configuration are similar to those computed for the pure intercalated systems Gr/Fe/Ir(111) (1.3 Å) [1] and Gr/Co/Ir(111) (1.4 Å) [8, 22]. It is worth noticing that we do not include van der Waals interactions in our approach since LDA has shown to give a good description of graphene corrugation and distance for Gr/Fe/Ir(111) [1], providing essentially the same scenario as DFT calculations done at the PBE level including van der Waals interactions [11], which only find slightly larger Gr-Fe distances.

The experimental evidence of narrow bands associated to FeCo in the energy region of E_{F} and the hybridization of π states of graphene described in section 1.2.2 is

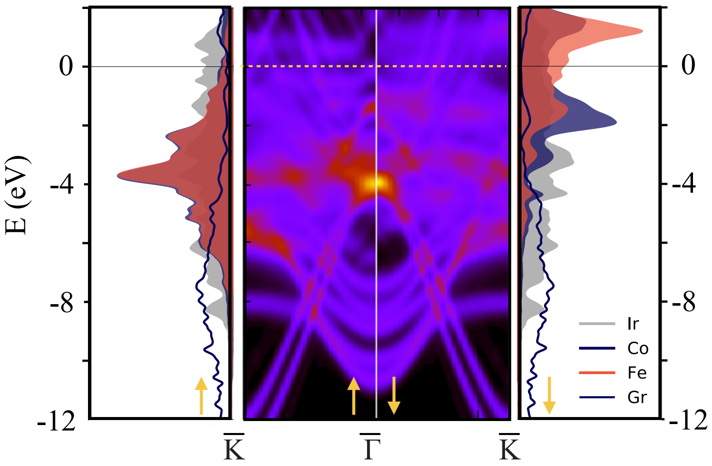

Figure 5.15: Central panel: majority and minority spin band structure computed within DFT for Gr/1ML-FeCo/Ir(111). Left (right) panel: majority (minority) spin DOS computed within DFT and projected on C, Fe, Co and Ir atomic orbitals.

confirmed by the DFT calculations. The spin-resolved electronic structure of Gr/1ML-FeCo/Ir(111), shown in Fig. 5.14 (b-e), is projected on atomic orbitals of different species and mapped into the 1×1 Gr BZ along the $\bar{\Gamma}$-$\bar{K}$ direction. With respect to free-standing Gr, the main effect on the π and σ bands is a non-rigid shift towards higher BE (Fig. 5.14b), as also found in the literature for pure intercalated systems [1, 9, 37, 39, 82]. In addition, our calculations clearly show a significant interaction of the Gr π-band with the FeCo-d majority states, that is stronger than with the minority bands. This is especially evident in the wide 0-5 eV energy range below E_F (Fig. 5.14a). The spin-down π band of Gr preserves its linear dispersion up to about -2 eV, where it strongly overlaps with the FeCo minority states (Fig. 5.14b-d), and their interaction pushes the π band maximum down, in agreement with our ARPES measurements. Therefore, in line with a recent paper of Gr grown on a Mn_5Ge_3 FM interface [262], the theoretical predictions demonstrate that the interaction of Gr with the FeCo layer gives rise to a downshifted Gr π band which is mainly minority-spin polarized.

This picture is further confirmed and summarized by the comparison of the total band structure (central panel of Fig. 5.15), with the spin DOS projected on C, Fe, Co and Ir atomic orbitals (left-right panels of Fig. 5.15), computed within DFT for Gr/1ML-FeCo/Ir(111). From the pDOS we can see that the Fe and Co 3d states, particularly in the majority spin channel, almost coincide (detailed analysis in Sections 5.3.4 and 5.3.3, including the role of DFT+U corrections). The majority spin channel is almost filled, with an intense peak centered at about -4 eV, where the spin-up Dirac cone is strongly hybridized and almost quenched. In the minority spin channel, the main superimposition of Fe and Co pDOS peaks is seen at about -2 eV and at the Fermi level, where indeed the transition metal states appear in our ARPES measurements.

The density of states and the spin electronic bands for bulk FeCo alloys have been deeply investigated and discussed in the literature [53, 263, 264]. The strong hybridization of Fe and Co in the bulk alloy produces an increase of the Fe exchange splitting and a saturation of the magnetic moments [263, 264]. More specifically, it has been shown that at about 30% Fe content the atomic magnetic moments become almost independent on the alloy composition, due to a redistribution of $3d$ minority electrons to the $3d$ majority states at the Fe sites. Furthermore, the reduced dimensionality and number of nearest neighbors at the FeCo interface also influence the d bandwidth and the spin splitting of the states [53, 263, 264].

Despite a number of differences with the Gr/FeCo/Ir interfaces studied here, such as the interaction with Gr or with the Ir surface, some of the features of FeCo alloys subsist. In particular, we observe a larger spin-splitting between majority and minority spin channels, and a narrowing bandwidth of the $3d$ states for this confined FeCo layer with respect to bulk Fe and FeCo [263]. A detailed comparison between the Gr/FeCo/Ir(111) interface and the bulk systems is presented in Sections 5.3.3 and 5.3.4. From the DFT simulations, the spin-resolved DOS of Fe and Co show almost completely filled $3d$-states in the spin-up channel, with about 4.76(4.70) electrons for Fe(Co), while about 2.08(3.09) electrons are localized in the $3d$ spin-down channel. Though the energy position of the FeCo $3d$ states depends on the values of U chosen for the Hubbard correction, there is always a significant overlap between the Fe and Co states, while the Gr states are almost insensitive to different values of U, as described in Section 5.3.3.

Therefore, the results shown in Fig. 5.15 demonstrate that the reduced symmetry and the structural configuration of the intercalated equiatomic FeCo layer induce a clear splitting of Fe $3d$-up and down bands, with a narrower bandwidth with respect to Fe bulk.

This picture is consistent with previous XMCD measurements on Gr/FeCo/Ir(111), showing a sensible enhancement of the magnetic moments [12] with a strong ferromagnetic coupling between Fe and Co.

In conclusion, within the present study we characterize the electronic and structural properties of few FeCo layers, embedded between Gr and Ir(111). By means of ARPES we show that the interaction of the π band of Gr with FeCo-$3d$ states pushes the strongly hybridized Dirac cone towards higher BE in analogy with pure intercalated systems. However, in proximity of E_{F} we identify new localized states associated to the FeCo alloy. By means of DFT we show that the homogeneous intermixing of the two FMs and the artificial structural phase, where the FeCo layer is stretched to the Ir(111) lattice constant, leads to a narrowing and to an enhanced spin splitting of the $3d$ states with respect to pure bulk systems. From an experimental point of view, we have succeeded in inducing such narrowing and enhanced spin splitting within a homogeneous 2D FeCo system. Therefore, our study provides a new artificial 2D FeCo system protected from contaminants through the Gr layer, inducing an enhanced magnetic response, which can be further engineered for integration in magnetic devices.

See Sections 5.3.3 and 5.3.4, for: selected core levels measurements; additional calculations of projected DOS with different values of Hubbard U parameter; projected DOS for 10 × 10 Gr/FeCo/Ir(111), 10 × 10 Gr/Fe/Ir(111), 10 × 10 Gr/Co/Ir(111) and DOS for corresponding FM bulk systems.

5.3.3 Parameters for the DFT+U scheme

Since LDA is known to underestimate the values of the orbital magnetic moments in transition metals [103], we have adopted a DFT+U scheme [117], with a Hubbard U parameter of 2 eV for Fe and 4 eV for Co in the calculations for the 10×10 Gr/FeCo/Ir(111) supercell.

The U value was chosen after systematic tests done on smaller model systems consisting in 1×1 and 2×2 cells where we kept fixed the LDA Ir lattice parameter. We considered interfaces with and without graphene. In the latter case, the graphene layer was artificially stretched in order to have commensurate interfaces. We begin by computing the Hubbard parameters using linear-response within the framework of density-functional perturbation theory [118] for the Fe/Ir(111) and Co/Ir(111) interfaces, obtaining respectively values of 2.4 and 4.8 eV. Since a similar calculation done on the large 10 × 10 supercell is forbiddingly heavy from the computational point of view, the choice for the values of U resorted to the analysis of the following data.

The magnetic moments computed for Fe and Co 1 × 1 interfaces for a set of different U values are reported in Tab. 5.9. As expected, the inclusion of U increases the magnetic moment of both Fe and Co. For the interfaces without graphene, the maximum magnetic moment is achieved for U=4 eV, whereas for the interfaces with graphene, the magnetic moment increases with U for all the values considered. In any case, the changes are more abrupt for the U values between 0 and 4 eV. We can observe that for all the values of U, the presence of graphene reduces the magnetic moment of both Fe and Co (though the reduction for Fe is significantly larger for $U \leq 4$ eV).

In Fig. 5.16 we show the the Projected Density Of States (pDOS) computed for a 2×2 Gr/FeCo/Ir supercell with different U parameters. For all the values of U considered we observe a significant hybridization of the Fe an Co states both in the majority and minority spin channels, together with a downshift of the majority spin states which depends on the chosen values of U. On the other hand, the graphene pDOS remains unaltered, being very similar for all the values of U. It is worth noticing that, in the 2×2 supercell considered here, the graphene lattice is stretched and therefore its pDOS differs from the one computed for the larger 10×10 supercell shown in the main text.

The values of U for the 10×10 Gr/FeCo/Ir(111) supercell were chosen by considering all the information described above. We have concluded that it was reasonable to use

U	Fe/Ir m(Fe)	Co/Ir m(Co)	Gr/Fe/Ir m(Fe)	Gr/Co/Ir m(Co)
0	2.67	1.74	2.09	1.13
2	2.93	1.88	2.42	1.40
4	3.20	2.01	2.61	2.10
5	3.16	1.86	2.63	1.96
6	3.14	2.26	2.62	2.02

Table 5.9: Magnetic moment per atom in μ_B/atom computed for the 1×1 Fe/Ir, Co/Ir, Gr/Fe/Ir and Gr/Co/Ir interfaces, considering different values of U, given in eV.

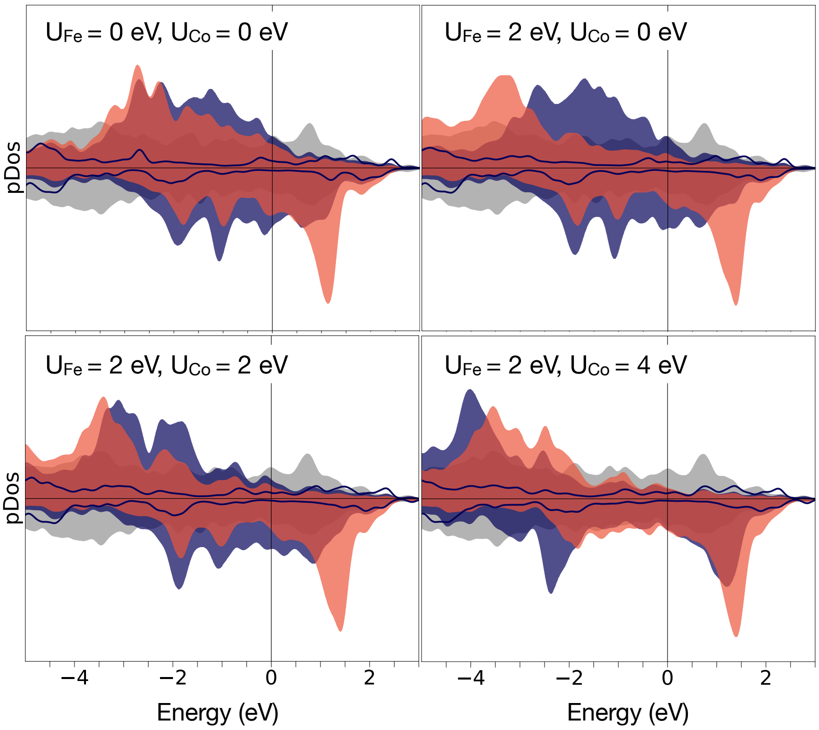

Figure 5.16: Projected density of States computed for a 2×2 Gr/FeCo/Ir supercell with different values of U, in eV. In all the panels: Fe states (red area), Co states (blue area), Ir (gray area), Gr (solid line).

	Gr/FeCo/Ir		**Gr/Fe/Ir**		**Gr/Co/Ir**	
	up	**down**	**up**	**down**	**up**	**down**
Fe	4.76	2.08	4.74	2.20	-	-
Co	4.70	3.09	-	-	4.71	3.00
Fe+Co	4.74	2.58	-	-	-	-

Table 5.10: Average occupation per atom and per spin of the valence states, $3d$, computed for the Gr/FeCo/Ir, Gr/Fe/Ir and Gr/Co/Ir interfaces. Values of U=2 eV and U=4 eV have been adopted for Fe and Co atoms, respectively.

the values of 2 and 4 eV for Fe and Co respectively. Similar values had been used for Gr/Co/Ir(111) [8] and Gr/Fe/Ir(111) [1]. In the main text we have reported that the majority spin states coincide in energy and the minority spin states also show a large overlap, keeping in mind that this behavior depends critically on the chosen values of U, as demonstrated by the analysis provided in Fig. 5.16.

5.3.4 Comparison of pDOS for different transition metals

In Figure 5.17 we present the DOS projected on the $3d$ metal and on graphene, computed within DFT+U for Gr/FeCo/Ir(111) and Gr/Fe/Ir(111) and Gr/Co/Ir(111). The calculations were done considering the complete moiré induced periodicity by using a 9×9 supercell of Ir(111), corresponding to a 10×10 supercell of pristine Gr, similarly to the results presented in the main text. For the reasons explained above, we have adopted a DFT+U scheme [117], with a Hubbard U parameter of 2 eV for Fe and 4 eV for Co, and again we would like to stress the critical dependence of the DOS on the chosen values of U.

The three systems present a large spin split of the $3d$ states, with the majority spin states fully occupied. The main differences are seen in the minority spin states. Despite the fact that all interfaces show two sets of peaks, one below and the other above the Fermi energy, the relative intensity and shape of the peaks is different: for Gr/Co/Ir(111) the set of peaks below Fermi has the same height but is broader than the one above; the opposite happens for Gr/Fe/Ir(111) and Gr/FeCo/Ir(111), that present similar DOS shapes and the unoccupied peak larger than the one below E_F. The values of the occupation averaged for Fe an Co for each spin state are summarized in Table 5.10. This is reflected in the magnetization. The total magnetization of the interface, including three Ir layers, is respectively 176, 203 and 139 μ_B for Gr/FeCo/Ir(111) and Gr/Fe/Ir(111) and Gr/Co/Ir(111). The average magnetic moment per atom for the $3d$ metals is 2.7 μ_B for Fe and 1.6 μ_B for Co in case of Gr/FeCo/Ir(111). These values are comparable with the ones computed for the pure intercalated layer, for Fe

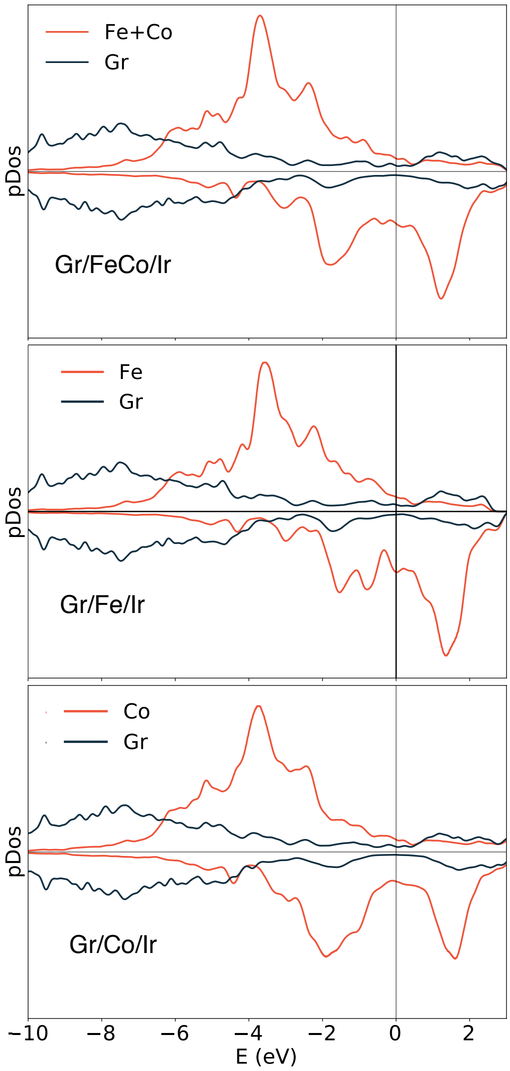

Figure 5.17: Density of states projected on the $3d$ metal and on graphene, computed for a 10×10 Gr/FeCo/Ir supercell compared with the pDOS computed for 10×10 Gr/Fe/Ir and 10×10 Gr/Co/Ir. Values of U=2 eV and U=4 eV have been adopted for Fe and Co atoms, respectively.

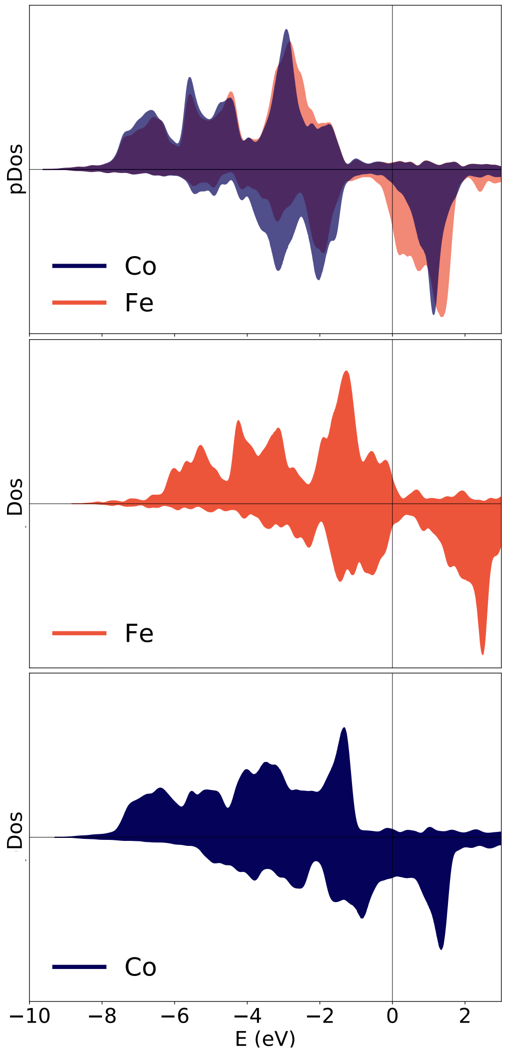

Figure 5.18: Density of States computed for the bulk systems bcc FeCo, bcc Fe and hpc Co with the same values of U used for the interfaces: U=2 eV and U=4 eV for Fe and Co atoms, respectively.

in Gr/Fe/Ir(111), 2.5 μ_B and for Co in Gr/Co/Ir(111), 1.7 μ_B, showing that the spin magnetic moment of Fe and Co does not change much with the relative Fe/Co concentration, as previously reported for Fe_xCo_{1-x}/Pt(111) [53]. The computed spin moment for Fe_xCo_{1-x}/Pt(111) are around 3 μ_B for Fe and 2 μ_B for Co, higher then the values reported here but the two model systems show several differences. In the case of Fe_xCo_{1-x}/Pt(111), the absence of the graphene layer and the fact that the studied geometry considers a commensurate interface, straining the FeCo layer by 10% to match the underlying Pt surface.

In Figure 5.18 we present the DOS for the Fe, Co and FeCo bulk systems, computed at the same level of theory. For the sake of comparison, we considered the same values of U, even if we expect them to be overestimated in this case. When comparing the pure systems with the league FeCo, we can see that there is a downshift in energy resulting in a coincidence of the Fe and Co states. For the minority spin states, there is a also a redistribution between the Fe and Co states which narrows the occupied minority spin states and results in a larger magnetic moment. In fact, when going from the pure systems to the league, the Fe magnetic moment increases form 2.4 μ_B to 2.9, and the Co moment form 1.5 μ_B to 1.7 μ_B. This increase is larger than what we see for the interfaces, for which, both in the case of the pure systems and Gr/FeCo/Ir(111), the occupied minority spin states are well separated from the occupied, resulting in two narrower sets of peaks.

5.4 GW/MPA calculations for the Gr/Co interface (preliminary results)

5.4.1 Summary of experimental results

The band structure of different Gr/Co interfaces has been determined experimentally by different groups with very consistent results [9, 39]: comparing the ARPES measurements for Gr/Co(0001) [39] with the results for Co intercalation in the Gr/Ir interface [9], both the Co and the Gr bands are similar. The Gr bands, such as π and σ have been well characterized, in particular the positions of the Dirac cone and how it changes due to the hybridization with Co. Figure 5.19 shows the band structures of graphene grown Co(0001) sampled along the M and K lines of the surface Brillouin zone of graphene as reported in [39]. The interaction with the substrate shifts the π band to higher binding energies: Its bottom at the Γ point is located at a much higher binding energy, 10.1 eV, as compared to freestanding graphene, 8.4 eV. The π band disperses upward into the second Brillouin zone and no band gap is visible at the K point. The Dirac-point binding energy of graphene on the Co surface is located at 2.82 eV. The π^*

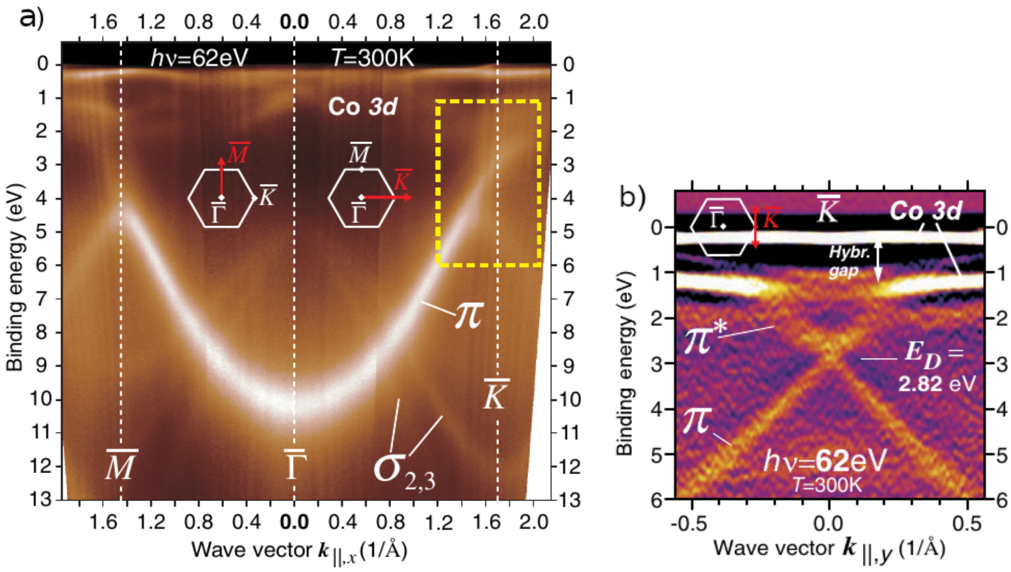

Figure 5.19: ARPES measurements of Gr deposited on a Co slab. The small region of the full spectrum framed in a), that correspond to a zone around the Dirac cone, is enlarged in b). The figures are adapted from Ref. [39].

band is linear, with a group velocity equal to the one of the π band. Co has a large magnetic exchange splitting and the peak at 1.2 eV is assigned to minority spin since the majority-spin peaks are strongly broadened and usually difficult to observe. Such difference between minority and majority states means that, for higher binding energies than the hybridization point of 1.2 eV, the π states of graphene are expected to become strongly spin polarized. One candidate for the corresponding Co majority-spin band is the weak band appearing around 2.0 eV, which hybridizes with the π^* band as well. This assignment is, however, not definite since the separation is much less than 1.4 eV. Nevertheless, some particular points in the experimental band structures exhibit a large uncertainty and therefore do not allows for a fine description of their differences. In addition, Co bands are much more subtle to see from the measurements and are suspected to match bulk Co bands.

5.4.2 Summary of DFT results

On the theoretical side, the experiments have been complemented by DFT simulations showing in general a good agreement with the ARPES measurements, however the quantitative agreement is not complete. For example, the position of the Dirac cone is lower by 0.6 eV. Also the position of the Gr σ band at Γ is higher by 0.8 eV. The energy deviation of the computed bands from the experimental results is not uniform and depends on the character of the orbitals and on the position in the Brillouin zone. Thus, by increasing the level of theory at the GW level adding non locality and long range interactions, we expect to improve the accuracy of the theoretical simulations.

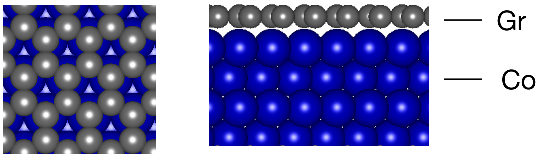

Figure 5.20: Top and side view of the model of the GrCo interface.

5.4.3 Challenges of GW calculations

The Gr/Co interface, was modeled as a semi-infinite system, with a Gr sheet on a Co slab. In Figure 5.20 we show the structure used to model the system. We inspected at DFT level the role of the thickness of the slabs required to converge the electronic structure of the system. In Figure 5.22 we show the band structure computed at the DFT level for Gr/Co from 4 to 10 layers of Co, and projected on the C and Co atomic orbitals, while the spin resolved band structure in the case of 4 layers is shown in Fig. 5.21. We can see that the Graphene bands do not change already from 4 to 6 layers. The density of Co states, as expected, increases with the number of layers. It is important to notice that this convergence with the number of Co layers is not transferable to the GW calculations due to the nonlocality of the interactions. This is important and subtle since heterogeneous structures are usually described with simple slab models of few layers.

At the many body perturbation theory level, the system under study presents several challenges. The first is the fact that it is constituted by two different materials, graphene and Co, a situation that may correspond to complex plasmonic interaction, for which a description based on a unique plasmon pole could be questionable. Moreover, being a metal it presents the same challenges already described in Section 4.3 for Cu, a plasmon energy close to $\omega = 0$ and an intraband term due to the partially filled bands that cross the Fermi energy. Moreover, we expect complex correction, different for s, p and d states, and therefore not reducible to a scissors and stretching model.

Both Quantum ESPRESSO, used in the DFT calculation, and Yambo, used to perform the GW calculations, use periodic boundary conditions. This means that the interface has to be isolated from its replicas by adding a layer of vacuum in the supercell (24 Å). The presence of a large amount of vacuum affects the convergence parameters since it increases the number of $\mathbf{G}$ vectors used in the polarizability matrix and the self-energy and also the number of empty states and therefore the number of bands needed for convergence. In addition, the graphene band structure, with its characteristic Dirac cone, modified by the hybridization with Co, requires a very dense $\mathbf{k}$-point grid. The combination of strong electronic correlations, as observed in Cu, and the interaction with the vacuum level may also hinder the convergence with respect to the number of

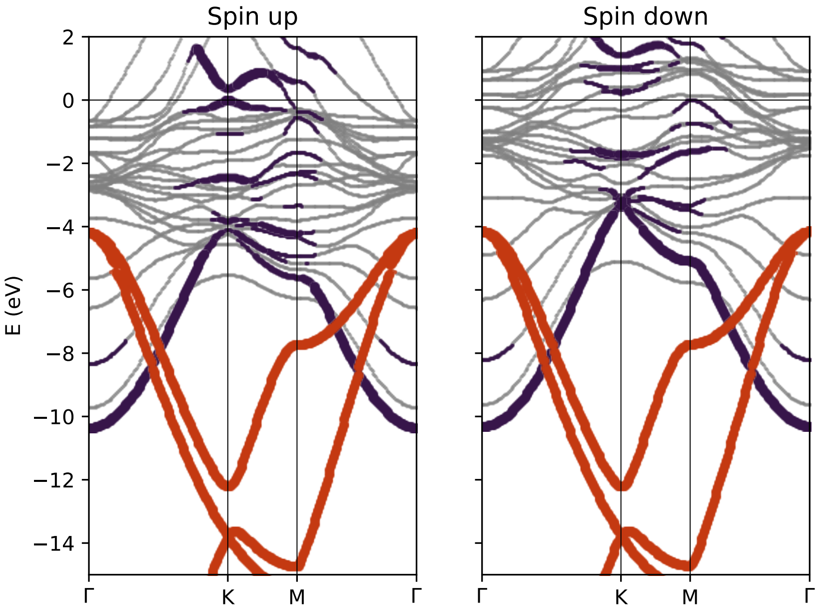

Figure 5.21: DFT spin resolved band structure of the GrCo interface modeled with 4 layer of Co and projected in the π (red) and σ (blue) graphene orbitals.

empty bands.

Regarding the description of the frequency dependence of the polarizability, the PPA has the same problems described for Cu with similar values for the number of matrix elements that fail the plasmon-pole condition and the average deviation. For this reason we have not performed systematic calculations using the PPA. On the other hand, a standard full frequency approach is computational too demanding to be performed with our current computational resources. For the current system, we have used the MARCONI 100 cluster, an accelerated cluster based on IBM Power9 architecture and Volta NVIDIA GPUs, with a peak performance of about 32 PFlop/s. We typically used 30 nodes, each of them with 4 GPU cards, and the largest calculations performed could last more than 15 hours. We then try to address such complex system with the MPA but even within this method, the computational cost limits the convergence of the calculation and for this reason we present here only preliminary results that nevertheless bring several insights to the problem.

5.4.4 Setup and preliminary results

Due to the noisy structure of the polarizability close to $\omega = 0$, we adopted the same sampling strategy described in Section 4.3.2 as a general strategy for metals with low energy plasmons, i.e. we slightly shifted along the imaginary axis the sampling point at $\omega = 0$.

Preliminary convergence tests were done considering 4 Co layers, i.e. the number of the layers needed to converge the band structure at the DFT level. In Fig. 5.23 we show

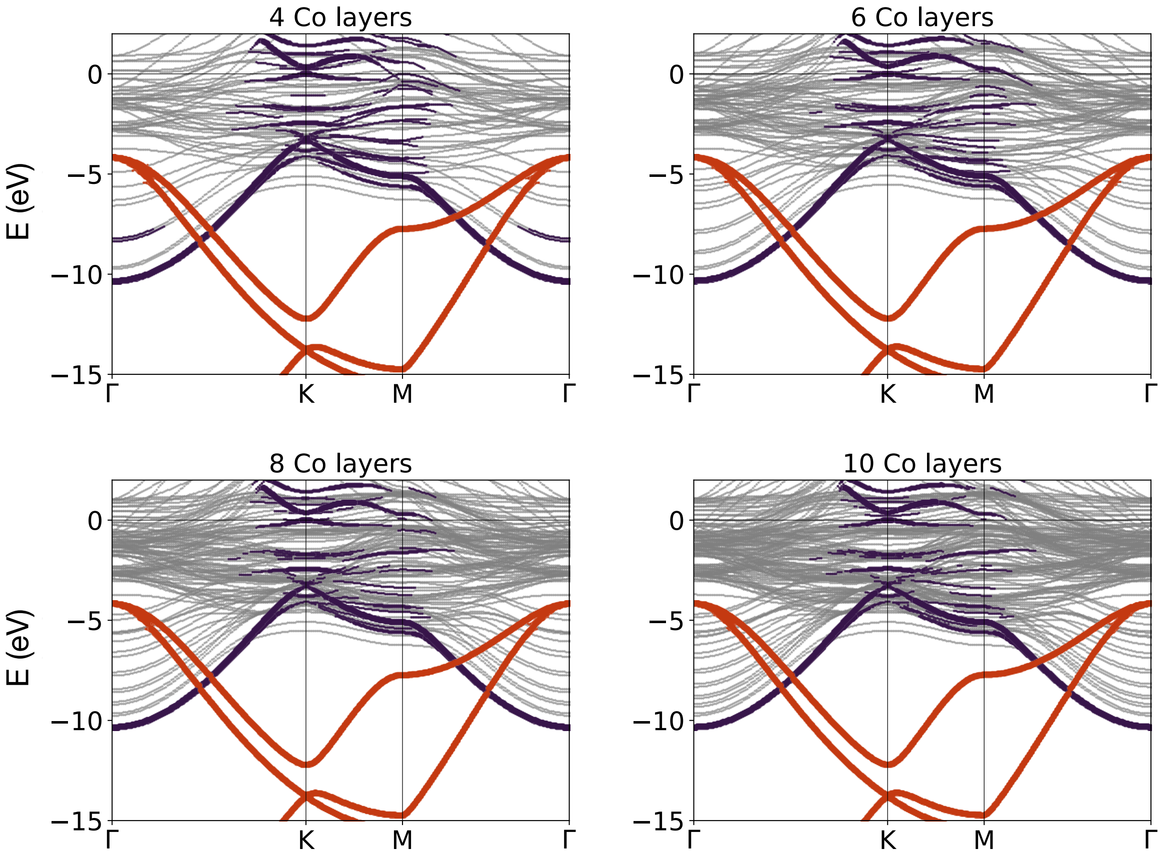

Figure 5.22: DFT band structure of the GrCo interface modeled with 4, 6, 8 and 10 layer of Co and projected in the π (red) and σ (blue) graphene orbitals.

the convergence with respect to the number of bands of the GW corrections to a set of selected quasi-particles, calculated with MPA with 15 poles. The grid of **k**-points is fixed to $6 \times 6 \times 1$ and the dimension of the polarizability matrix to 20 Ry. The range of the quasi-particle energy corrections is large, spanning from -1.5 to 0.1 eV, and for 800 bands they seem to be converged within 20 meV. The calculations done with 400 and 800 bands differ in average by 85 meV. In order to study the convergence with respect to the **k**-points mesh and taking into account the limitations of our computational resources, we fixed the number of bands to 400.

We started by doing a study using MPA with a single pole while increasing the number of **k**-points. In Fig. 5.24 the DFT and the GW energies for an unoccupied Gr state are shown, in the same figure we also plotted the asymptotic value of an extrapolation with respect to the number of **k**-points. The correction presents changes of the order of 0.5 eV up to a grid of $36 \times 36 \times 1$ and the extrapolation was made with a dependence proportional to $1/N_q^{1/3}$, where N_q is the total number of **k**-points. The extrapolated value differs by 0.15 eV from the correction computed with the largest **k** grid. We then computed a series of quasi-particle corrections using 15 poles and two different **k** grids, $6 \times 6 \times 1$ and $27 \times 27 \times 1$. The comparison between the $6 \times 6 \times 1$ and the $27 \times 27 \times 1$ grids shows differences in the quasiparticle corrections ranging from 0.17 to 0.39 eV. The results obtained with the $6 \times 6 \times 1$ grid do not improve the DFT values with respect to the experiment. The $27 \times 27 \times 1$ grid improves considerably the quasi-particles with respect to the $6 \times 6 \times 1$ grid, but does not shorten enough the large deviations from the experimental values obtained for deep states below the Fermi level.

In order to understand the nature of these differences we studied possible non-local effects underestimated in our slab model. As we mentioned earlier, the band structure computed at the DFT level and shown in Figure 5.22, in particular the graphene bands do not change already from 4 to 6 Co layers. For the MPA calculations we increased the number of Co layers to 8 and use a supercell with a size on the perpendicular direction of 35 Å and 760 bands. This number of bands was chosen, on the basis of the parameters used in the 4 Co layer case, proportionally to the number of occupied states. The results, including DFT energies, are reported in Fig. 5.25, as the difference of the simulations with respect to the experimental values extracted from Fig. 5.19 for 4 selected graphene quasi-particles: σ and π bands at Γ and K respectively. The quasi-particles are arranged in the plot according to their energy.

The difference between KS-DFT and ARPES energies fluctuates, being larger for the states close to Fermi and smaller for deeper states. On the other hand, for both 4 and 8 Co layers, the GW calculations present a systematic positive error, almost linear with the energies of the quasi-particles, that is larger for states further below the Fermi level. Therefore the GW quasi-particle corrections are highly non trivial, suggesting that GW correctly distinguishes the different character of the states, in particular π and σ. This

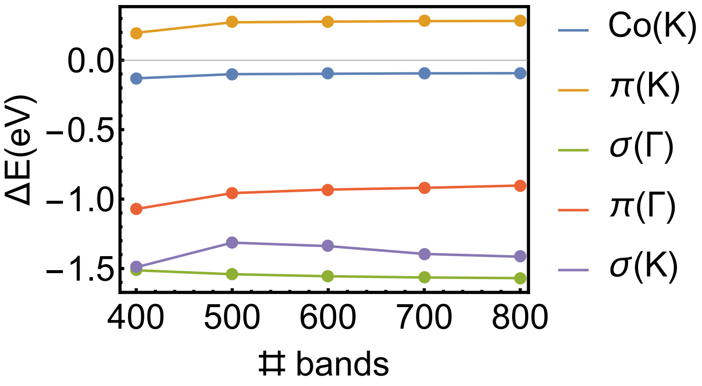

Figure 5.23: Convergence of the GW/MPA corrections to 5 selected quasi-particles with respect to the number of bands.

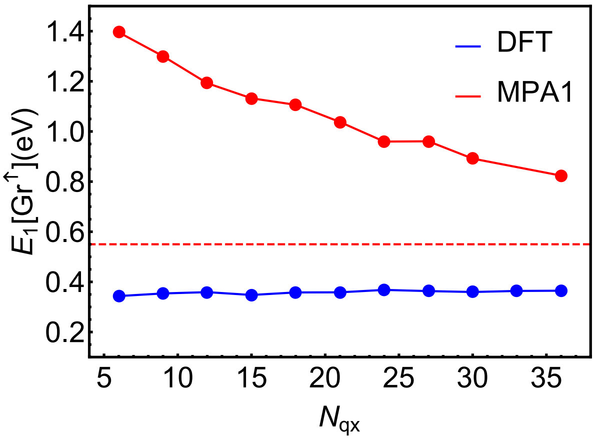

Figure 5.24: Convergence of the quasi-particle energy corresponding to the first unoccupied state of the spin up channel of the Gr/Co interface with respect to an in-plane dimension of the number of k-points, N_{qx}. This quasi-particle define, with his counterpart occupied state, the Gr mini-gap located at K in the majority spin channel, as shown in fig. 5.21. GW MPA results are compered with the DFT results. The MPA calculations were performed using a single pole reaching a maximum grid of $36 \times 36 \times 1$. The dashed line represents the asymptotic value extrapolated using the form $(a/N_q^{1/3} + b)$.

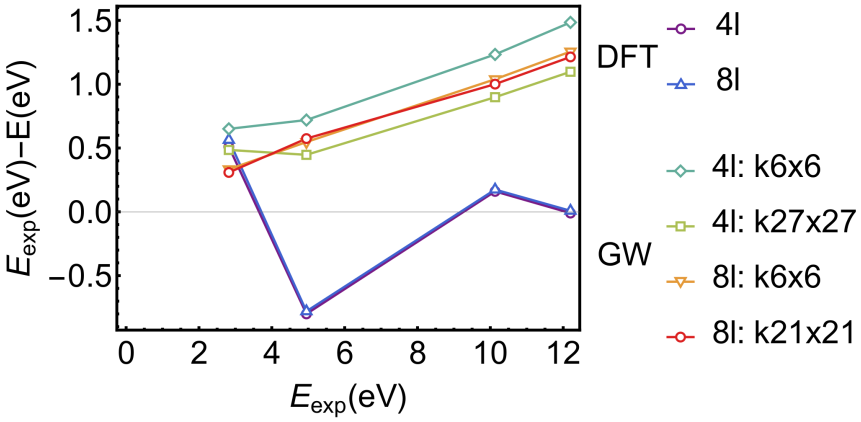

Figure 5.25: Deviations of the selected σ and π quasi-particle energies calculated via DFT and MPA with respect to the experimental results. E_{exp} refers to experimental ARPES binding energies, such that larger values correspond to deeper valence states.

is at variance with the local/semilocal approximations to the DFT v_{xc} potential that tend to treat them in the same way (as a reminder, KS states are nevertheless not meant to reproduce ARPES energies).

When comparing the 4 and 8 Co layer slabs, both DFT results are similar, as discussed above, while the errors of GW with 8 layers are reduced by about 0.2 eV, with respect to the results with 4 layers. This again shows the effect of long range interactions that are not captured at the DFT level. However, an increased number of layers does not change significantly the slope of the curve, still presenting deviations with respect to experiment that increase with the binding energy of the states. On the other hand, for the interface with 4 Co layers a denser **k**-point mesh reduce the error for all the quasi-particles and slightly decreasing the error slope, while for 8 Co layers the calculations with the two different grids are very close to each other. Tentatively, the results for the thicker slab suggests that, since it has more occupied states than the thinner one, there are more missing intra-band contributions hindering the convergence with respect to the **k**- and **q**-grids, such that the $21 \times 21 \times 1$ mesh still does not show significant changes with respect to the $6 \times 6 \times 1$, only introducing a small change in the error slope.

5.4.5 Partial conclusions

Even if the present results are preliminary, we can draw some conclusions, as follows. (*i*) The MPA method allowed us to perform GW calculations that were shown largely unstable using the PPA approach due to representability errors. Indeed, the number of matrix elements corrected by the failure condition described in Section 3.6.1 within PPA oscillate between 40-60%, and the resulting quasi-particle corrections were found unphysical. In contrast, the MPA approach, with its generalized correction given in Eq. (3.77) allows us to obtain meaningful results without resorting to FF methods which turn out to be computationally extremely expensive for the system under study.

(*ii*) The MPA quasi-particles corrections have shown to be highly non trivial. When considering the differences between the computed and the experimental results, the MPA method greatly decreases the fluctuations of the DFT energies of different states and shows instead a systematic error that increases for states further away from the Fermi level, correctly capturing the different character of the states, such as π and σ orbitals of graphene or d states of Co.

(*iii*) The results obtained so far still do not allow for a fully quantitative comparison with experiments, in particular for deeper valence states. However, despite the number of tests already performed, in view of the complexity of the system, more tests have to be taken to make sure that all numerical aspects are fully under control. These include the dependency of the results on the **k**-grid, and on the number of metal layers considered when modeling the system, which could be critical parameters affecting the quality of the results.

Of course we cannot exclude the possibility that other issues besides convergence need to be addressed. For instance, we expect the intra-band contributions (currently neglected) to the polarizability to play a role in this complex interface. As shown in Ref. [232], neglecting the intra-band term in metals results in an artificial opening of a gap, which decreases as the **k**-point grid becomes denser. In our case we see an enlargement of the Gr mini-gap at K between the last occupied and first unoccupied states in the spin up channel. Even if we expect that GW increases the gap, the corrections observed for those states are enhanced by the missing intra-band term, as seen in Fig. 5.24.

(*iv*) Despite the present calculations, the accuracy of converged GW calculations in reproducing ARPES experiments for complicated magnetic systems still needs to be further assessed. At the DFT level there seem to be error cancellations between the model of the slab with a finite number of Co layers and the locality of the theory (both due to the semilocal approximation of the functional, and to the KS framework itself), especially for deep states below ~ -5 eV. On the other hand, our GW calculations improve over DFT concerning the position of the states near the Fermi level. Still the GW level of theory could be insufficient to properly describe the ARPES measurements in the present case. For instance, the limitations of GW in describing electronic correlations beyond electron-plasmon are well-known, and in turn related to the neglect of vertex corrections.

In particular, being Gr/Co a magnetic interface, it would be interesting to add vertex corrections aimed at improving the description of systems with partially filled $3d$ electrons, such as the recently proposed GW+DMFT approach [265, 266].

Nevertheless, all these improvements and tests are beyond the scope of the present Thesis, that proposes a new frequency treatment of the polarizability, going beyond the plasmon pole approximation without significantly increasing the computational cost, as is applicable to different types of systems, ranging from semiconductors to metal, from extended systems to molecules.

Chapter 6

Conclusions

6.1 Gr/metal interfaces

By means of *ab initio* calculations I have studied the structural, electronic, and magnetic properties of a class of surfaces with potential applications for magnetic systems with tunable properties. Our DFT results complement extensive experiments done within a collaboration with the experimental group of Prof. Maria Graxia Betti and Carlo Mariani in Rome, ranging from XPS, NEXFAS and XMCD, to ARPES and IPES. In particular, we have studied Fe and FeCo intercalation on Gr/Ir interfaces reporting fine details of their electronic and magnetic configurations. Both the Fe and FeCo magnetic layers are artificial 2D systems protected from contaminants and rearrangement by the Gr layer, which we find to be suitable candidates to be integrated into magnetic devices.

Combining ARPES and DFT calculations we show that the interaction of the π band of Gr with Fe-$3d$ and FeCo-$3d$ states pushes the strongly hybridized Dirac cone towards larger binding energies (BE). However, in proximity of E_{F} we identify new localized states associated to the Fe or the FeCo alloy. We also show that the intermixing of the two ferromagnets (FMs) and the artificial structural phase, where the Fe and the FeCo layers assume the Ir(111) lattice constant, lead to a narrowing and to an enhanced spin splitting of the $3d$ states with respect to pure bulk systems.

From the theoretical side, we have addressed the role played by oxygen intercalated under Gr, showing that it prevents the hybridization between graphene and Co states and increases the graphene-Co distance. Therefore, O intercalation is another possible option for designing and controlling the electronic and magnetic properties of this class of systems.

6.2 Development of the MPA method

In the context of the GW method, We have developed a new approach beyond the plasmon-pole approximation (PPA) for the description of the frequency dependence in the evaluation of the self-energy, with an accuracy comparable with full-frequency (FF) methods, but at a much lower computational cost. The MPA technique is build on a multipole model of the polarizability with a tunable number of poles, bridging in this sense the PPA and FF approaches. The key feature of our development is the use of optimal sampling strategies, that we have shown to be a fundamental ingredient in order to achieve the best performance. We propose what we called a *double parallel sampling*, which we have benchmarked in several classes of materials, including bulk semiconductors, molecules, bulk metals and magnetic interfaces.

The validation of the MPA on Si, hBN and TiO_2 semiconductors shows an excellent agreement with FF results not only for the quasi-particles corrections, but also for the full-frequency dependence of the self-energy and the spectral function. In the case of the molecules, the calculations for the F_2 molecule were limited by the computational cost that did not allow us to use converged parameters, such as the number of bands and the size of the polarizability matrix. Nevertheless, the extrapolated results compare well with the existing GW100 [158] data.

Regarding the validation on metallic systems, there are issues not related with the frequency description of the polarizability, such as the intraband contribution in the long wavelength limit, that will be addressed within the Yambo implementation in the near future. This issues limit the comparison with the experimental measurements, however, in the case of bulk Cu, we managed to reduce the weight of the missing intraband contribution by considerably increasing in the number of **k**-points. This was possible due to reduced computational cost of the MPA, and allowed us to obtain results in good agreement with the literature. Comparing with the experimental results available for Cu, our final GW/MPA corrections improve all the DFT quasi-particles in a non-trivial way, a feature only reported within very costly FF approaches. As discussed in Section 5.4.5, in the case of the magnetic Gr/Co interface there are many more difficulties in addition to the absence of the intraband term, and we report only preliminary results.

In the framework of the MPA approach our systematic development of an optimal sampling strategy bought insights that contribute to the understanding of the successes and failures of the PPA. In particular, we have also discussed two common formulations of the PPA (Godby-Needs and Hybertsen-Louie plasmon pole models) showing how they can be seen in a unified frame with a sampling variation. We have also illustrated the main problem with the use of a plasmon-pole model for metals with low energy plasmons like Cu. In this cases, several plasmonic peaks present in the frequency dependence of the self-energy can be described within MPA by a model with more than one pole.

The MPA convergence with respect to the number of poles, for all the materials studied within the present thesis, is achieved with around 10 poles (20 frequencies), using the double parallel sampling. The computational cost of the present approach is comparable to analytic-continuation approaches. In this regime we have shown that MPA reaches an accuracy comparable with standard FF contour deformation methods [134, 158], significantly more demanding. Moreover, we believe MPA presents several advantages with respect to this method. In the contour deformation approach, the number of frequencies used in the evaluation of W increases with the distance of the state to be corrected from the Fermi level due to the increasing number of poles of G entering in the contour [195], whereas within MPA all the quasi-particles have the same computational cost. Another advantage of MPA relies on its analytic form, which allows one to solve analytically the frequency integral of the self-energy, that also has a multipole form. Moreover, the frequency structure of the polarizability is physically meaningful and permits the analysis of the plasmonic excitations.

Overall, our findings show that the multipole approach can be used to obtain a simple and effective representation of response functions. We illustrated how to analyse simple types of sampling in order to understand and design good recipes. We show that the MPA with optimal sampling strategies in the complex plane can lead to a level of accuracy comparable with full-frequency methods at much lower costs, not only for the quasi-particle energies, but also for the whole energy range relevant for the self-energy.

6.3 Future perspectives

The MPA approach can be easily combined with other techniques. In particular, it is independent of the methodology to treat the intraband contribution, since they aim at correcting the matrix elements of the polarizability around its head (long wave-length limit). Therefore, the MPA sampling and interpolation can be performed afterwords without altering the approach. The inclusion of the intraband term is on the top of our next priorities. There is also the possibility of accelerating convergence with respect to the grid of **k**-points. The calculation of the QP band structure of low dimensional semiconductors may require a very dense BZ sampling due to the sharp q-dependence of the dielectric matrix in the long-wavelength limit ($q \to 0$). By combining Monte Carlo integration with an interpolation scheme able to represent the screened potential between the numerical grid points, the convergence of the QP corrections of 1-2D semiconductors with respect to the q sampling is drastically improved [267–271]. Since GW calculations involve an integration over the Brillouin zone and the integral in the frequency domain, and these variables are independent, it is also possible to merge the two methodologies in order to optimize the calculations with respect to both parameters and improve considerably the computational cost of the calculations for 2D materials.

On the other hand, we plan to take advantage on the multipole form and build a multipole approximation for the self-energy in order to interpolate its full frequency dependence from a small number of frequency points, selected in the same fashion of the double parallel sampling already proposed for the polarizability. The MPA for the self-energy can be use for solving the quasi-particle equation analytically, instead of using numerical solver like the secant method as an alternative to the less accurate linearization of the quasi-particle equation. Moreover, the multipole models of both, X and Σ, can be made compliant with their respective sum-rules [159], completeness-sums [230] or spectral collapses [229], as in the cases already proposed for accelerating convergences, for instance, with respect to the number of bands within the PPA [230]. The implementation of such approach could be fundamental in order to obtain converged results in the case of the GW100 set, without the needs of extrapolations.

Having the self-energy written in a simple multipole form may have many others advantages, it could become a fundamental tool for reducing the computational cost of accurate quasi-particle self-consistent GW calculations. Furthermore, we can also obtain a multipole expansion for the interacting Green function, that could be use not only for fully self-consistent GW calculations, but also for many-body approaches beyond GW.

Chapter 7

List of publications

- Claudia Cardoso, Giulia Avvisati, Pierluigi Gargiani, Marco Sbroscia, Madan S. Jagadeesh, Carlo Mariani, **Dario A. Leon**, Daniele Varsano, Andrea Ferretti, and Maria Grazia Betti. Magnetic response and electronic states of well defined Graphene/Fe/Ir(111) heterostructure. Phys. Rev. Materials **5**, 014405 (2021), doi: `https://doi.org//10.1103/PhysRevMaterials.5.014405`
- Daniela Pacilé, Claudia Cardoso, Giulia Avvisati, Ivana Vobornik, Carlo Mariani, **Dario A. Leon**, Pietro Bonfá, Daniele Varsano, Andrea Ferretti, and Maria Grazia Betti. Narrowing of d bands of FeCo layers intercalated under graphene. Applied Physics Letters **118**, 121602 (2021), doi: `https://doi.org/10.1063/5.0047266`
- **D.A. Leon**, Claudia Cardoso, Tommaso Chiarotti, Daniele Varsano, Elisa Molinari, and Andrea Ferretti. Frequency dependence in *GW* made simple using a multipole approximation. Phys. Rev. B. **104**, 115157 `https://doi.org/10.1103/PhysRevB.104.115157`.
- **D.A. Leon**, Claudia Cardoso, Daniele Varsano, Elisa Molinari, and Andrea Ferretti. Oxygen adsorption on Co and Co/Ir substrates and intercalation on Gr/Co interfaces. (submitted 2021).
- **D.A. Leon**, Claudia Cardoso, Daniele Varsano, Elisa Molinari, and Andrea Ferretti. A multipole approach for dielectric screening in metallic systems. (in preparation).

Bibliography

[1] Claudia Cardoso et al. “Magnetic response and electronic states of well defined Graphene/Fe/Ir(111) heterostructure”. In: *Phys. Rev. Materials* 5 (1 2021), p. 014405. DOI: `https://doi.org/10.1103/PhysRevMaterials.5.014405`.

[2] Daniela Pacilè et al. “Narrowing of d bands of FeCo layers intercalated under graphene”. In: *Applied Physics Letters* 118.12 (2021), p. 121602. DOI: `https://doi.org/10.1063/5.0047266`.

[3] Andrea Marini et al. “yambo: An ab initio tool for excited state calculations”. In: *Comput. Phys. Commun.* 180 (8 2009), pp. 1392–1403. DOI: `https://doi.org/10.1016/j.cpc.2009.02.003`.

[4] D. Sangalli et al. “Many-body perturbation theory calculations using the yambo code”. In: *J. Phys.: Condens. Matter* 31 (32 2019), p. 325902. DOI: `https://doi.org/10.1016/j.cpc.2009.02.003`.

[5] Dario A. Leon et al. “Frequency dependence in *GW* made simple using a multipole approximation”. In: *Phys. Rev. B* 104 (11 2021), p. 115157. DOI: `https://doi.org/10.1103/PhysRevB.104.115157`.

[6] Matthias Batzill. “The surface science of graphene: Metal interfaces, CVD synthesis, nanoribbons, chemical modifications, and defects”. In: *Surf. Sci. Rep.* 67.3 (2012), pp. 83–115. DOI: `https://doi.org/10.1016/j.surfrep.2011.12.001`.

[7] Martin Weser et al. “Electronic structure and magnetic properties of the graphene/Fe/Ni(111) intercalation-like system”. In: *Phys. Chem. Chem. Phys.* 13 (2011), p. 7534. DOI: `https://doi.org/10.1039/C1CP00014D`.

[8] Régis Decker et al. “Atomic-scale magnetism of cobalt-intercalated graphene”. In: *Phys. Rev. B* 87 (4 2013), p. 041403. DOI: `https://doi.org/10.1103/PhysRevB.87.041403`.

[9] D. Pacilè et al. “Electronic Structure of Graphene/Co Interfaces”. In: *Phys. Rev. B* 90.19 (2014), pp. 1–6. ISSN: 1550235X. DOI: `https://doi.org/10.1103/PhysRevB.90.195446`.

[10] H. Vita et al. “Electronic structure and magnetic properties of cobalt intercalated in graphene on Ir(111)”. In: *Phys. Rev. B* 90 (16 2014), p. 165432. DOI: `https://doi.org/10.1103/PhysRevB.90.165432`.

[11] R. Decker et al. “Local tunnel magnetoresistance of an iron intercalated graphene-based heterostructure”. In: *J. Phys.: Condens. Mat.* 26 (2014), p. 394004. DOI: `https://doi.org/10.1088/0953-8984/26/39/394004`.

[12] Giulia Avvisati et al. “Strong ferromagnetic coupling and tunable easy magnetization directions of FexCo1-x layer(s) intercalated under graphene”. In: *Appl. Surf. Sci.* 527 (2020), p. 146599. ISSN: 0169-4332. DOI: `https://doi.org/10.1016/j.apsusc.2020.146599`.

[13] Daniela Pacilè et al. “Artificially Lattice-Mismatched Graphene/Metal Interface: Graphene/Ni/Ir(111)”. In: *Phys. Rev. B* 87.3 (2013), p. 035420. DOI: `https://doi.org/10.1103/PhysRevB.87.035420`.

[14] Yuriy Dedkov and Elena Voloshina. “Spectroscopic and DFT studies of graphene intercalation systems on metals”. In: *J. Electron. Spectrosc. Relat. Phenom.* 219 (2017), p. 77. DOI: `https://doi.org/10.1016/j.elspec.2016.11.012`.

[15] G. Avvisati et al. “FePc adsorption on the moiré superstructure of graphene intercalated with a Co layer”. In: *J. Phys. Chem. C* 121 (2017), p. 1639. DOI: `https://doi.org/10.1021/acs.jpcc.6b09875`.

[16] Ming Yang et al. “Metal-graphene interfaces in epitaxial and bulk systems: A review”. In: *Prog. Mater. Sci.* 110 (2020), p. 100652. DOI: `https://doi.org/10.1016/j.pmatsci.2020.100652`.

[17] P. Gargiani et al. “Graphene-based synthetic antiferromagnets and ferrimagnets”. In: *Nat. Commun.* 8.1 (2017), p. 699. DOI: `https://doi.org/10.1038/s41467-017-00825-9`.

[18] J. Coraux et al. “Air-protected epitaxial graphene/ferromagnet hybrids prepared by chemical vapor deposition and intercalation”. In: *J. Phys. Chem. Lett.* 3 (2012), pp. 2059–2063. DOI: `https://doi.org/10.1021/jz3007222`.

[19] M. Cattelan et al. “The nature of the Fe–graphene interface at the nanometer level”. In: *Nanoscale* 7 (6 2015), pp. 2450–2460. DOI: `https://doi.org/10.1039/C4NR04956J`.

[20] Robert S. Weatherup et al. “Long-Term Passivation of Strongly Interacting Metals with Single-Layer Graphene”. In: *J. Am. Chem. Soc.* 137.45 (2015), pp. 14358–14366. DOI: `https://doi.org/10.1021/jacs.5b08729`.

[21] Maciej Bazarnik et al. "Multi-layer and multi-component intercalation at the graphene/Ir(111) interface". In: *Surf. Sci.* 639 (2015), pp. 70–74. DOI: https://doi.org/10.1016/j.susc.2015.04.021.

[22] G. Avvisati et al. "Ferromagnetic and antiferromagnetic coupling of spin molecular interfaces with high thermal stability". In: *Nano Lett.* 18 (2018), pp. 2268–2273. DOI: https://doi.org/10.1021/acs.nanolett.7b04836.

[23] Maciej Bazarnik et al. "Tailoring Molecular Self-Assembly of Magnetic Phthalocyanine Molecules on Fe- and Co-Intercalated Graphene". In: *ACS Nano* 7.12 (2013), pp. 11341–11349. DOI: https://doi.org/10.1021/nn405172q.

[24] Giulia Avvisati et al. "Superexchange pathways stabilize the magnetic coupling of MnPc with Co in a spin interface mediated by graphene". In: *Phys. Rev. B* 98 (11 2018), p. 115412. DOI: https://doi.org/10.1103/PhysRevB.98.115412.

[25] Giulia Avvisati et al. "Graphene-mediated Interaction between FePc and intercalated Co layers". In: *Applied Surface Science* 432 (2018), pp. 2–6. DOI: 10.1016/j.apsusc.2017.05.089. URL: http://dx.doi.org/.

[26] A.K. Geim and K.S. Novoselov. "Graphene growth on epitaxial Ru thin films on sapphire". In: *Nature Mater.* 6 (2007), pp. 183–191. DOI: https://doi.org/10.1038/nmat1849.

[27] E. Sutter et al. "Graphene growth on epitaxial Ru thin films on sapphire". In: *Appl. Phys. Lett.* 97.21 (2010), p. 213101. DOI: https://doi.org/10.1063/1.3518490.

[28] A.K. Geim. "Graphene: Status and Prospects". In: *Science* 324 (5934 2009), pp. 1530–1534. DOI: https://doi.org/10.1126/science.1158877.

[29] Li Huang et al. "Intercalation of metal islands and films at the interface of epitaxially grown graphene and Ru(0001) surfaces". In: *Appl. Phys. Lett.* 99.16 (2011), p. 163107. DOI: https://doi.org/10.1063/1.3653241.

[30] I. Forbeaux, J.-M. Themlin, and J.-M. Debever. "Heteroepitaxial graphite on $6H-\mathrm{SiC}(0001)$: Interface formation through conduction-band electronic structure". In: *Phys. Rev. B* 58 (24 1998), pp. 16396–16406. DOI: https://doi.org/10.1103/PhysRevB.58.16396.

[31] Peter Sutter, Jerzy T. Sadowski, and Eli Sutter. "Graphene on Pt(111): Growth and substrate interaction". In: *Phys. Rev. B* 80 (24 2009), p. 245411. DOI: https://doi.org/10.1103/PhysRevB.80.245411.

[32] Mattia Scardamaglia et al. "Metal-phthalocyanine array on the moiré pattern of a graphene sheet". In: *J. Nanopart. Res.* 13.11 (2011), pp. 6013–6020. DOI: https://doi.org/10.1007/s11051-011-0384-1.

[33] Alessandro Lodesani et al. “Graphene as an ideal buffer layer for the growth of high-quality ultrathin Cr2O3 layers on Ni (111)”. In: *ACS Nano* 13.4 (2019), pp. 4361–4367. DOI: https://doi.org/10.1021/acsnano.8b09588.

[34] Matteo Jugovac et al. “Tunable coupling by means of oxygen intercalation and removal at the strongly interacting graphene/cobalt interface”. In: *Carbon* 163 (2020), pp. 341–347. DOI: https://doi.org/10.1016/j.carbon.2020.03.034.

[35] Nikolaos Tombros et al. “Electronic spin transport and spin precession in single-graphene layers at room temperature”. In: *Nature* 448 (2007), pp. 571–574. DOI: https://doi:10.1038/nature06037.

[36] W. Han et al. “Graphene spintronic”. In: *Nature Nanotechnology* 9 (2014), pp. 794–807. DOI: https://doi:10.1038/nature06037.

[37] Dmitry Usachov et al. “Observation of Single-Spin Dirac Fermions at the Graphene/Ferromagnet Interface”. In: *Nano Lett.* 15.4 (2015), pp. 2396–2401. DOI: https://doi.org/10.1021/nl504693u.

[38] L. V. Dzemiantsova et al. “Multiscale magnetic study of Ni(111) and graphene on Ni(111)”. In: *Phys. Rev. B* 84 (20 2011), p. 205431. DOI: https://doi.org/10.1103/PhysRevB.84.205431.

[39] A. Varykhalov et al. “Intact Dirac Cones at Broken Sublattice Symmetry: Photoemission Study of Graphene on Ni and Co”. In: *Phys. Rev. X* 2 (4 2012), p. 041017. DOI: https://doi.org/10.1103/PhysRevX.2.041017.

[40] Lorenzo Massimi et al. “Interaction of iron phthalocyanine with the graphene/Ni (111) system”. In: *Beilstein J. Nanotechnol.* 5.1 (2014), pp. 308–312. DOI: https://doi.org/10.3762/bjnano.5.34.

[41] M. Weser et al. “Induced magnetism of carbon atoms at the graphene/Ni(111) interface”. In: *Appl. Phys. Lett.* 96.1, 012504 (2010), pp. -. DOI: https://doi.org/10.1063/1.3280047.

[42] I. Pletikosi ć et al. “Dirac Cones and Minigaps for Graphene on Ir(111)”. In: *Phys. Rev. Lett.* 102 (5 2009), p. 056808. DOI: https://doi.org/10.1103/PhysRevLett.102.056808.

[43] A. T. N’Diaye et al. “Growth of graphene on Ir(111)”. In: *New J. Phys.* 11 (2009), p. 023006. DOI: https://doi.org/10.1088/1367-2630/11/2/023006.

[44] Arjun Dahal and Matthias Batzill. “Graphene–nickel interfaces: a review”. In: *Nanoscale* 6 (5 2014), pp. 2548–2562. DOI: https://doi.org/10.1039/C3NR05279F.

[45] N. A. Vinogradov et al. “Formation and Structure of Graphene Waves on Fe(110)”. In: *Phys. Rev. Lett.* 109 (2 2012), p. 026101. DOI: `https://doi.org/10.1103/PhysRevLett.109.026101`.

[46] N.A. Vinogradov et al. “The structural evolution of graphene/Fe(110) systems upon annealing”. In: *Carbon* 111 (2017), pp. 113–120. DOI: `https://doi.org/10.1016/j.carbon.2016.09.058`.

[47] A. Varykhalov et al. “Tunable Fermi level and hedgehog spin texture in gapped graphene”. In: *Nat. Commun.* 6.1 (2015), p. 7610. DOI: `https://doi.org/10.1038/ncomms8610`.

[48] H. Okamoto. “The C-Fe (carbon-iron) system”. In: *J. Phase Equilibria* 13.5 (1992), pp. 543–565. DOI: `https://doi.org/10.1007/BF02665767`.

[49] S. Vlaic et al. “Graphene as a mechanically active, deformable two-dimensional surfactant”. In: *J. Phys. Chem. Lett.* 9 (2018), pp. 2523–2531. DOI: `https://doi.org/10.1021/acs.jpclett.8b00586`.

[50] P. James et al. “Calculated magnetic properties of binary alloys between Fe, Co, Ni, and Cu”. In: *Phys. Rev. B* 59 (1 1999), pp. 419–430. DOI: `https://doi.org/10.1103/PhysRevB.59.419`.

[51] F. Luo et al. “Tuning the perpendicular magnetic anisotropy in tetragonally distorted Fe_xCo_{1-x} alloy films on Rh(001) by varying the alloy composition”. In: *Appl. Phys. Lett.* 91 (2007), p. 262512. DOI: `https://doi.org/10.1063/1.2821370`.

[52] M. Getzlaff et al. “Structure, composition and magnetic properties of size-selected FeCo alloy clusters on surfaces”. In: *Appl. Phys. A* 82 (2006), pp. 95–101. DOI: `https://doi.org/10.1007/s00339-005-3347-5`.

[53] G. Moulas et al. “High magnetic moments and anisotropies for Fe_xCo_{1-x} monolayers on Pt(111)”. In: *Phys. Rev. B* 78 (2008), p. 214424. DOI: `https://doi.org/10.1103/PhysRevB.78.214424`.

[54] P. Gambardella et al. “Giant magnetic anisotropy of single cobalt atoms and nanoparticles”. In: *Science* 300 (2003), pp. 1130–1133. DOI: `https://doi.org/10.1126/science.1082857`.

[55] B. Nonas et al. “Strongly enhanced orbital moments and anisotropies of adatoms on the Ag(001) surface”. In: *Phys. Rev. Lett.* 86 (2001), pp. 2146–2149. DOI: `https://doi.org/10.1103/PhysRevLett.86.2146`.

[56] P. Gambardella et al. “Ferromagnetism in one-dimensional monatomic metal chains”. In: *Nature* 416 (2002), pp. 301–304. DOI: `https://doi.org/10.1038/416301a`.

[57] N. Sethulakshmi et al. "Magnetism in two-dimensional materials beyond graphene". In: *Mater. Today* 27 (2019), pp. 107–122. DOI: https://doi.org/10.1016/j.mattod.2019.03.015.

[58] B. D. Terris and T. Thomson. "Nanofabricated and self-assembled magnetic structures as data storage media". In: *J. Phys. D: Appl. Phys.* 38 (2005), R199–R222. DOI: https://doi.org/10.1088/0022-3727/38/12/r01.

[59] S. Bhatti et al. "Spintronics based random access memory: a review". In: *Mater. Today* 20 (2017), pp. 530–548. DOI: https://doi.org/10.1016/j.mattod.2017.07.007.

[60] D. I. Bardos. "Mean magnetic moments in bcc Fe-Co alloys". In: *J. Appl. Phys.* 40 (1969), pp. 1371–1372. DOI: https://doi.org/10.1063/1.1657673.

[61] E. Di Fabrizio et al. "Spin density of ordered FeCo: a failure of the local-spin-density-approximation". In: *Phys. Rev. B* 40 (1989), pp. 9502–9507. DOI: https://doi.org/10.1103/PhysRevB.40.9502.

[62] C. Paduani and J. C. Krause. "Electronic structure and magnetization of Fe–Co alloys and multilayers". In: *J. Appl. Phys.* 86 (1999), pp. 578–583. DOI: https://doi.org/10.1063/1.370769.

[63] W. Pepperhoff and M. Acet. *Constitution and Magnetism of Iron and its Alloys.* Springer-Verlag Berlin Heidelberg, 2001.

[64] R. S. Sundar and S. C. Deevi. "Soft magnetic FeCo alloys: alloy development, processing, and properties". In: *Int. Mater. Rev.* 50 (2005), pp. 157–192. DOI: https://doi.org/10.1179/174328005X14339.

[65] T. Hasegawa et al. "Conversion of FeCo from soft to hard magnetic material by lattice engineering and nanopatterning". In: *Sci. Rep.* 7 (2017), p. 13215. DOI: https://doi.org/10.1038/s41598-017-13602-x.

[66] Mario Einax, Wolfgang Dieterich, and Philipp Maass. "Colloquium: Cluster growth on surfaces: Densities, size distributions, and morphologies". In: *Rev. Mod. Phys.* 85 (3 2013), pp. 921–939. DOI: https://doi.org/10.1103/RevModPhys.85.921.

[67] Elena Voloshina, Nikolai Berdunov, and Yuriy Dedkov. "Restoring a nearly free-standing character of graphene on Ru(0001) by oxygen intercalation". In: *Sci. Rep.* 6.1 (2016), p. 20285. DOI: https://doi.org/10.1038/srep20285.

[68] Luca Bignardi et al. "Key role of rotated domains in oxygen intercalation at graphene on Ni (1 1 1)". In: *2D Materials* 4.2 (2017), p. 025106. DOI: https://doi.org/10.1088/2053-1583/aa702c.

[69] Dmitry Yu Usachov et al. "Raman Spectroscopy of Lattice-Matched Graphene on Strongly Interacting Metal Surfaces". In: *ACS Nano* 11 (6 2017), pp. 6336–6345. DOI: https://doi.org/10.1021/acsnano.7b02686.

[70] Huei-Ying Ho, Jyh-Shen Tsay, and Yu-Shan Chen. "Oxygen Adsorption and Magnetic Properties of Ultrathin Co/Ir(111) Films". In: *Jp. J. App. Phys.* 49.7 (2010), p. 075802. DOI: https://doi.org/10.1143/jjap.49.075802.

[71] S.H. Ma et al. "First-principles studies of oxygen chemisorption on Co(0001)". In: *Surf. Sci.* 619 (2014), pp. 90–97. ISSN: 0039-6028. DOI: https://doi.org/10.1016/j.susc.2013.09.015.

[72] S. Förster et al. "Oxygen adsorption on Fe/W(110) and Co/W(110) thin films: Surface magnetic properties". In: *Phys. Rev. B* 66 (13 2002), p. 134427. DOI: https://doi.org/10.1103/PhysRevB.66.134427.

[73] M. Getzlaff et al. "Surface magnetic properties of oxygen on ferromagnetic films: a spin resolved MDS study". In: *Surf. Sci.* 331-333 (1995), pp. 1404–1407. ISSN: 0039-6028. DOI: https://doi.org/10.1016/0039-6028(95)00143-3.

[74] J.S. Tsay and Y.S. Chen. "Oxygen adsorption on ultrathin Co/Ir(111) films: Compositional anomaly". In: *Surf. Sci.* 600.18 (2006), pp. 3555–3559. ISSN: 0039-6028. DOI: https://doi.org/10.1016/j.susc.2006.02.050.

[75] Alberto Calloni et al. "Empty electron states in cobalt-intercalated graphene". In: *J. Chem. Phys.* 153.21 (2020), p. 214703. DOI: https://doi.org/10.1063/5.0021814.

[76] Alpha T N'Diaye et al. "Structure of epitaxial graphene on Ir(111)". In: *New J. Phys.* 10.4 (2008), p. 043033. DOI: https://doi.org/10.1088/1367-2630/10/4/043033.

[77] David A. Duncan et al. "Corrugated graphene exposes the limits of a widely used ab initio van der Waals DFT functional". In: *Phys. Rev. Mater.* 3 (12 2019), p. 124001. DOI: https://doi.org/10.1103/PhysRevMaterials.3.124001.

[78] Carsten Busse et al. "Graphene on Ir(111): Physisorption with Chemical Modulation". In: *Phys. Rev. Lett.* 107 (3 2011), p. 036101. DOI: https://doi.org/10.1103/PhysRevLett.107.036101.

[79] V. L. Moruzzi et al. "Ferromagnetic phases of bcc and fcc Fe, Co, and Ni". In: *Phys. Rev. B* 34 (3 Aug. 1986), pp. 1784–1791. DOI: 10.1103/PhysRevB.34.1784. URL: https://link.aps.org/doi/10.1103/PhysRevB.34.1784.

[80] Andrea Damascelli, Zahid Hussain, and Zhi-Xun Shen. "Angle-resolved photoemission studies of the cuprate superconductors". In: *Rev. Mod. Phys.* 75 (2 2003), pp. 473–541. DOI: https://doi.org/10.1103/RevModPhys.75.473.

[81] Marko Kralj et al. “Graphene on Ir(111) characterized by angle-resolved photoemission”. In: *Phys. Rev. B* 84 (7 2011), p. 075427. DOI: https://doi.org/10.1103/PhysRevB.84.075427.

[82] Jens Brede et al. “Tuning the Graphene on Ir(111) adsorption regime by Fe/Ir surface-alloying”. In: *2D Materials* 4.1 (2016), p. 015016. DOI: https://doi.org/10.1088/2053-1583/4/1/015016.

[83] K. Suenaga and M. Koshino. “Atom-by-atom spectroscopy at graphene edge”. In: *Nature* 468 (2010), p. 1088. DOI: https://doi.org/10.1038/nature09664.

[84] D. Pacilè et al. “Near-Edge X-Ray Absorption Fine-Structure Investigation of Graphene”. In: *Phys. Rev. Lett.* 101 (0 2008), p. 066806. DOI: https://doi.org/10.1103/PhysRevLett.101.066806.

[85] S. Entani et al. “Growth of nanographite on Pt(111) and its edge state”. In: *Appl. Phys. Lett.* 88 (2006), p. 153126. DOI: https://doi.org/10.1063/1.2194867.

[86] Mattia Scardamaglia et al. “Graphene-Induced Substrate Decoupling and Ideal Doping of a Self-Assembled Iron-Phthalocyanine Single Layer”. In: *J. Phys. Chem. C* 117.6 (2013), pp. 3019–3027. DOI: https://doi.org/10.1021/jp308861b.

[87] B. T. Thole et al. “X-ray circular dichroism as a probe of orbital magnetization”. In: *Phys. Rev. Lett.* 68 (1992), pp. 1943–1946. DOI: https://doi.org/10.1103/PhysRevLett.68.1943.

[88] P. Carra et al. “X-ray circular dichroism and local magnetic fields”. In: *Phys. Rev. Lett.* 70 (1993), pp. 694–697. DOI: https://doi.org/10.1103/PhysRevLett.70.694.

[89] K. von Bergmann et al. “Observation of a Complex Nanoscale Magnetic Structure in a Hexagonal Fe Monolayer”. In: *Phys. Rev. Lett.* 96 (2006), p. 167203. DOI: https://doi.org/10.1103/PhysRevLett.96.167203.

[90] Kirsten von Bergmann et al. “Complex magnetism of the Fe monolayer on Ir(111)”. In: *New J. Phys.* 9 (2007), p. 396. DOI: https://doi.org/10.1088/1367-2630/9/10/396.

[91] Kirsten von Bergmann et al. “Influence of the Local Atom Configuration on a Hexagonal Skyrmion Lattice”. In: *Nano Lett.* 15 (2015), pp. 3280–3285. DOI: https://doi.org/10.1021/acs.nanolett.5b00506.

[92] J. Grenz et al. “Probing the nano-skyrmion lattice on Fe/Ir(111) with magnetic exchange force microscopy”. In: *Phys. Rev. Lett.* 119 (2017), p. 047205. DOI: https://doi.org/10.1103/PhysRevLett.119.047205.

[93] Stefan Schumacher et al. "The Backside of Graphene: Manipulating Adsorption by Intercalation". In: *Nano Letters* 13.11 (2013), pp. 5013–5019. DOI: `https://doi.org/10.1021/nl402797j`. eprint: `https://doi.org/10.1021/nl402797j`. URL: `https://doi.org/10.1021/nl402797j`.

[94] Stefan Schumacher et al. "Europium underneath graphene on Ir(111): Intercalation mechanism, magnetism, and band structure". In: *Phys. Rev. B* 90 (23 2014), p. 235437. DOI: `https://doi.org/10.1103/PhysRevB.90.235437`.

[95] D. R. Hartree. "The Wave Mechanics of an Atom with a Non-Coulomb Central Field. Part I. Theory and Methods". In: *Mathematical Proceedings of the Cambridge Philosophical Society* 24.1 (1928), pp. 89–110. DOI: `https://doi.org/10.1017/S0305004100011919`.

[96] V. Fock. "Näherungsmethode zur Lösung des quantenmechanischen Mehrkörperproblems". In: *Zeitschrift für Physik* 61 (1930), pp. 126–148. DOI: `https://doi.org/10.1007/BF01340294`.

[97] L. H. Thomas. "The calculation of atomic fields". In: *Mathematical Proceedings of the Cambridge Philosophical Society* 23.5 (1927), pp. 542–548. DOI: `https://doi.org/10.1017/S0305004100011683`.

[98] Rend. Accad. Naz. Lincei E. Fermi. "Statistical method to determine some properties of atoms". In: 6 (1927), pp. 602–607.

[99] P. Hohenberg and W. Kohn. "Inhomogeneous Electron Gas". In: *Phys. Rev.* 136 (3B 1964), B864–B871. DOI: `https://doi.org/10.1103/PhysRev.136.B864`.

[100] W. Kohn and L. J. Sham. "Self-Consistent Equations Including Exchange and Correlation Effects". In: *Phys. Rev.* 140 (4A 1965), A1133–A1138. DOI: `https://doi.org/10.1103/PhysRev.140.A1133`.

[101] Robert van Leeuwen. "Density functional approach to the many-body problem: key concepts and exact functionals". In: *Advances in Quantum Chemistry* 43 (2003), pp. 24–94. DOI: `https://doi.org/10.1016/S0065-3276(03)43002-5`.

[102] D. M. Ceperley and B. J. Alder. "Ground State of the Electron Gas by a Stochastic Method". In: *Phys. Rev. Lett.* 45 (7 1980), pp. 566–569. DOI: `https://doi.org/10.1103/PhysRevLett.45.566`.

[103] Christopher J. Cramer and Donald G. Truhlar. "Density functional theory for transition metals and transition metal chemistry". In: *Phys. Chem. Chem. Phys.* 11 (46 2009), pp. 10757–10816. DOI: `https://doi.org/10.1039/B907148B`.

[104] N. Marzari, A. Ferretti, and C. Wolverton. "Electronic-structure methods for materials design". In: *Nature Materials* 20 (6 2021), pp. 736–749. DOI: `https://doi.org/10.1038/s41563-021-01013-3`.

[105] A comprehensive list of common electronic structure codes can be found e.g. in L. M. Ghiringhelli, C. Carbogno, S. Levchenko, F. Mohamed, G. Huhs, M. Lüders, M. Oliveira, and M. Scheffler, NPJ Comput. Materials 3, 46 (2017); or in L. Talirz, L. Ghiringhelli, and B. Smit, arXiv:2108.12350v1 (2021).

[106] Richard M. Martin. *Electronic structure basic theory and practical methods.* Cambridge: Cambridge University Press, 2020.

[107] Paolo Giannozzi et al. "QUANTUM ESPRESSO: a modular and open-source software project for quantum simulations of materials". In: *J. Phys.: Condens. Matter* 21.39 (2009), p. 395502. DOI: `https://doi.org/10.1088/0953-8984/21/39/395502`.

[108] P Giannozzi et al. "Advanced capabilities for materials modelling with Quantum ESPRESSO". In: *J. Phys.: Condens. Matter* 29.46 (2017), p. 465901. DOI: `https://doi.org/10.1088/1361-648x/aa8f79`.

[109] Wei Ku, Tom Berlijn, and Chi-Cheng Lee. "Unfolding First-Principles Band Structures". In: *Phys. Rev. Lett.* 104 (21 2010), p. 216401. DOI: `https://doi.org/10.1103/PhysRevLett.104.216401`.

[110] Voicu Popescu and Alex Zunger. "Extracting E versus k effective band structure from supercell calculations on alloys and impurities". In: *Phys. Rev. B* 85 (8 2012), p. 085201. DOI: `https://doi.org/10.1103/PhysRevB.85.085201`.

[111] Paulo V. C. Medeiros et al. "Unfolding spinor wave functions and expectation values of general operators: Introducing the unfolding-density operator". In: *Phys. Rev. B* 91 (4 2015), p. 041116. DOI: `https://doi.org/10.1103/PhysRevB.91.041116`.

[112] Sara G Mayo, Felix Yndurain, and Jose M Soler. "Band unfolding made simple". In: *Journal of Physics: Condensed Matter* 32.20 (2020), p. 205902. DOI: `https://doi.org/10.1088/1361-648x/ab6e8e`.

[113] P. Bonfà. `https://bitbucket.org/bonfus/unfold-x`.

[114] U von Barth and L Hedin. "A local exchange-correlation potential for the spin polarized case. i". In: *Journal of Physics C: Solid State Physics* 5.13 (1972), pp. 1629–1642. DOI: `https://doi.org/10.1088/0022-3719/5/13/012`.

[115] M.M. Pant and A.K. Rajagopal. "Theory of inhomogeneous magnetic electron gas". In: *Solid State Communications* 10.12 (1972), pp. 1157–1160. ISSN: 0038-1098. DOI: `https://doi.org/10.1016/0038-1098(72)90934-9`.

[116] Burak Himmetoglu et al. "Hubbard-corrected DFT energy functionals: The LDA+U description of correlated systems". In: *International Journal of Quantum Chemistry* 114.1 (2014), pp. 14–49. DOI: `https://doi.org/10.1002/qua.24521`.

[117] Matteo Cococcioni and Stefano de Gironcoli. “Linear response approach to the calculation of the effective interaction parameters in the LDA + U method”. In: *Phys. Rev. B* 71 (3 2005), p. 035105. DOI: `https://doi.org/10.1103/PhysRevB.71.035105`.

[118] Iurii Timrov, Nicola Marzari, and Matteo Cococcioni. “Hubbard parameters from density-functional perturbation theory”. In: *Phys. Rev. B* 98 (8 2018), p. 085127. DOI: `https://doi.org/10.1103/PhysRevB.98.085127`.

[119] Jan Hermann, Robert A. DiStasio, and Alexandre Tkatchenko. “First-Principles Models for van der Waals Interactions in Molecules and Materials: Concepts, Theory, and Applications”. In: *Chem. Soc. Rev.* 117 (6 2017), pp. 4714–4758. DOI: `https://doi.org/10.1021/acs.chemrev.6b00446`.

[120] Martin Stöhr, Troy Van Voorhis, and Alexandre Tkatchenko. “Theory and practice of modeling van der Waals interactions in electronic-structure calculations”. In: *Chem. Soc. Rev.* 48 (15 2019), pp. 4118–4154. DOI: `https://doi.org/10.1039/C9CS00060G`.

[121] Stefan Grimme et al. “A consistent and accurate ab initio parametrization of density functional dispersion correction (DFT-D) for the 94 elements H-Pu”. In: *J. Chem. Phys.* 132.15 (2010), p. 154104. DOI: `https://doi.org/10.1063/1.3382344`.

[122] Murray Gell-Mann and Francis Low. “Bound States in Quantum Field Theory”. In: *Phys. Rev.* 84 (2 1951), pp. 350–354. DOI: `https://doi.org/10.1103/PhysRev.84.350`.

[123] B. A. Lippmann and Julian Schwinger. “Variational Principles for Scattering Processes. I”. In: *Phys. Rev.* 79 (3 1950), pp. 469–480. DOI: `https://doi.org/10.1103/PhysRev.79.469`.

[124] G. C. Wick. “The Evaluation of the Collision Matrix”. In: *Phys. Rev.* 80 (2 1950), pp. 268–272. DOI: `https://doi.org/10.1103/PhysRev.80.268`.

[125] So Hirata et al. “One-particle many-body Green’s function theory: Algebraic recursive definitions, linked-diagram theorem, irreducible-diagram theorem, and general-order algorithms”. In: *The Journal of Chemical Physics* 147.4 (2017), p. 044108. DOI: `https://doi.org/10.1063/1.4994837`.

[126] Richard D. Mattuck. *A guide to Feynman diagrams in the many-body problem.* 2nd ed. Dover books on physics and chemistry. Dover Publications, 1992. ISBN: 9780486670478,0486670473.

[127] Alexander L. Fetter and John Dirk Walecka. *Quantum theory of many-particle systems.* McGraw-Hill, New York, 1971.

[128] Richard M. Martin, Lucia Reining, and David M. Ceperley. *Interacting Electrons*. Cambridge: Cambridge University Press, 2016.

[129] V. M. Galitskii and A. B. Migdal. “Application of quantum field theory methods to the many body problem”. In: *Soviet Physics JETP* 34 (7).1 (1958), pp. 4118–4154. URL: `https://www.osti.gov/biblio/4348538`.

[130] Lars Hedin. “New Method for Calculating the One-Particle Green’s Function with Application to the Electron-Gas Problem”. In: *Phys. Rev.* 139 (3A 1965), A796–A823. DOI: `https://doi.org/10.1103/PhysRev.139.A796`.

[131] Giovanni Onida, Lucia Reining, and Angel Rubio. “Electronic excitations: density-functional versus many-body Green’s-function approaches”. In: *Rev. Mod. Phys.* 74.2 (2002), p. 601. DOI: `https://doi.org/10.1103/RevModPhys.74.601`.

[132] F. Aryasetiawan and O. Gunnarsson. “The GW method”. In: *Rep. Prog. Phys.* 61 (1998), p. 237. DOI: `https://doi.org/10.1088/0034-4885/61/3/002`.

[133] Lucia Reining. “The GW approximation: content, successes and limitations”. In: *WIREs Computational Molecular Science* 8.3 (2018), e1344. DOI: `https://doi.org/10.1002/wcms.1344`.

[134] Dorothea Golze, Marc Dvorak, and Patrick Rinke. “The GW Compendium: A Practical Guide to Theoretical Photoemission Spectroscopy”. In: *Front. Chem.* 7 (2019), p. 377. DOI: `https://doi.org/10.3389/fchem.2019.00377`.

[135] Lars Hedin, John Michiels, and John Inglesfield. “Transition from the adiabatic to the sudden limit in core-electron photoemission”. In: *Phys. Rev. B* 58 (23 1998), pp. 15565–15582. DOI: `https://doi.org/10.1103/PhysRevB.58.15565`.

[136] Qimin Yan et al. “Band parameters and strain effects in ZnO and group-III nitrides”. In: *Semiconductor Science and Technology* 26.1 (2010), p. 014037. DOI: `https://doi.org/10.1088/0268-1242/26/1/014037`.

[137] M Dauth et al. “Angle resolved photoemission from organic semiconductors: orbital imaging beyond the molecular orbital interpretation”. In: *New J. Phys.* 16.10 (2014), p. 103005. DOI: `https://doi.org/10.1088/1367-2630/16/10/103005`.

[138] Jianqiang Sky Zhou et al. “Unraveling intrinsic correlation effects with angle-resolved photoemission spectroscopy”. In: *Proc. Nat. Ac. Sci.* 117.46 (2020), pp. 28596–28602. DOI: `https://doi.org/10.1073/pnas.2012625117`.

[139] F. Bechstedt et al. “Dynamical screening and quasiparticle spectral functions for nonmetals”. In: *Phys. Rev. B* 49 (11 1994), pp. 7357–7362. DOI: `https://doi.org/10.1103/PhysRevB.49.7357`.

[140] Ulf von Barth and Bengt Holm. "Self-consistent GW_0 results for the electron gas: Fixed screened potential W_0 within the random-phase approximation". In: *Phys. Rev. B* 54 (12 1996), pp. 8411–8419. DOI: https://doi.org/10.1103/PhysRevB.54.8411.

[141] Matteo Guzzo et al. "Valence Electron Photoemission Spectrum of Semiconductors: Ab Initio Description of Multiple Satellites". In: *Phys. Rev. Lett.* 107 (16 2011), p. 166401. DOI: https://doi.org/10.1103/PhysRevLett.107.166401.

[142] Fabio Caruso et al. "Electron-plasmon and electron-phonon satellites in the angle-resolved photoelectron spectra of n-doped anatase TiO_2". In: *Phys. Rev. B* 97 (16 2018), p. 165113. DOI: https://doi.org/10.1103/PhysRevB.97.165113.

[143] Andrea Marini et al. "Quasiparticle band-structure effects on the d hole lifetimes of copper within the GW approximation". In: *Phys. Rev. B* 66 (16 2002), p. 161104. DOI: https://doi.org/10.1103/PhysRevB.66.161104.

[144] Maurizia Palummo, Marco Bernardi, and Jeffrey C. Grossman. "Exciton Radiative Lifetimes in Two-Dimensional Transition Metal Dichalcogenides". In: *Nano Letters* 15.5 (2015), pp. 2794–2800. DOI: https://doi.org/10.1021/nl503799t.

[145] Stefan Albrecht et al. "Ab Initio Calculation of Excitonic Effects in the Optical Spectra of Semiconductors". In: *Phys. Rev. Lett.* 80 (20 1998), pp. 4510–4513. DOI: https://doi.org/10.1103/PhysRevLett.80.4510.

[146] X. Blase, C. Attaccalite, and V. Olevano. "First-principles GW calculations for fullerenes, porphyrins, phtalocyanine, and other molecules of interest for organic photovoltaic applications". In: *Phys. Rev. B* 83 (11 2011), p. 115103. DOI: https://doi.org/10.1103/PhysRevB.83.115103.

[147] Xinguo Ren et al. "Beyond the GW approximation: A second-order screened exchange correction". In: *Phys. Rev. B* 92 (8 2015), p. 081104. DOI: https://doi.org/10.1103/PhysRevB.92.081104.

[148] Fabien Bruneval et al. "molgw 1: Many-body perturbation theory software for atoms, molecules, and clusters". In: *Comput. Phys. Commun.* 208 (2016), pp. 149–161. ISSN: 0010-4655. DOI: https://doi.org/10.1016/j.cpc.2016.06.019.

[149] Jan Wilhelm et al. "Toward GW Calculations on Thousands of Atoms". In: *J. Phys. Chem. Lett.* 9.2 (2018), pp. 306–312. DOI: 10.1021/acs.jpclett.7b02740.

[150] M. Shishkin and G. Kresse. "Implementation and performance of the frequency-dependent GW method within the PAW framework". In: *Phys. Rev. B* 74 (3 2006), p. 035101. DOI: https://doi.org/10.1103/PhysRevB.74.035101.

[151] X. Gonze et al. “ABINIT: First-principles approach to material and nanosystem properties”. In: *Comput. Phys. Commun.* 180.12 (2009), pp. 2582–2615. DOI: `https://doi.org/10.1016/j.cpc.2009.07.007`.

[152] Jack Deslippe et al. “BerkeleyGW: A massively parallel computer package for the calculation of the quasiparticle and optical properties of materials and nanostructures”. In: *Comput. Phys. Commun.* 183.6 (2012), pp. 1269–1289. ISSN: 0010-4655. DOI: `https://doi.org/10.1016/j.cpc.2011.12.006`.

[153] Tonatiuh Rangel et al. “Reproducibility in G_0W_0 calculations for solids”. In: *Comput. Phys. Commun.* 255 (2020), p. 107242. DOI: `https://doi.org/10.1016/j.cpc.2020.107242`.

[154] M. van Schilfgaarde, Takao Kotani, and S. Faleev. “Quasiparticle Self-Consistent GW Theory”. In: *Phys. Rev. Lett.* 96.22 (2006), p. 226402. DOI: `https://doi.org/10.1103/PhysRevLett.96.226402`.

[155] Takao Kotani, Mark van Schilfgaarde, and Sergey V. Faleev. “Quasiparticle self-consistent *GW* method: A basis for the independent-particle approximation”. In: *Phys. Rev. B* 76 (16 2007), p. 165106. DOI: `https://doi.org/10.1103/PhysRevB.76.165106`.

[156] Christoph Friedrich, Stefan Blügel, and Arno Schindlmayr. “Efficient implementation of the *GW* approximation within the all-electron FLAPW method”. In: *Phys. Rev. B* 81 (12 2010), p. 125102. DOI: `https://doi.org/10.1103/PhysRevB.81.125102`.

[157] Hong Jiang and Peter Blaha. “*GW* with linearized augmented plane waves extended by high-energy local orbitals”. In: *Phys. Rev. B* 93 (11 2016), p. 115203. DOI: `https://doi.org/10.1103/PhysRevB.93.115203`.

[158] Michiel J. van Setten et al. “GW100: Benchmarking G0W0 for Molecular Systems”. In: *J. Chem. Theory Comput.* 11.12 (2015), pp. 5665–5687. DOI: `https://doi.org/10.1021/acs.jctc.5b00453`.

[159] Mark S. Hybertsen and Steven G. Louie. “Electron correlation in semiconductors and insulators: Band gaps and quasiparticle energies”. In: *Phys. Rev. B* 34 (1986), p. 5390. DOI: `https://doi.org/10.1103/PhysRevB.34.5390`.

[160] X. Blase et al. “Quasiparticle band structure of bulk hexagonal boron nitride and related systems”. In: *Phys. Rev. B* 51 (11 1995), pp. 6868–6875. DOI: `https://doi.org/10.1103/PhysRevB.51.6868`.

[161] Andrea Marini, Giovanni Onida, and Rodolfo Del Sole. “Quasiparticle Electronic Structure of Copper in the GW Approximation”. In: *Phys. Rev. Lett.* 88.1 (2002), p. 016403. DOI: `https://doi.org/10.1103/physrevlett.88.016403`.

[162] Michael Rohlfing et al. “Structural and Optical Properties of the Ge(111)-(2×1) Surface”. In: *Phys. Rev. Lett.* 85 (25 2000), pp. 5440–5443. DOI: `https://doi.org/10.1103/PhysRevLett.85.5440`.

[163] P. García-González and R.W. Godby. “GW self-energy calculations for surfaces and interfaces”. In: *Comput. Phys. Commun.* 137.1 (2001), pp. 108–122. ISSN: 0010-4655. DOI: `https://doi.org/10.1016/S0010-4655(01)00174-6`.

[164] R. Shaltaf et al. “Band Offsets at the Si/SiO$_2$ Interface from Many-Body Perturbation Theory”. In: *Phys. Rev. Lett.* 100 (18 2008), p. 186401. DOI: `https://doi.org/10.1103/PhysRevLett.100.186401`.

[165] Daniele Varsano et al. “Role of Quantum-Confinement in Anatase Nanosheets”. In: *The Journal of Physical Chemistry Letters* 8.16 (2017), pp. 3867–3873. DOI: `https://doi.org/10.1021/acs.jpclett.7b01717`.

[166] Diana Y. Qiu, Felipe H. da Jornada, and Steven G. Louie. “Optical Spectrum of MoS$_2$: Many-Body Effects and Diversity of Exciton States”. In: *Phys. Rev. Lett.* 111 (21 2013), p. 216805. DOI: `https://doi.org/10.1103/PhysRevLett.111.216805`.

[167] Falco Hüser, Thomas Olsen, and Kristian S. Thygesen. “Quasiparticle GW calculations for solids, molecules, and two-dimensional materials”. In: *Phys. Rev. B* 87 (23 2013), p. 235132. DOI: `https://doi.org/10.1103/PhysRevB.87.235132`.

[168] Kristian Sommer Thygesen. “Calculating excitons, plasmons, and quasiparticles in 2D materials and van der Waals heterostructures”. In: *2D Materials* 4.2 (2017), p. 022004. DOI: `https://doi.org/10.1088/2053-1583/aa6432`.

[169] Antimo Marrazzo et al. “Prediction of a Large-Gap and Switchable Kane-Mele Quantum Spin Hall Insulator”. In: *Phys. Rev. Lett.* 120 (11 2018), p. 117701. DOI: `https://doi.org/10.1103/PhysRevLett.120.117701`.

[170] Pablo Aguado-Puente, Stephen Fahy, and Myrta Grüning. “*GW* study of pressure-induced topological insulator transition in group-IV tellurides”. In: *Phys. Rev. Research* 2 (4 2020), p. 043105. DOI: `https://doi.org/10.1103/PhysRevResearch.2.043105`.

[171] Young-Woo Son, Marvin L. Cohen, and Steven G. Louie. “Half-metallic graphene nanoribbons”. In: *Nature* 444.7117 (2006), pp. 347–349. DOI: `https://doi.org/10.1038/nature05180`.

[172] Deborah Prezzi et al. “Quantum dot states and optical excitations of edge-modulated graphene nanoribbons”. In: *Phys. Rev. B* 84 (4 2011), p. 041401. DOI: `https://doi.org/10.1103/PhysRevB.84.041401`.

[173] Andrea Ferretti et al. "Ab initio complex band structure of conjugated polymers: Effects of hydrid density functional theory and GW schemes". In: *Phys. Rev. B* 85 (23 2012), p. 235105. DOI: `https://doi.org/10.1103/PhysRevB.85.235105`.

[174] Daniele Varsano et al. "Carbon nanotubes as excitonic insulators". In: *Nature Commun.* 8.1 (2017), p. 1461. DOI: `https://doi.org/10.1038/s41467-017-01660-8`.

[175] Daniele Varsano, Stefano Caprasecca, and Emanuele Coccia. "Theoretical description of protein field effects on electronic excitations of biological chromophores". In: *Journal of Physics: Condensed Matter* 29.1 (2016), p. 013002. DOI: `https://doi.org/10.1088/0953-8984/29/1/013002`.

[176] P. Umari, Geoffrey Stenuit, and Stefano Baroni. "GW quasiparticle spectra from occupied states only". In: *Phys. Rev. B* 81 (11 2010), p. 115104. DOI: `https://doi.org/10.1103/PhysRevB.81.115104`.

[177] Feliciano Giustino, Marvin L Cohen, and Steven G Louie. "GW method with the self-consistent Sternheimer equation". In: *Phys. Rev. B* 81.11 (2010), p. 115105. DOI: `https://doi.org/10.1103/PhysRevB.81.115105`.

[178] Marco Govoni and Giulia Galli. "Large Scale GW Calculations". In: *J. Chem. Theory Comput.* 11.6 (2015), pp. 2680–2696. DOI: `https://doi.org/10.1021/ct500958p`.

[179] S. B. Zhang et al. "Evaluation of quasiparticle energies for semiconductors without inversion symmetry". In: *Phys. Rev. B* 40 (5 1989), pp. 3162–3168. DOI: `https://doi.org/10.1103/PhysRevB.40.3162`.

[180] R. W. Godby and R. J. Needs. "Metal-insulator transition in Kohn-Sham theory and quasiparticle theory". In: *Phys. Rev. Lett.* 62 (1989), p. 1169. DOI: `https://doi.org/10.1103/PhysRevLett.62.1169`.

[181] Wolfgang von der Linden and Peter Horsch. "Precise quasiparticle energies and Hartree-Fock bands of semiconductors and insulators". In: *Phys. Rev. B* 37 (14 1988), pp. 8351–8362. DOI: `https://doi.org/10.1103/PhysRevB.37.8351`.

[182] G. E. Engel and Behnam Farid. "Generalized plasmon-pole model and plasmon band structures of crystals". In: *Phys. Rev. B* 47.23 (1993), p. 15931. DOI: `https://doi.org/10.1103/PhysRevB.47.15931`.

[183] Paul Larson, Marc Dvorak, and Zhigang Wu. "Role of the plasmon-pole model in the GW approximation". In: *Phys. Rev. B* 88 (2013), p. 125205. DOI: `http://dx.doi.org/10.1103/PhysRevB.88.125205`.

[184] G. Lehmann and M. Taut. “On the Numerical Calculation of the Density of States and Related Properties”. In: *Phys. Status Solidi (b)* 54.2 (1972), pp. 469–477. DOI: `https://doi.org/10.1002/pssb.2220540211`.

[185] Keun-Ho Lee and K. J. Chang. “First-principles study of the optical properties and the dielectric response of Al”. In: *Phys. Rev. B* 49 (4 1994), pp. 2362–2367. DOI: `https://doi.org/10.1103/PhysRevB.49.2362`.

[186] F. Aryasetiawan in. “Strong Coulomb Correlations in Electronic Structure Calculations”. In: 1st ed. `https://doi.org/10.1201/9781482296877`. London: CRC Press., 2000, p. 96. ISBN: 9780429081613. DOI: `https://doi.org/10.1201/9781482296877`.

[187] Fang Liu et al. “Numerical integration for ab initio many-electron self energy calculations within the GW approximation”. In: *J. Comput. Phys.* 286 (2015), pp. 1–13. DOI: `https://doi.org/10.1016/j.jcp.2015.01.023`.

[188] Takashi Miyake and Ferdi Aryasetiawan. “Efficient algorithm for calculating noninteracting frequency-dependent linear response functions”. In: *Phys. Rev. B* 61 (11 2000), pp. 7172–7175. DOI: `https://doi.org/10.1103/PhysRevB.61.7172`.

[189] H. N. Rojas, R. W. Godby, and R. J. Needs. “Space-Time Method for Ab Initio Calculations of Self-Energies and Dielectric Response Functions of Solids”. In: *Phys. Rev. Lett.* 74 (1995), p. 1827. DOI: `https://doi.org/10.1103/PhysRevLett.74.1827`.

[190] Andrey Kutepov et al. “Electronic structure of Pu and Am metals by self-consistent relativistic *GW* method”. In: *Phys. Rev. B* 85 (15 2012), p. 155129. DOI: `https://doi.org/10.1103/PhysRevB.85.155129`.

[191] Peitao Liu et al. “Cubic scaling GW: Towards fast quasiparticle calculations”. In: *Phys. Rev. B* 94 (2016), p. 165109. DOI: `https://doi.org/10.1103/PhysRevB.94.165109`.

[192] R. W. Godby, M. Schlüter, and L. J. Sham. “Self-energy operators and exchange-correlation potentials in semiconductors”. In: *Phys. Rev. B* 37 (17 1988), pp. 10159–10175. DOI: `https://doi.org/10.1103/PhysRevB.37.10159`.

[193] A. Oschlies, R. W. Godby, and R. J. Needs. “GW self-energy calculations of carrier-induced band-gap narrowing in n-type silicon”. In: *Phys. Rev.B* 51.3 (1995), p. 1527. DOI: `https://doi.org/10.1103/PhysRevB.51.1527`.

[194] Christoph Friedrich. “Tetrahedron integration method for strongly varying functions: Application to the *GT* self-energy”. In: *Phys. Rev. B* 100 (7 2019), p. 075142. DOI: `https://doi.org/10.1103/PhysRevB.100.075142`.

[195] Ivan Duchemin and Xavier Blase. “Robust Analytic-Continuation Approach to Many-Body GW Calculations”. In: *J. Chem. Theory Comput.* 16.3 (2020), pp. 1742–1756. DOI: https://doi.org/10.1021/acs.jctc.9b01235.

[196] Martin M. Riegera et al. “The GW space-time method for the self-energy of large systems”. In: *Comput. Phys. Commun.* 117.3 (1999), pp. 211–228. DOI: https://doi.org/10.1016/S0010-4655(98)00174-X.

[197] J. A. Soininen, J. J. Rehr, and Eric L. Shirley. “Electron self-energy calculation using a general multi-pole approximation”. In: *J. Phys.: Condens. Matter* 15 (2003), pp. 2573–2586. DOI: https://doi.org/10.1088/0953-8984/15/17/312.

[198] J. J. Kas et al. “Many-pole model of inelastic losses in X-ray absorption spectra”. In: *Phys. Rev. B* 76 (2007), p. 195116. DOI: http://dx.doi.org/10.1103/PhysRevB.76.195116.

[199] J. J. Kas et al. “Many-Pole Model of Inelastic Losses Applied to Calculations of XANES”. In: *J. Phys. Conf. Ser.* 190 (2009), p. 012009. DOI: 10.1088/1742-6596/190/1/012009.

[200] Sylvia J. Bintrim and Timothy C. Berkelbach. “Full-frequency GW without frequency”. In: *J. Chem. Phys.* 154 (2021), p. 041101. DOI: https://doi.org/10.1063/5.0035141.

[201] Tommaso Chiarotti, Nicola Marzari, and Andrea Ferretti. *A unified Green’s function approach for spectral and thermodynamic properties from algorithmic inversion of dynamical potentials.* https://arxiv.org/abs/2109.07972. 2021.

[202] L. Hedin, B. I. Lundqvist, and S. Lundqvist. “On the single-particle spectrum of an interacting electron gas”. In: *Int. J. Quantum Chem.* 1 (S1 1967), pp. 791–801. DOI: https://doi.org/10.1002/qua.560010688.

[203] A. W. Overhauser. “Simplified Theory of Electron Correlations in Metals”. In: *Phys. Rev. B* 3 (6 1971), pp. 1888–1898. DOI: https://doi.org/10.1103/PhysRevB.3.1888.

[204] Heinz Raether. *Excitation of Plasmons and Interband Transitions by Electrons.* 1st ed. Vol. 88. Springer Tracts in Modern Physics 88. Springer, Berlin, Heidelberg, 1980. ISBN: 978-3-540-09677-1. DOI: https://doi.org/10.1007/BFb0045951.

[205] L.K. Jordan and E.J. Scheibner. “Characteristic energy loss spectra of copper crystals with surfaces described by LEED”. In: *Surface Science* 10.3 (1968), pp. 373–391. ISSN: 0039-6028. DOI: https://doi.org/10.1016/0039-6028(68)90106-4.

[206] M. Giantomassi et al. "Electronic properties of interfaces and defects from many-body perturbation theory: Recent developments and applications". In: *Phys. Status Solidi (b)* 248.2 (2011), pp. 275–289. DOI: `https://doi.org/10.1002/pssb.201046094`.

[207] Andrea Marini. *PhD thesis: Optical and electronic properties of Copper and Silver: from Density Functional Theory to Many Body Effects.* Università degli Studi di Roma Tor Vergata (Italy). 2002.

[208] J. A. Soininen, J. J. Rehr, and Eric L. Shirley. "Multipole representation of the dielectric matrix". In: *Phys. Scripta* 2005 (2005), p. 243. DOI: `https://doi.org/10.1238/physica.topical.115a00243`.

[209] Sohrab Ismail-Beigi. "Correlation energy functional within the GW-RPA: Exact forms, approximate forms, and challenges". In: *Phys. Rev. B* 81 (2010), p. 195126. DOI: `http://dx.doi.org/10.1103/PhysRevB.81.195126`.

[210] H. J. Vidberg and J. W. Serene. "Solving the Eliashberg equations by means of N-point Padé approximants". In: *J. Low Temp. Phys.* 29 (1977), pp. 179–192. DOI: `https://doi.org/10.1007/BF00655090`.

[211] Keun-Ho Lee and K. J. Chang. "Analytic continuation of the dynamic response function using an N-point Padé approximant". In: *Phys. Rev. B* 54.12 (1996), R8285–R8288. DOI: `https://doi.org/10.1103/physrevb.54.r8285`.

[212] Young-Gu Jin and K. J. Chang. "Dynamic response function and energy-loss spectrum for Li using an N-point Padé approximant". In: *Phys. Rev. B* 59.23 (1999), R8285–R8288. DOI: `https://doi.org/10.1103/PhysRevB.59.14841`.

[213] Bernard Ycart. *A case of mathematical eponymy: the Vandermonde determinant.* `https://arxiv.org/abs/1204.4716`. 2012.

[214] N. Macon and A. Spitzbart. "Inverses of Vandermonde Matrices". In: *The American Mathematical Monthly* 65.2 (1958), pp. 95–100. DOI: `https://doi.org/10.2307/2308881`.

[215] Basil B. Crowley. *Generalized plasmon-pole approximation for the dielectric function of a multicomponent plasma.* `https://arxiv.org/arXiv:1508.05606`. 2015.

[216] M. Stankovski et al. "G^0 W^0 band gap of ZnO: Effects of plasmon-pole models". In: *Phys. Rev. B* 84 (2011), p. 241201. DOI: `http://dx.doi.org/10.1103/PhysRevB.84.241201`.

[217] A. Miglio et al. "Effects of plasmon pole models on the $G0^0W^0$ electronic structure of various oxides". In: *Eur. Phys. J. B* 85 (2012), p. 322. DOI: `http://dx.doi.org/10.1140/epjb/e2012-30121-4`.

[218] Andrey Kutepov, Sergey Y. Savrasov, and Gabriel Kotliar. "Ground-state properties of simple elements from GW calculations". In: *Phys. Rev. B* 80 (2009), p. 041103. DOI: https://doi.org/10.1103/PhysRevB.80.041103.

[219] Darshana Wickramaratne, Leigh Weston, and Chris G. Van de Walle. "Monolayer to Bulk Properties of Hexagonal Boron Nitride". In: *J. Phys. Chem. C* 122 (2018), pp. 25524–25529. DOI: https://doi.org/10.1021/acs.jpcc.8b09087.

[220] K. A. Mengle and E. Kioupakisa. "Impact of the stacking sequence on the bandgap and luminescence properties of bulk, bilayer, and monolayer hexagonal boron nitride". In: *APL Mater.* 7 (2 2019), p. 021106. DOI: https://doi.org/10.1063/1.5087836.

[221] Carlo A. Rozzi et al. "Exact Coulomb cutoff technique for supercell calculations". In: *Phys. Rev. B* 73 (20 2006), p. 205119. DOI: https://doi.org/10.1103/PhysRevB.73.205119.

[222] Johannes Lischner et al. "Effects of self-consistency and plasmon-pole models on GW calculations for closed-shell molecules". In: *Phys. Rev. B* 90 (11 2014), p. 115130. DOI: https://doi.org/10.1103/PhysRevB.90.11513.

[223] Marco Cazzaniga. "*GW* and beyond approaches to quasiparticle properties in metals". In: *Phys. Rev. B* 86 (3 2012), p. 035120. DOI: https://doi.org/10.1103/PhysRevB.86.035120.

[224] T. Miyake et al. "Effects of momentum-dependent self-energy in the electronic structure of correlated materials". In: *Phys. Rev. B* 87 (11 2013), p. 115110. DOI: https://doi.org/10.1103/PhysRevB.87.115110.

[225] M. J. van Setten, F. Weigend, and F. Evers. "The GW-Method for Quantum Chemistry Applications: Theory and Implementation". In: *Journal of Chemical Theory and Computation* 9.1 (2013), pp. 232–246. DOI: https://doi.org/10.1021/ct300648t.

[226] Volker Blum et al. "Ab initio molecular simulations with numeric atom-centered orbitals". In: *Computer Physics Communications* 180.11 (2009), pp. 2175–2196. DOI: https://doi.org/10.1016/j.cpc.2009.06.022.

[227] Glenn J. Martyna and Mark E. Tuckerman. "A reciprocal space based method for treating long range interactions in ab initio and force-field-based calculations in clusters". In: *J. CHem. Phys.* 110.6 (1999), pp. 2810–2821. DOI: 10.1063/1.477923.

[228] D. R. Hamann. "Optimized norm-conserving Vanderbilt pseudopotentials". In: *Phys. Rev. B* 88 (8 2013), p. 085117. DOI: https://doi.org/10.1103/PhysRevB.88.085117.

[229] J. A. Berger, Lucia Reining, and Francesco Sottile. “Ab initio calculations of electronic excitations: Collapsing spectral sums”. In: *Phys. Rev. B* 82 (4 2010), p. 041103. DOI: `https://doi.org/10.1103/PhysRevB.82.041103`.

[230] Fabien Bruneval and Xavier Gonze. “Accurate *GW* self-energies in a plane-wave basis using only a few empty states: Towards large systems”. In: *Phys. Rev. B* 78 (8 2008), p. 085125. DOI: `https://doi.org/10.1103/PhysRevB.78.085125`.

[231] P. O. Nilsson and C. G. Larsson. “Dynamical exchange and correlation effects in photoemission from metals”. In: *Phys. Rev. B* 27 (10 1983), pp. 6143–6151. DOI: `https://doi.org/10.1103/PhysRevB.27.6143`.

[232] Marco Cazzaniga et al. “Ab initio self-energy corrections in systems with metallic screening”. In: *Phys. Rev. B* 77 (3 2008), p. 035117. DOI: `https://doi.org/10.1103/PhysRevB.77.035117`.

[233] Marco Cazzaniga et al. “Ab initio intraband contributions to the optical properties of metals”. In: *Phys. Rev. B* 82 (3 2010), p. 035104. DOI: `https://doi.org/10.1103/PhysRevB.82.035104`.

[234] Krystyna Kolwas and Anastasiya Derkachova. “Impact of the Interband Transitions in Gold and Silver on the Dynamics of Propagating and Localized Surface Plasmons”. In: *Nanomaterials* 10 (7 2020), p. 1411. DOI: `https://doi.org/10.3390/nano10071411`.

[235] R. Courths and S. Hüfner. “Photoemission experiments on copper”. In: *Physics Reports* 112.2 (1984), pp. 53–171. DOI: `https://doi.org/10.1016/0370-1573(84)90167-4`.

[236] M. Vos et al. “Electronic structure of copper studied by electron momentum spectroscopy”. In: *Phys. Rev. B* 70 (20 2004), p. 205111. DOI: `https://doi.org/10.1103/PhysRevB.70.205111`.

[237] V. P. Zhukov, E. V. Chulkov, and P. M. Echenique. “Lifetimes of d holes in Cu and Au: Full-potential LMTO approach”. In: *Phys. Rev. B* 68 (4 2003), p. 045102. DOI: `https://doi.org/10.1103/PhysRevB.68.045102`.

[238] M. Springer and F. Aryasetiawan. “Frequency-dependent screened interaction in Ni within the random-phase approximation”. In: *Phys. Rev. B* 57 (8 1998), pp. 4364–4368. DOI: `https://doi.org/10.1103/PhysRevB.57.4364`.

[239] Giulia Avvisati et al. “Tuning the Magnetic Coupling of a Molecular Spin Interface via Electron Doping”. In: *Nano Lett.* 21.1 (2021), 666–672. DOI: `{https://doi.org/10.1021/acs.nanolett.0c04256}`.

[240] Yu Wang et al. “Precise Spin Manipulation of Single Molecule Positioning on Graphene by Coordination Chemistry”. In: *J. Phys. CHem. Lett.* 11.22 (2020), 9819–9827. DOI: {https://doi.org/10.1021/acs.jpclett.0c03026}.

[241] Emil Sierda et al. “Probing Weakly Hybridized Magnetic Molecules by Single-Atom Magnetometry”. In: *Nano Lett.* 19.12 (2019), pp. 9013–9018. DOI: https://doi.org/10.1021/acs.nanolett.9b04025.

[242] Giulia Avvisati et al. “Metal phthalocyanines interaction with Co mediated by a moire graphene superlattice”. In: *J. Chem. Phys.* 150.5 (2019). DOI: {https://doi.org/10.1063/1.5080533}.

[243] F. Vincent and M. Figlarz. “Quelques précisions sur les paramétres cristallins et l’intensité des raies debye-scherrer du cobalt cubique et du cobalt hexagonal”. In: *C. R. Hebd Séances Acad Sci.,* 264C (1967), p. 1270.

[244] W. Jauch et al. “Crystallographic symmetry and magnetic structure of CoO”. In: *Phys. Rev. B* 64 (5 2001), p. 052102. DOI: https://doi.org/10.1103/PhysRevB.64.052102.

[245] Monica Pozzo et al. “Thermal Expansion of Supported and Freestanding Graphene: Lattice Constant versus Interatomic Distance”. In: *Phys. Rev. Lett.* 106 (13 2011), p. 135501. DOI: https://doi.org/10.1103/PhysRevLett.106.135501.

[246] John W. Arblaster. “Crystallographic Properties of Iridium”. In: *Platinum Metals Rev* 54 (2010), p. 93. DOI: https://doi.org/10.1595/147106710X493124.

[247] John P. Perdew, Kieron Burke, and Matthias Ernzerhof. “Generalized Gradient Approximation Made Simple”. In: *Phys. Rev. Lett.* 77 (18 1996), pp. 3865–3868. DOI: https://doi.org/10.1103/PhysRevLett.77.3865.

[248] Wenxu Zhang et al. “Magnetic phase transition in CoO under high pressure: A challenge for LSDA+U”. In: *Phys. Rev. B* 79 (15 2009), p. 155123. DOI: https://doi.org/10.1103/PhysRevB.79.155123.

[249] P. A. Ignatiev et al. “Doping of cobalt oxide with transition metal impurities: Ab initio study”. In: *Phys. Rev. B* 81 (23 2010), p. 235123. DOI: https://doi.org/10.1103/PhysRevB.81.235123.

[250] Vladimir I. Anisimov, Jan Zaanen, and Ole K. Andersen. “Band theory and Mott insulators: Hubbard U instead of Stoner I”. In: *Phys. Rev. B* 44 (3 1991), pp. 943–954. DOI: https://doi.org/10.1103/PhysRevB.44.943.

[251] Fabien Tran et al. “Hybrid exchange-correlation energy functionals for strongly correlated electrons: Applications to transition-metal monoxides”. In: *Phys. Rev. B* 74 (15 2006), p. 155108. DOI: https://doi.org/10.1103/PhysRevB.74.155108.

[252] U. D. Wdowik and K. Parlinski. “Lattice dynamics of CoO from first principles”. In: *Phys. Rev. B* 75 (10 2007), p. 104306. DOI: https://doi.org/10.1103/PhysRevB.75.104306.

[253] Wolfram Research, Inc.
https://periodictable.com/Properties/A/LatticeConstants.html. 2014.

[254] John W. Arblaster. “Stability, structure, and electronic properties of chemisorbed oxygen and thin surface oxides on Ir(111)”. In: *Phys. Rev. B* 78 (2008), p. 045436. DOI: https://doi.org/10.1103/PhysRevB.78.045436.

[255] J. P. Perdew and A. Zunger. “Self-interaction correction to density-functional approximations for many-electron systems”. In: *Phys. Rev. B* 23.10 (1981), pp. 5048–5079. DOI: https://doi.org/10.1103/PhysRevB.23.5048.

[256] Stefan Grimme. “Semiempirical GGA-type density functional constructed with a long-range dispersion correction”. In: *J. Comput. Chem.* 27.15 (Nov. 2006), pp. 1787–1799. DOI: 10.1002/jcc.20495.

[257] Note that the DFT-D2 correction for van der Walls interactions has been reparametrized in these works.

[258] Yuriy Dedkov and Elena Voloshina. “Graphene growth and properties on metal substrates”. In: *J. Phys.: Condens. Matter* 27.30 (July 2015), p. 303002. DOI: 10.1088/0953-8984/27/30/303002.

[259] Note that comparing ARPES data with KS-DFT calculations absolute quantitative agreement in the position of the features cannot be expected.

[260] S. Heinze et al. “Spontaneous atomic-scale magnetic skyrmion lattice in two dimensions”. In: *Nat. Phys.* 7 (2011), pp. 713–718. DOI: https://doi.org/10.1038/NPHYS2045.

[261] Jens Brede et al. “Long-range magnetic coupling between nanoscale organic–metal hybrids mediated by a nanoskyrmion lattice”. In: *Nat. Nanotechnol.* 9.12 (2014), pp. 1018–1023. DOI: https://doi.org/10.1038/nnano.2014.235.

[262] Elena Voloshina, Beate Paulus, and Yuriy Dedkov. “Graphene Layer Morphology as an Indicator of the Metal Alloy Formation at the Interface”. In: *J. Phys. Chem. Lett.* 12 (2021), pp. 19–25. DOI: https://doi.org/10.1021/acs.jpclett.0c03271.

[263] R. H. Victora, L. M. Falicov, and Shoji Ishida. “Calculated surface electronic structure of ferromagnetic iron and the ferromagnetic ordered iron-cobalt alloy”. In: *Phys. Rev. B* 30 (7 1984), pp. 3896–3902. DOI: https://doi.org/10.1103/PhysRevB.30.3896.

[264] S. Pizzini et al. “Magnetic circular x-ray dichroism measurements of Fe-Co alloys and Fe/Co multilayers”. In: *Phys. Rev. B* 50 (1994), pp. 3779–3788. DOI: https://doi.org/10.1103/PhysRevB.50.3779.

[265] Sangkook Choi et al. “First-principles treatment of Mott insulators: linearized QSGW+DMFT approach”. In: *npj Quantum Materials* 1.1 (2016), p. 16001. DOI: https://doi.org/10.1038/npjquantmats.2016.1.

[266] Lorenzo Sponza et al. “Self-energies in itinerant magnets: A focus on Fe and Ni”. In: *Phys. Rev. B* 95 (4 2017), p. 041112. DOI: https://doi.org/10.1103/PhysRevB.95.041112.

[267] Filip A. Rasmussen et al. “Efficient many-body calculations for two-dimensional materials using exact limits for the screened potential: Band gaps of $\mathbf{MoS}_2$, *h*-BN, and phosphorene”. In: *Phys. Rev. B* 94 (15 2016), p. 155406. DOI: https://doi.org/10.1103/PhysRevB.94.155406.

[268] Kristian Sommer Thygesen. “Calculating excitons, plasmons, and quasiparticles in 2D materials and van der Waals heterostructures”. In: *2D Materials* 4.2 (2017), p. 022004. DOI: https://doi.org/10.1088/2053-1583/aa6432.

[269] Pierluigi Cudazzo, Ilya V. Tokatly, and Angel Rubio. “Dielectric screening in two-dimensional insulators: Implications for excitonic and impurity states in graphane”. In: *Phys. Rev. B* 84 (8 2011), p. 085406. DOI: https://doi.org/10.1103/PhysRevB.84.085406.

[270] Felipe H. da Jornada, Diana Y. Qiu, and Steven G. Louie. “Nonuniform sampling schemes of the Brillouin zone for many-electron perturbation-theory calculations in reduced dimensionality”. In: *Phys. Rev. B* 95 (3 2017), p. 035109. DOI: https://doi.org/10.1103/PhysRevB.95.035109.

[271] Weiyi Xia et al. “Combined subsampling and analytical integration for efficient large-scale GW calculations for 2D systems”. In: *npj Computational Materials* 6.1 (2020), p. 118. DOI: https://doi.org/10.1038/s41524-020-00385-5.

Related references

NANO LETTERS

Letter

Cite This: *Nano Lett.* 2018, 18, 2268−2273

pubs.acs.org/NanoLett

Ferromagnetic and Antiferromagnetic Coupling of Spin Molecular Interfaces with High Thermal Stability

Giulia Avvisati,[†] Claudia Cardoso,[‡] Daniele Varsano,[‡] Andrea Ferretti,[‡] Pierluigi Gargiani,[§] and Maria Grazia Betti*,[†]

[†] Dipartimento di Fisica, Università di Roma "La Sapienza", I-00185 Roma, Italy

[‡] Centro S3, CNR-Istituto Nanoscienze, I-41125 Modena, Italy

[§] ALBA Synchrotron Light Source, E-08290 Cerdanyola del Valles, Barcelona, Spain

Supporting Information

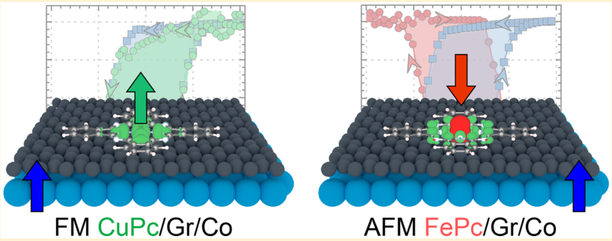

ABSTRACT: We report an advanced organic spin-interface architecture with magnetic remanence at room temperature, constituted by metal phthalocyanine molecules magnetically coupled with Co layer(s), mediated by graphene. Fe- and Cu-phthalocyanines assembled on graphene/Co have identical structural configurations, but FePc couples antiferromagnetically with Co up to room temperature, while CuPc couples ferromagnetically with weaker coupling and thermal stability, as deduced by element-selective X-ray magnetic circular dichroic signals. The robust antiferromagnetic coupling is stabilized by a superexchange interaction, driven by the out-of-plane molecular orbitals responsible of the magnetic ground state and electronically decoupled from the underlying metal via the graphene layer, as confirmed by ab initio theoretical predictions. These archetypal spin interfaces can be prototypes to demonstrate how antiferromagnetic and/or ferromagnetic coupling can be optimized by selecting the molecular orbital symmetry.

KEYWORDS: *Spin interface, superexchange interaction, X-ray magnetic circular dichroism, density functional theory*

Paramagnetic molecules become potential building blocks in spintronics when their magnetic moments are stabilized against thermal fluctuations, for example, by a controlled interaction with a magnetic substrate. Spin molecular interfaces with preserved magnetic activity and exhibiting magnetic remanence at room temperature (RT) can open the route to engineer highly spin-polarized, nanoscale current sources. The need to fully control the organic spin interface and the tuning of ferromagnetic (FM) or antiferromagnetic (AFM) coupling to achieve a stable conductance has motivated a vast experimental interest.[1−5]

In this work, we propose to optimize the thermal stability and the magnetic coupling of molecular systems, while preserving their electronic properties,[6,7] by exploiting interlayer exchange coupling within an advanced organic spin-interface architecture: arrays of metal phthalocyanines (MPc, M = Fe, Cu) arranged on Co layer(s) intercalated below graphene.[8−10] Herewith we demonstrate how the superexchange interaction can be mediated by the organic ligands and the graphene layer, preserving the magnetic state of the molecule and favoring a tunable FM or AFM coupling with Co layer(s), as deduced by X-ray magnetic circular dichroism (XMCD) measurements. These results are confirmed by state of the art theoretical predictions, unveiling the extreme sensitivity of the superexchange interaction to the symmetry of the orbitals responsible for the magnetic state.

Magnetic properties of molecular systems on metal surfaces can be readily modified by the molecular packing or by the orbital intermixing with the metallic states,[11] which lead to the suppression of their local magnetic moment.[4,12] Thanks to the electronic decoupling of the graphene layer, the symmetry of the molecular orbitals carrying the magnetic moments is preserved and can be selected to optimize and stabilize the magnetic configuration of the MPcs. A major challenge is to stabilize these spin interface prototypes against thermal fluctuations in order to achieve RT remanence. We prove that the superexchange mechanism can induce a sizable magnetization of FePc coupled with Co layers, mediated by graphene, with a residual coupling even at RT. On the other side, the hindered superexchange path, as found for CuPc coupled with Co, results in a ferromagnetic order with reduced thermal stability. Furthermore, the easy magnetization axis of a single layer of Co intercalated under graphene is out-of-plane and switches in-plane when more than 4−5 layers are intercalated.[13] Switching the Co magnetic moment by increasing the Co thickness amplifies the magnetic response of the FePc with aligned magnetic axis, unveiling high thermal

Received: November 15, 2017
Revised: February 26, 2018
Published: March 20, 2018

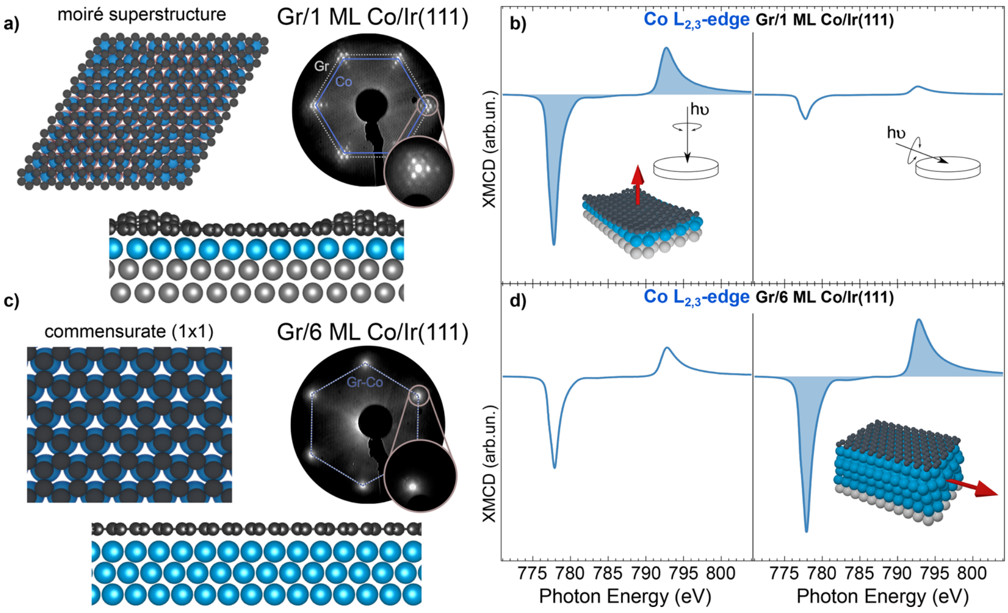

Figure 1. Moiré superstructure of Gr on Ir(111) upon intercalation of 1 ML Co (a) and flat and commensurate Gr/Ir upon 6 ML Co intercalation (c), as deduced by ab initio DFT calculation at the LDA level and confirmed by the LEED patterns. XMCD spectra of Co $L_{2,3}$ absorption edges for Gr/1 ML Co and Gr/6 ML Co acquired in remanance at RT in normal and grazing incidence geometries. Magnetic anisotropy switches from perpendicular (Gr/1 ML Co, panel b) to parallel (Gr/6 ML Co, panel d) to the surface plane.

stability and remanence at RT, while the coupling with magnetically unaligned CuPc molecules is frustrated.[14]

The magnetic (and structural) configuration of Co layer(s) intercalated under graphene can be tuned as a function of Co thickness.[13] The structural evolution of the Gr sheet upon intercalation from 1 to 6 ML of Co is consistent with what reported in refs 15 and 16, giving a picture confirmed by the theoretical predictions taking into account the complete moiré unit cell. When a single layer is intercalated, the Co atoms arrange pseudomorphically to the Ir(111) surface, without altering the periodicity and symmetry of the Gr moiré superstructure (Figure 1a) while its corrugation is enhanced. Further Co intercalation induces the relaxation of the lattice mismatch and the Co film recovers the bulk Co(0001) arrangement, almost commensurate with the Gr lattice, as sketched in Figure 1c. The 1 × 1 hexagonal pattern confirms that Gr is commensurate and flat on the Co film. Density functional theory (DFT) simulations, taking into account the complete moiré unit cell, fully reproduce these structural configurations. The geometry obtained for the IrCoGr 9 × 9/10 × 10 system shows, at the LDA level, a 1.4 Å corrugation for the graphene moiré superstructure with a minimum graphene-Co distance of 1.90 Å,[17] Figure 1a. Similar findings have also been reported in ref 15. At variance, the graphene−Co distance computed for the commensurate 1 × 1 interface is found to be 2.05 Å at the LDA level,[17] Figure 1c.

Turning to the magnetic properties, the XMCD spectra at the Co $L_{2,3}$ edge for a single Co layer and a Co film intercalated under the Gr sheet are reported in the right panels of Figure 1. The spectra at RT are obtained as the difference between the absorption edges acquired with left- and right-circularly polarized radiation, in remanence condition, that is, with no applied external field. The higher dichroic response with photon impinging at normal incidence (NI) unravels the out-of-plane magnetic anisotropy of the Co layer in the incommensurate configuration with a stretched Co−Co distance, Figure 1b, in agreement with refs 15 and 18. Conversely, the higher dichroic response for Co $L_{2,3}$ XMCD at grazing incidence (GI) for the thicker intercalated Co film, reveals a magnetic state with the Co bulk in-plane easy magnetization axis. The Gr/Co heterostructures, exhibiting a tunable easy magnetization axis direction, are ideal templates to test the magnetic coupling of paramagnetic flat-lying FePc and CuPc molecules.[10]

At the early deposition stages, MPcs adsorption on graphene can be driven by the corrugated moiré superstructure.[8,9,19] MPc molecules deposited on Gr/1 ML Co/Ir are trapped in the valley regions[9] driven by the lateral electric dipole, caused by the local contraction and expansion of the Gr lattice,[20] and hence order in a Kagome lattice.[8,19] The total energy landscape, as deduced by our DFT simulations is almost identical for FePc and CuPc, displaying similar distances with respect to the Gr layer (3.25 Å from LDA, 3.10 Å from PBE-D2) and similar flat configurations upon adsorption. Since the adsorption geometries for FePc and CuPc on Gr/Co/Ir are equivalent, the magnetic state can only be determined by the symmetry of the molecular orbitals involved in the magnetic coupling with the extended states of Co-intercalated graphene.[9,10]

In this respect, FePc and CuPc are paradigmatic to unveil the role of the symmetry of the active molecular orbitals in the magnetic coupling: FePc has a mostly in-plane (IP) intrinsic easy magnetization axis, while CuPc shows an out-of-plane (OOP) magnetic anisotropy.[21,22] The FePc molecule has a d^6 electronic ground state with $S = 1$ spin, due to the $b_{2g}^2\, e_g^3\, a_{1g}^1\, b_{1g}^0$ configuration with half-filled e_g ($d_{xz,yz}$) and a_{1g} (d_{z^2}) orbitals. On the other hand, CuPc molecules, with a d^9 ground state and $S = 1/2$, only have a half-filled b_{1g} ($d_{x^2-y^2}$) orbital with a strongly anisotropic magnetic state perpendicular to the molecular plane.[21]

In Figure 2, we report the XAS and XMCD spectra at the $L_{2,3}$ absorption edges of Fe and Cu, measured respectively at $T = 1.7$ and 2.0 K, for FePc and CuPc on Gr/1 ML Co (Figure

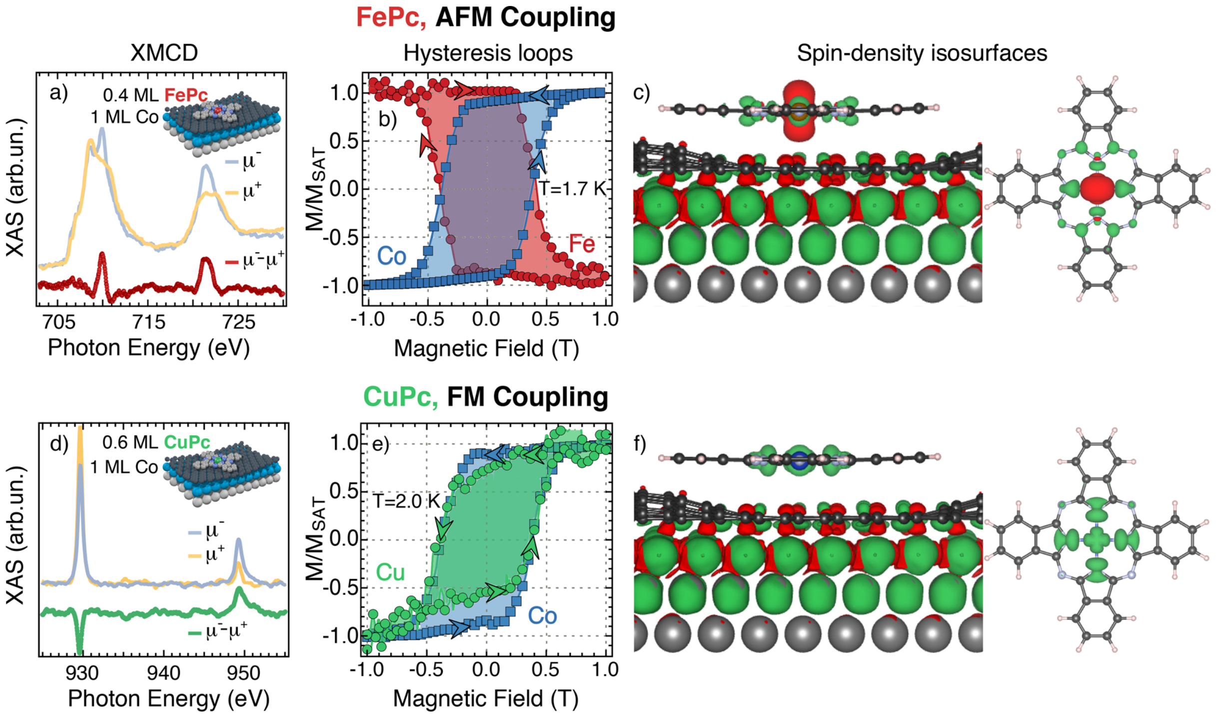

Figure 2. XMCD from Fe and Cu $L_{2,3}$ absorption edges (a,d), element-resolved hysteresis loops of FePc (b) and CuPc (e) on Gr/1 ML Co. The change in the sign of the XMCD (a,d) and of the field-dependent magnetization (b,e) indicates an AFM alignment for FePc/Gr/Co and a FM one for CuPc/Gr/Co. Spin-density isosurfaces plots for FePc and CuPc on Gr/Co/Ir (side and top view with hidden substrate), computed at the DFT-PBE+U level, U = 4 eV (c,f). The geometry optimization included PBE-D2 van der Waals corrections. Green (red) isosurfaces correspond to the up (down) spin density.

2a,d), having an OOP easy magnetization axis. FePc molecules couple antiferromagnetically with the intercalated Co layer, as revealed by the sign switching in the element-sensitive XMCD signal (Figure 2a,b) with respect to the bare Gr/OOP Co (Figure 1b). On the other hand, CuPc molecules couple ferromagnetically when deposited on Gr/1 ML Co (Figure 2d,e). All the XAS and XMCD spectra in presence (absence) of magnetic field are reported in the Supporting Information to clearly describe the role of FePc and CuPc molecular orbitals in the magnetic state. It is worth noting that the XAS and XMCD lineshapes are preserved, except for a slight change in the relative intensities of the spectral features, for the FePc and CuPc molecules upon adsorption on Gr/Co. Thus, the spin and orbital contribution to the magnetic moments, as deduced applying the sum rules to the XMCD signals[23,24] and confirmed by theoretical predictions, are comparable with what reported for the free-standing molecule and/or molecular films,[7,12,25] confirming the decoupling role of the graphene layer.

Magnetism generally emerges from short-ranged interactions between molecular units due to the localization of the atomic wave functions. To achieve a magnetic interaction over a large distance, a superexchange mechanism can be invoked, where the bridging over nonmagnetic organic ligands mediates higher-order virtual hopping processes. In metal phthalocyanines, the organic ligands can mediate the coupling between the central transition metal ions and a magnetic layer.[11,14,26,27] In our spin interface architecture a Fe−N−Gr−Co superexchange path can be driven by a weak hybridization between the π orbitals of the pyrrolic N atoms and the e_g ($d_{xz,yz}$) and a_{1g} (d_{z^2}) orbitals of the central Fe ion. In the CuPc molecule, the orbitals protruding out of the molecular plane are completely filled and the magnetic moment is mostly carried by a single planar orbital; therefore, the proposed superexchange interaction path is hindered and the interaction switches to FM.

The confirmation of the AFM and FM coupling found experimentally and the role of the molecular orbitals involved in the magnetic response are clarified by DFT calculations. In Figure 2c,f, we report the computed spin densities for FePc and CuPc on a Gr/1 ML Co/Ir at PBE+U level with the spin up (down) iso-surfaces represented in green (red). The Fe−N−Gr−Co superexchange path is determined by a spin imbalance located at the central ion and at the surrounding N and C atoms. The spin of the central ion is oriented opposite to the one of N and C and antiferromagnetically coupled with the underlying Co spin moment. In the case of CuPc, the spin imbalance is located at the central ion and on the surrounding N atoms and coupled ferromagnetically with the Co spin moment. Top views of the spin densities (panels c,f) better display the shape of the orbitals involved and the flips of the local magnetic moments. Quantitative data (atom-resolved magnetic moments, as given by Löwdin charge analysis) are provided in the Supporting Information.

A detailed analysis of Löwdin charges can also be used to further discriminate the symmetry of the molecular orbitals involved in the magnetic coupling. In the case of CuPc, upon adsorption the magnetic moment of the molecule is mostly carried by the half-filled $d_{x^2-y^2}$ orbital of the Cu ion, corresponding to the b_{1g} state of CuPc free molecule, highly hybridized with the pyrrolic N atoms of the macrocycle,[28] as evident in Figure 2f. The situation is slightly more complicated for FePc, where at least two or three Fe-d orbitals are involved. In particular, as shown in Table S3 in Supporting Information, the magnetic moment is carried by d_{z^2} and either one or both d_{xz} and d_{yz} (depending on the functional, see Supporting Information for the detailed discussion), corresponding to the a_{1g} and e_g orbitals of free-standing FePc. The above picture is very robust against the use of different exchange and correlation functionals (LDA, PBE, PBE+U, discussed in the Supporting Information) and is in excellent agreement with the experimental data, fully supporting the picture where the magnetic coupling of MPc with Gr/Co/Ir is mainly driven by a superexchange channel, selected by the symmetry of the involved molecular orbitals. Indeed, we herewith report on two superexchange paths, both actively mediated by the Gr sheet and the molecule organic backbone, inducing either an AFM (180° superexchange, FePc) or a FM (90° superexchange, CuPc) coupling at the spin interface. These mechanisms dominate the magnetic interaction, as deduced by the increase of the magnetic moment projected on the C and N atoms of the molecule macrocycle upon adsorption (see Table S2 in the Supporting Information). Nevertheless, a direct interaction between the Fe d_{z^2} state and the Gr π-orbitals, AFM coupled with the intercalated Co layer[15,18] and hence reinforcing the antiparallel spin alignment, cannot be excluded.

A further step forward in the optimization of this spin-interface is to enlighten the role of the relative orientation of MPc/Co easy magnetization axes on the stability of the magnetic coupling. FePc and CuPc molecules adsorb flat-lying on the commensurate Gr on the Co film with in-plane magnetization. XMCD spectra for FePc and CuPc, respectively on Gr/6 ML Co and Gr/8 ML Co, are reported together with the field-dependence of the normalized magnetization in Figure 3. While an AFM coupling is confirmed for FePc/Gr/Co when the easy magnetization axes are aligned (left panel), the CuPc molecules adsorbed on the flat graphene layer on Co has a negligilble XMCD signal at zero magnetic field (right panel). The magnetic coupling is more effective when the magnetization easy axis of the Gr-covered Co layer(s) and the one of the molecules are aligned, that is, when the FePc molecules are adsorbed on the thick Gr/Co film and the CuPc on the single Gr/Co layer, regardless on the origin of the magnetic interaction. More details on the field- and direction-dependence of the CuPc and FePc magnetic state are reported in the Supporting Information.

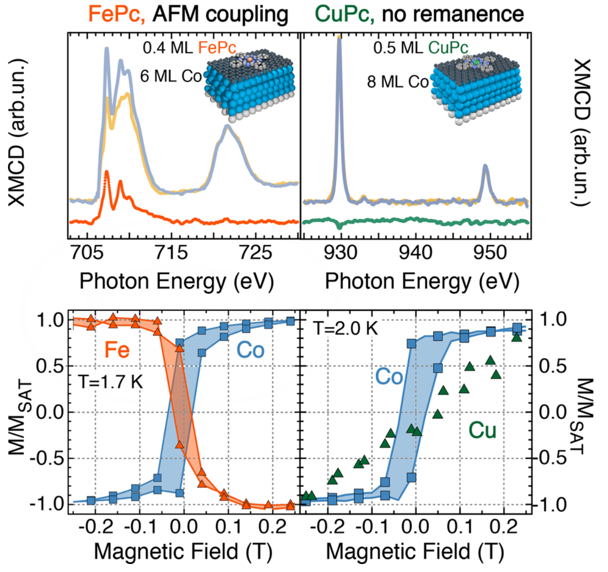

Figure 3. XMCD from Fe and Cu $L_{2,3}$ absorption edges for FePc (left) and CuPc (right) molecules deposited on Gr/IP Co in the upper panels. Hysteresis loops are presented in the lower panels, confirming that the coupling is AFM for FePc/Gr/6 ML Co, while the CuPc has no remanence.

A fine-tuning of these spin interface architectures requires to evaluate the robustness of the magnetic response against thermal fluctuations, thanks to temperature-dependent XMCD measurements (Figure 4). It is worth to point out that all measurements were acquired in absence of a magnetic field and over several hours, indicating a very long relaxation time and a stable magnetic configuration of the coupled MPc−Gr−Co systems.

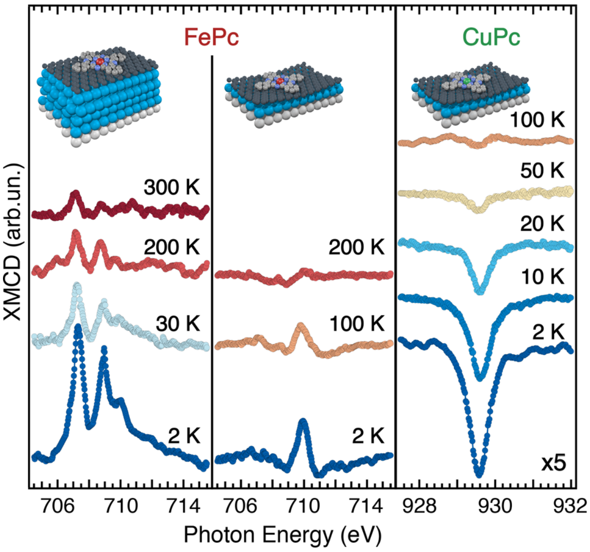

Figure 4. Thermal evolution of the XMCD signal for FePc/Gr on IP (left) and OOP (middle) Co, and CuPc/Gr on OOP Co (right).

Indeed, the superexchange path stabilizes the AFM coupling up to 200 K for FePc/Gr/OOP Co, while for FePc/Gr/IP Co a residual XMCD signal is detectable even at RT. The FePc magnetic state coupled to Gr/OOP Co and Gr/IP Co can be understood in terms of the relative orientation between the molecule and substrate easy magnetization axes, because an extra amount of energy is needed to turn the FePc magnetization, from its intrinsic IP direction, to adapt to the OOP Co easy magnetization axis. The magnetic-coupling for CuPc/Gr/OOP Co is much weaker, as reflected by the disappearance of any XMCD remanent signal above 50 K. These differences can be quantitatively evaluated by performing a Brillouin fit over the thermal evolution of the XMCD intensity, leading to a coupling energy of 2.8 ± 0.6 and 2.1 ± 0.5 meV for FePc on Gr/1 and 6 ML Co, respectively, while the less stable CuPc/Gr/1 ML Co system exhibits a much lower coupling energy of 0.6 ± 0.2 meV (for detailed discussion see the Supporting Information).

A direct magnetic coupling has been also detected for FePc molecules adsorbed on Gr grown on Ni(111), leading to a ferromagnetic alignment[29] while in-plane AFM coupling mediated by graphene was recently observed between a Ni thin-film and Co-porphyrin molecules up to 200 K.[27] Despite a comparable exchange energy, the magnetic stability against thermal fluctuations up to room temperature is here observed for the first time. In these peculiar spin interfaces the Gr layer plays a dual role: on the one hand it acts as a buffer layer, inhibiting the MPc-Co electronic interaction and preserving the magnetic properties of the adsorbed molecules, whereas on the other hand it actively contributes to the magnetic coupling, either by a direct coupling[29] or by opening an effective superexchange channel.[27]

In conclusion, these graphene-spaced spin molecular interfaces present either AFM or FM coupling driven by different superexchange paths, as supported by the ab initio theoretical calculations and the experimental XMCD results. Despite the almost identical structural configurations and a large distance between the Fe(Cu) metal centers and the magnetic Co substrate, the magnetic coupling is very robust against thermal fluctuations. In particular, the Fe−N−Gr−Co superexchange channel drives an AFM coupling, favored by the presence of out-plane molecular orbitals, mediated by the organic ligands and graphene. On the other side, in the Cu−N−Gr−Co channel the magnetic coupling is strongly weakened by 90° superexchange interaction path leading to a FM coupling of the molecule to the Co layer. This scenario, completely supported by the theoretical spin density calculated on the whole moiré cell, is robust against different exchange and correlation functionals. The choice of an effective superexchange path can ensure the stability against thermal fluctuations, even at RT, and it can be further optimized with a fine control of the relative orientation of the easy magnetization axes at the spin interface. In perspective, the magnetic remanence at RT of these archetypal spin interfaces, once paired with a tunable magnetic substrate, opens the possibility to produce future operational spintronic devices.

Experimental and Computational Methods. *Sample Preparation.* The Ir(111) surface was prepared with several cycles of 2 keV Ar^+ sputtering, followed by annealing above 1300 K. The Gr sheet was grown on the clean and ordered Ir(111) surface by exposing the substrate to a partial pressure of 10^{-6} mbar of ethylene (C_2H_4) and annealing the covered surface above 1500−1600 K. The completion of a single domain Gr layer was confirmed by the presence of sharp and bright spots of the moiré superstructure in the LEED diffraction pattern. Metallic Co was then sublimated with an e-beam evaporator and deposited on Gr/Ir(111) kept at room temperature. Finally, the Co/Gr/Ir(111) sample was annealed at 600−800 K to favor Co intercalation, following refs 15, 16, and 18. The quantity of intercalated Co was determined with a quartz crystal microbalance and double-checked with an Auger-calibrated growth compared with the XAS jump edge ratio (see Supporting Information of ref 30), highlighting a layer-by-layer growth. MPc powders (M = Fe, Cu) were sublimated with a homemade resistively heated quartz crucible, at a constant rate of 0.3 Å/min, measured with a quartz crystal microbalance.

XAS and XMCD Measurements. X-ray absorption spectroscopy and magnetic circular dichroism (XAS and XMCD) measurements were performed at the BOREAS beamline of the Alba synchrotron radiation facility[31] in total electron yield (TEY) by measuring the sample drain current normalized with respect to incident flux, measured as the drain current on a clean gold grid. The measurements were performed in two different experimental geometries, in order to probe the magnetic response along the easy as well as the hard magnetization axis. The in-plane magnetic state was studied by impinging the sample at GI, namely at 70° incidence angle, whereas the out-of-plane magnetic response is determined at NI. The hysteresis curves have been obtained by normalizing the field-dependent L_3 XMCD intensity at a pre-edge signal in order to cancel-out any field-induced artifact.

Theoretical Modeling. Plane wave density functional theory calculations were performed using the Quantum ESPRESSO[32,33] package at the LDA,[34] GGA-PBE,[35] and PBE+U[36] level (with a value of U = 4 eV for the d-orbitals of the MPc central ion). Structural relaxations were carried out using LDA and PBE exchange-correlation potential, including van der Waals interactions within the semiempirical method of Grimme (DFT-D2).[37] The IrCoGr system was simulated with a supercell consisting of a IrCo slab (three Ir and one Co layers) with a 9 × 9 lattice in-plane periodicity and an overlaying 10 × 10 graphene layer. The same system was then relaxed with one FePc (CuPc) molecule adsorbed on graphene. Technical details of the calculation are reported in the Supporting Information.

■ ASSOCIATED CONTENT

Ⓢ Supporting Information

The Supporting Information is available free of charge on the ACS Publications website at DOI: 10.1021/acs.nanolett.7b04836.

> Detailed material related to the XAS measurement at the Fe and Cu $L_{2,3}$ edges (with and without magnetic field) in the two experimental geometries for the spin interface. Computational details for the DFT modeling and orbital magnetization (PDF)

■ AUTHOR INFORMATION

Corresponding Author

*E-mail: maria.grazia.betti@roma1.infn.it.

ORCID

Giulia Avvisati: 0000-0002-3126-838X
Daniele Varsano: 0000-0001-7675-7374
Pierluigi Gargiani: 0000-0002-6649-0538
Maria Grazia Betti: 0000-0002-6244-0306

Notes

The authors declare no competing financial interest.

■ ACKNOWLEDGMENTS

These experiments were performed at the BOREAS beamline at ALBA Synchrotron with the collaboration of ALBA staff. The authors thank Pierluigi Mondelli for experimental assistance during the beamtime. A.F., D.V., and C.C. acknowledge financial support from the EU Centre of Excellence “MaX - Materials Design at the Exascale” (Horizon 2020 EINFRA-5, Grant 676598). Computational resources were partly provided by PRACE (Grant Pra11_2921) on the Marconi machine at CINECA. G.A. and M.G.B. acknowledge fundings from Sapienza University of Rome. P.G. acknowledges funding from the Spanish MINECO (Grant FIS2013-45469-C4-3-R).

■ REFERENCES

(1) Christou, G.; Gatteschi, D.; Hendrickson, D. N.; Sessoli, R. *MRS Bull.* **2000**, *25*, 66−71.

(2) Wende, H.; Bernien, M.; Luo, J.; Sorg, C.; Ponpandian, N.; Kurde, J.; Miguel, J.; Piantek, M.; Xu, X.; Eckhold, P.; et al. *Nat. Mater.* **2007**, *6*, 516−520.

(3) Annese, E.; Fujii, J.; Vobornik, I.; Panaccione, G.; Rossi, G. *Phys. Rev. B: Condens. Matter Mater. Phys.* **2011**, *84*, 174443.

(4) Annese, E.; Casolari, F.; Fujii, J.; Rossi, G. *Phys. Rev. B: Condens. Matter Mater. Phys.* **2013**, *87*, 054420.

(5) Brede, J.; Atodiresei, N.; Kuck, S.; Lazić, P.; Caciuc, V.; Morikawa, Y.; Hoffmann, G.; Blügel, S.; Wiesendanger, R. *Phys. Rev. Lett.* **2010**, *105*, 047204.

(6) Scardamaglia, M.; Lisi, S.; Lizzit, S.; Baraldi, A.; Larciprete, R.; Mariani, C.; Betti, M. G. *J. Phys. Chem. C* **2013**, *117*, 3019−3027.

(7) Lisi, S.; Gargiani, P.; Scardamaglia, M.; Brookes, N. B.; Sessi, V.; Mariani, C.; Betti, M. G. *J. Phys. Chem. Lett.* **2015**, *6*, 1690−1695.

(8) Bazarnik, M.; Brede, J.; Decker, R.; Wiesendanger, R. *ACS Nano* **2013**, *7*, 11341−11349.

(9) Avvisati, G.; Lisi, S.; Gargiani, P.; Della Pia, A.; De Luca, O.; Pacilé, D.; Cardoso, C.; Varsano, D.; Prezzi, D.; Ferretti, A.; et al. *J. Phys. Chem. C* **2017**, *121*, 1639−1647.

(10) Avvisati, G.; Mondelli, P.; Gargiani, P.; Betti, M. G. *Appl. Surf. Sci.* **2018**, *432*, 2−6.

(11) Klar, D.; Brena, B.; Herper, H. C.; Bhandary, S.; Weis, C.; Krumme, B.; Schmitz-Antoniak, C.; Sanyal, B.; Eriksson, O.; Wende, H. *Phys. Rev. B: Condens. Matter Mater. Phys.* **2013**, *88*, 224424.

(12) Gargiani, P.; Rossi, G.; Biagi, R.; Corradini, V.; Pedio, M.; Fortuna, S.; Calzolari, A.; Fabris, S.; Cezar, J. C.; Brookes, N. B.; et al. *Phys. Rev. B: Condens. Matter Mater. Phys.* **2013**, *87*, 165407.

(13) Yang, H.; Vu, A. D.; Hallal, A.; Rougemaille, N.; Coraux, J.; Chen, G.; Schmid, A. K.; Chshiev, M. *Nano Lett.* **2016**, *16*, 145−151.

(14) Lodi Rizzini, A.; Krull, C.; Mugarza, A.; Balashov, T.; Nistor, C.; Piquerel, R.; Klyatskaya, S.; Ruben, M.; Sheverdyaeva, P. M.; Moras, P.; et al. *Surf. Sci.* **2014**, *630*, 361−374.

(15) Decker, R.; Brede, J.; Atodiresei, N.; Caciuc, V.; Blügel, S.; Wiesendanger, R. *Phys. Rev. B: Condens. Matter Mater. Phys.* **2013**, *87*, 041403.

(16) Pacilé, D.; Lisi, S.; Di Bernardo, I.; Papagno, M.; Ferrari, L.; Pisarra, M.; Caputo, M.; Mahatha, S. K.; Sheverdyaeva, P. M.; Moras, P.; et al. *Phys. Rev. B: Condens. Matter Mater. Phys.* **2014**, *90*, 195446.

(17) The inclusion of van der Waals interactions at the PBE-D2 level does not change significantly the picture with a graphene corrugation of 1.3 Å and a minimum graphene−Co distance of 1.84 Å. At variance, the Gr−Co distance for the 1 × 1 commensurate system is found to be 2.13 Å for PBE-D2.

(18) Vita, H.; Böttcher, S.; Leicht, P.; Horn, K.; Shick, A. B.; Máca, F. *Phys. Rev. B: Condens. Matter Mater. Phys.* **2014**, *90*, 165432.

(19) Mao, J.; Zhang, H.; Jiang, Y.; Pan, Y.; Gao, M.; Xiao, W.; Gao, H.-J. *J. Am. Chem. Soc.* **2009**, *131*, 14136−14137.

(20) Zhang, H. G.; Sun, J. T.; Low, T.; Zhang, L. Z.; Pan, Y.; Liu, Q.; Mao, J. H.; Zhou, H. T.; Guo, H. M.; Du, S. X.; et al. *Phys. Rev. B: Condens. Matter Mater. Phys.* **2011**, *84*, 245436.

(21) Bartolomé, J.; Monton, C.; Schuller, I. K. In *Molecular Magnets*; Bartolomé, J., Luis, F., Fernández, J. F., Eds.; Springer-Verlag: Berlin, 2014; Chapter 9, pp 221−245.

(22) Stepanow, S.; Mugarza, A.; Ceballos, G.; Moras, P.; Cezar, J. C.; Carbone, C.; Gambardella, P. *Phys. Rev. B: Condens. Matter Mater. Phys.* **2010**, *82*, 014405.

(23) Thole, B. T.; Carra, P.; Sette, F.; van der Laan, G. *Phys. Rev. Lett.* **1992**, *68*, 1943−1946.

(24) Carra, P.; Thole, B. T.; Altarelli, M.; Wang, X. *Phys. Rev. Lett.* **1993**, *70*, 694−697.

(25) Bartolomé, J.; Bartolomé, F.; García, L. M.; Filoti, G.; Gredig, T.; Colesniuc, C. N.; Schuller, I. K.; Cezar, J. C. *Phys. Rev. B: Condens. Matter Mater. Phys.* **2010**, *81*, 195405.

(26) Bernien, M.; Miguel, J.; Weis, C.; Ali, M. E.; Kurde, J.; Krumme, B.; Panchmatia, P. M.; Sanyal, B.; Piantek, M.; Srivastava, P.; et al. *Phys. Rev. Lett.* **2009**, *102*, 047202.

(27) Hermanns, C. F.; Tarafder, K.; Bernien, M.; Krüger, A.; Chang, Y.-M.; Oppeneer, P. M.; Kuch, W. *Adv. Mater.* **2013**, *25*, 3473−3477.

(28) Rosa, A.; Baerends, E. J. *Inorg. Chem.* **1994**, *33*, 584−595.

(29) Candini, A.; Bellini, V.; Klar, D.; Corradini, V.; Biagi, R.; De Renzi, V.; Kummer, K.; Brookes, N. B.; del Pennino, U.; Wende, H.; et al. *J. Phys. Chem. C* **2014**, *118*, 17670−17676.

(30) Gargiani, P.; Cuadrado, R.; Vasili, H. B.; Pruneda, M.; Valvidares, M. *Nat. Commun.* **2017**, *8*, 699.

(31) Barla, A.; Nicolás, J.; Cocco, D.; Valvidares, S. M.; Herrero-Martín, J.; Gargiani, P.; Moldes, J.; Ruget, C.; Pellegrin, E.; Ferrer, S. *J. Synchrotron Radiat.* **2016**, *23*, 1507−1517.

(32) Giannozzi, P.; Baroni, S.; Bonini, N.; Calandra, M.; Car, R.; Cavazzoni, C.; Ceresoli, D.; Chiarotti, G. L.; Cococcioni, M.; Dabo, I.; et al. *J. Phys.: Condens. Matter* **2009**, *21*, 395502.

(33) Giannozzi, P.; Andreussi, O.; Brumme, T.; Bunau, O.; Buongiorno Nardelli, M.; Calandra, M.; Car, R.; Cavazzoni, C.; Ceresoli, D.; Cococcioni, M.; et al. *J. Phys.: Condens. Matter* **2017**, *29*, 465901.

(34) Perdew, J. P.; Zunger, A. *Phys. Rev. B: Condens. Matter Mater. Phys.* **1981**, *23*, 5048−5079.

(35) Perdew, J. P.; Ernzerhof, M.; Burke, K. *J. Chem. Phys.* **1996**, *105*, 9982−9985.

(36) Cococcioni, M.; de Gironcoli, S. *Phys. Rev. B: Condens. Matter Mater. Phys.* **2005**, *71*, 035105.

(37) Grimme, S. *J. Comput. Chem.* **2006**, *27*, 1787−1799.

DOI: 10.1021/acs.nanolett.7b04836
Nano Lett. 2018, 18, 2268−2273

Supporting information for: Ferromagnetic and antiferromagnetic coupling of spin molecular interfaces with high thermal stability

Giulia Avvisati,[†] Claudia Cardoso,[‡] Daniele Varsano,[‡] Andrea Ferretti,[‡]
Pierluigi Gargiani,[¶] and Maria Grazia Betti[*,†]

†*Dipartimento di Fisica, Università di Roma "La Sapienza", I-00185 Roma, Italy*

‡*Centro S3, CNR-Istituto Nanoscienze, I-41125 Modena, Italy*

¶*ALBA Synchrotron Light Source, E-08290 Cerdanyola del Valles, Barcelona, Spain*

E-mail: maria.grazia.betti@roma1.infn.it

Molecular orbital symmetry and XMCD measurements

The ground state electronic configuration for FePc (left) and CuPc (right) is presented in Fig.S1, together with sketches of the different occupation and symmetry of the metal-related molecular orbitals.[S1] The XAS at the Fe and Cu L_3 absorption edge acquired at grazing incidence (GI) for FePc (left) and CuPc (right) thick films, exhibits different in-plane/out-of-plane symmetry, as described in the bottom panel of Fig.S1, according to Ref.S2. Considering the symmetry, the different main absorption features can be assigned taking into account the ligand field splitting of the Fe(Cu)-related molecular states, the sequence of spin-split molecular orbitals, and the final spin state (S=1 for FePc and S=1/2 for CuPc). In particular, the $a_{1g}(d_{z^2})$ and the out-of-plane component of the $e_g(d_{xz,yz})$ orbitals are visible at GI while the in-plane projection of the e_g orbitals appears in the NI measurements, together with the $b_{1g}(d_{x^2-y^2})$ state. It is worth noting that a slight mixing of the molecular states upon adsorption on graphene intercalated with Co can break the symmetry of the molecular states, but energy position of the states is preserved, though the relative intensity are influenced by the interaction process.[S3] Element selective XMCD collected for sub-monolayer of FePc and CuPc,changing the incidence angle of the incoming X-ray beam, and accordingly of the magnetic field can be compared with the reference XAS spectra for the FePc and CuPc thin films.

The XAS and the XMCD signals at the Fe and Cu $L_{2,3}$ absorption edges for MPc grown on graphene intercalated with Co layer(s) are reported in Figs.S2 and S3. The measurements were performed with and without magnetic field as well as along the easy and the hard magnetization axes. The dichroic effects, comparing the XMCD spectra acquired with the different experimental geometries, can better address the influence of orbital symmetry of the molecular states involved in the magnetic coupling with the ferromagnetic intercalant.

MPcs on Gr/Out of Plane Co/Ir(111)

The magnetic response of 0.4 ML FePc (left) and 0.6 ML CuPc (right) deposited on Gr/1 ML Co is reported in Fig. S2. The strength of the Gr-mediated Fe-Co magnetic coupling is first probed by

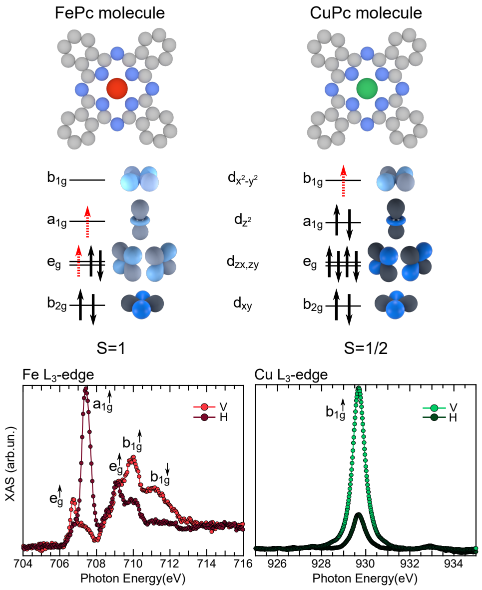

Figure S1: Sketch of the ground state occupation and symmetry of the metal-related molecular orbitals for the FePc (left) and CuPc (right) molecule (upper panel). XAS spectra at the Fe and Cu L_3 absorption edge for FePc (left) and CuPc (right) thin films (lower panel). The measurements were acquired at GI and with the polarization vector both parallel to (V) and forming a 70° angle with the surface plane (H).

applying an intense 6T magnetic field, that would align the spins and break a weak AFM coupling, while enhancing a FM one. In the right panel of Fig. S2 we can see that the presence of the magnetic field only slightly reduces the XMCD signal, indicating a fairly strong AFM coupling. On the other hand, the CuPc zero-field XMCD signal (Fig. S2, right panel) is increased by almost a factor three by the presence of the 6T magnetic field, pinpointing towards a much weaker Cu-Co magnetic coupling.

If we compare the intensity of the zero-field XMCD signals at NI and GI we notice that, in the case of FePc, the easy magnetization axis is switched out-of-plane by the presence of the Co layer, while the intrinsic one of the molecule lies parallel to the molecular plane (see for example S2).

MPcs on Gr/In Plane Co

In Fig. S3 we present the magnetic characterization of MPcs adsorbed on Gr/IP Co/Ir(111), performed to highlight the role of the relative orientation between the molecule and substrate easy

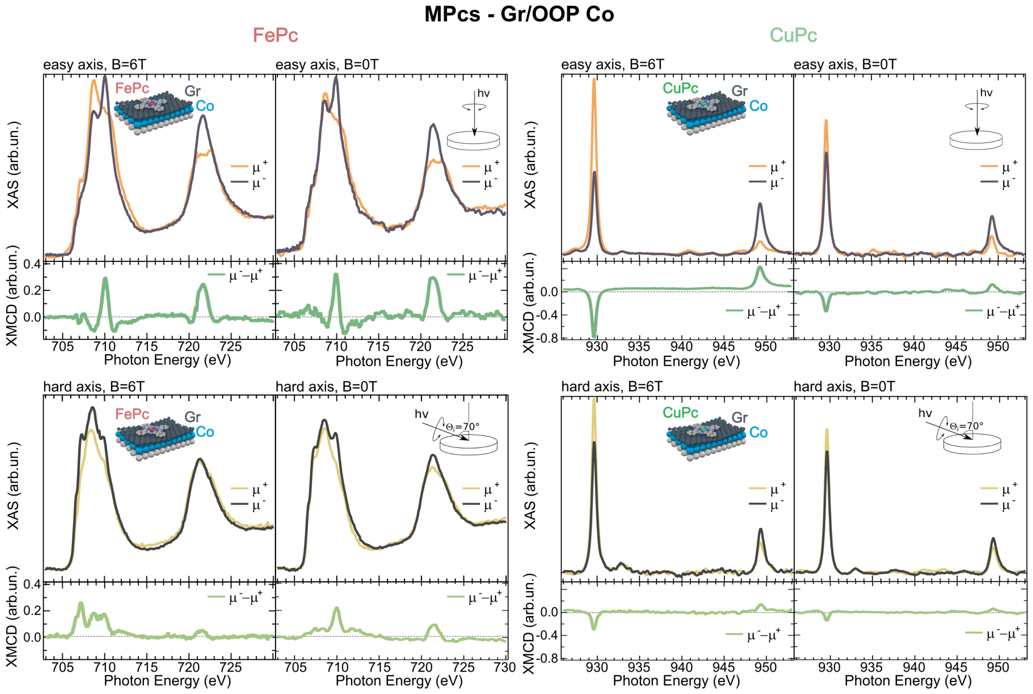

Figure S2: XAS at the Fe and Cu $L_{2,3}$ absorption edges (acquired with parallel and antiparallel helicities) for FePc (left) and CuPc (right) adsorbed on Gr/1 ML Co/Ir(111) are presented together with the XMCD difference spectra. The measurements were performed both with and without a magnetic field (B=6T), oriented parallel to the incident X-ray beam, and along the easy and the hard axis (see sketches for the experimental geometry).

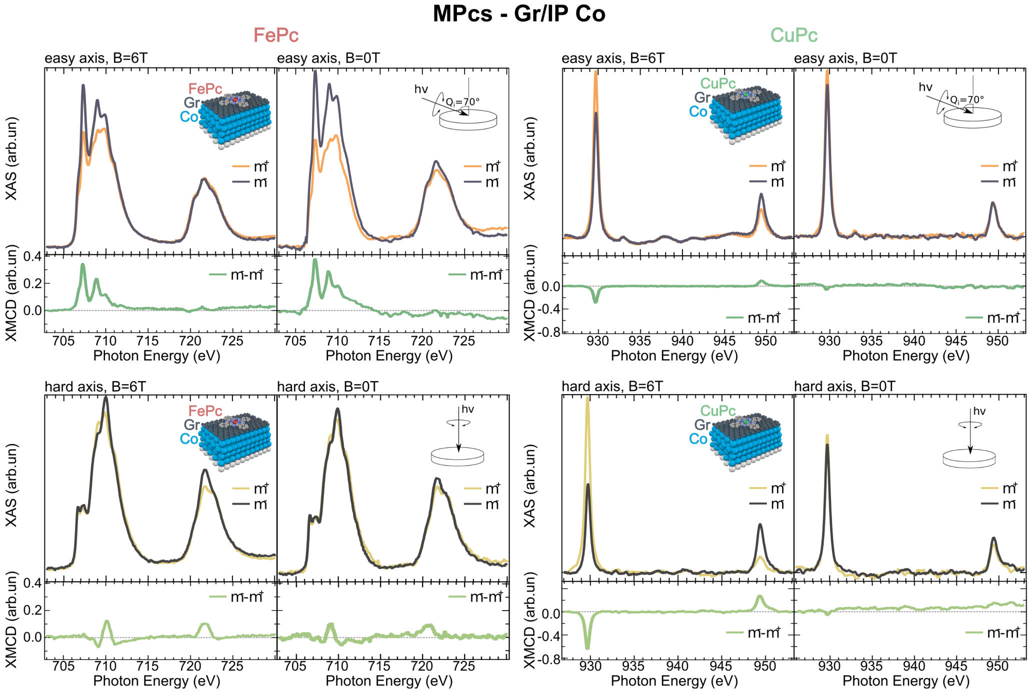

Figure S3: XAS at the Fe and Cu $L_{2,3}$ absorption edges (acquired with parallel and antiparallel helicities) for FePc (left) and CuPc (right) adsorbed on Gr/6 ML Co/Ir(111 are presented together with the XMCD difference spectra. The measurements were performed both with and without a magnetic field (B=6T), oriented parallel to the incident X-ray beam, and along the easy and the hard axis (see sketches for the experimental geometry).

magnetization axes on the strength of the magnetic coupling. If we concentrate on the left panel of Fig. S3, i.e. on the magnetic response of FePc/Gr/6 ML Co, we notice that the coupling is more pronounced (higher XMCD signal) in this configuration, when the molecule and substrate easy magnetization axes lie parallel. CuPc molecules, on the other hand, having only a half-filled b_{1g} orbital with a $d_{x^2-y^2}$ spatial symmetry, are strongly anisotropic with an out-of-plane easy magnetization axis. Hence, when CuPc molecules are deposited on Gr/8 ML Co, exhibiting an in-plane magnetization, the magnetic coupling is frustrated,^{S4} and no zero-field remanence can be detected along both directions, as reported in the right panel of Fig. S3.

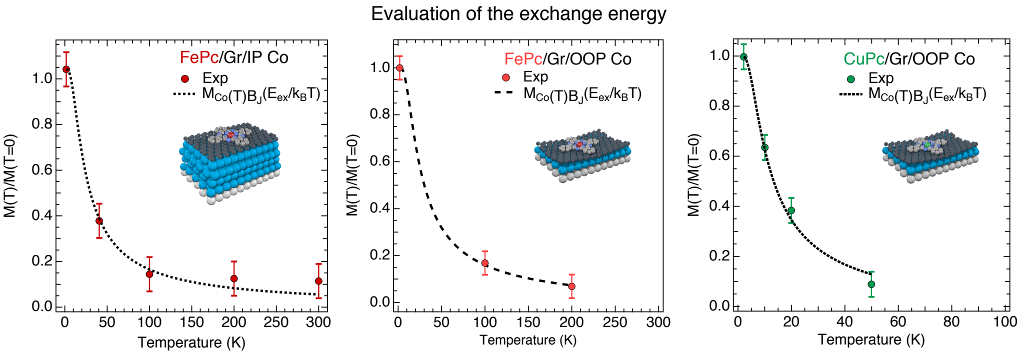

Figure S4: Fitting of the XMCD signal thermal evolution with a Brillouin function, performed in order to extrapolate the exchange energy of the FM/AFM coupling.

Evaluation of the Exchange energy

The thermal evolution of the XMCD signal acquired at the Fe (Cu) $L_{2,3}$ absorption edge and normalized with respect to the "zero" temperature signal intensity, is presented in Fig.S4. In order to extrapolate the Fe(Cu)-Co coupling energy through the graphene sheet a Brillouin function has been used and the fitting curves and parameters are reported in Table S1 and Fig.S4.

Table S1: Brillouin fitting parameters for the different samples.

Sample	J	E_{ex} (meV)
FePc/Gr/IP Co	1	2.8 ± 0.6
FePc/Gr/OOP Co	1	2.1 ± 0.5
CuPc/Gr/OOP Co	0.5	0.6 ± 0.2

Computational Details

Density functional theory calculations were performed using the Quantum ESPRESSO[S5] package. Structural relaxations were performed using the LDA and PBE exchange-correlation potential,[S6] including van der Waals interactions within the semiempirical method of Grimme (DFT-D2).[S7] Electronic strucuture calculations were performed using the PBE+U method (with a value of U=4 eV for the d-orbitals of the MPc central ion) and also GGA-PBE[S6] exchange-correlation potential and the LDA Perdew-Zunger parametrization[S8]). The kinetic energy cutoff for the wave functions was set to 75 Ry and we adopted norm-conserving pseudo-potentials to model the electron-ion interaction. The value of U in the PBE+U method was chosen according to Ref.[S9] The IrCoGr system was simulated with a supercell consisting of a IrCo slab with a 9×9 lattice in-plane periodicity and an overlaying 10×10 graphene layer, the slab is composed of three Ir and one Co layers. The same system was then relaxed with one FePc (CoPc) adsorbed on graphene. The Brillouin zone was sampled by using a 2×2×1 grid of **k**-points.

Spin densities: Robustness against DFT functionals

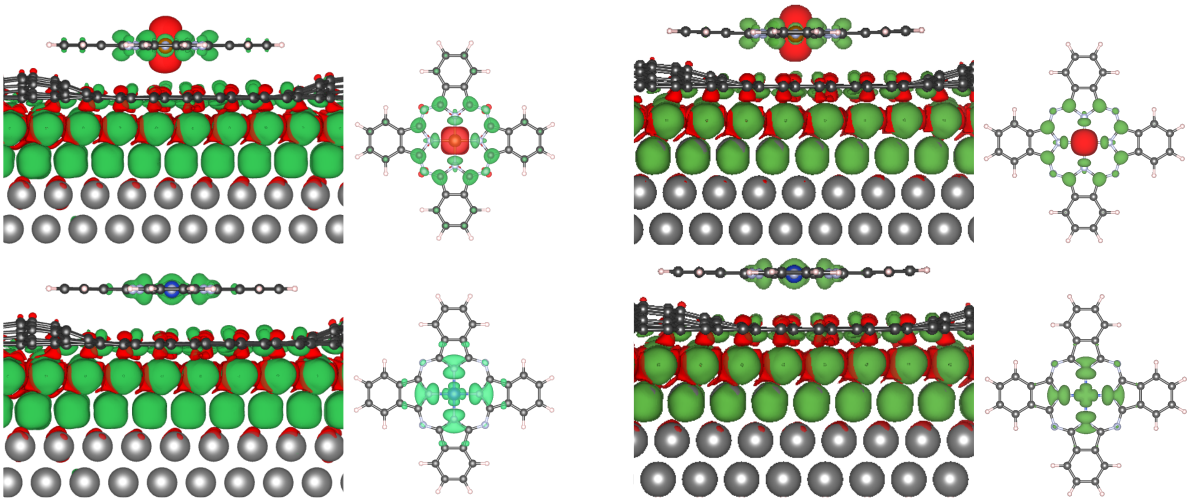

Figure S5: Spin density isosurfaces plots for FePc (upper panels) and CuPc (lower panels) on Gr/Co/Ir (side and top view with hidden substrate) as computed at the LDA (left panels) and DFT-PBE (right panels) levels of theory. Green (red) isosurfaces correspond to the up (down) spin density. In the base of the DFT-PBE calcualtions, the geometries include PBE-D2 van der Waals corrections.

In this Section we report the spin densities for Fe and Cu-Pc adsorbed on Gr/Co/Ir as computed using different functionals, such as LDA and PBE, beside the PBE+U (with a value of U=4 eV for the d-orbitals of the MPc central ion) shown in the main text. Results reported in Fig. S5 for LDA and PBE are very similar to the PBE+U calculations shown in the main paper (Fig. 2), validating the robustness of the calculated quantities. Some (relatively small) differences among the results are visible for the case of FePc, where the spin densities around the central metal ion show a different shape and/or symmetry (while the main qualitative features: AFM coupling, atomic involvement, and orbital orientation, are reproduced). This is due to a different symmetry of one of the orbitals carrying the magnetic moment, as detailed in the next Section. In all cases, the d_{z^2} contribution (a_{1g} of the free standing molecule) is present.

To complete the discussion we also address the sign alternation pattern in the spin density plots. The picture can be made more quantitative by looking at the atomically resolved magnetic moments, reported in Tab. S2 for LDA, PBE, and PBE+U functionals.

For FePc, all functionals predict a flip of the magnetic moment when going from the central metal ion to the Pc macrocycle, at variance with CuPc where the magnetic moment stays with the same sign. This can be ascribed to the shape of the b_{1g} orbital of CuPc. Further to that, PBE and PBE+U also predict a flip of the magnetic moment when crossing the graphene layer, for both Fe and CuPc. The magnetic moment per C atom is nevertheless very small, making the feature rather mild.

Table S2: Atom-resolved spin polarization as given by Löwdin charge analysis. Magnetizations given in Bohr magneton (μ_B) units per cell (1 TM atom, 8 N atoms, 32 C atoms for the molecule and 200 C atoms for Gr, 81 Co and Ir atoms per layer). Data for LDA, PBE, PBE+U (U=4 eV) are reported. Value in parenthesis refer to the isolated FePc molecule.

Atomic Magnetization [μ_B]

	TM	**N mol**	**C mol**	**Gr**	**Co**	**Ir**
LDA						
FePc	-1.72 (2.09)	0.09 (-0.02)	0.40 (-0.08)	0.17	101.70	14.22
CuPc	+0.47	0.51	0.05	0.15	101.81	14.27
PBE						
FePc	-1.88 (2.15)	0.08 (-0.06)	0.53 (-0.11)	-0.40	120.64	15.87
CuPc	+0.57	0.47	0.06	-0.42	120.61	15.91
PBE+U (U=4 eV)						
FePc	-2.10 (2.20)	0.20 (-0.03)	0.22 (-0.19)	-0.42	120.58	15.90
CuPc	+0.54	0.48	0.06	-0.42	120.61	15.91

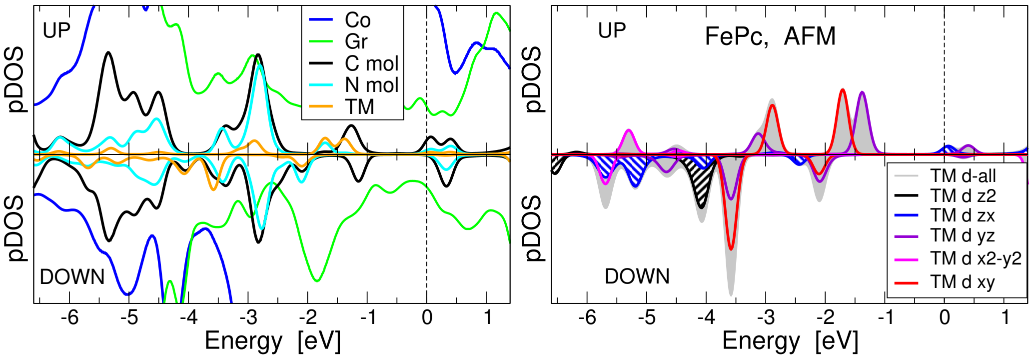

Figure S6: pDOS of FePc at Gr/Co/Ir computed with PBE+U. Left panel: Atomically projected pDOS. Right panel: spherical harmonics resolution of the Fe pDOS. Orbitals carrying the largest magnetic moments (d_{z^2} and d_{zx}) are shown with dashed filling.

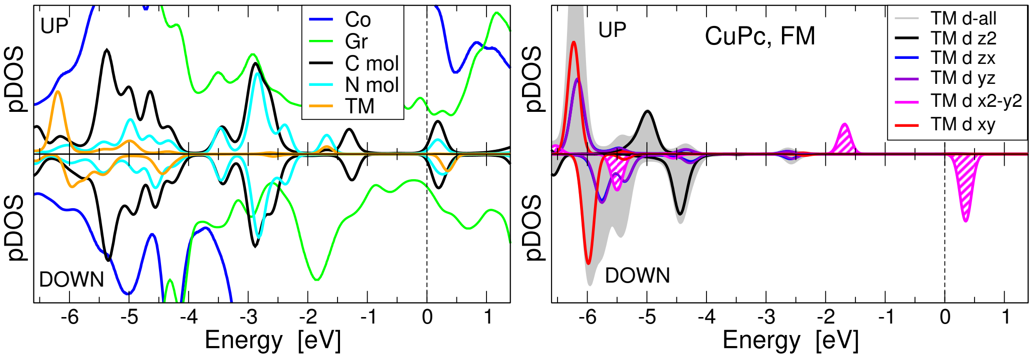

Figure S7: pDOS of CuPc at Gr/Co/Ir computed with PBE+U. Left panel: Atomically projected pDOS. Right panel: spherical harmonics resolution of the Cu pDOS. Orbitals carrying the largest magnetic moments ($d_{x^2-y^2}$) are shown with dashed filling.

Orbital magnetization

In Figs. S6 and S7 we report the projected density of states (pDOS) analysis for FePc and CuPc adsorbed on Gr/Co/Ir, as computed at the PBE+U level. The total and atomic pDOS are reported in the left panels, while right panels show the transition metal (TM) contributions resolved in spherical harmonics. In the case of FePc, the magnetic moment (obtained as the difference of Löwdin charges) is carried mostly by orbitals involving d_{z^2} and d_{xz} components (corresponding to a_{1g} and e_g for the isolated FePc). Instead, the magnetic moment of CuPc (about 0.5 μ_B) is carried by $d_{x^2-y^2}$ (corresponding to b_{1g} for the isolated molecule). This analysis points out that the different magnetic properties of the adsorbed FePc and CuPc are related to the different orientation of the orbitals carrying the magnetic moment (out-of-plane for FePc and in-plane for CuPc).

Table S3: Transition metal (d) magnetic moments (computed using Löwdin charges) resolved with respect to angular symmetry for FePc and CuPc upon adsorption. Different degrees of theoretical description are shown (PBE+U, PBE, LDA). For each molecule, the largest magnetic moments are shown in bold.

TM-d magnetic moments [μ_B]

	$\mathbf{z^2}$	zx	zy	$\mathbf{x^2 - y^2}$	xy	**Tot**
FePc						
PBE+U	**0.92**	**0.91**	0.07	0.12	0.01	2.03
PBE	**0.88**	**0.33**	**0.34**	0.08	0.15	1.78
LDA	**0.76**	**0.27**	**0.28**	0.06	0.12	1.50
CuPc						
PBE+U	0.05	0.02	0.02	**0.55**	0.00	0.56
PBE	0.01	0.00	0.00	**0.56**	0.00	0.58
LDA	0.01	0.01	0.01	**0.49**	0.00	0.51

In Tab. S3 we report the detailed analysis of the symmetry of the local magnetic moments on the transition metal ions (d-manifold) for the two molecules for the different DFT functionals used (LDA, PBE, PBE+U). The situation is quite robust against the use of different functionals. Besides a rather limited change in the absolute magnetic moment of FePc, the main qualitative difference across functionals is the split of the e_g states (d_{xz} and d_{yz}) in the PBE+U calculation for FePc, leading to just one of the two orbitals being spin polarized. The situation is quite different from the case of the isolated FePc molecule, where different symmetry of the magnetic ground states have been reported in the literature, see e.g. Refs S10–S12, depending on the numerical treatments or the theoretical description used.

References

[S1] Bartolomé, J.; Monton, C.; Schuller, I. K. In *Molecular Magnets*; Bartolomé, J., Luis, F., Fernández, J. F., Eds.; Springer-Verlag Berlin Heidelberg, 2014; Chapter 9, pp 221–245.

[S2] Bartolomé, J.; Bartolomé, F.; García, L. M.; Filoti, G.; Gredig, T.; Colesniuc, C. N.; Schuller, I. K.; Cezar, J. C. *Phys. Rev. B* **2010**, *81*, 195405.

[S3] Avvisati, G.; Lisi, S.; Gargiani, P.; Della Pia, A.; De Luca, O.; Pacilé, D.; Cardoso, C.; Varsano, D.; Prezzi, D.; Ferretti, A. et al. *J. Phys. Chem. C* **2017**, *121*, 1639–1647.

[S4] Lodi Rizzini, A.; Krull, C.; Mugarza, A.; Balashov, T.; Nistor, C.; Piquerel, R.; Klyatskaya, S.; Ruben, M.; Sheverdyaeva, P. M.; Moras, P. et al. *Surf. Sci.* **2014**, *630*, 361 – 374.

[S5] Giannozzi, P.; Baroni, S.; Bonini, N.; Calandra, M.; Car, R.; Cavazzoni, C.; Ceresoli, D.; Chiarotti, G. L.; Cococcioni, M.; Dabo, I. et al. *J. Phys.: Condens. Mat.* **2009**, *21*, 395502.

[S6] Perdew, J. P.; Ernzerhof, M.; Burke, K. *J. Chem. Phys.* **1996**, *105*, 9982–9985.

[S7] Grimme, S. *J. Comput. Chem.* **2006**, *27*, 1787–1799.

[S8] Perdew, J. P.; Zunger, A. *Phys. Rev. B* **1981**, *23*, 5048–5079.

[S9] Wehling, T. O.; Lichtenstein, A. I.; Katsnelson, M. I. *Phys. Rev. B* **2011**, *84*, 235110.

[S10] Marom, N.; Hod, O.; Scuseria, G. E.; Kronik, L. *J. Chem. Phys.* **2008**, *128*, 164107.

[S11] Brena, B.; Puglia, C.; de Simone, M.; Coreno, M.; Tarafder, K.; Feyer, V.; Banerjee, R.; Göthelid, E.; Sanyal, B.; Oppeneer, P. M. et al. *J. Chem. Phys.* **2011**, *134*, 074312.

[S12] Liao, M.-S.; Scheiner, S. *J. Chem. Phys.* **2001**, *114*, 9780–9791.

The Journal of Chemical Physics ARTICLE scitation.org/journal/jcp

Empty electron states in cobalt-intercalated graphene

Cite as: J. Chem. Phys. **153**, 214703 (2020); doi: 10.1063/5.0021814
Submitted: 14 July 2020 • Accepted: 6 November 2020 •
Published Online: 1 December 2020

Alberto Calloni,[1,a)] Gianlorenzo Bussetti,[1] Giulia Avvisati,[2] Madan S. Jagadeesh,[1] Daniela Pacilè,[3] Andrea Ferretti,[4] Daniele Varsano,[4] Claudia Cardoso,[4] Lamberto Duò,[1] Franco Ciccacci,[1] and Maria Grazia Betti[2]

AFFILIATIONS

[1] Dipartimento di Fisica, Politecnico di Milano, piazza Leonardo da Vinci 32, I-20133 Milano, Italy
[2] Dipartimento di Fisica, Università di Roma "La Sapienza", I-00185 Roma, Italy
[3] Dipartimento di Fisica, Università della Calabria, I-87036 Arcavacata di Rende (Cs), Italy
[4] Centro S3, CNR-Istituto Nanoscienze, I-41125 Modena, Italy

[a)] Author to whom correspondence should be addressed: alberto.calloni@polimi.it

ABSTRACT

The dispersion of the electronic states of epitaxial graphene (Gr) depends significantly on the strength of the bonding with the underlying substrate. We report on empty electron states in cobalt-intercalated Gr grown on Ir(111), studied by angle-resolved inverse photoemission spectroscopy and x-ray absorption spectroscopy, complemented with density functional theory calculations. The weakly bonded Gr on Ir preserves the peculiar spectroscopic features of the Gr band structure, and the empty spectral densities are almost unperturbed. Upon intercalation of a Co layer, the electronic response of the interface changes, with an intermixing of the Gr π^* bands and Co d states, which breaks the symmetry of π/σ states, and a downshift of the upper part of the Gr Dirac cone. Similarly, the image potential of Ir(111) is unaltered by the Gr layer, while a downward shift is induced upon Co intercalation, as unveiled by the image state energy dispersion mapped in a large region of the surface Brillouin zone.

I. INTRODUCTION

The intercalation of metal layers under graphene (Gr) has been the subject of keen interest in the past decade for fundamental and applied physics, in particular due to the possibility of creating a magnetic system with tunable properties.[1–6] The main outcomes of the metal intercalation are the modulation of the Gr electronic structure near the Dirac cone,[7–9] the evolution of the interfacial moiré pattern and surface corrugation,[10–14] and the effects of Gr on protecting the vulnerable surface properties of the underneath substrate. In fact, thanks to its chemical stability, Gr protects highly reactive surfaces and stabilizes magnetic thin films against oxidation.[8]

The electronic properties of epitaxial Gr significantly depend on the supporting substrate and on the interface. For instance, Gr grown on Ir(111) presents a rippled moiré superstructure, indicating a weak interaction with the metallic substrate and preserving the peculiar spectroscopic features of the Gr band structure, such as the Dirac cone.[15,16] Conversely, the growth of Gr onto transition metal (TM) surfaces, such as Ni(111) or Co(0001), of interest for their ferromagnetic coupling, generally results in a better lattice matching at the expense of a perturbed band structure,[17] as shown by angle-resolved photoemission spectroscopy (AR-PES).[18,19]

While the precise evolution of the Gr-filled electronic states and of the Dirac cone has been determined for a large class of intercalated Gr systems,[20–22] the response of the empty states has been much less investigated. Recently, angle-resolved two photon-photoemission (AR-2PPE)[23,24] and scanning tunneling spectroscopy[25] have unveiled processes involving image-potential states (ISs) in metal surfaces covered by Gr. ISs are observed within the surface-projected bulk bandgap and are related to electrons trapped by the attractive image-charge potential just outside the surface. The response of ISs to the composite dielectric/metal systems involving Gr is itself of fundamental physical interest. Theoretically, a dual Rydberg-like series of even and odd symmetry image-potential states is expected in a single freestanding sheet of Gr.[26]

The underlying metal substrate can break the mirror symmetry of the Gr layer as reported for Gr on Ru(0001) and Gr on Pt(111),[27] while scanning tunneling spectroscopy measurements[25] unveil two series of ISs in Gr single and bilayer grown on SiC. Image-potential states are very sensitive to any change of shape or/and environment of the Gr sheet. The topography, the interlayer and impurity interactions, the intercalated layers, and the evolution of the metallic surface states upon intercalation can all strongly affect the IS energy and dispersion.[23,24] In this respect, angle-resolved inverse photoemission spectroscopy (AR-IPES) is an ideal probe to map empty states, and ISs in particular, especially when looking at a wide region of the surface Brillouin zone.

In this paper, we report on the direct band structure mapping of empty states for cobalt-intercalated Gr on Ir(111) by means of AR-IPES and Near Edge X-ray Absorption Fine Structure (NEXAFS). Noticeably, image-potential states are explicitly addressed by AR-IPES data. First principles simulations based on density functional theory (DFT) were also performed to calculate the electronic structure (DOS and bands) and simulate NEXAFS for Gr/Ir(111) and Gr/1ML-Co/Ir(111). At variance with AR-2PPE, AR-IPES can explore uncharted regions of the energy space $E(\mathbf{k})$, allowing for a direct comparison of the evolution of the empty states of Ir(111), a single layer of Gr on Ir(111), and the cobalt layer sandwiched between Gr and Ir(111). Carbon-projected band dispersion for freestanding Gr and Gr/Co(0001) systems is also analyzed and used to discuss the AR-IPES data.

This paper is organized as follows. In Sec. II A, we describe the experimental methods, including growth, characterization of the samples, NEXAFS, and AR-IPES setup, while in Sec. II B, we report the details of the first principles computational approach. Next, in Sec. III A, we discuss experimental and theoretical results, including NEXAFS data, concerning the characterization of the samples before and after cobalt intercalation. Finally, empty states, sampled using AR-IPES, are reported and discussed in Sec. III B, together with band structures computed at the Kohn–Sham DFT level.

II. METHODS

A. Experimental details

Sample preparation and AR-IPES measurements took place in an ultra-high vacuum system working at a base pressure in the 1×10^{-10} mbar range.[28] The Ir(111) substrate was cleaned by sputtering and annealing cycles (up to 1470 K). The substrate was then exposed to oxygen at a pressure of 1.3×10^{-7} mbar (overall exposure is 8 L, considering $1\ \mathrm{L} = 1.33 \times 10^{-6}$ mbar × s) with the surface kept at 1170 K in order to segregate and desorb carbon. Subsequent flashes at 1470 K removed adsorbed oxygen.[29] The quality of the samples and the consistency with literature data of the entire procedure are ensured by low energy electron diffraction (LEED) and photoemission (see Refs. 29 and 30 for more details). The Gr layer was prepared by repeatedly exposing the Ir(111) surface up to 45 L of ethylene (C_2H_4) and annealing at 1300 K. The quality of the Gr layer was then assessed by x-ray photoemission, considering the Ir $4f$ to C $1s$ core level intensity ratio,[31] and the sharpness of the moiré pattern with LEED.

Cobalt was deposited on Gr/Ir(111) at room temperature (RT) by molecular beam epitaxy, using a homemade e-beam sublimation cell loaded with a high purity (6N) Co rod. The intercalation of Co is achieved by annealing at about 670 K (i.e., well below the temperature threshold for Co–Ir interface alloying[32,33]). The nominal Co thickness was 2.5 Å, estimated by means of a quartz microbalance, i.e., slightly in excess of the Co ML thickness, assumed to be close to the bulk Ir(111) interplanar spacing (2.22 Å[34]) for a pseudomorphic-type of growth.

IPES measurements were performed by extracting electrons with laser light from a GaAs(100) photocathode prepared according to standard procedures,[35,36] and detecting 9.6 eV photons emitted in the inverse photoemission process by means of a bandpass detector. The system operates in the isochromatic mode, i.e., at fixed photon energy and by changing the energy of impinging electrons.[37–39] The full width at half maximum energy (angular) resolution is about 0.7 eV (3°).

NEXAFS and photoemission measurements were performed at the SuperESCA beamline of the synchrotron radiation facility ELETTRA (Trieste, Italy). The C K edge was acquired in the Auger yield mode, collecting the tail of the KLL Auger electrons, at a kinetic energy of about 260 eV, within an energy window of 12 eV and with an overall energy resolution of 100 meV. Measurements were acquired with horizontal linearly polarized radiation and with the electric field vector either parallel or almost normal (about 70°) with respect to the surface plane, by rotating the sample position.

B. Computational details

DFT simulations were performed using the plane-wave and pseudopotential implementation provided by the QUANTUM ESPRESSO distribution[40,41] using the Local Density Approximation (LDA) exchange-correlation functional, according to the Perdew–Zunger parameterization.[42] Consistent with our previous work,[2] Gr/Ir(111) and Gr/1ML-Co/Ir(111) were simulated including the complete moiré-induced periodicity by using a 9 × 9 supercell of Ir(111), corresponding to a 10 × 10 supercell of pristine Gr. For comparison, freestanding Gr and 1 × 1 Gr/Co(0001) were also computed.

Since, for the case of a single layer of Co intercalated under graphene, Co assumes the same structure of Ir(111) [see LEED in Fig. 1(d)], the moiré superstructures of Gr/Ir(111) and Gr/1ML-Co/Ir(111) have the same periodicity. In practice, we have treated the Co layer with the same registry of one extra Ir layer, except for the interlayer distance, which has been relaxed. For both interfaces, we have considered the lattice parameters of Ir bulk relaxed at the LDA level using ultrasoft pseudopotentials (USPP), resulting in an Ir–Ir distance of 2.7048 Å (corresponding to a hexagonal cell of 46.001 Bohr radii) for the moiré structure. Four metallic layers (3 Ir plus one Co layer or 4 Ir layers) were included in the calculations. A layer of H atoms was included at the bottom of the slab to make the two sides of the slab inequivalent. Atomic

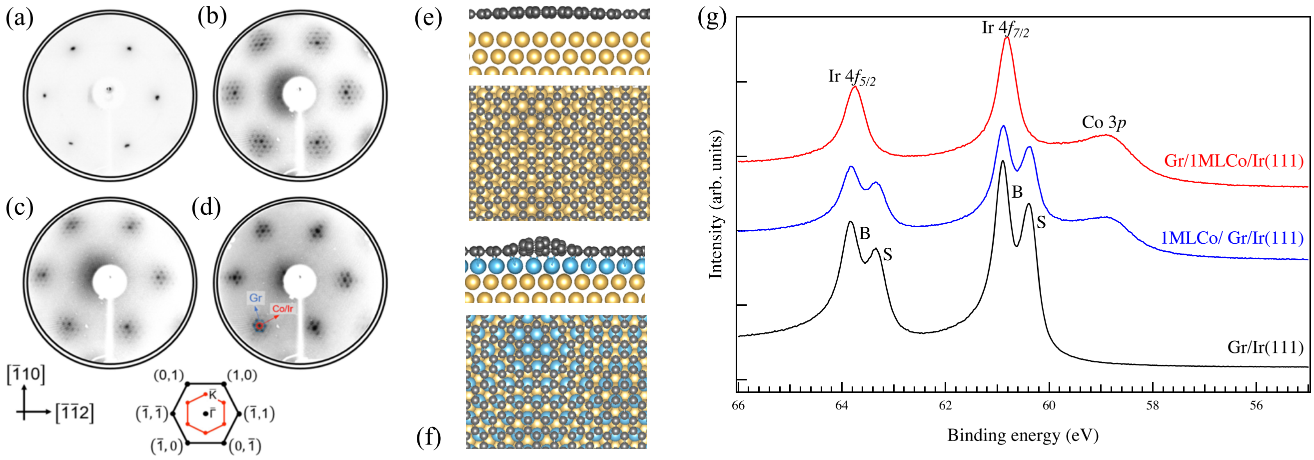

FIG. 1. Left panels: low energy electron diffraction (LEED) images taken at a beam energy of 140 eV: (a) Ir(111), (b) Gr/Ir(111), (c) as deposited 1ML-Co/Gr/Ir(111), and (d) after Co intercalation by annealing at 670 K [i.e., Gr/1ML-Co/Ir(111)]. At the bottom: sketch of the diffraction pattern of the Ir(111) surface. The surface Brillouin zone (SBZ) is shown in red. Middle panels: (e) side and top views of the corrugation and moiré pattern of Gr/Ir(111) and (f) of Gr/1ML-Co/Ir(111), as determined by DFT. Right panel: (g) Ir 4*f* core level photoemission, taken at $h\nu$ = 176 eV, of Gr/Ir(111) (black curve), 1ML-Co/Gr/Ir(111) (blue curve) and Gr/1ML-Co/Ir(111) (red curve). All spectra show Ir $4f_{5/2}$ and Ir $4f_{7/2}$ core levels [with a bulk (B) and surface (S) component before Co intercalation], and Co 3*p* core level (after Co deposition).

positions were then fully relaxed (except for the two bottom Ir layers and the H saturation layer) until ionic forces were smaller than 0.001 Ry/bohr. All the self-consistent calculations were performed by using a 2 × 2 grid of **k**-points, norm-conserving pseudopotentials, and a kinetic energy cutoff of 75 Ry to represent Kohn–Sham wavefunctions.

NEXAFS spectra were simulated using the XSPECTRA code.[43–45] The absorption from the core levels was simulated by considering a carbon pseudopotential including a half core-hole (HCH).[46–49] One HCH atom per cell (i.e., every 200 C atoms), substituting a regular C atom, was placed at different positions in order to sample valley, intermediate, and peak regions of the moiré superstructure, as well as the two sub-lattices of Gr. The final spectrum was obtained by averaging the spectra over 8 selected sampling points. More details on the averaging procedure are provided in the supplementary material.

The C-projected band structures for Gr/Co(0001) in the 1 × 1 unit cell (shown in Fig. 6) have been computed for a slab including Gr, 10 layers of Co, and a saturating back layer of H atoms. The lattice parameter of the slab (2.430 Å) has been taken from a full relaxation of the Co hcp structure, done at the DFT-LDA level (see also the supplementary material for more details). Comparison with calculations done using 4, 6, and 8 Co layers is provided in the supplementary material.

III. RESULTS AND DISCUSSION

A. Co intercalation and NEXAFS data

The intercalation of a single layer of cobalt, sandwiched between the Ir(111) surface and Gr, results in a corrugated Gr layer with a moiré superstructure superimposed to the hexagonal lattice of Gr, as deduced from the LEED patterns reported in the left panels of Fig. 1. The Ir(111) LEED [Fig. 1(a)] shows bright hexagonal spots and after Gr growth [Fig. 1(b)], a larger hexagonal pattern surrounded by hexagonal satellites (up to third order diffraction features), consistent with the smaller Gr lattice parameter, and a moiré superstructure caused by the lattice mismatch between Gr and Ir.[50] After Co deposition [Fig. 1(c)], the surface shows an unaltered pattern, only slightly attenuated after the Co addition, while the number of satellite spots is reduced when the Co layer is intercalated underneath Gr [Fig. 1(d)]. These differences are likely correlated with the changes in the Gr morphology in the presence of the Co intercalation.[11]

The Co–C interaction in the moiré superstructure depends on the C site, with the result of increasing the corrugation of the Gr layer. The interaction with Gr is stronger in top-hollow and bridge sites, while the van der Waals-like interaction is reported for other sites (showing fcc/hcp stacking),[19] as confirmed by DFT structural models.[2,31,51] The increase of the Gr corrugation upon Co intercalation and the structural details of the moiré structures, as computed in our DFT calculations, are illustrated in Figs. 1(e) and 1(f).

The graphene layer, almost unperturbed by the Ir(111) underlying surface, is highly perturbed upon Co intercalation, and a strong C–Co interaction is observed. This can be clearly unveiled by photoemission from the Ir $4f_{5/2}$ and Ir $4f_{7/2}$ core levels, both with components originating from bulk (B) and surface (S), as shown in Fig. 1(g). The surface components, at about 0.5 eV lower binding energy, due to emission from the topmost atomic layer of Ir(111), are unaffected by the formation of the Gr layer (black curve), corroborating the formation of a quasi-freestanding electronic structure of Gr, and they are essentially unchanged after the deposition of Co on Gr (blue curve, a mere attenuation of both surface and volume contributions is seen as due to the Co overlayer). Coming to Co intercalation under the graphene layer (red curve), the

Co 3*p* levels are only slightly attenuated in intensity with respect to the non-intercalated case (blue curve). While a Co_xIr_{1-x} interface alloying has been recently reported at annealing temperatures higher than 900 K,[33] here, the intensity ratio between Co 3*p* and Ir 4*f* states is almost unchanged, showing that at the intercalation temperature (well below 900 K), the bulk solubility of Co atoms must be negligible.

On the other side, the intercalation of Co at 670 K induces a sudden quenching of the Ir surface components [Fig. 1(g), red curve] and strongly influences the photoemission from the overlying Gr membrane, as exhaustively discussed in previous papers.[19,31] Moreover, cobalt deposited on top of the Gr layer does not influence the C 1*s* line shape, as shown in the spectra reported in the supplementary material. After intercalation, the C 1*s* core level photoemission presents a multi-component line shape with two main features, at 284.42 eV and 284.92 eV.[19,31] These are assigned to the C atoms in the Gr layer weakly and strongly bound to the intercalated Co layer, respectively. Such experimental evidence and the disappearance of the Ir surface components prove a homogeneous Co intercalation, featuring a Co–Gr interaction upon intercalation with a redistribution of the charge density at the Gr/1ML-Co/Ir(111) interface, in turn preventing any Co–Ir alloying.

A further signature of the interaction of corrugated Gr with the underlying Co layer can be highlighted by the C K absorption spectra (NEXAFS) for Gr/Ir(111) and Gr/1ML-Co/Ir(111) reported in panels [(a) and (b)] of Fig. 2. The electric field oriented almost normal (70° with respect to the surface plane) allows one to enhance the signal from the π^* states, even though this setup does not completely quench the σ^* state contribution. Concerning Gr/Ir(111), the main peak at 285.5 eV is associated with the π^* conduction states. Moreover, a shoulder located at about 284.2 eV can be seen in Fig. 2(a). This feature observed for single layer Gr on metals, graphene flakes[52,53] and nano-graphite grains,[54] was attributed to edge-derived electronic states. However, in the present case, the highly ordered corrugated Gr structure with large single domains cannot justify a contribution from edge defects to the pre-edge feature. On the other hand, a small *p*-doping observed for Gr/Ir(111)[55] can induce a tiny density of empty states below the Dirac cone apex available for the excited core electrons. This is supported by our DFT simulations where the comparison between the DOS computed for freestanding Gr and Gr on Ir reveals a small *p*-doping corresponding to an excess charge of about 1.1×10^{-3} electrons per C atom (DOS plots and more details in Fig. S4 of the supplementary material). The higher energy features are due to transitions toward higher-lying states resonant with contributions coming from the

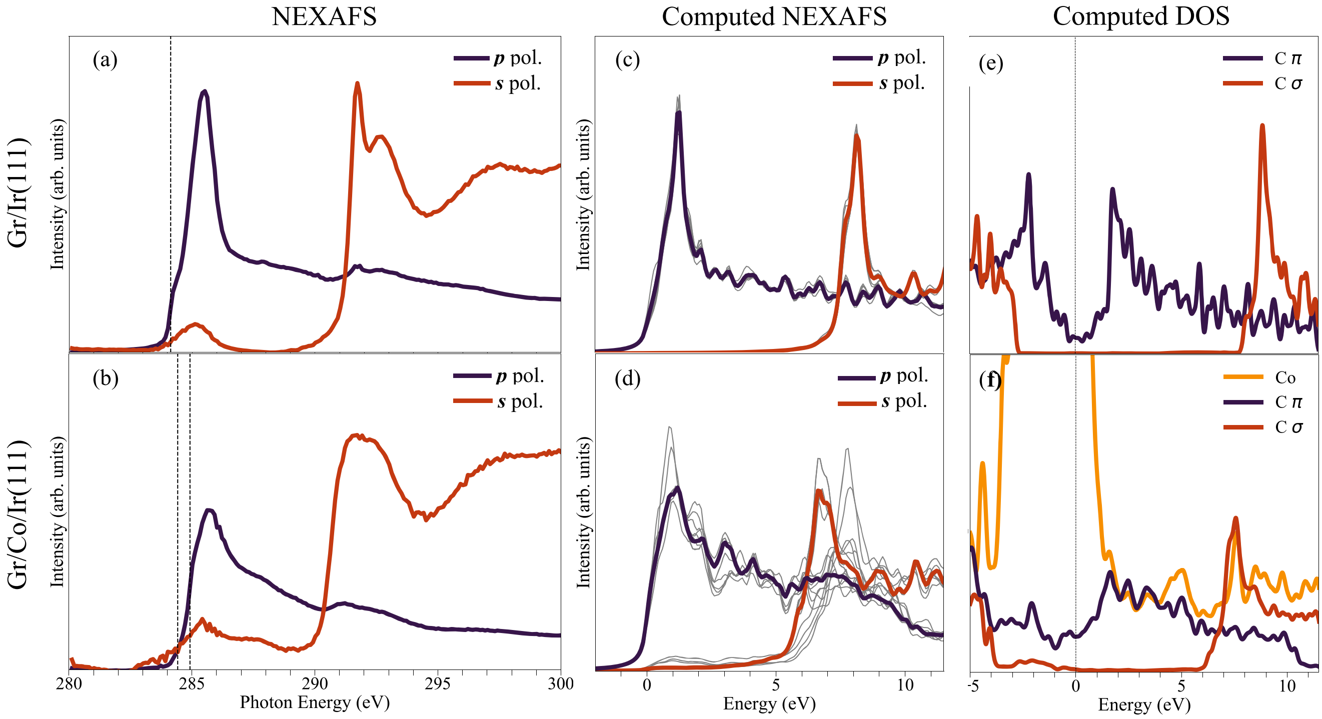

FIG. 2. Measured NEXAFS [(a) and (b)], computed NEXAFS [(c) and (d)], and DOS data [(e) and (f)] for Gr/Ir(111) (upper panels) and Gr/1ML-Co/Ir(111) (lower panels), respectively. Purple and red lines correspond to C 1*s* levels excited by out-of-plane and in-plane polarized photons. Vertical dashed lines correspond to the Fermi level reference, as deduced by the energy position of the C 1*s* core levels (284.13 eV for Gr/Ir; 284.92 eV and 284.42 for Gr/Co/Ir). Central panels: simulated NEXAFS spectra averaged over different positions of the half core-hole (see the supplementary material). The gray lines represent the spectra computed for different core-holes and give an idea of the initial-state induced broadening of the spectra. Right panels: computed DOS projected on Co and Gr σ (C $s + p_x + p_y$) and π (C p_z) orbitals for the same systems. The zero of the energy scale corresponds to the Fermi level.

σ^* conduction states, thus more visible in the *s* configuration (red curve).

The measured C K absorption edge of Gr/1ML-Co/Ir(111) is reported in Fig. 2(b). Three main signatures diversify the NEXAFS spectra before and after the Co intercalation: (i) the disappearance of the pre-edge feature due to the small *p*-doping observed for Gr/Ir(111), (ii) a broadening of the spectral features related to the π^* and σ^* transitions, and (iii) an energy shift of the absorption onset larger for the σ^* transitions than for the π^* ones.

The quenching of the pre-edge can be ascribed to the removal of *p*-doping due to a shift of the Dirac cone, as described in the computed band reported in Fig. 6 (Sec. III B). As far as it concerns the π^* transitions, the main peak, centered at 285.7 eV, appears weaker and broader. Moreover, in the energy region above the onset, between 287 eV and 290 eV, a wide shoulder appears in both *p* and *s* configurations, as observed also for Gr grown on highly interacting substrates like Gr/Ru(0001), Gr/Rh(111), or Gr/Ni(111).[56] The origin of the smearing of these features can be due to both initial state effects and hybridization of the out-of-plane C-π and Co-*d* final states. The initial state effect is due to the spatially modulated adsorption potential of C upon Co-intercalation, which stems from the moiré structure of Gr/Ir(111), reflected in different binding energies of the C 1*s* Gr core levels. After intercalation, the C 1*s* core level photoemission presents a multi-component line shape with two main features, at 284.42 eV and 284.92 eV,[19,31] assigned to C atoms in the Gr layer weakly and strongly bound to the intercalated Co layer, respectively, as reported in the supplementary material.

The presence of these features induces a convolution of a multi-edge onset; however, they cannot fully explain the large broadening of the spectral density in the energy range of 285 eV–290 eV, where the contribution from the hybridized Co–C states dominates. As supported by the DFT calculations [see below and Fig. 2(f)], a contribution to the π^* transition spectral density can be certainly ascribed to the hybridization of C-π and Co states induced by the intercalation. Such contribution is further evidenced by changing the light polarization from *p* to *s*. In fact, in-plane σ^* states present an onset at about 291 eV for Gr/Ir(111) with two well-defined structures, while for Gr/1ML-Co/Ir(111), the absorption from the σ^* states is observed also at lower photon energies (285 eV–290 eV), with slightly smeared structures. This is consistent with a broken symmetry of the π^*-conduction states as mixed with the Co *d* states, resulting in a non-negligible signal with *s*-polarization.

In order to interpret the experimental results discussed above, we have simulated the NEXAFS spectra for the in-plane and out-of-plane polarizations using DFT and including core-hole effects (see Sec. II B). The results are reported in Figs. 2(c) and 2(d) for Gr/Ir(111) and Gr/1ML-Co/Ir(111), respectively. In both figures, we show the spectra computed considering the half core-hole located on different carbon atoms, sampling moiré valleys, hills, and intermediate regions (gray lines) and the final spectra obtained by performing a weighted average (blue and red lines) that takes into account the C–metal distance, as detailed in the supplementary material. The comparison of the averaged spectra clearly shows a broadening of the peaks for Gr/1ML-Co/Ir(111) when compared with Gr/Ir(111), in agreement with experiments.

In order to further clarify the differences seen in the NEXAFS spectra after Co intercalation, we report in Figs. 2(e) and 2(f) the computed projected density of states (where no core-hole is considered) of the two systems, focusing on the Gr π^*- and σ^*-projections. A less structured and more broadened DOS is clearly evident for the case of Gr in Gr/1ML-Co/Ir(111), confirming the idea of a contribution from the change of the final-state eigenpairs to the experimentally observed broadening of the NEXAFS spectrum. The σ^* states located at 8.9 eV for Gr/Ir(111) are also shifted toward lower energies, at 7.6 eV, for Gr/1ML-Co/Ir(111). Such a shift allows for the superposition of the Gr σ^* and Co peaks and is in agreement with the downshift of the σ^* peaks seen for Gr/1ML-Co/Ir(111), in the measured and computed NEXAFS spectra.

By comparing the NEXAFS spectra obtained with the half core-hole located on different carbon atoms, it is evident that, in the case of Gr/Ir(111), all the spectra are nearly superimposed. In contrast, for Gr/1ML-Co/Ir(111), the position of the maxima of the different spectra spans a larger range of energies. This initial state effect is clearly one of the contributions to the smearing of the final averaged spectra. On the other hand, a close look at the same individual contributions also shows that the Gr/1ML-Co/Ir(111) spectra present broader features than Gr/Ir(111), which can be ascribed to the hybridized Co–C states (changes in the final state wavefunctions and eigenvalues). We can then conclude that both mechanisms (changes in the initial- and final-state eigenpairs) contribute to the observed broadening of the NEXAFS spectra.

Besides the broadening of the spectra, a shift in the energy position of the σ^* and π^* main peaks of Gr/1ML-Co/Ir(111) with respect to Gr/Ir(111) is observed. In agreement with experiments, where a shift of about 0.8 V is measured, the main σ^* peak is found in calculations 1.1 eV lower in energy for Gr/1ML-Co/Ir(111) than for Gr/Ir(111). This means that the weaker the Gr–metal interaction [Gr/Ir(111) compared to Gr/1ML-Co/Ir(111), but also C atoms further away from the surface in the moiré structure of Gr/1ML-Co/Ir(111)], the higher the energy of the main σ^* peak in the NEXAFS spectra. A downshift in the energy of the electronic σ^* bands calculated for Gr/Co with respect the Gr layer is reported in Fig. 6 (Sec. III B), confirming the observed shift of the onset of the σ^* transition in the C K edge and the influence of the Co layer under graphene even on the empty states far from the Fermi level.

The detailed comparison between the C K edge and the simulated NEXAFS spectra and the projected density of empty states clearly reproduce both the broadening and the energy shift of the C states, and the superposition of these states with Co states, signatures of the hybridization between Gr and Co orbitals, resulting also in the spin polarization of the Gr states. It is interesting to notice that these features are already present in the computed DOS of Gr/Co(0001), in which the Gr corrugation due to the moiré pattern is not included. In fact, Fig. S4 of the supplementary material and Fig. 6 in Sec. III B, again corroborate the hybridization mechanism as responsible for the broadening observed in the NEXAFS spectra. This adds up to the structural effect due to the moiré structure, being, however, much smaller than the hybridization mechanism, as shown in the supplementary material.

B. Co intercalation: Angle-resolved inverse photoemission

We will now address the empty electronic structure, paying special attention to image-potential states (ISs). Figure 3 displays the AR-IPES spectra acquired on clean Ir(111), Gr/Ir(111), and Gr/1ML-Co/Ir(111). The angle-resolved measurements were performed by rotating the sample from normal incidence to 18° along the $[\bar{1}\bar{1}2]_{\mathrm{Ir}}$ axis, i.e., along the $\bar{\Gamma} - \bar{\mathrm{K}}$ direction of the surface Brillouin zone (SBZ), shown below the [(c) and (d)] panels of Fig. 1. The Ir(111) spectra [Fig. 3(a)] are characterized by two main features. The first one, slightly dispersive and located close to the Fermi level (E_{F}), is related to transitions toward Ir 5*d* states.[29] The second feature, labeled *I*, is detected at 5.1 eV. Considering a work function of 5.8 eV for Ir(111),[57] this corresponds to a binding energy (BE) (with respect to the vacuum level) of 0.7 eV for the *I* state, which is well within the BE range reported for the n = 1 IS of several other TM (111) surfaces.[58,59]

AR-IPES spectra from Gr/Ir(111) are reported in Fig. 3(b). They do not present any appreciable difference with respect to the clean Ir(111) surface, since Gr basically grows as an almost free-standing ordered sheet on Ir(111), without affecting the states localized at the surface.[60] An important exception is peak I', which shifts toward lower energies, lying at 3.9 eV in the normal incidence spectrum. A similar feature is reported for both HOPG and Gr, and it is attributed to an image potential state.[12,61] Considering that epitaxial Gr decreases the work function of Ir(111) to 4.65 eV,[57] the BE of such a state is 0.8 eV, i.e., similar to the value found for Ir(111). Co deposition on top of the graphene layer leaves the AR-IPES spectral density almost unperturbed, except for a decrease in the intensity of all the empty electronic states with respect to the Ir substrate.

Finally, AR-IPES spectra for Co-intercalated Gr/Ir(111), reported in Fig. 3(c), show an attenuation of bulk features close to E_{F}, while the peak corresponding to the IS labeled I'' is now located at about 2.8 eV. The work function of Gr/1ML-Co/Ir(111) is considerably reduced to a value around 3.3 eV,[62] thus giving an IS binding energy of about 0.5 eV in this system. After the intercalation of the first Co layer, the surface component of the Ir 4*f* surface states is quenched and the Rashba–Shockley state disappears,[60] as observed in photoemission experiments. These Ir(111) surface hallmarks, preserved with the graphene cover[60] and also when cobalt is deposited on top, are damped by the Co–Ir interaction if the Co layer is sandwiched between graphene and the Ir substrate, inducing a strong modification of the surface potential. The characteristics of the I'' state, therefore, account for the modifications in the surface potential due to the work function lowering[62] and a different screening due to the presence of the metal layer on Ir(111).

The energy dispersion $E(\mathbf{k})$ along the $\bar{\Gamma} - \bar{\mathrm{K}}$ direction of the image-potential states *I*, I', and I'' is shown in Fig. 4, together with the experimental results of Ref. 23 measured by means of two-photon photoemission. The *I* and I'' states of Ir(111) and Gr/1ML-Co/Ir(111) present a small dispersion, not allowing for a sensible evaluation of the their corresponding effective masses. This is instead possible for the I' state, visible on a larger **k**-space region and showing a sizable dispersion. The parabolic fit of the energy dispersion, shown as a red line in Fig. 4, gives an effective mass of 1.1 m_{e}. In addition, the analysis of the I' state on a wider **k**-space region definitively confirms the attribution of this feature to an IS done in the previously reported 2PPE analysis.[23]

In order to explore a **k**-region closer to the $\bar{\mathrm{K}}$ point of the SBZ, where C-derived structures are expected, we extended the AR-IPES investigation to larger incidence angles for the Gr/Ir(111) and the

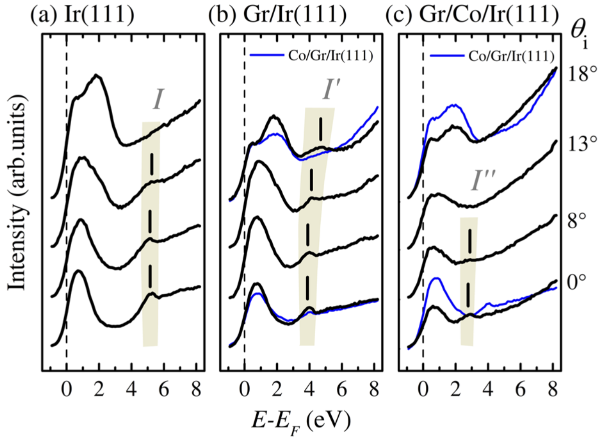

FIG. 3. AR-IPES spectra taken at various angles along the $\bar{\Gamma} - \bar{\mathrm{K}}$ direction of: (a) Ir(111), (b) Gr/Ir(111), and (c) Gr/1ML-Co/Ir(111). Spectra related to as-deposited 1ML-Co/Gr/Ir(111), acquired at selected angles, are drawn in panels (b) and (c) with thinner blue lines after an appropriate normalization. The spectra were acquired at room temperature.

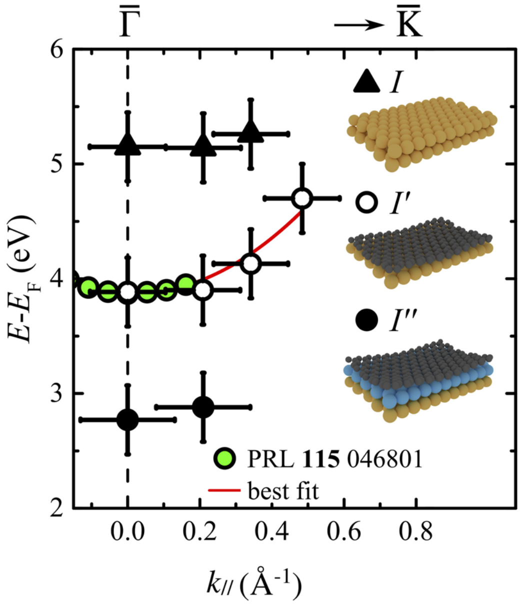

FIG. 4. Experimental AR-IPES data showing the momentum dispersion of states *I*, I', and I''. Experimental results from Ref. 23 are added for comparison. The red line represents the best fit of I' dispersion.

Gr/1ML-Co/Ir(111) samples. Our results are presented in Figs. 5(a) and 5(b): close to E_F, the spectra are dominated by the Ir(111) substrate contribution, as discussed in the supplementary material. We focus here on the most significant features present at higher energies, highlighted by a shaded area and labeled as G' and G'' for Gr/Ir(111) and Gr/1ML-Co/Ir(111), respectively. In the case of Gr/Ir(111), the shape, intensity, and angular dispersion of G' are in good agreement with the AR-IPES results of highly oriented pyrolytic graphite (HOPG)[61] and of multilayer Gr grown on 6H–SiC(0001),[12] where G' is attributed to an electronic transition to the anti-bonding π^* state. For increasing incidence angle, G' shifts toward lower energies. Its $E(\mathbf{k})$ dispersion is plotted in Fig. 6 (orange dots), where the experimental points show a linear dispersion whose extrapolation crosses E_F at the $\bar{K}$ point of the SBZ, as expected for the Dirac cone of Gr. Cobalt deposited on top of the graphene layer does not influence the topology of the Dirac cone, and the linearity is preserved, as deduced by the blue spectra reported in Fig. 5 for 1ML-Co/Gr/Ir(111). Similar peaks related to transitions to the π^* states of the Dirac cone are also found for Gr/1ML-Co/Ir(111), but shifted about 1 eV toward lower energies. They are labeled as G'' in Fig. 5(b), and their dispersion is shown in Fig. 6 (light blue dots).[63]

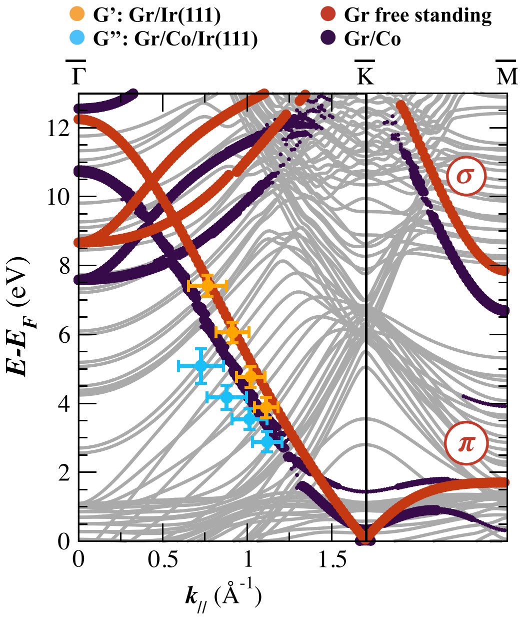

FIG. 6. AR-IPES data for Gr/Ir(111) (G', orange dots) and Gr/1ML-Co/Ir(111) (G'', light blue dots) compared to the bands computed, respectively, for freestanding Gr (red dots) and flat Gr/Co(0001) (blue dots), taken as models of the two measured systems as explained in the main text. The bands were computed in the 1 × 1 unit cell and projected on atomic orbitals (after a Lödwin orthogonalization is performed, as implemented in the QUANTUM ESPRESSO package[40,41]). In the plot, the size of the dots corresponds to the projection amplitude of the Kohn–Sham orbitals of the whole system onto C atomic orbitals (graphene). For simplicity, only four dot sizes are shown, corresponding to 5%, 15%, 30%, and 50%, respectively. Using the LDA lattice parameter of Co-bulk (a = 2.430 Å), $\bar{K}$ is located at 1.7238 Å^{-1}. This is compatible with the $\bar{K}$ point of the Gr/Ir(111) SBZ, set at 1.70 ± 0.02 Å^{-1} from LEED and in agreement with Ref. 18.

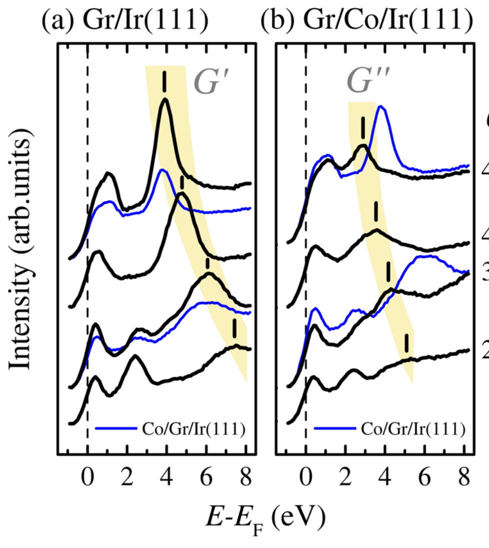

FIG. 5. AR-IPES spectra taken at various angles along the $\bar{\Gamma} - \bar{K}$ direction of: (a) Gr/Ir(111) and (b) Gr/1ML-Co/Ir(111). Spectra related to as-deposited 1ML-Co/Gr/Ir(111), acquired at selected angles, are drawn with thinner blue lines after an appropriate normalization.

In order to better understand the $E(\mathbf{k})$ evolution of Gr empty states, we compare our AR-IPES data with the band structure computed within Kohn–Sham DFT. For a full theoretical simulation, it would be in principle necessary to compute the bands for a 10 × 10 Gr layer on top of the metal surface, and then to unfold the electronic states to the Gr primitive cell.[64–66] However, we preferred to follow a simpler approach performing simulations for the 1 × 1 counterparts of Gr/Ir(111) and Gr/1ML-Co/Ir(111), namely, freestanding Gr and Gr/Co(0001) treated in their primitive cells. The choice of freestanding graphene is justified by the weak Gr/Ir interaction. The Co(0001) surface, in contrast with Ir, has a lattice parameter similar to graphene, and therefore, the interface can be described by a 1 × 1 unit cell. On the other hand, the fact that the two components of the interface are commensurate results in a graphene sheet with no corrugation, contrary to what happens for Gr/1ML-Co/Ir(111). The validity of the above approximation is supported by the similarity of the electronic structure of the systems, as explained in detail in the supplementary material, and allows for a simpler analysis of the band dispersion. The computed results for the Gr π^* bands are also reported in Fig. 6 as red and blue dots for Gr and Gr/Co(0001), respectively. The size of the dots corresponds to the projection amplitude of the Kohn–Sham orbitals of the whole system onto atomic orbitals of graphene, and the labels, π and σ, correspond to Cp_z and C (s, p_x, p_y) orbital symmetries, respectively. In the figure, the dot scale ranges from 5% to 50%, indicating a projection amplitude of at least the given value, justifying the apparent discontinuity of the bands. A plot including the C projected bands for a larger reciprocal space region is presented in Fig. S5 of the supplementary material. Notwithstanding the difference between the systems investigated, a good qualitative agreement is found between the experimental G' feature and the dispersion of the π^* bands of

Gr. Similar to freestanding Gr, the π^* band starts at the $\bar{\Gamma}$ point at a large energy (10.75 eV) and ends up close to E_F at the $\bar{K}$ point, forming a Dirac cone. Good agreement is also found between the experimental behavior of the G'' feature and the theoretical modeling. In particular, the downward shift in energy for the Gr states in Gr/1ML-Co/Ir(111) with respect to Gr/Ir(111) is well reproduced by calculations.

Interestingly, an energy shift of about 2 eV of the occupied Gr π-bands at the $\bar{\Gamma}$ point has also been reported in (direct) photoemission upon 1ML-Co intercalation.[19,62] However, both empty state dispersion and the good agreement with theoretical results prove that the Co intercalation effect cannot be simply modeled as a downshift of the Gr-bands, but rather needs to include hybridization effects, which are expected also for empty states of the Gr/1ML–Co/Ir(111) interface, close to the Fermi level. Unambiguous detection of such states by IPES is prevented by the presence of the Ir states dominating the spectra close to the Fermi level. However, an experimental signature has been already clearly observed in the broadening of the C K edge ascribed to hybridized Co–C states, confirmed by the computed projected density of states shown in Fig. 2.

IV. CONCLUSIONS

The intercalation of Co on Gr/Ir(111) induces a significant modification of the Gr states at the interface, while Co deposition on top of Gr/Ir(111) preserves the graphene electronic structure. Thanks to the negligible bulk solubility of Co atoms in the Ir substrate, Co sandwiched between Ir and Gr constitutes a single homogeneous layer influencing the Gr electronic structure. The downward shift of the Dirac cone is unveiled by AR-IPES and DFT calculations. A larger corrugation of Gr upon Co intercalation and the symmetry breaking of the π/σ states hybridized with the metallic Co bands induce also a broadening of the NEXAFS features for Gr/1ML-Co/Ir(111) when compared with Gr/Ir(111), as confirmed by the evolution of the projected density of empty states deduced by DFT calculations.

A description of the changes occurring to the empty-state electronic structure during the various steps leading to the formation of Co-intercalated Gr/Ir(111), starting from the bare Ir(111) substrate, is unraveled by AR-IPES. Thanks to its angular resolution, it provides complementary information on the spectroscopic features related to the Gr layer. In particular, the unoccupied π^* states shift away from the Fermi level along the $\bar{\Gamma} - \bar{K}$ direction. It is worth noting that the deposition of Co on top of the Gr/Ir(111) structure does not modify the Dirac cone, consistent with the formation of Co clusters,[32] while the Co-intercalation induces a shift of the Dirac cone and a symmetry breaking of the π/σ states. The image states of Ir(111), more sensitive to the potential at the surface, are almost unperturbed when Gr covers the surface, even when the Co is deposited on the Gr cover, while they are depressed and shifted by the potential altered by the intercalated Co layer. Combined AR-IPES, NEXAFS, and DFT have proved to be particularly effective in determining in detail the empty electronic structure of interacting graphene systems, unveiling the clear transition from a nearly freestanding to a hybridized character of the graphene band structure.

SUPPLEMENTARY MATERIAL

See the supplementary material for the detailed description of the core-hole positions used to average the computed NEXAFS spectra, the similarity of the DOS for Gr and Gr/Ir(111), and for Gr/Co(0001) and Gr/1ML-Co/Ir(111). AR-IPES spectra acquired on the Ir(111) substrate and a figure summarizing the major spectroscopic changes occurring during the various phases of Co intercalation are also included.

ACKNOWLEDGMENTS

We gratefully acknowledge stimulating discussions with Dario A. Leon. We also acknowledge Elettra Sincrotrone Trieste for providing access to its synchrotron radiation facilities and thank P. Lacovig for assistance in using beamline SuperESCA. This work was partially supported by the MaX—MAterials design at the eXascale—Centre of Excellence, funded by the European Union program H2020-INFRAEDI-2018-1 (Grant No. 824143). Computational time on the Marconi-A2 machine at CINECA was provided by the Italian ISCRA program.

DATA AVAILABILITY

The data that support the findings of this study are available within the article and its supplementary material.

REFERENCES

[1] H. Vita, S. Böttcher, P. Leicht, K. Horn, A. Shick, and F. Máca, Phys. Rev. B **90**, 165432 (2014).

[2] G. Avvisati, C. Cardoso, D. Varsano, A. Ferretti, P. Gargiani, and M. G. Betti, Nano Lett. **18**, 2268 (2018).

[3] M. Bazarnik, J. Brede, R. Decker, and R. Wiesendanger, ACS Nano **7**, 11341 (2013).

[4] G. Avvisati, P. Gargiani, P. Mondelli, F. Presel, A. Baraldi, and M. G. Betti, Phys. Rev. B **98**, 115412 (2018).

[5] G. Avvisati, P. Mondelli, P. Gargiani, and M. G. Betti, Appl. Surf. Sci. **432**, 2 (2018).

[6] G. Avvisati, P. Gargiani, D. Lizzit, M. Valvidares, P. Lacovig, C. Petrillo, F. Sacchetti, and M. G. Betti, Appl. Surf. Sci. **527**, 146599 (2020).

[7] A. K. Geim and K. S. Novoselov, Nat. Mater. **6**, 183 (2007).

[8] E. Sutter, P. Albrecht, F. E. Camino, and P. Sutter, Carbon **48**, 4414 (2010).

[9] A. K. Geim, Science **324**, 1530 (2009).

[10] L. Huang, Y. Pan, L. Pan, M. Gao, W. Xu, Y. Que, H. Zhou, Y. Wang, S. Du, and H.-J. Gao, Appl. Phys. Lett. **99**, 163107 (2011).

[11] R. Decker, J. Brede, N. Atodiresei, V. Caciuc, S. Blügel, and R. Wiesendanger, Phys. Rev. B **87**, 041403 (2013).

[12] I. Forbeaux, J.-M. Themlin, and J.-M. Debever, Phys. Rev. B **58**, 16396 (1998).

[13] P. Sutter, J. T. Sadowski, and E. Sutter, Phys. Rev. B **80**, 245411 (2009).

[14] M. Scardamaglia, G. Forte, S. Lizzit, A. Baraldi, P. Lacovig, R. Larciprete, C. Mariani, and M. G. Betti, J. Nanopart. Res. **13**, 6013 (2011).

[15] I. Pletikosić, M. Kralj, P. Pervan, R. Brako, J. Coraux, A. T. N'Diaye, C. Busse, and T. Michely, Phys. Rev. Lett. **102**, 056808 (2009).

[16] A. T. N'Diaye, M. Engler, C. Busse, D. Wall, N. Buckanie, F.-J. M. zu Heringdorf, R. van Gastel, B. Poelsema, and T. Michely, New J. Phys. **11**, 039801 (2009).

[17] A. Dahal and M. Batzill, Nanoscale **6**, 2548 (2014).

[18] D. Pacilè, P. Leicht, M. Papagno, P. M. Sheverdyaeva, P. Moras, C. Carbone, K. Krausert, L. Zielke, M. Fonin, Y. S. Dedkov, F. Mittendorfer, J. Doppler, A. Garhofer, and J. Redinger, Phys. Rev. B **87**, 035420 (2013).

[19] D. Pacilè, S. Lisi, I. Di Bernardo, M. Papagno, L. Ferrari, M. Pisarra, M. Caputo, S. K. Mahatha, P. M. Sheverdyaeva, P. Moras, P. Lacovig, S. Lizzit, A. Baraldi, M. G. Betti, and C. Carbone, Phys. Rev. B **90**, 195446 (2014).

[20] L. Kong, C. Bjelkevig, S. Gaddam, M. Zhou, Y. H. Lee, G. H. Han, H. K. Jeong, N. Wu, Z. Zhang, J. Xiao, P. A. Dowben, and J. A. Kelber, J. Phys. Chem. C **114**, 21618 (2010).

[21] M. S. Jagadeesh, A. Calloni, G. Bussetti, L. Duò, and F. Ciccacci, Phys. Status Solidi **255**, 1700415 (2018).

[22] S. Bhardwaj, M. Kumar, C. C. Cudia, M. Pedio, and C. Cepek, Phys. Status Solidi **249**, 2519 (2012).

[23] S. Tognolini, S. Achilli, L. Longetti, E. Fava, C. Mariani, M. I. Trioni, and S. Pagliara, Phys. Rev. Lett. **115**, 046801 (2015).

[24] Y. Lin, Y. Li, J. T. Sadowski, W. Jin, J. I. Dadap, M. S. Hybertsen, and R. M. Osgood, Jr., Phys. Rev. B **97**, 165413 (2018).

[25] S. Bose, V. M. Silkin, R. Ohmann, I. Brihuega, L. Vitali, C. H. Michaelis, P. Mallet, J. Y. Veuillen, M. A. Schneider, E. V. Chulkov, P. M. Echenique, and K. Kern, New J. Phys. **12**, 023028 (2010).

[26] V. M. Silkin, J. Zhao, F. Guinea, E. V. Chulkov, P. M. Echenique, and H. Petek, Phys. Rev. B **80**, 121408 (2009).

[27] N. Armbrust, J. Güdde, P. Jakob, and U. Höfer, Phys. Rev. Lett. **108**, 056801 (2012).

[28] G. Berti, A. Calloni, A. Brambilla, G. Bussetti, L. Duò, and F. Ciccacci, Rev. Sci. Instrum. **85**, 073901 (2014).

[29] A. Calloni, M. Cozzi, M. S. Jagadeesh, G. Bussetti, F. Ciccacci, and L. Duò, J. Phys.: Condens. Matter **30**, 015001 (2018).

[30] I. Pletikosić, M. Kralj, D. Šokčević, R. Brako, P. Lazić, and P. Pervan, J. Phys.: Condens. Matter **22**, 135006 (2010).

[31] G. Avvisati, S. Lisi, P. Gargiani, A. Della Pia, O. De Luca, D. Pacilè, C. Cardoso, D. Varsano, D. Prezzi, A. Ferretti, and M. G. Betti, J. Phys. Chem. C **121**, 1639 (2017).

[32] J. Drnec, S. Vlaic, I. Carlomagno, C. J. Gonzalez, H. Isern, F. Carlà, R. Fiala, N. Rougemaille, J. Coraux, and R. Felici, Carbon **94**, 554 (2015).

[33] I. Carlomagno, J. Drnec, A. M. Scaparro, S. Cicia, S. Vlaic, R. Felici, and C. Meneghini, J. Appl. Phys. **120**, 195302 (2016).

[34] J. E. Bickel, F. Meier, J. Brede, A. Kubetzka, K. von Bergmann, and R. Wiesendanger, Phys. Rev. B **84**, 054454 (2011).

[35] D. T. Pierce, R. J. Celotta, G.-C. Wang, W. N. Unertl, A. Galejs, C. E. Kuyatt, and S. R. Mielczarek, Rev. Sci. Instrum. **51**, 478 (1980).

[36] F. Ciccacci and G. Chiaia, J. Vac. Sci. Technol., A **9**, 2991 (1991).

[37] F. Ciccacci, E. Vescovo, G. Chiaia, S. De Rossi, and M. Tosca, Rev. Sci. Instrum. **63**, 3333 (1992).

[38] M. Finazzi, A. Bastianon, G. Chiaia, and F. Ciccacci, Meas. Sci. Technol. **4**, 234 (1993).

[39] F. Ciccacci, S. De Rossi, A. Taglia, and S. Crampin, J. Phys.: Condens. Matter **6**, 7227 (1994).

[40] P. Giannozzi, S. Baroni, N. Bonini, M. Calandra, R. Car, C. Cavazzoni, D. Ceresoli, G. L. Chiarotti, M. Cococcioni, I. Dabo *et al.*, J. Phys.: Condens. Matter **21**, 395502 (2009).

[41] P. Giannozzi, O. Andreussi, T. Brumme, O. Bunau, M. Buongiorno Nardelli, M. Calandra, R. Car, C. Cavazzoni, D. Ceresoli, M. Cococcioni, N. Colonna, I. Carnimeo, A. Dal Corso, S. de Gironcoli, P. Delugas, R. A. DiStasio, Jr., A. Ferretti, A. Floris, G. Fratesi, G. Fugallo, R. Gebauer, U. Gerstmann, F. Giustino, T. Gorni, J. Jia, M. Kawamura, H.-Y. Ko, A. Kokalj, E. Küçükbenli, M. Lazzeri, M. Marsili, N. Marzari, F. Mauri, N. L. Nguyen, H.-V. Nguyen, A. O. de-la Roza, L. Paulatto, S. Poncé, D. Rocca, R. Sabatini, B. Santra, M. Schlipf, A. P. Seitsonen, A. Smogunov, I. Timrov, T. Thonhauser, P. Umari, N. Vast, X. Wu, and S. Baroni, J. Phys.: Condens. Matter **29**, 465901 (2017).

[42] J. P. Perdew and A. Zunger, Phys. Rev. B **23**, 5048 (1981).

[43] O. Bunău and M. Calandra, Phys. Rev. B **87**, 205105 (2013).

[44] C. Gougoussis, M. Calandra, A. P. Seitsonen, and F. Mauri, Phys. Rev. B **80**, 075102 (2009).

[45] M. Taillefumier, D. Cabaret, A.-M. Flank, and F. Mauri, Phys. Rev. B **66**, 195107 (2002).

[46] L. Triguero, L. G. M. Pettersson, and H. Ågren, Phys. Rev. B **58**, 8097 (1998).

[47] B. Hetényi, F. De Angelis, P. Giannozzi, and R. Car, J. Chem. Phys. **120**, 8632 (2004).

[48] M. Cavalleri, M. Odelius, D. Nordlund, A. Nilsson, and L. G. M. Pettersson, Phys. Chem. Chem. Phys. **7**, 2854 (2005).

[49] G. Fratesi, S. Achilli, N. Manini, G. Onida, A. Baby, A. Ravikumar, A. Ugolotti, G. P. Brivio, A. Milani, and C. S. Casari, Materials **11**, 2556 (2018).

[50] A. T. N'Diaye, J. Coraux, T. Plasa, C. Busse, and T. Michely, New J. Phys. **10**, 043033 (2008).

[51] D. A. Duncan, N. Atodiresei, S. Lisi, P. J. Blowey, V. Caciuc, J. Lawrence, T.-L. Lee, M. G. Betti, P. K. Thakur, A. Della Pia, S. Blügel, G. Costantini, and D. P. Woodruff, Phys. Rev. Mater. **3**, 124001 (2019).

[52] K. Suenaga and M. Koshino, Nature **468**, 1088 (2010).

[53] D. Pacilè, M. Papagno, A. F. Rodríguez, M. Grioni, L. Papagno, Ç. Ö. Girit, J. C. Meyer, G. E. Begtrup, and A. Zettl, Phys. Rev. Lett. **101**, 066806 (2008).

[54] S. Entani, S. Ikeda, M. Kiguchi, K. Saiki, G. Yoshikawa, I. Nakai, H. Kondoh, and T. Ohta, Appl. Phys. Lett. **88**, 153126 (2006).

[55] M. Scardamaglia, S. Lisi, S. Lizzit, A. Baraldi, R. Larciprete, C. Mariani, and M. G. Betti, J. Phys. Chem. C **117**, 3019 (2013).

[56] M. Weser, Y. Rehder, K. Horn, M. Sicot, M. Fonin, A. B. Preobrajenski, E. N. Voloshina, E. Goering, and Y. S. Dedkov, Appl. Phys. Lett. **96**, 012504 (2010).

[57] D. Niesner, T. Fauster, J. I. Dadap, N. Zaki, K. R. Knox, P.-C. Yeh, R. Bhandari, R. M. Osgood, M. Petrović, and M. Kralj, Phys. Rev. B **85**, 081402 (2012).

[58] D. Straub and F. J. Himpsel, Phys. Rev. B **33**, 2256 (1986).

[59] S. L. Hulbert, P. D. Johnson, N. G. Stoffel, W. A. Royer, and N. V. Smith, Phys. Rev. B **31**, 6815 (1985).

[60] A. Varykhalov, D. Marchenko, M. R. Scholz, E. D. L. Rienks, T. K. Kim, G. Bihlmayer, J. Sánchez-Barriga, and O. Rader, Phys. Rev. Lett. **108**, 066804 (2012).

[61] I. Schäfer, M. Schlüter, and M. Skibowski, Phys. Rev. B **35**, 7663 (1987).

[62] S. Vlaic, A. Kimouche, J. Coraux, B. Santos, A. Locatelli, and N. Rougemaille, Appl. Phys. Lett. **104**, 101602 (2014).

[63] See also Fig. S7 of the supplementary material summarizing the major spectroscopic changes occurring during the various phases of Co intercalation.

[64] V. Popescu and A. Zunger, Phys. Rev. Lett. **104**, 236403 (2010).

[65] P. V. C. Medeiros, S. Stafström, and J. Björk, Phys. Rev. B **89**, 041407 (2014).

[66] P. V. C. Medeiros, S. S. Tsirkin, S. Stafström, and J. Björk, Phys. Rev. B **91**, 041116 (2015).

Empty electron states in cobalt-intercalated graphene: Supplementary Material

Alberto Calloni,[1] Gianlorenzo Bussetti,[1] Giulia Avvisati,[2] Madan S. Jagadeesh,[1] Daniela Pacilè,[3] Andrea Ferretti,[4] Daniele Varsano,[4] Claudia Cardoso,[4] Lamberto Duò,[1] Franco Ciccacci,[1] and Maria Grazia Betti[2]
[1] *Dipartimento di Fisica, Politecnico di Milano, piazza Leonardo da Vinci 32, I-20133 Milano, Italy*
[2] *Dipartimento di Fisica, Università di Roma "La Sapienza", I-00185 Roma, Italy*
[3] *Dipartimento di Fisica, Università della Calabria, I-87036 Arcavacata di Rende, (Cs) Italy*
[4] *Centro S3, CNR-Istituto Nanoscienze, I-41125 Modena, Italy*

Keywords: intercalation; inverse photoemission; graphene; moiré structure; Ir(111)

I. CORE LEVELS

In Fig. 1 we show C 1s core level spectra, taken at $h\nu$=400 eV, of Gr/Ir(111) (black curve), 1ML Co/Gr/Ir(111) (blue curve) and Gr/1ML-Co/Ir(111) (red curve). The C 1s peak of Gr/Ir(111) exhibits a sharp profile centred at 284.13 eV, with a faint broadening after the deposition of Co atoms. Indeed, metals tend to form 3D clusters on top of graphene without long-range order[1,2] in the present experimental conditions (thermal evaporation of Co and sample at RT). As discussed in a previous publication,[3] upon intercalation, a double peaked line-shape arises at higher binding energy, with main components at 284.92 eV and 284.42 eV, due to carbon atoms in valleys and hills, respectively.

II. SIMULATION OF THE NEXAFS SPECTRA

The ground state electronic structure was computed within Density functional theory using the QUANTUM ESPRESSO (QE) package[4,5] with the LDA exchange-correlation functional, according to the Perdew-Zuger parametrization.[6] The NEXAFS spectra were simulated using the `Xspectra` code[7–9] within the QE distribution. The absorption from the core levels was calculated considering a carbon pseudopotential including a half core-hole (HCH).[10–13] This approach can be rationalized in terms of the Slater transition-state method,[14,15] where, given the Janak's theorem[16] stating $\frac{dE}{df_i} = \epsilon_i$ and valid for KS-DFT, by Taylor expansion one approximates ionization energies as eigenvalues computed at half occupation, $E[f_i = 0] - E[f_i = 1] = -\epsilon_i[f_i = \frac{1}{2}] + o(f_i^3)$. Such an approach can be also applied to (independent-particle) optical absorption, where half occupation would be needed for both the occupied and empty states involved in the one-particle transitions. Nevertheless, the half occupation of the final state is typically disregarded because of convenience and in view of the (usually) more delocalized nature of the states.

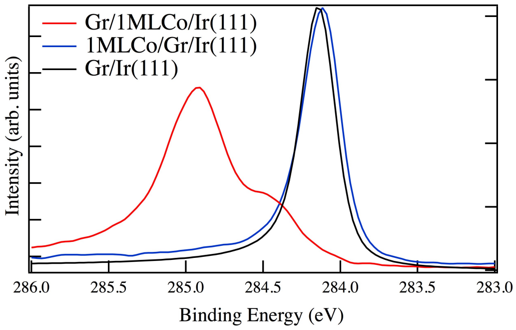

FIG. 1. C 1s core level spectra, taken at $h\nu$=400 eV, of Gr/Ir(111) (black curve), 1ML-Co/Gr/Ir(111) (blue curve) and Gr/1ML-Co/Ir(111) (red curve).

One HCH atom per cell (*i.e.* every 200 C atoms), substituting a regular C atom, was placed at different positions in order to sample both graphene sublattices located in the valleys, intermediate, and peak regions of the moiré superstructure. Since the calculation of all the 200 spectra for the two surfaces is very demanding computationally, the spectrum shown in the main text was obtained by averaging the spectra over the 8 selected sampling points described above. The average considers that the differences between spectra computed for difference C sites depend mainly on the interaction with the underlying metal layer, and this depends in turn on the graphene-metal distance (see also Ref. 17 for a discussion of the XPS spectra in the presence of the moiré corrugation). For this reason each of the spectra was weighted considering the number of C atoms at a certain graphene-metal distance. In fact, in the case of Gr/Ir, for which the graphene corrugations is smaller, the NEXAFS spectra are basically all superimposed, whereas, for Gr/Co/Ir, with a larger corrugation, the spectra vary both in intensity and energy peak position, contributing to the broadening of the averaged spectra and supporting the hypothesis of the dependence of the spectra on the graphene-metal distance.

In Fig. 2 we show the π and σ polarization of NEXAFS spectra computed for each of the 8 C sites, for Gr/Ir(111) and Gr/1ML-Co/Ir(111). In Fig. 3 we show the histogram of the C vertical positions (right side), used to weight the individual spectra and the sites corresponding to the spectra plotted in the panels of Fig. 2.

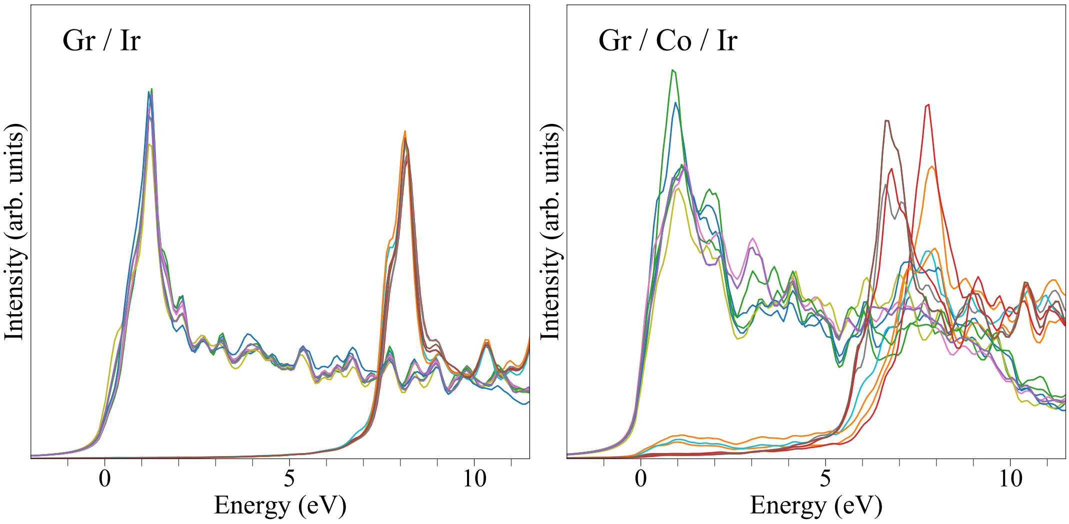

FIG. 2. Simulated NEXAFS for Gr/Ir(111) and Gr/1ML-Co/Ir(111) (left and right panel, respectively), computed for different positions of the C 1*s* half core-hole included in the calculations. Both π (lower energy peak) and σ (higher energy peak) polarization are shown.

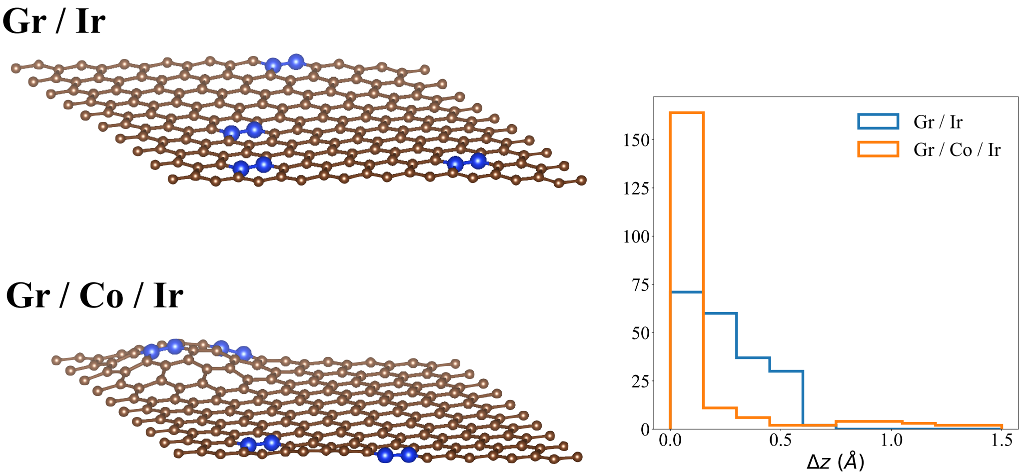

FIG. 3. Left panel: Carbon 1*s* sites sampled (by including a half-core hole) in the average over atomic sites performed to simulate the NEXAFS spectra. Right panel: histogram with the distribution of heights for the C atoms of graphene due to corrugation [blue: Gr/Ir(111); orange: Gr/1ML-Co/Ir(111)].

III. DENSITY OF STATES AND BAND STRUCTURE

In Section III B of the main text, we compare experimental AR-IPES data for Gr/Ir(111) and Gr/1ML-Co/Ir(111) with the corresponding calculated bands. However, instead of the bands computed for the complete systems, the 10×10 Gr layer on top of the metal surface, we present the bands of free-standing graphene and flat graphene/Co(0001). The reason for this is that the bands of the 10×10 unit cell would be folded, making them difficult to interpret and we would need in principle to unfold[18–20] the 10×10 Gr super cell to the Gr primitive cell. Graphene and the Co(0001) surface have similar lattice parameters (lattice mismatch smaller than 1%) and are therefore commensurate. This means that the calculation can be done in the 1×1 unit cell, since there is no moiré pattern and no graphene corrugation. Despite the structural differences, the electronic properties show many similarities. For the sake of clarity, the lattice parameters of the studied systems are collected in Tab. I.

To validate this choice, we compare the DOS of free standing graphene, with the one computed for the 10×10 Gr/Ir(111) supercell and Gr/Co(0001) with the DOS of 10×10 Gr/1ML-Co/Ir(111). The calculations used a 100×100 **k**-point grid in the case of the 1×1 unit cells, and a 6×6 **k**-point grid in the case of the supercells. In Fig. 4 we show the DOS projected on the C atoms of

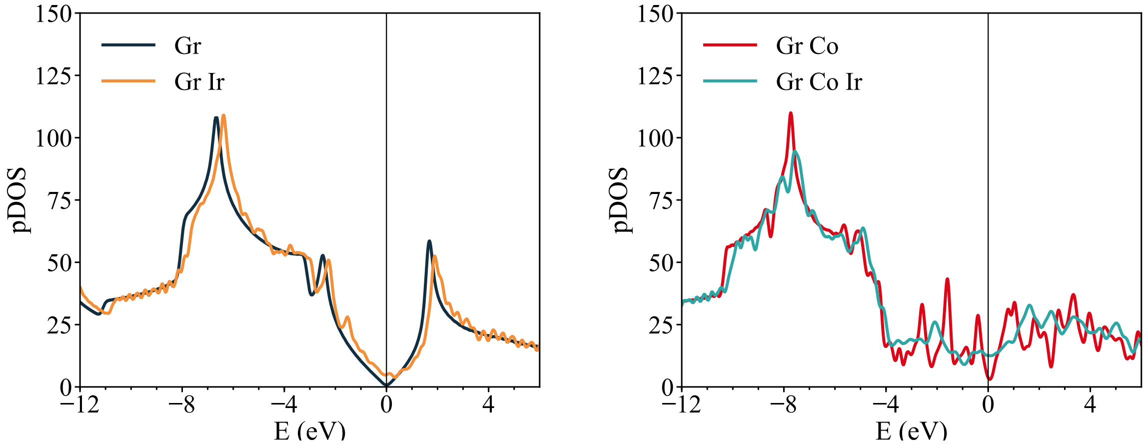

FIG. 4. Comparison of the density of states computed for free standing graphene and for the 10×10 Gr/Ir(111) supercell (left panel) and of the density of states computed for Gr/Co(0001) with the one of 10×10 Gr/1ML-Co/Ir(111) (right panel). Spin up and down channels are summed over.

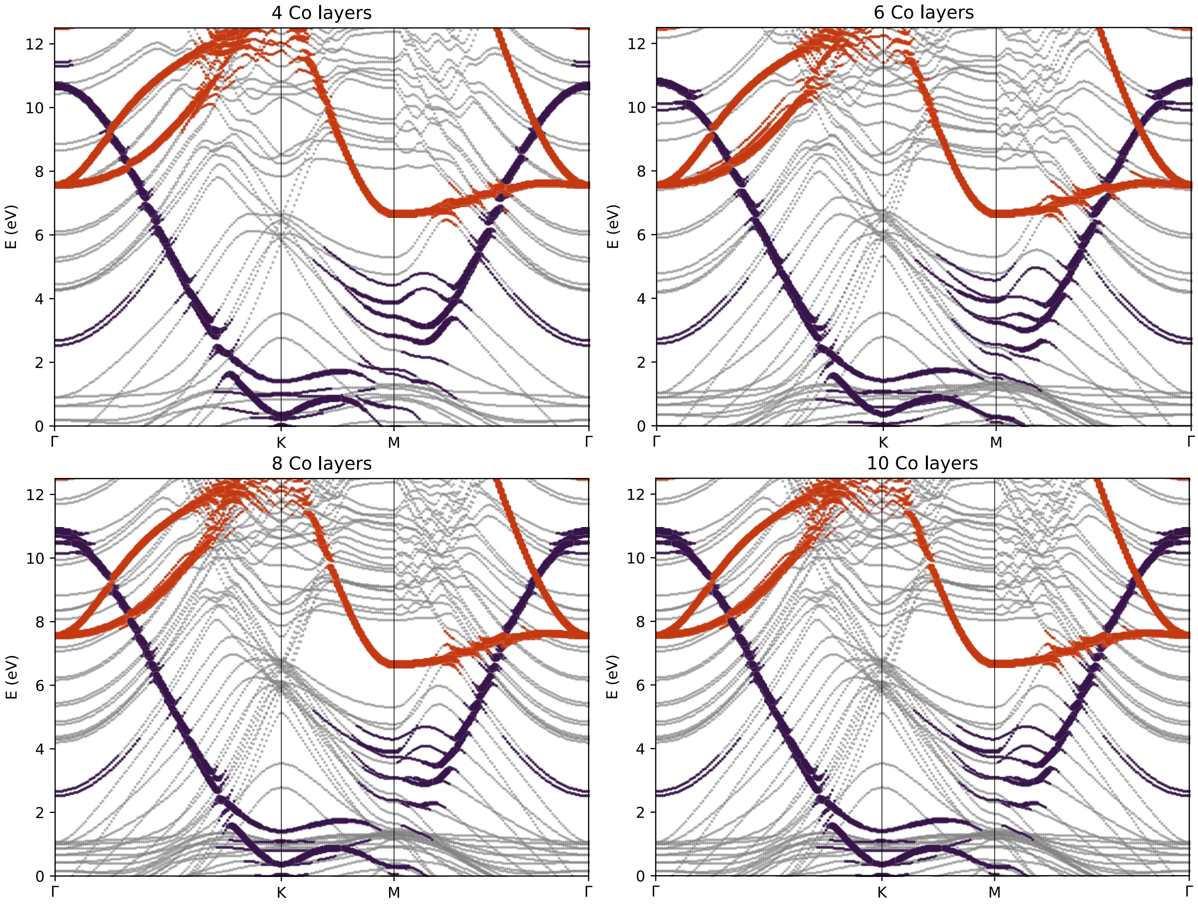

FIG. 5. Computed band structure for flat graphene/Co(0001) in the 1×1 unit cell with increasing number of Co layers. The bands were projected on carbon π^*, purple symbols, and σ^* orbitals, red symbols. Non-projected bands (governed by Co contributions) are represented in grey.

System	**Lattice parameters**		**Bond length**
Ir bulk	fcc	a =3.8252	2.7048
Co bulk	hcp	a =2.430 c/a = 1.613	2.430
Gr	2D hex	a = 2.4410	1.409
Gr/Ir(111)	2D hex	a = 24.343	–
Gr/1ML Co/Ir(111)	2D hex	a = 24.343	–

TABLE I. Lattice parameters for the systems considered in this work. Ir and Co bulk systems were computed at the LDA level (see methods in the main text). Iridium lattice was then used to build the Gr/Ir and Gr/Co/Ir moiré structures, while Cobalt bulk was used for Gr/Co(0001). In the two latter cases no lattice relaxation was performed. Graphene lattice parameter is reported for reference. All numbers are given in Å units.

the four systems. The results show that the shape of the C DOS in the supercells follows very closely the one computed for the 1 × 1 unit cells, with only minor differences. In the case of Gr/Ir, the DOS is very similar to the one of freestanding graphene, with only a small shift of about 0.21 eV towards higher energies, revealing a small p-doping. Considering that the density of state per unit cell, as computed for freestanding graphene, is given by $\rho(E) = 0.1E$ (eV^{-1}), the excess charge is about $2.2{\times}10^{-3}$ electrons per graphene unit cell or $1.1{\times}10^{-3}$ electrons per C atom.

In Fig. 5 we show the band structure (including projections) computed for flat graphene/Co(0001) in the 1 × 1 unit cell, with a number of layers varying from 4 to 10. Although the total number of states increases with the number of Co atoms considered in the calculation, the bands projected on graphene are essentially unchanged. Furthermore, this justifies the use of 4 metal layers in the calculations involving the 10×10 Gr/1ML-Co/Ir(111), in particular for the calculation of the NEXAFS spectra and the DOS, shown in Fig. 2 of the main text.

IV. ANGLE RESOLVED INVERSE PHOTOEMISSION SPECTRA

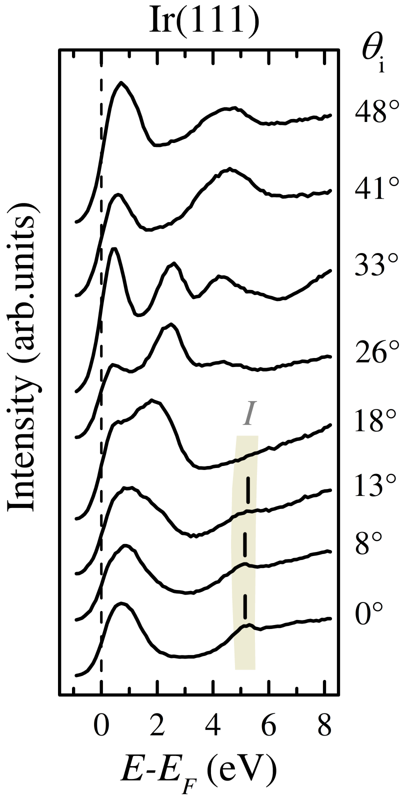

FIG. 6. Angle resolved inverse photoemission spectra acquired on Ir(111) by tilting the sample up to an angle of 48° around the $[\bar{1}\bar{1}2]_{\mathrm{Ir}}$ axis, *i.e.* along the $\bar{\Gamma} - \bar{\mathrm{K}}$ direction of the Ir(111) surface Brillouin zone. The shaded area and vertical lines highlight the position of the image-potential state I (see the main text for further details).

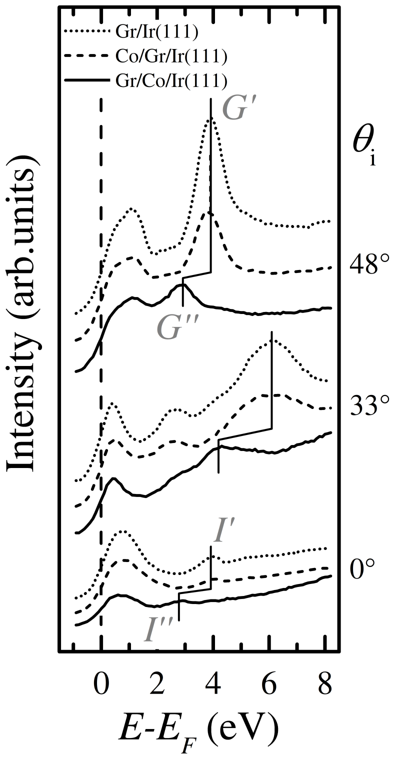

FIG. 7. Angle resolved inverse photoemission spectra acquired on Gr/Ir(111) (dotted lines), Co/Gr/Ir(111), *i.e.* after the deposition of 1 ML of cobalt onto Gr/Ir(111) (dashed lines), and Co intercalated Gr/Ir(111), namely the Gr/Co/Ir(111) surface (continuous lines). The sample was tilted around the $[\bar{1}\bar{1}2]_{\mathrm{Ir}}$ axis along the $\bar{\Gamma} - \bar{\mathrm{K}}$ direction on of the Ir(111) surface Brillouin zone. Vertical lines highlight the position of the G' and G'' graphene π^* states and, at normal incidence, the I' and I'' image-potential states (see the main text for further details). Spectra from different datasets have been rescaled and offset for a better comparison.

[1] S. Sarkar, M. L. Moser, X. Tian, X. Zhang, Y. F. Al-Hadeethi, and R. C. Haddon, Chem. Mater. **26**, 184 (2014).

[2] X. Liu, Y. Han, J. W. Evans, A. K. Engstfeld, R. Behm, M. C. Tringides, M. Hupalo, H.-Q. Lin, L. Huang, K.-M. Ho, D. Appy, P. A. Thiel, and C.-Z. Wang, Prog. Surf. Sci. **90**, 397 (2015).

[3] D. Pacilè, S. Lisi, I. Di Bernardo, M. Papagno, L. Ferrari, M. Pisarra, M. Caputo, S. K. Mahatha, P. M. Sheverdyaeva, P. Moras, P. Lacovig, S. Lizzit, A. Baraldi, M. G. Betti, and C. Carbone, Phys. Rev. B **90**, 195446 (2014).

[4] P. Giannozzi, S. Baroni, N. Bonini, M. Calandra, R. Car, C. Cavazzoni, D. Ceresoli, G. L. Chiarotti, M. Cococcioni, I. Dabo, et al., J. Phys.: Condens. Matter **21**, 395502 (2009).

[5] P. Giannozzi, O. Andreussi, T. Brumme, O. Bunau, M. Buongiorno Nardelli, M. Calandra, R. Car, C. Cavazzoni, D. Ceresoli, M. Cococcioni, N. Colonna, I. Carnimeo, A. Dal Corso, S. de Gironcoli, P. Delugas, R. A. DiStasio Jr., A. Ferretti, A. Floris, G. Fratesi, G. Fugallo, R. Gebauer, U. Gerstmann, F. Giustino, T. Gorni, J. Jia, M. Kawamura, H.-Y. Ko, A. Kokalj, E. Küçükbenli, M. Lazzeri, M. Marsili, N. Marzari, F. Mauri, N. L. Nguyen, H.-V. Nguyen, A. O. de-la Roza, L. Paulatto, S. Poncé, D. Rocca, R. Sabatini, B. Santra, M. Schlipf, A. P. Seitsonen, A. Smogunov, I. Timrov, T. Thonhauser, P. Umari, N. Vast, X. Wu, and S. Baroni, J. Phys.: Condens. Matter **29**, 465901 (2017).

[6] J. P. Perdew and A. Zunger, Phys. Rev. B **23**, 5048 (1981).

[7] O. Bunău and M. Calandra, Phys. Rev. B **87**, 205105 (2013).

[8] C. Gougoussis, M. Calandra, A. P. Seitsonen, and F. Mauri, Phys. Rev. B **80**, 075102 (2009).

[9] M. Taillefumier, D. Cabaret, A.-M. Flank, and F. Mauri, Phys. Rev. B **66**, 195107 (2002).

[10] L. Triguero, L. G. M. Pettersson, and H. Ågren, Phys. Rev. B **58**, 8097 (1998).

[11] B. Hetényi, F. De Angelis, P. Giannozzi, and R. Car, J. Chem. Phys. **120**, 8632 (2004).

[12] M. Cavalleri, M. Odelius, D. Nordlund, A. Nilsson, and L. G. M. Pettersson, Phys. Chem. Chem. Phys. **7**, 2854 (2005).

[13] F. Guido, A. Simona, N. Manini, G. Onida, A. Baby, A. Ravikumar, A. Ugolotti, G. P. Brivio, A. Milani, and C. S. Casari, Materials **11**, 2556 (2018).

[14] J. C. Slater and K. H. Johnson, Phys. Rev. B **5**, 844 (1972).

[15] K. Schwarz, Chem. Phys. **7**, 100 (1975).

[16] J. F. Janak, Phys. Rev. B **18**, 7165 (1978).

[17] G. Avvisati, S. Lisi, P. Gargiani, A. Della Pia, O. De Luca, D. Pacilè, C. Cardoso, D. Varsano, D. Prezzi, A. Ferretti, and M. G. Betti, J. Phys. Chem. C **121**, 1639 (2017).

[18] V. Popescu and A. Zunger, Phys. Rev. Lett. **104**, 236403 (2010).

[19] P. V. C. Medeiros, S. Stafström, and J. Björk, Phys. Rev. B **89**, 041407 (2014).

[20] P. V. C. Medeiros, S. S. Tsirkin, S. Stafström, and J. Björk, Phys. Rev. B **91**, 041116 (2015).

PHYSICAL REVIEW MATERIALS **00**, 004400 (2021)

Magnetic response and electronic states of well defined Graphene/Fe/Ir(111) heterostructure

Claudia Cardoso,[1] Giulia Avvisati,[2] Pierluigi Gargiani,[3] Marco Sbroscia,[2] Madan S. Jagadeesh,[2] Carlo Mariani,[2]
Dario A. Leon,[4,1] Daniele Varsano,[1] Andrea Ferretti,[1] and Maria Grazia Betti[2]
[1]*Centro S3, CNR-Istituto Nanoscienze, I-41125 Modena, Italy*
[2]*Dipartimento di Fisica, Università di Roma "La Sapienza", I-00185 Roma, Italy*
[3]*ALBA Synchrotron Light Source, Carrer de la Llum, 2-26 08290 Barcelona, Spain*
[4]*Università di Modena e Reggio Emilia, I-41125 Modena, Italy*

(Received 27 October 2020; accepted 22 December 2020; published xxxxxxxxxx)

We investigate a well defined heterostructure constituted by magnetic Fe layers sandwiched between graphene (Gr) and Ir(111). The challenging task to avoid Fe-C solubility and Fe-Ir intermixing has been achieved with atomic controlled Fe intercalation at moderate temperature below 500 K. Upon intercalation of a single ordered Fe layer in registry with the Ir substrate, an intermixing of the Gr bands and Fe d states breaks the symmetry of the Dirac cone, with a downshift in energy of the apex by about 3 eV, and well-localized Fe intermixed states induced in the energy region just below the Fermi level. First principles electronic structure calculations show a large spin splitting of the Fe states, resulting in a majority spin channel almost fully occupied and strongly hybridized with Gr π states. X-ray magnetic circular dichroism on the Gr/Fe/Ir heterostructure reveals an ordered spin configuration with a ferromagnetic response of Fe layer(s), with enhanced spin and orbital configurations with respect to the bcc-Fe bulk values. The magnetization switches from a perpendicular easy magnetization axis when the Fe single layer is lattice matched with the Ir(111) surface to a parallel one when the Fe thin film is almost commensurate with graphene.

DOI: 10.1103/PhysRevMaterials.00.004400

I. INTRODUCTION

Graphene can be a very promising spin channel material owing to its long spin-diffusion lengths of several micrometers [1], gate-tunable carrier concentration, and high electronic mobility [2]. Graphene coupled with ferromagnetic systems can open new perspectives when efficient injection of spin-polarized electrons can be achieved, as observed for a graphene membrane on Co(0001) [3]. It is well known that nearly flat epitaxial graphene of high structural quality can be formed on several magnetic $3d$ metal substrates, like the lattice-matched Ni(111) [4–7] and Co(0001) [3,8–10] surfaces. It has been shown that a tiny magnetic moment arises on the carbon atoms, induced by the strong hybridization of graphene π orbitals with Ni or Co $3d$ states [3,8,11,12]. Furthermore, graphene grown on metals protects highly reactive magnetic surfaces and stabilizes them against oxidation [13–15]. Whereas recently a large research effort has been dedicated to investigate Gr-Ni and Gr-Co heterostructures, only a few experimental results for graphene grown on Fe surfaces are available [16–18], though iron is the most widespread transition metal, and the technology of passivated Fe films with a graphene membrane can be appealing for several reasons. Among them, the considerable price reduction in comparison with other transition metal substrates and, most importantly, its strong magnetic response.

The main hurdle for the formation of graphene on top of Fe surfaces is related to the rich Fe-C phase diagram [19]. In fact, the high carbon diffusion coefficient and solubility in iron are detrimental for chemical vapor deposition processes, where a high annealing temperature is necessary to ensure high quality graphene on top of the metal surfaces. Thus, the epitaxial growth of a graphene membrane on a Fe film/single crystal is made difficult because of the formation of iron carbide, which is thermodynamically favored [19]. The epitaxial growth of graphene on Fe is also prevented because none of the bcc-Fe facets is lattice matched with graphene, at variance with close-packed surfaces of other $3d$ metals, like Co and Ni. Recently, a detailed structural study has demonstrated that the Fe(110) face, with its distorted hexagonal symmetry, can be a good candidate, because of a partial match with the graphene lattice [16,17]. In that study, the substrate temperature was kept below 675 K to guarantee the formation of a graphene membrane on iron reducing the presence of iron carbides or segregation of diluted carbon from iron.

A more challenging strategy has been proposed exploiting Fe intercalation beneath graphene [20] as a viable route to overcome the hurdles to realize a direct growth on Fe surfaces. Intercalation of metals below Gr has proven to efficiently lead to the formation of atomically smooth metallic layer(s) [8–10,12,21], in a layer-by-layer growth mode [22], where the graphene cover acts as a protective membrane of the confined epitaxial metallic layer(s) [13,14]. Recently, a scanning tunneling microscopy (STM) experiment demonstrates that successful Fe intercalation under graphene grown on Ir(111) can be obtained with the substrate temperature in the range between 450 K and 550 K [23], giving rise to a smooth Fe layer pseudomorphic with Ir(111) and a highly corrugated graphene membrane on top.

In this work, following this successful strategy for Fe growth, we have realized well-defined smooth Fe layers intercalated between Gr and Ir(111), preventing any alloying and Fe-C intermixing. By means of a combined experimental and theoretical approach, we gain a detailed insight into the physical properties of the iron-intercalated Gr/Ir(111) heterostructure. The sandwiched Fe layers present a redistribution of the minority and majority electronic density of states triggered by the spatial confinement and by the peculiar strained structural configurations, as predicted by first principles spin resolved electronic structure calculations and experimentally confirmed by angular resolved photoemission and x-ray magnetic dichroism.

II. METHODS

Angular resolved photoelectron spectroscopy (ARPES) and low-energy electron-diffraction (LEED) experiments were carried out at the Nanostructure at Surfaces laboratory, Department of Physics, Sapienza University [24]. The ARPES apparatus is equipped with a Scienta SE200 multi-channel-plate electron analyzer and a monochromatic Gammadata VUV 5000 microwave He source, with main lines at 20.218 eV (He I_α) and 40.814 eV (He II_α) photon energies. The ARPES apparatus was set for an experimental energy and angular resolution of 16 meV and 0.18°, respectively.

The x-ray magnetic circular dichroism (XMCD) measurements were performed at the BOREAS beamline of the ALBA synchrotron radiation facility [25]. Data were taken in the total electron yield (TEY) mode, by measuring the drain current with respect to a clean gold grid, used for photon flux normalization. We used two different geometries, grazing incidence (GI) with 70° incidence angle and normal incidence (NI), so to probe the magnetic signal along the easy and hard magnetic axes; further details are available in Ref. [26].

In all laboratories, the Ir(111) surface was cleaned by cycles of ion sputtering (Ar^+, 1.5–2.0 keV) and annealing (1 minute at temperatures higher than 1300 K). The quality of the obtained surface is confirmed by the sharp LEED pattern. The Gr layer was prepared by thermal decomposition of ethylene, by exposing the clean Ir surface to 5×10^{-8}–2×10^{-7} mbar of C_2H_4 and annealing at around 1300–1320 K. Metallic Fe was deposited, at 0.3 Å/min on the Gr/Ir(111) surface kept at about 500 K, in order to ensure a high quality of Fe layer(s) intercalated beneath Gr and to avoid any intermixing, that occurs at higher annealing temperature (600–800 K) [27]. The C $1s$, Ir $4f$, and Fe $2p_{3/2}$ core levels as measured at the Superesca beamline of the Elettra synchrotron radiation facility, are presented in the Supplemental Material [28].

The completion of a single layer of Fe can be identified by following the evolution of the π states of Gr in the ARPES valence band, as discussed in detail in the next sections. At the BOREAS beamline, the Fe density in the intercalated film was evaluated via its jump-edge ratio, previously calibrated with Auger electron spectroscopy, as reported in the Supporting Information of Ref. [22].

Density functional theory (DFT) simulations were carried out using the QUANTUM ESPRESSO package [29,30] where wave functions are expanded in plane waves and pseudopotentials are used to account for the electron-ion interaction. We used the local density approximation (LDA) for the exchange-correlation potential, according to the Perdew-Zunger parametrization [31]. Similarly to our previous works [26,32], we simulated the Gr/1ML-Fe/Ir(111) interface considering the complete moiré induced periodicity by using a 9 × 9 supercell of Ir(111), corresponding to a 10 × 10 supercell of pristine Gr. The lattice parameters were obtained by relaxing Ir bulk at the LDA level using ultrasoft pseudopotentials (USPP), resulting in a Ir-Ir bond distance of 2.7048 Å (corresponding to a hexagonal cell of 46.001 Bohr radius for the moiré structure). In all the calculation we included four metallic layers (3 Ir plus one Fe layer or 4 Ir layers). In order to make the two sides of the slab inequivalent we added a layer of H atoms in one of the two sides. Atomic positions were then fully relaxed (except for the two bottom Ir layers and the H saturation layer) until ionic forces were smaller than 0.001 Ry/Bohr. For all the self-consistent calculations we used a 2 × 2 grid of **k** points, ultra soft pseudopotentials to model the electron-ion interaction and a kinetic energy cutoff of 30 and 300 Ry to represent Kohn-Sham wave functions and density, respectively.

Since LDA is known to underestimate the values of the orbital magnetic moments in transition metals [33], we have adopted a DFT + U scheme [34], with a Hubbard U parameter of 2 eV. In order to compare calculated band structures with ARPES data, we applied an unfolding procedure [35,36] to the computed bands of Gr/Fe/Ir(111) and Gr/Ir(111). With this procedure, the band structure computed for the 10 × 10 supercell is mapped into the graphene 1 × 1 Brillouin zone by using the UNFOLD-X code [36]. In this way we obtain an effective band structure corresponding to the graphene unit cell. In this picture, the **k** dispersion is broadened by the break of the 1 × 1 translational symmetry induced by the 10 × 10 moiré pattern.

III. RESULTS AND DISCUSSION

A. Intercalation and structural properties

A single layer of iron, intercalated under Gr grown on Ir(111), induces a corrugation of the Gr membrane and preserves the periodicity of the moiré superstructure, superimposed to the hexagonal Gr lattice, as unraveled by the LEED patterns reported in Fig. 1(a)–1(b). The diffraction pattern of Gr/Ir(111) [Fig. 1(a)] shows bright spots in a hexagonal pattern surrounded by satellites, consistent with the moiré superstructure caused by the lattice mismatch between Gr and Ir [37,38]. After Fe intercalation, the pattern is only slightly attenuated [Fig. 1(b)], thus the first Fe layer appears commensurate to the Ir(111) surface lattice. This evidence is corroborated by a recent work [12] where STM measurements show that a few monolayers (ML) of Fe intercalated under graphene arrange in registry with the hexagonal Ir(111) surface, with a corrugation of 1.3 Å, larger than the one measured for Gr/Ir(111) [39].

We have further investigated the structural properties of this system by means of DFT at the LDA + U level. The Gr/Fe/Ir(111) heterostructure was modeled as described in

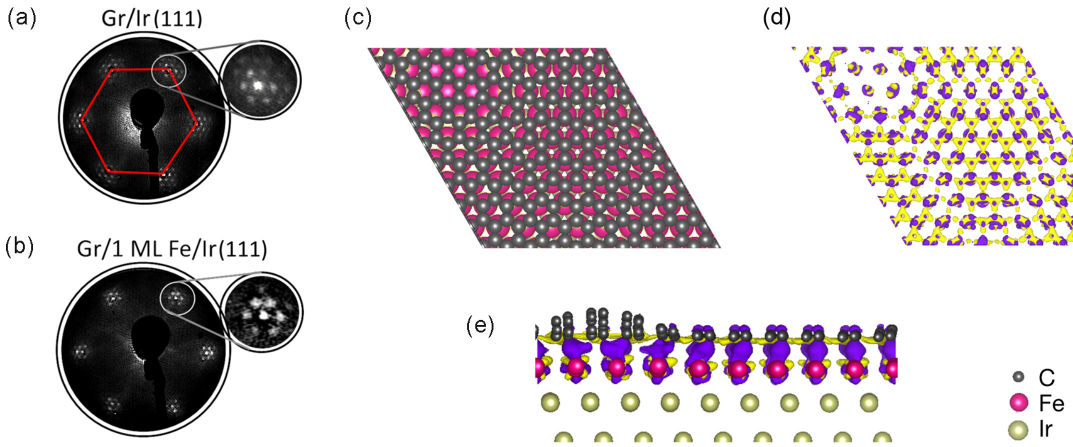

FIG. 1. Low energy electron diffraction (LEED) patterns (electron beam energy 140 eV) for (a) Gr/Ir(111) and (b) Gr/1 ML Fe/Ir(111); (c) atomic structure as deduced by DFT, top view of the moiré pattern of Gr/Fe/Ir(111) with C atoms represented in gray, Fe in red, and Ir in cream; (d),(e) charge difference with respect to the free standing Gr and the pristine Fe/Ir(111) slab, computed with DFT: (d) top view of the charge difference isosurfaces (positive shown in purple, negative in yellow) and (e) side view of the Gr/Fe/Ir(111) structure showing the graphene corrugation and charge difference isosurfaces, using the same colors described for the previous panels.

Sec. II. The calculations confirm the large corrugation of the graphene layer (1.44 Å), with a minimum graphene-Fe interplanar distance of 1.85 Å and a maximum of 3.29 Å on the crests of the hills, as shown in Fig. 1(c). Previous DFT calculations [12] done at the PBE level including van der Waals interactions by using the DFT-D2 method [40,41] found a similar scenario, with slightly larger Gr-Fe distances (2.05 and 3.33 Å for valleys and hills, respectively).

The topography of the Gr/Fe/Ir(111) heterostructure is similar to the corrugated moiré superstructure observed for the Gr/Co/Ir(111) system [26], but very different from the structure reported for Gr directly grown on bcc-Fe(110) [16]. Previous STM measurements and DFT calculations performed at the LDA level, for Gr/bcc-Fe(110) point out the formation of a periodic corrugated pattern of the graphene layer parallel to the [001] direction of the substrate, consisting of a supercell of 7 × 17 graphene hexagons with a smaller corrugation of 0.6/0.9 Å and only a small fraction of the C atoms considerably elevated over the Fe surface, thus making the entire graphene membrane strongly interacting with the metal substrate.

In the present case, the larger graphene corrugation modulates the Gr/Fe interaction. This is illustrated by the charge difference computed for Gr/Fe/Ir(111) shown in Figs. 1(d) and 1(e). The excess of negative charge (yellow isosurface) is accumulated in the graphene membrane, donated by the Fe intercalated layer. The redistribution of charge is more pronounced in the valley regions and milder in the areas corresponding to the crests of the hills, corroborating a different strength of hybridization between graphene and Fe going from the valleys to the crests due to the increasing graphene-Fe distance. The periodicity of strongly and weakly bound regions in which covalent and van der Waals bonding dominate, respectively, induces a different balance in the charge transfer determined also by the registry with respect to the underlying Fe atoms.

Another signature of the similarity of the registry and graphene corrugation resulting from Co and Fe intercalated layers can be deduced by comparing the C 1*s* core level photoemission data for Gr/Fe/Ir(111) (as reported in Supplemental Material [28]) and Gr/Co/Ir(111). In fact, there is a multicomponent C 1*s* line shape for both systems, in which the two main features are assigned to C atoms in the Gr layer weakly (on the crests) and strongly (in the valleys) bound to the Co and Fe layers [9,21,42]. In contrast, when graphene is grown directly on the bcc-Fe(110) surface, a single C 1*s* core level component is present, explained by the presence of extended regions of graphene coupled to the Fe(110) substrate, even at the crests of the moiré superstructure [16,17]. For the graphene membrane directly grown on Fe(110), a small feature in the C 1*s* core level has been detected at lower binding energy (BE), linked to the presence of Fe carbide resulting from the Fe-C solubility due to the high temperature reached during the chemical vapor deposition growth procedure [16,17]. The similarity of the Fe intercalation process under Gr/Ir(111) with the Gr/Co/Ir(111) heterostructure and the absence of a C 1*s* component due to the formation of iron carbide (see details in Supplemental Material [28]) demonstrate the successful strategy to intercalate Fe under graphene at low temperature, preventing any solubility into C.

The corrugation of the Gr membrane discussed so far is attenuated when the number of Fe intercalated layers increases above a few ML, with a reduction of the brightness of the superstructure LEED spots, as reported in Figs. 2(a)–2(c). At 7 ML, we observe the formation of a Fe film with a lattice constant smaller than Ir(111) and therefore closer to the graphene structural parameters. However, even when the strain induced by the Ir(111) surface is released, the Fe film remains slightly incommensurate with graphene, as shown in Fig. 2(a). This is in contrast with the case of Co intercalation beneath graphene on Ir(111): when the Co film is formed, it recovers its hpc lattice constant and becomes commensurate with the graphene layer [9,42]. Indeed, while the hcp Co(0001) surface lattice parameter (2.50 Å) is comparable with the 2.46 Å of Gr, none of the bcc-Fe faces is lattice matched with graphene. In fact, graphene directly grown on

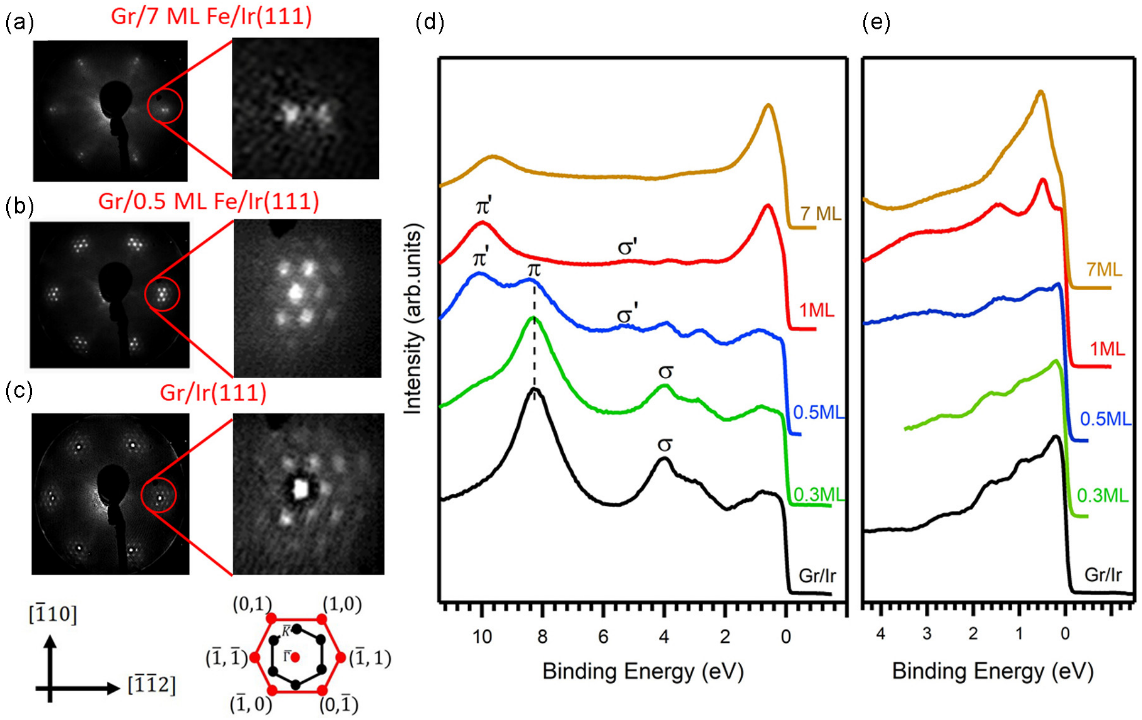

FIG. 2. LEED patterns (electron beam energy 140 eV) and zoomed pattern around the (10) diffraction spot for Gr/7ML Fe/Ir(111) (a), Gr/0.5ML Fe/Ir(111) (b) and Gr/Ir(111) (c); below: sketch of the main symmetry directions and of the diffraction pattern of the Ir(111) surface (red dots); the Surface Brillouin Zone (SBZ) is shown in black. Photoemission energy distribution curves (EDC) taken at 40.814 eV (He II_{α}); angular integrated spectra around Γ (d) and *K* (e) points of the SBZ for different thickness of the intercalated Fe layer between Gr and Ir.

bcc-Fe(110) presents a distorted hexagonal symmetry with only a partial match with the graphene lattice, as deduced by STM [16]. In our case, the Fe intercalated multilayer has a novel strained structural configuration with a 8% mismatch with respect to the graphene lattice constant (see details of the LEED spot intensity analysis in the Supplemental Material [28]).

Importantly, the magnetic response of Fe films is extremely sensitive to tiny variations of the structural configuration [43], and the strained lattice of the Fe film intercalated under graphene can give rise to an altered distribution of the electronic majority and minority states and to different spin and orbital configurations with respect to the bulk reference [44].

B. Electronic structure

A deeper insight into the interaction between Gr and the Fe intercalated layer(s) can be unveiled by the electronic spectral density deduced by angular resolved photoelectron spectroscopy of the Gr/Fe/Ir(111) heterostructure, compared with *ab initio* theoretical predictions of the electronic density of states (DOS) and band structure calculated by DFT.

1. Experimental data

The photoemission spectral density as a function of Fe intercalation thickness is reported in Figs. 2(d) and 2(e), at the Γ and *K* points of the surface Brillouin zone (SBZ), respectively. The Gr/Ir(111) valence band at the Γ and *K* points presents the expected electronic spectral density [45,46] whereas the intercalated system shows three new features when compared with the bare Gr/Ir(111): (i) the appearance of a peak at 10 eV and the disappearance of the one related to the π bands of bare Gr/Ir(111) at 8 eV at the Γ point; (ii) the quenching of the intensity from the Ir surface states close to the Fermi level; (iii) the emergence of extra spectral density in the low binding energy region.

Concerning (i), the intensity of the peak at 8 eV BE at Γ, corresponding to the bottom of the π band for bare Gr/Ir(111), decreases with increasing Fe thickness. The peak emerging at 10.0 eV BE can be associated to the shifted π band, due to the interaction of Gr with the intercalated Fe layer. An interacting π band has also been observed for Co and Ni layers sandwiched between Gr and Ir [5,7,9,10]. The presence of two features associated with the π bands, with opposite intensity behavior before the completion of the first Fe ML, demonstrates the coexistence of bare Gr/Ir regions and regions of intercalated Fe atoms, up to the formation of a smooth Fe single layer, when the peak at 8 eV (bare Gr/Ir) is eventually quenched.

Furthermore, (ii) the progressive intensity lowering of the Ir(111) surface states in the energy region 0–3 eV BE, upon Fe intercalation, without any energy shift, suggests the absence of Fe-Ir intermixing observed at higher intercalation temperatures [23,27]. The emergence of a spectral density (iii) at low binding energy close to the Fermi level can be ascribed to electronic states mainly localized in the Fe layer, since their intensity definitely raises at increasing Fe thickness, as can be clearly observed in the spectral density

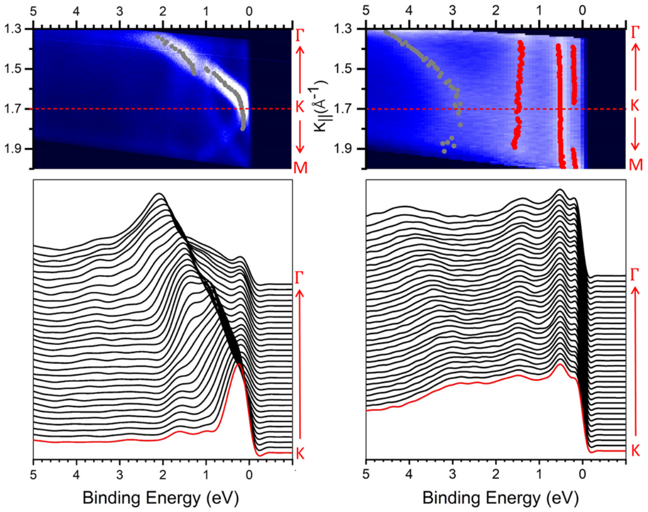

FIG. 3. Angular resolved photoelectron spectroscopy $h\nu = 40.814$ eV spectra of Gr/Ir(111) (left panels) and Gr/1 ML Fe/Ir(111) (right panels), around the K point of the SBZ. Electronic band structure vs $k_{//}$ as intensity plot (upper panels); spectral density plotted as sequential EDC curves from the K point towards Γ (bottom panels).

of 7 ML Fe intercalated under graphene [orange curve in Fig. 2(e)].

A clearer assignment of the electronic states due to the Fe-Gr interaction process can be derived from the electronic state dispersion. The ARPES data around the K point of the SBZ for Gr/Ir(111) and Gr/1 ML Fe/Ir(111) are shown in Fig. 3 (left and right panels, respectively). Considering the energy region closer to the Fermi level, three localized Fe states can be identified at about 0.2 eV, 0.5 eV, and 1.5 eV BE, and found to be only slightly dispersing over the whole SBZ (Fig. 3 right panel), as expected for a confined Fe film. Inspecting the spectra at higher binding energies, other Fe-related states are observed in the energy region of 3–4 eV BE, resonant with the graphene π-band states. Besides the presence of these localized Fe states close to the Fermi level, the most evident consequence of Fe intercalation under graphene is the downshift of the Dirac cone at the K point of the SBZ, similarly to the case of Gr/Co/Ir(111) [9]. In fact, the π band, as deduced by the EDCs (Fig. 3), is broadened and less defined after intercalation and there is a coexistence of other Fe related states in this energy region (3–4 eV). The position of the Dirac cone vertex (at K) is downshifted by 3 eV, while the bottom of the π band is less shifted at Γ. It is worth noting that the Dirac cone is shifted by 2 eV towards higher binding energy also for graphene directly grown on Fe(110) [18], suggesting a weaker interaction in that case.

2. Theory

The measured ARPES data are complemented by DFT calculations, as shown in Fig. 4, where the electronic structures computed for Gr/Ir(111) and Gr/Fe/Ir(111) are unfolded and mapped into the 1 × 1 graphene Brillouin zone along the Γ-K direction, as described in Sec. II. Projected DOS (and projected bands in Supplemental Material [28]) are also provided to complement the band information. The bands obtained for Gr/Ir(111) are in good agreement with existing literature, as from, e.g., Ref. [47]. Concerning the Fe intercalated system, as also observed in the experiments, the Gr π and σ bands are shifted to higher binding energies by the effect of Fe intercalation (i). While for Gr/Ir(111) the π bands are clearly recognizable, in the case of Gr/Fe/Ir(111) they are strongly hybridized with Fe states above -6 eV and the upper part of the cone is identifiable only for the minority spin states. The bottom of the π bands at Γ moves from about -7.5 eV in Gr/Ir to about -10.0 eV in Gr/Fe/Ir (see Fig. S4 in Supplemental Material [28]), with an overall downshift of $\sim$2.5 eV, in quite good agreement with the experimental findings.

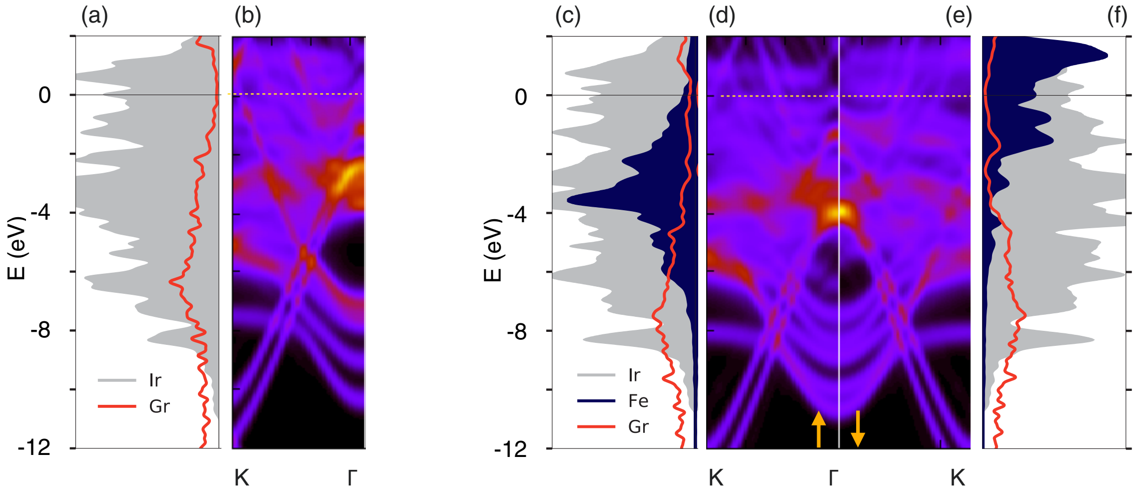

FIG. 4. Band structure and projected density of states (pDOS) computed within DFT for Gr/Ir(111) and Gr/1 ML Fe/Ir(111): (a) Gr/Ir(111) DOS projected on C and Ir atomic orbitals and (b) Gr/Ir(111) band structure, unfolded on the 1 × 1 graphene unit cell as described in the main text; (c) Gr/Fe/Ir(111) majority spin DOS projected on C, Fe, and Ir atomic orbitals; (d) majority and (e) minority spin band structure, unfolded on the 1 × 1 graphene unit cell; (f) Gr/Fe/Ir(111) minority spin pDOS.

Similarly, the σ bands of graphene undergo a downshift by about -1.5 eV at both Γ (going from -2.5 to -4 eV) and K (from -10.5 to -12 eV). While the experimental offset of these features is found at larger binding energies [namely 4.0 eV and 5.5 eV as marked by σ and σ' in Fig. 2(d)], the downshift is quite consistent with the calculations [48].

In order to identify Fe-related states, we consider the projected DOS, shown in Figs. 4(c) and 4(f), where a strong spin splitting of the Fe components is observed (see discussion below). For instance, a large peak of the Fe pDOS is found in the energy region of 3–4 eV BE, in good agreement with the experimental data, and mainly located in the majority spin channel. Such a peak then overlaps with the π bands of Gr disrupting the Dirac cone for majority states. In contrast, the Dirac cone is still faintly visible in the minority spin bands at about 2.5–3 eV. In both spin channels the pDOS reveals overlapping peaks due to Fe and graphene states, suggesting that the shadowing of the vertex of the Dirac cone observed in the experimental photoemission data is clearly induced by the hybridization of the graphene π states with the Fe d majority states. Furthermore, the spin resolved DOS in the energy region closer to the Fermi level shows that the main Fe-related peak of the minority spin states lies above the Fermi level, with smaller peaks between -2 eV and the Fermi energy, in good agreement with the experimental observation (iii). Overall, this picture is further confirmed by the projected unfolded bands provided in Fig. S4 of Supplemental Material [28].

C. Magnetic properties and spin and orbital configuration of the Fe layer

In contrast with Fe grown on Ir(111), for which the loss of inversion symmetry at the interface of the magnetic layer and substrate stabilizes different skyrmion lattices depending on the Fe/Ir stacking [49–53], when a Fe monolayer is intercalated between Gr and Ir(111), the heterostructure exhibits a ferromagnetic order with an out-of-plane easy magnetization axis [12]. For this reason, and based on the experimental evidence described below, in the present DFT calculations we have considered only collinear magnetic configurations, excluding in this way skyrmions or spin spiral textures.

The pDOS computed for the Gr/Fe/Ir(111) heterostructure shows a large spin split of the Fe states, with the maxima of the two spin pDOS almost 5 eV apart. In particular, the majority spin states are almost fully occupied while the largest peak of the minority spin states is empty, which results in an average Fe-magnetic moment of 2.2 μ_B/atom. The computed ground state magnetic configuration is ferromagnetic even if the Fe magnetic moment shows a modulation over different sites ranging from 2.0 to 2.7 μ_B/atom, in good agreement with previous calculation [54]. The modulation is determined by the graphene layer, with the Fe atoms located below the graphene crests, i.e., with larger Fe-C distances, having the largest values. Concerning graphene, the C magnetic moments are nonzero but quite small (at the LDA + U level ranging from -0.02 to 0.01 μ_B/atom), similarly to what was reported for Gr/Co/Ir(111) [10,26], with a distance- and sublattice-dependent modulation.

Overall, we find that the Fe monolayer displays a clear spin splitting, as an effect of the band narrowing and subsequent increased number of majority electrons. This is confirmed by the strong localization of the Fe-induced electronic states observed in the photoemission spectral density. It is interesting to point out that a different scenario is found for the Gr/Co/Ir(111) interface [10] (see Supplemental Material [28] for a detailed comparison with Gr/Co/Ir(111) pDOS) where Co spectral weight in the minority channel is shifted at lower energies leading to a spin split significantly smaller than in the present case.

The strong ferromagnetic behavior is confirmed by the x-ray absorption spectra and the XMCD at the $L_{2,3}$ edges for 1.4 ML and 7 ML of Fe sandwiched between Gr and Ir(111), shown in Fig. 5. XAS are acquired in remanence conditions with circularly polarized radiation and with photons impinging normal (left panel) and grazing (right panel) to the surface. The XMCD spectra are obtained as the difference between the absorption edges acquired with left- and right-circularly polarized radiation. The higher dichroic response with photon impinging at normal incidence (left panel) reveals an out-of-plane magnetic anisotropy of the Fe layer when it is pseudomorphic to the Ir(111) surface, with a stretched Fe-Fe distance with respect the bulk bcc(110) or (111) surfaces. The higher dichroic response for Fe $L_{2,3}$ XMCD at grazing incidence (right panel) for the thicker intercalated Fe film unveils a switch of the easy magnetization axis from perpendicular to the surface to in-plane. This is consistent with the magnetic response of heterostructures of single Co or Fe_xCo_{1-x} layers on Ir(111) covered with a Gr membrane [21,26].

The spin and the orbital moments at the Fe site, as deduced via XMCD sum rules, show a doubled L/S_{eff} ratio ($S_{\mathrm{eff}} = S + 7D$ and D is the dipolar moment [55,56]), with respect to the bulk element (0.11 ± 0.01 for a Fe single layer and 0.09 ± 0.01 for the 7 ML). These experimental results, related only to the intensity of the dichroic signal and independent on the number of 3d holes, suggest an enhanced magnetic response due to the redistribution of the majority spin states in the conduction Fe bands. The evaluated average total moment is 2.1 ± 0.2 μ_B/atom for 7 ML of Fe intercalated under Gr, in fair agreement with 2.2 μ_B/atom (spin moment), as deduced by the DFT predictions. The orbital and spin moment for a single layer of Fe, where interface effects can play a role, shows a comparable magnetic response, as deduced by the similar dichroic signals reported in Fig. 5. As mentioned above, the pseudomorphic hexagonal Fe single layer grown directly on Ir(111) presents a complex magnetic structure with skyrmionic spin spiral textures stabilized by the 3d–5d hybridization between Fe and Ir. [50–53]. On the other hand, other magnetic materials like Europium have been successfully intercalated underneath graphene on the same Ir(111) surface [57] and, depending on its coverage, Eu displays either a paramagnetic or a ferromagnetic behavior [58]. The clear magnetic dichroism response of the single Fe layer intercalated under graphene suggests a different spin configuration. Furthermore, this confined single Fe intercalated layer, with stretched Fe-Fe distances, presents spin and orbital configurations similar to those of the thin Fe intercalated film, where the influence of the Fe-Ir interface is completely released.

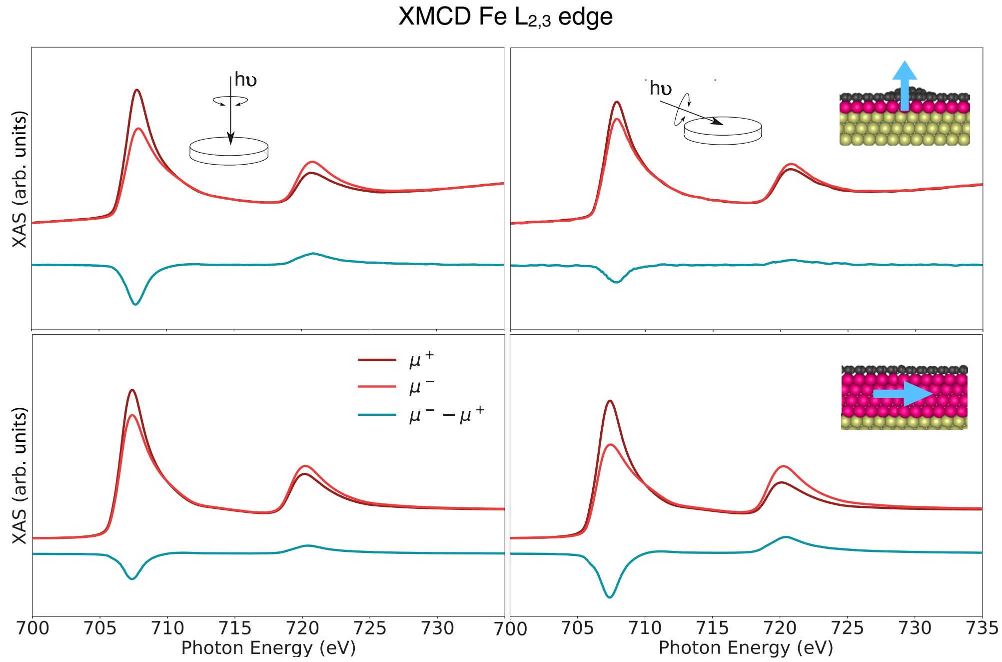

FIG. 5. XMCD spectra of Fe $L_{2,3}$ absorption edges for Gr/1.4 ML Fe/Ir(111) (top) and Gr/7ML Fe/Ir(111) (bottom) acquired in remanence at RT in normal (left) and grazing (right) incidence geometries (see sketches for the experimental geometry). The easy magnetization direction switching from perpendicular (top) to parallel (bottom) to the surface plane is indicated by the blue arrows.

IV. CONCLUSIONS

The strategy to sandwich the Fe layer beneath the graphene membrane with an intercalation process at moderate temperature (500 K) prevents any alloying, and the absence of any hallmark of Fe-Ir and Fe-C intermixing proves the formation of a well-defined homogeneous Fe layer in registry with the Ir(111) surface. Such a single layer of Fe, protected by the graphene membrane, induces a downshift in energy and a symmetry breaking of the Dirac cone due to the interaction between Gr and Fe majority states resonant in the energy region of the vertex of the cone. The redistribution of the spin resolved Fe pDOS with a narrowing of the Fe bands and a larger spin splitting between majority (fully occupied) and minority states (almost empty) of the Fe states associated with increased total Fe magnetic moment influences the magnetic response of the Fe intercalated layer(s).

In contrast to the case of direct growth of Fe on Ir(111), where, despite the large Fe magnetic moment, a noncollinear magnetic order has been observed [49–52], the Fe layer with graphene on top reveals a ferromagnetic long range order with spin and orbital moments that are higher than the ones found for the bulk phases. The graphene top layer acts not only as a protective membrane but also allows for a stable ferromagnetic configuration, counteracting the effect of Ir substrate. The concomitant dimensionality reduction with a narrowing of the *d* bands and a reduced superimposition between the spin-split majority and minority Fe bands further contributes to the transition of a single Fe layer (or few layers of Fe), from weak to strong ferromagnet, when intercalated beneath graphene. These 3*d* confined layers protected by a graphene membrane with a novel structural configuration with respect to the bulk lattice arrangement offer a powerful playground to tune their electronic structure and magnetic state for magnetic/spintronic devices.

ACKNOWLEDGMENTS

The authors thank the experimental assistance of BOREAS beamline staff at ALBA, of SuperESCA beamline staff at Elettra, and of Alessio Vegliante in LOTUS laboratory in Rome. G.A. and M.G.B. acknowledge support from translational access CalipsoPlus funding. C.C., D.V., A.F., and D.A.L. acknowledge partially support from the MaX—MAterials design at the eXascale—Centre of Excellence, funded by the European Union program H2020-INFRAEDI-2018-1 (Grant No. 824143). They also thank SUPER (Supercomputing Unified Platform—Emilia-Romagna) from Emilia-Romagna POR-FESR 2014-2020 regional funds. The work was partially supported by PRIN FERMAT (2017KFY7XF) from Italian Ministry MIUR and by Sapienza Ateneo funds. Computational time on the Marconi100 machine at CINECA was provided by the Italian ISCRA program.

[1] N. Tombros, C. Jozsa, M. Popinciuc, H. T. Jonkman, and B. J. van Wees, Nature (London) **448**, 571 (2007).

[2] W. Han, R. Kawakami, M. Gmitra, and J. Fabian, Nat. Nanotechnol. **9**, 794 (2014).

[3] D. Usachov, A. Fedorov, M. M. Otrokov, A. Chikina, O. Vilkov, A. Petukhov, A. G. Rybkin, Y. M. Koroteev, E. V. Chulkov, V. K. Adamchuk, A. Grüneis, C. Laubschat, and D. V. Vyalikh, Nano Lett. **15**, 2396 (2015).

[4] L. V. Dzemiantsova, M. Karolak, F. Lofink, A. Kubetzka, B. Sachs, K. von Bergmann, S. Hankemeier, T. O. Wehling, R. Frömter, H. P. Oepen, A. I. Lichtenstein, and R. Wiesendanger, Phys. Rev. B **84**, 205431 (2011).

[5] D. Pacilè, P. Leicht, M. Papagno, P. M. Sheverdyaeva, P. Moras, C. Carbone, K. Krausert, L. Zielke, M. Fonin, Y. S. Dedkov, F. Mittendorfer, J. Doppler, A. Garhofer, and J. Redinger, Phys. Rev. B **87**, 035420 (2013).

[6] A. Varykhalov, D. Marchenko, J. Sánchez-Barriga, M. R. Scholz, B. Verberck, B. Trauzettel, T. O. Wehling, C. Carbone, and O. Rader, Phys. Rev. X **2**, 041017 (2012).

[7] L. Massimi, S. Lisi, D. Pacilè, C. Mariani, and M. G. Betti, Beilstein J. Nanotech. **5**, 308 (2014).

[8] R. Decker, J. Brede, N. Atodiresei, V. Caciuc, S. Blügel, and R. Wiesendanger, Phys. Rev. B **87**, 041403(R) (2013).

[9] D. Pacilè, S. Lisi, I. Di Bernardo, M. Papagno, L. Ferrari, M. Pisarra, M. Caputo, S. K. Mahatha, P. M. Sheverdyaeva, P. Moras, P. Lacovig, S. Lizzit, A. Baraldi, M. G. Betti, and C. Carbone, Phys. Rev. B **90**, 195446 (2014).

[10] H. Vita, S. Böttcher, P. Leicht, K. Horn, A. B. Shick, and F. Máca, Phys. Rev. B **90**, 165432 (2014).

[11] M. Weser, Y. Rehder, K. Horn, M. Sicot, M. Fonin, A. B. Preobrajenski, E. N. Voloshina, E. Goering, and Y. S. Dedkov, Appl. Phys. Lett. **96**, 012504 (2010).

[12] R. Decker, M. Bazarnik, N. Atodiresei, V. Caciuc, S. Blügel, and R. Wiesendanger, J. Phys.: Condens. Matter **26**, 394004 (2014).

[13] J. Coraux, A. T. N'Diaye, N. Rougemaille, C. Vo-Van, A. Kimouche, H.-X. Yang, M. Chshiev, N. Bendiab, O. Fruchart, and A. K. Schmid, J. Phys. Chem. Lett. **3**, 2059 (2012).

[14] M. Cattelan, G. W. Peng, E. Cavaliere, L. Artiglia, A. Barinov, L. T. Roling, M. Favaro, I. Píš, S. Nappini, E. Magnano, F. Bondino, L. Gavioli, S. Agnoli, M. Mavrikakis, and G. Granozzi, Nanoscale **7**, 2450 (2015).

[15] A. Lodesani, A. Picone, A. Brambilla, D. Giannotti, M. S. Jagadeesh, A. Calloni, G. Bussetti, G. Berti, M. Zani, M. Finazzi *et al.*, ACS nano **13**, 4361 (2019).

[16] N. A. Vinogradov, A. A. Zakharov, V. Kocevski, J. Rusz, K. A. Simonov, O. Eriksson, A. Mikkelsen, E. Lundgren, A. S. Vinogradov, N. Mårtensson, and A. B. Preobrajenski, Phys. Rev. Lett. **109**, 026101 (2012).

[17] N. Vinogradov, K. Simonov, A. Generalov, J. Drnec, F. Carlá, A. Vinogradov, A. Preobrajenski, N. Mårtensson, and R. Felici, Carbon **111**, 113 (2017).

[18] A. Varykhalov, J. Sánchez-Barriga, D. Marchenko, P. Hlawenka, P. S. Mandal, and O. Rader, Nat. Commun. **6**, 7610 (2015).

[19] H. Okamoto, J. Phase Equilib. **13**, 543 (1992).

[20] S. Vlaic, N. Rougemaille, A. Artaud, V. Renard, L. Huder, J.-L. Rouviére, A. Kimouche, B. Santos, A. Locatelli, V. Guisset *et al.*, J. Phys. Chem. Lett. **9**, 2523 (2018).

[21] G. Avvisati, P. Gargiani, D. Lizzit, M. Valvidares, P. Lacovig, C. Petrillo, F. Sacchetti, and M. G. Betti, Appl. Surf. Sci. **527**, 146599 (2020).

[22] P. Gargiani, R. Cuadrado, H. B. Vasili, M. Pruneda, and M. Valvidares, Nat. Commun. **8**, 699 (2017).

[23] M. Bazarnik, R. Decker, J. Brede, and R. Wiesendanger, Surf. Sci. **639**, 70 (2015).

[24] https://sites.google.com/uniroma1.it/nano-surface-physics/.

[25] A. Barla, J. Nicolás, D. Cocco, S. M. Valvidares, J. Herrero-Martán, P. Gargiani, J. Moldes, C. Ruget, E. Pellegrin, and S. Ferrer, J. Synchrotron Radiat. **23**, 1507 (2016).

[26] G. Avvisati, C. Cardoso, D. Varsano, A. Ferretti, P. Gargiani, and M. G. Betti, Nano Lett. **18**, 2268 (2018).

[27] J. Brede, J. Sławińska, M. Abadia, C. Rogero, J. E. Ortega, I. Piquero-Zulaica, J. Lobo-Checa, A. Arnau, and J. I. Cerdá, 2D Mater. **4**, 015016 (2016).

[28] See Supplemental Material at http://link.aps.org/supplemental/10.1103/PhysRevMaterials.xx.xxxxxx for the detailed description of the C 1s, Ir 4 f7/2, and Fe 2p3/2 core levels; the LEED spot intensity analysis for Gr/Ir (111), Gr/1ML Fe/Ir(111) and Gr/7ML Fe/Ir(111); the unfolded bands of Gr/1ML-Fe/Ir(111); the spin-resolved pDOS for Gr/1ML-Fe/Ir(111) and Gr/1ML-Co/Ir(111).

[29] P. Giannozzi, S. Baroni, N. Bonini, M. Calandra, R. Car, C. Cavazzoni, D. Ceresoli, G. L. Chiarotti, M. Cococcioni, I. Dabo *et al.*, J. Phys.: Condens. Matter **21**, 395502 (2009).

[30] P. Giannozzi, O. Andreussi, T. Brumme, O. Bunau, M. Buongiorno Nardelli, M. Calandra, R. Car, C. Cavazzoni, D. Ceresoli, M. Cococcioni, N. Colonna, I. Carnimeo, A. Dal Corso, S. de Gironcoli, P. Delugas, R. A. DiStasio Jr., A. Ferretti, A. Floris, G. Fratesi, G. Fugallo, R. Gebauer, U. Gerstmann, F. Giustino, T. Gorni, J. Jia, M. Kawamura, H.-Y. Ko, A. Kokalj, E. Küçükbenli, M. Lazzeri, M. Marsili, N. Marzari, F. Mauri, N. L. Nguyen, H.-V. Nguyen, A. O. de-la Roza, L. Paulatto, S. Poncé, D. Rocca, R. Sabatini, B. Santra, M. Schlipf, A. P. Seitsonen, A. Smogunov, I. Timrov, T. Thonhauser, P. Umari, N. Vast, X. Wu, and S. Baroni, J. Phys.: Condens. Matter **29**, 465901 (2017).

[31] J. P. Perdew and A. Zunger, Phys. Rev. B **23**, 5048 (1981).

[32] A. Calloni, G. Bussetti, G. Avvisati, M. S. Jagadeesh, D. Pacilè, A. Ferretti, D. Varsano, C. Cardoso, L. Duò, F. Ciccacci, and M. G. Betti, J. Chem. Phys. **153**, 214703 (2020).

[33] C. J. Cramer and D. G. Truhlar, Phys. Chem. Chem. Phys. **11**, 10757 (2009).

[34] M. Cococcioni and S. de Gironcoli, Phys. Rev. B **71**, 035105 (2005).

[35] V. Popescu and A. Zunger, Phys. Rev. B **85**, 085201 (2012).

[36] P. Bonfà, https://bitbucket.org/bonfus/unfold-x.

[37] A. N'Diaye, J. Coraux, T. Plasa, C. Busse, and T. Michely, New J. Phys. **10**, 043033 (2008).

[38] M. Scardamaglia, G. Forte, S. Lizzit, A. Baraldi, P. Lacovig, R. Larciprete, C. Mariani, and M. G. Betti, J. Nanopart. Res. **13**, 6013 (2011).

[39] C. Busse, P. Lazić, R. Djemour, J. Coraux, T. Gerber, N. Atodiresei, V. Caciuc, R. Brako, A. T. N'Diaye, S. Blügel, J. Zegenhagen, and T. Michely, Phys. Rev. Lett. **107**, 036101 (2011).

[40] S. Grimme, J. Comput. Chem. **27**, 1787 (2006).

[41] Note that the DFT-D2 correction for van der Walls interactions has been reparametrized in these works.

[42] G. Avvisati, S. Lisi, P. Gargiani, A. Della Pia, O. De Luca, D. Pacilè, C. Cardoso, D. Varsano, D. Prezzi, A. Ferretti, and M. G. Betti, J. Phys. Chem. C **121**, 1639 (2017).

[43] V. L. Moruzzi, P. M. Marcus, K. Schwarz, and P. Mohn, Phys. Rev. B **34**, 1784 (1986).

[44] G. Moulas, A. Lehnert, S. Rusponi, J. Zabloudil, C. Etz, S. Ouazi, M. Etzkorn, P. Bencok, P. Gambardella, P. Weinberger, and H. Brune, Phys. Rev. B **78**, 214424 (2008).

[45] I. Pletikosić, M. Kralj, P. Pervan, R. Brako, J. Coraux, A. T. N'Diaye, C. Busse, and T. Michely, Phys. Rev. Lett. **102**, 056808 (2009).

[46] M. Kralj, I. Pletikosić, M. Petrović, P. Pervan, M. Milun, A. T. N'Diaye, C. Busse, T. Michely, J. Fujii, and I. Vobornik, Phys. Rev. B **84**, 075427 (2011).

[47] Y. Dedkov and E. Voloshina, J. Phys.: Condens. Matter **27**, 303002 (2015).

[48] Note that comparing ARPES data with KS-DFT calculations absolute quantitative agreement in the position of the features cannot be expected.

[49] S. Heinze, K. von Bergmann, M. Menzel, J. Brede, A. Kubetzka, R. Wiesendanger, G. Bihlmayer, and S. Blügel, Nat. Phys. **7**, 713 (2011).

[50] K. von Bergmann, S. Heinze, M. Bode, G. Bihlmayer, S. Blügel, and R. Wiesendanger, New J. Phys. **9**, 396 (2007).

[51] K. von Bergmann, S. Heinze, M. Bode, E. Y. Vedmedenko, G. Bihlmayer, S. Blügel, and R. Wiesendanger, Phys. Rev. Lett. **96**, 167203 (2006).

[52] K. von Bergmann, M. Menzel, A. Kubetzka, and R. Wiesendanger, Nano Lett. **15**, 3280 (2015).

[53] J. Grenz, A. Köhler, A. Schwarz, and R. Wiesendanger, Phys. Rev. Lett. **119**, 047205 (2017).

[54] J. Brede, N. Atodiresei, V. Caciuc, M. Bazarnik, A. Al-Zubi, S. Blügel, and R. Wiesendanger, Nat. Nanotechnol. **9**, 1018 (2014).

[55] B. T. Thole, P. Carra, F. Sette, and G. van der Laan, Phys. Rev. Lett. **68**, 1943 (1992).

[56] P. Carra, B. T. Thole, M. Altarelli, and X. Wang, Phys. Rev. Lett. **70**, 694 (1993).

[57] S. Schumacher, T. O. Wehling, P. Lazić, S. Runte, D. F. Förster, C. Busse, M. Petrović, M. Kralj, S. Blügel, N. Atodiresei, V. Caciuc, and T. Michely, Nano Lett. **13**, 5013 (2013).

[58] S. Schumacher, F. Huttmann, M. Petrović, C. Witt, D. F. Förster, C. Vo-Van, J. Coraux, A. J. Martínez-Galera, V. Sessi, I. Vergara, R. Rückamp, M. Grüninger, N. Schleheck, F. Meyer zu Heringdorf, P. Ohresser, M. Kralj, T. O. Wehling, and T. Michely, Phys. Rev. B **90**, 235437 (2014).

Magnetic response and electronic states of well defined Gr/Fe/Ir(111) heterostructure
Supplemental Material

Claudia Cardoso,[1] Giulia Avvisati,[2] Pierluigi Gargiani,[3] Marco Sbroscia,[2] Madan S. Jagadeesh,[2]
Carlo Mariani,[2] Dario A. Leon,[4, 1] Daniele Varsano,[1] Andrea Ferretti,[1] and Maria Grazia Betti[2]

[1] *Centro S3, CNR-Istituto Nanoscienze, I-41125 Modena, Italy*
[2] *Dipartimento di Fisica, Università di Roma "La Sapienza", I-00185 Roma, Italy*
[3] *ALBA Synchrotron Light Source, Carrer de la Llum, 2-26 08290 Barcelona (Spain)*
[4] *Università di Modena e Reggio Emilia I-41125 Modena, Italy*

(Dated: April 28, 2021)

I. CORE LEVELS

In Fig. S1 we report the C1*s* core level for 0.8 ML Fe intercalated between Gr and Ir(111), along with a fit of the different components, performed using Voigt line-shapes (Lorentzian-Gaussian curves taking into account core-hole lifetime and experimental uncertainty, respectively). The C1*s* exhibits a sharp profiled peak centered at 284.2 eV, associated to the dominant sp^2 component of the Gr/Ir system, while two further components are present at higher binding energy, at 284.4 eV and 284.9 eV, due to carbon atoms in valleys and hills of the moiré superstructure, respectively. The binding energy of the two extra-peaks is comparable to that of recent experimental results and theoretical prediction of a single Co layer intercalated under Gr/Ir(111), that shows analogous valley-hill corrugation [1]. In contrast, a recent core level photoemission experiment on graphene CVD-grown directly on the Fe(110) surface [2] reports a huge broad C1*s* component at 284.9 eV, due to a strong interaction of all the C atoms of the graphene layer with the underlying Fe substrate, along with a pronounced shoulder in the photoemission signal at 283.3 eV, suggesting the presence of iron carbide in the sample or at least carbon atoms dissolved in the iron substrate [2]. It is worth noting that in our Gr/Fe/Ir(111) hetero-structure, not any Fe-C component due to the possible formation of Fe-carbides is detectable.

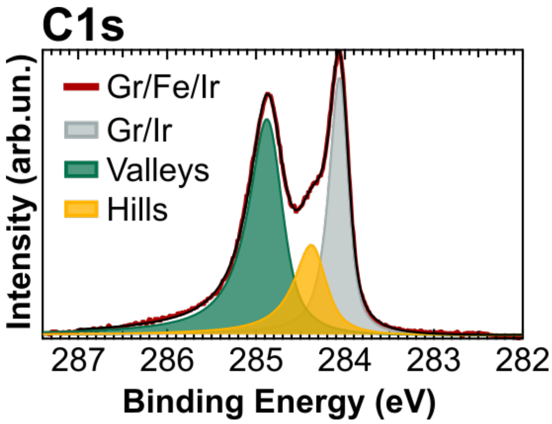

FIG. S1: C 1*s* core level, taken at $h\nu$=400 eV, of Gr/0.8ML-Fe/Ir(111). Experimental data (red dots), fitting curve (red line) and single fitting components (colored curves). The fitting procedure unveils three components: the C 1s related to the Gr/Ir(111) (gray curve), the C 1s component of the C atoms in the valleys (green curve) and in the hills (yellow curve) of the moiré superstructure.

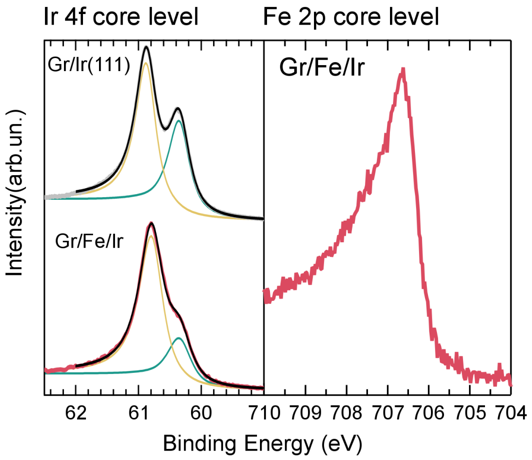

FIG. S2: Left panel: Ir 4f$_{7/2}$ core levels, taken at $h\nu$=400 eV, of Gr/Ir(111) (top gray curve) and Gr/0.8 ML Fe/Ir(111) after intercalation (bottom red curve). The fitting curves are drawn as black lines, and the single fitting components are reported in yellow for the bulk component and in green for the surface component. Right panel: Fe 2p$_{3/2}$ core level for Gr/Fe/Ir taken at $h\nu$=800 eV.

In the left panel of Fig. S2, we report the Ir 4$f_{7/2}$ core level of the Gr/Ir(111) substrate before and after intercalation of Fe. In the Gr/Ir(111) system, the neat surface core level component of this Ir surface is maintained, unperturbed by the graphene layer [3]. On the other hand, the reduction of the Ir surface state after 0.8 ML Fe intercalation, is due to the Fe-iridium interaction, as observed also when a single layer of Co or FeCo are intercalated [4, 5]. The Fe 2p$_{3/2}$ core level reported in the right panel of Fig. S2 does not present any reacted component due to Fe-C intermixing. Recently, J. Brede et al. [6] have observed an energy shift of the Ir 4f core levels by about 150 meV towards lower binding energies due to Fe interdiffusion in the Ir substrate, forming a superficial alloy, already at 600-650 K. Keeping the Fe

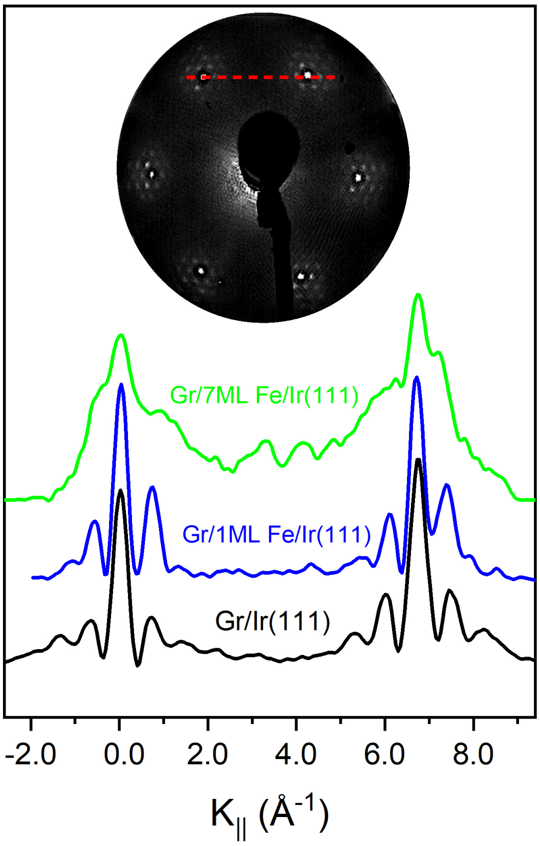

FIG. S3: Top: LEED diffraction pattern for Gr/Ir(111) taken at 140 eV. Diffraction spot intensity profile of LEED patterns taken along azimuthal direction $[\overline{1}\overline{1}2]$ (red dashed line in LEED patten) from Gr/Ir(111), Gr/1ML Fe/Ir(111) and Gr/7ML Fe/Ir(111) (from bottom to top); the corresponding LEED patterns are reported in Figure 2 of the main paper.

intercalation temperature at 500K, thus avoiding alloy formation, we do not appreciate any energy shift in the photoemission of Ir core levels.

II. LEED SPOT INTENSITY ANALYSIS

The spot intensity profiles of the LEED patterns for Gr/Ir (111), Gr/1ML Fe/Ir(111), and Gr/7ML Fe/Ir(111) taken at 140 eV primary energy are reported in Fig. S3. The spot intensity profile was taken along the $[\overline{1}\overline{1}2]$ azimuthal direction (path shown in the LEED pattern). The spot profiles for Gr/Ir(111) and Gr/1 ML Fe/Ir(111) along with the moiré pattern peak intensities are comparable, confirming that the Fe intercalated layer is commensurate to the Ir(111) surface lattice parameter. After further Fe intercalated layers the spot profile of Gr/7ML Fe/Ir(111) unveils broader peaks with a decreased intensity of the extra-spots and a mismatch by about 8% of the main peaks along the $[\overline{1}\overline{1}2]$ direction, with respect to the Ir(111) one, but it is not commensurate to the graphene covering layer. The LEED pattern does not present any longitudinal stripes while a slight signal due to a weakened moiré pattern is still distinguishable for all the spots observed in the main diffraction directions, as also the hexagonal symmetry is preserved overall the sample. The absence of longitudinal pattern and the periodicity of the spots cannot be associated to the structural configuration proposed for graphene directly grown on bcc-Fe(110) where the distorted hexagonal symmetry reveals an array of 1D stripes with a wave-like longitudinal pattern with periodicity of 17 Å along the stripes [7]. In conclusion, the Fe intercalated multilayers present a strained structural arrangement with hexagonal symmetry slightly mismatched with respect to the graphene topmost layer.

III. PROJECTED BANDS AND DENSITY OF STATES

In order to better compare with Gr/Ir and to support the identification and assignment of the electronic structure features described in Sec. III B of the main paper, in Fig. S4 we plot the unfolded bands of GrFeIr, computed analogously to those in Fig. 4 (main text), but projected on C, Fe, and Ir atoms. In particular, this allows one to better appreciate the downshift of graphene-related states, the position of Fe-related states in the majority and minority channels, and the role of Iridium states.

In order to compare with the case of GrCoIr,in Fig. S5 we present the Density of States, projected onto C, Fe and Co orbitals, computed within DFT for Gr/Fe/Ir(111) and Gr/Co/Ir(111), including the complete moiré induced periodicity by using a 9×9 supercell of Ir(111), corresponding to a 10×10 supercell of pristine Gr. As discussed in the main text, LDA+U with U=2 is used for GrFeIr, while U is not included for GrCoIr. The main differences between the two systems are seen in the Fe and Co pDOs. The first presents a larger spin split, with the majority *d* states almost fully occupied, and less occupied minority states, when compered with Co. Fe also shows a pronounced peak around 4 eV below the Fermi energy. These Fe *d* states are resonant hybridized with the graphene π states.

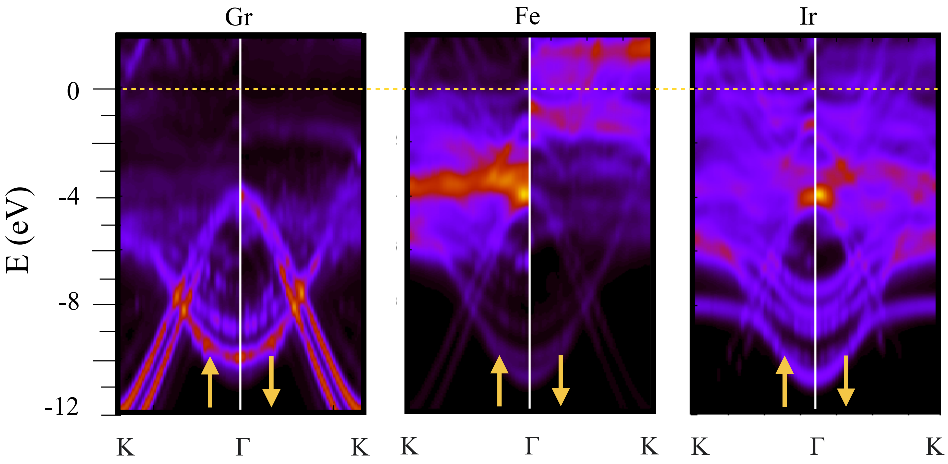

FIG. S4: Bands computed for the Gr/1ML-Fe/Ir(111) unfolded on the Graphene 1×1 cell and projected on C (graphene), Fe, and Ir.

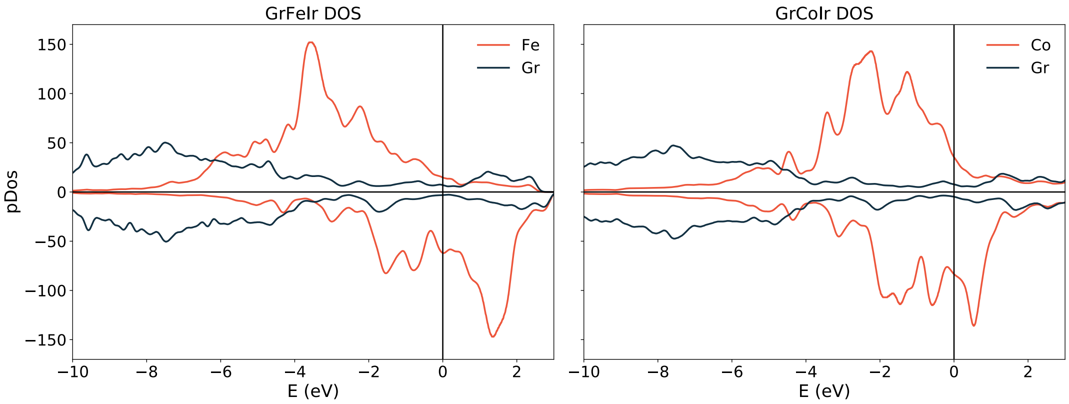

FIG. S5: Comparison of the Density of states projected on graphene and Fe or Co, computed for the Gr/1ML-Fe/Ir(111) and Gr/1ML-Co/Ir(111)

[1] D. Pacilè, S. Lisi, I. Di Bernardo, M. Papagno, L. Ferrari, M. Pisarra, M. Caputo, S. K. Mahatha, P. M. Sheverdyaeva, P. Moras, P. Lacovig, S. Lizzit, A. Baraldi, M. G. Betti, and C. Carbone, Phys. Rev. B **90**, 195446 (2014).

[2] N. Vinogradov, K. Simonov, A. Generalov, J. Drnec, F. Carlà, A. Vinogradov, A. Preobrajenski, N. Mårtensson, and R. Felici, Carbon **111**, 113 (2017).

[3] M. Scardamaglia, S. Lisi, S. Lizzit, A. Baraldi, R. Larciprete, C. Mariani, and M. G. Betti, J. Phys. Chem. C **117**, 3019 (2013).

[4] G. Avvisati, S. Lisi, P. Gargiani, A. Della Pia, O. De Luca, D. Pacilè, C. Cardoso, D. Varsano, D. Prezzi, A. Ferretti, and M. G. Betti, J. Phys. Chem. C **121**, 1639 (2017).

[5] G. Avvisati, P. Gargiani, D. Lizzit, M. Valvidares, P. Lacovig, C. Petrillo, F. Sacchetti, and M. G. Betti, Applied Surface Science **527**, 146599 (2020).

[6] J. Brede, J. Sławińska, M. Abadia, C. Rogero, J. E. Ortega, I. Piquero-Zulaica, J. Lobo-Checa, A. Arnau, and J. I. Cerdá, 2D Materials **4**, 015016 (2016).

[7] N. A. Vinogradov, A. A. Zakharov, V. Kocevski, J. Rusz, K. A. Simonov, O. Eriksson, A. Mikkelsen, E. Lundgren, A. S. Vinogradov, N. Mårtensson, and A. B. Preobrajenski, Phys. Rev. Lett. **109**, 026101 (2012).

Applied Physics Letters ARTICLE scitation.org/journal/apl

Narrowing of *d* bands of FeCo layers intercalated under graphene

Cite as: Appl. Phys. Lett. **118**, 121602 (2021); doi: 10.1063/5.0047266
Submitted: 11 February 2021 · Accepted: 8 March 2021 ·
Published Online: 22 March 2021

View Online Export Citation CrossMark

Daniela Pacilè,[1,a)] Claudia Cardoso,[2,a)] Giulia Avvisati,[3] Ivana Vobornik,[4] Carlo Mariani,[3] Dario A. Leon,[2,5] Pietro Bonfà,[2,6] Daniele Varsano,[2] Andrea Ferretti,[2] and Maria Grazia Betti[3]

AFFILIATIONS

[1]Dipartimento di Fisica, Università della Calabria, I-87036 Arcavacata di Rende (Cs), Italy
[2]Centro S3, CNR-Istituto Nanoscienze, I-41125 Modena, Italy
[3]Dipartimento di Fisica, Università di Roma "La Sapienza," I-00185 Roma, Italy
[4]Istituto Officina dei Materiali (IOM)-CNR, Laboratorio TASC, Area Science Park, S.S.14, Km 163.5, 34149 Trieste, Italy
[5]Università di Modena e Reggio Emilia, I-41125 Modena, Italy
[6] Università di Parma, Dipartimento di Scienze Matematiche, Fisiche e Informatiche, I-43124 Parma, Italy

[a)]Authors to whom correspondence should to addressed: daniela.pacile@fis.unical.it and claudiamaria.cardosopereira@nano.cnr.it

ABSTRACT

We report on the electronic properties of an artificial system obtained by the intercalation of equiatomic FeCo layers under graphene grown on Ir(111). Upon intercalation, the FeCo film grows epitaxially on Ir(111), resulting in a lattice-mismatched system. By performing density functional theory calculations, we show that the intercalated FeCo layer leads to a pronounced corrugation of the graphene film. At the same time, the FeCo intercalated layers induce a clear transition from a nearly undisturbed to a strongly hybridized graphene π-band, as measured by angle-resolved photoemission spectroscopy. A comparison of experimental results with the computed band structure and the projected density of states unveils a spin-selective hybridization between the π band of graphene and FeCo-3*d* states. Our results demonstrate that the reduced dimensionality, as well as the hybridization within the FeCo layers, induces a narrowing and a clear splitting of Fe 3*d*-up and Fe 3*d*-down-spin bands of the confined FeCo layers with respect to bulk Fe and Co.

Ferromagnetic metals (FMs) and their alloys can be finely manipulated by changing their chemical composition[1] and structural configuration,[2] and by reducing the dimensionality.[3,4] Modified symmetry and scaled dimension, indeed, may induce in FMs higher magnetic moments and larger uniaxial magnetic anisotropy energy (MAE) with respect to their 3D counterparts.[4–8] The enhanced magnetism in nanostructures can be used, e.g., for engineering spintronic devices,[9] high-density magnetic storage,[10] and permanent magnets.[11]

Among all iron-based alloys, including also pure iron, equiatomic FeCo exhibits the highest Curie temperature and magnetic moment driven by an almost filled Fe majority spin band.[12–15] On the other hand, due to its cubic symmetry, the FeCo alloy also shows a low MAE.[16] Indeed, modifying dimensionality or symmetry has been shown to be a viable route in order to improve the magnetic response of FeCo alloys,[8,17] although clustering and granularity may hinder a controlled growth of artificial systems.[18] Intercalation of metals underneath graphene (Gr) has led to the formation of atomically smooth metallic layers,[19–29] where Gr on top is also a protective membrane against contaminants.[30,31] Although several metals have been intercalated under Gr, the combined intercalation of Fe and Co to form an equiatomic alloy is more challenging, as segregation without intermixing may be dominant.[31] Recently, we have grown homogeneous and smooth Fe_xCo_{1-x} layers underneath Gr/Ir(111), co-depositing Fe and Co at the same evaporation rate and keeping the substrate temperature at about 500 K, to avoid any Fe-Ir and Co-Ir alloying formation and clustering. By performing X-ray Magnetic Circular Dichroism (XMCD) measurements, we showed that Fe and Co are well intermixed and magnetically coupled underneath Gr, leading to an enhancement of the magnetic moments with respect to pure Fe and Co films and exhibiting a strong ferromagnetic exchange coupling between the two species.[8]

In the present work, we investigate the electronic and structural properties of the equiatomic FeCo layers (about 1–2 monolayers of thickness) grown epitaxially on Ir(111) underneath a Gr cover, by means of Angular Resolved Photoemission Spectroscopy (ARPES) and Density Functional Theory (DFT). We show that the reduced dimensionality in the artificially confined system leads to a narrowing and a redistribution of majority and minority 3*d* states with respect to the pure species, also enhancing the splitting between Fe 3*d*-up and Fe 3*d*-down-spin bands. Our description of the electronic structure in equiatomic FeCo layers sheds light on the enhanced magnetism previously demonstrated by XMCD[8] and provides a useful insight into the engineering of low dimensional FM alloys.

The Ir(111) surface was cleaned by cycles of sputtering (Ar^+, 1.5–2.0 keV) and annealing at about 1300 K. The Gr sheet is obtained by exposing the clean surface to 5×10^{-8}–2×10^{-7} mbar of C_2H_4 and annealing at 1300–1320 K. Metallic Fe and Co were simultaneously deposited, at previously calibrated same evaporation rates (about 0.3 Å/min) to deposit nominal 3 monolayers (MLs) of FeCo on the Gr/Ir(111) substrate kept in the range of 500–530 K. As recently reported,[8] core level photoemission and absorption spectroscopy unveil homogeneous intercalation of equiatomic FeCo layers, without any alloy formation with the underlying substrate[8](as shown in the supplementary material), at variance e.g., with recent observations for Mn intercalation on Gr/Ir.[32]

The sample preparation and ARPES experiments were carried out at the APE beamline of the Elettra Synchrotron Light Source (Trieste, Italy). The photoelectrons, excited with a photon energy of 86 eV, were collected with a VG Scienta DA30 electron energy analyzer, which operates in deflection mode and allows for detailed **k**-space mapping at fixed sample geometry.

Density functional theory (DFT) simulations were carried out using the plane wave implementation of the QUANTUM ESPRESSO[33,34] distribution. We used the local density approximation (LDA) for the exchange-correlation potential, according to the Perdew-Zunger parametrization.[35] Since LDA is known to underestimate the values of the orbital magnetic moments in transition metals,[36] we have adopted a DFT+U scheme,[37] with a Hubbard U parameter of 2 eV for Fe and 4 eV for Co. The choice of the values is explained in detail in the SI. Similar to our previous works,[27,38,39] we simulated the Gr/1ML-FeCo/Ir(111) interface considering the complete moiré induced periodicity by using a 9×9 supercell of Ir(111), corresponding to a 10×10 supercell of pristine Gr. More details about the structure can be found in the supplementary material.

In order to obtain a simpler representation of the Gr/FeCo/Ir(111) band structure, we have applied an unfolding procedure[40,41] in which the band structure computed for the 10×10 supercell is mapped into the Gr 1×1 Brillouin Zone (BZ) by using the unfold-x code.[41] This approach has been further extended to include atomic projections on Lödwin orthogonalized atomic orbitals as provided by the QUANTUM ESPRESSO package.[33,34]

Figure 1 shows the low energy electron diffraction (LEED) patterns of Gr/Ir(111), taken with a primary energy of about 90 eV, before (a) and after (b) the intercalation of nominal 3ML of FeCo. The moiré superstructure characteristic of the corrugated Gr/Ir(111) system is maintained after FeCo intercalation, attesting that the equiatomic FeCo layers arrange pseudomorphically on the hexagonal Ir(111) surface. The moiré pattern is only slightly smeared out at an increasing amount of intercalated atoms, with an intensity reduction of the extra spots. The persistence of multiple reflection spots suggests that the thickness of the intercalated FeCo layer is within 1 and 2 MLs, as deduced by comparison with the LEED patterns of pure Co[23] and Fe[27] intercalated systems.

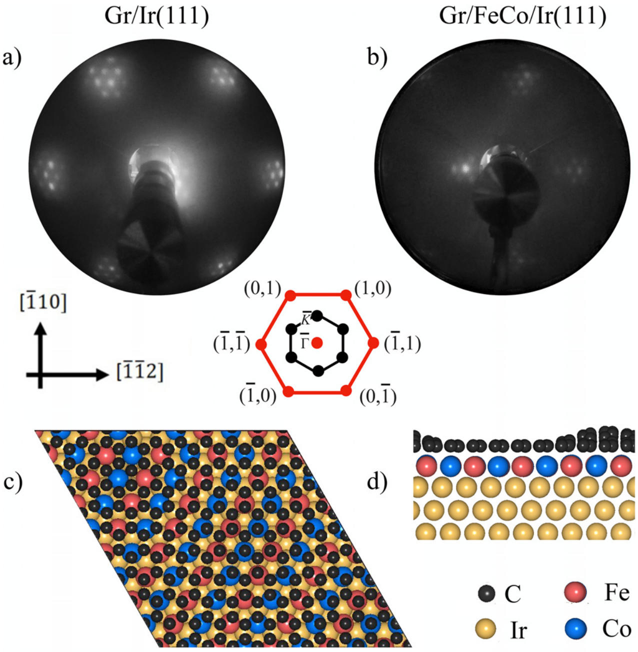

FIG. 1. Low energy electron diffraction (LEED) patterns (electron beam energy: 90 eV) of (a) Gr/Ir(111) and (b) Gr/FeCo/Ir(111), taken slightly off-normal. In the middle: sketch of the diffraction pattern and Brillouin Zone (BZ) of Ir(111), referred to (a) and (b) panels. (c) Atomic structure as deduced by DFT, top view of the moiré pattern of Gr/FeCo/Ir(111) with C atoms represented in gray, Fe in red, Co in blue, and Ir in cream; (d) side view of the Gr/FeCo/Ir(111) structure showing the Gr corrugation, using the same colors described in the previous panel.

The Gr/FeCo/Ir(111) interface was modeled at the DFT level as described previously. The calculations indicate a large corrugation of the Gr layer (1.40 Å), with Gr-FeCo interplanar distances of 1.90 Å and 3.30 Å at valleys and hills, respectively, as shown in Figs. 1(c) and 1(d). The corrugation of the Gr/FeCo/Ir(111) and the energy landscape of the stable structural configuration are similar to those computed for the pure intercalated systems Gr/Fe/Ir(111) (1.3 Å)[27] and Gr/Co/Ir(111) (1.4 Å).[22,38] It is worth noticing that we do not include van der Waals interactions in our approach since LDA has shown to give a good description of graphene corrugation and distance for Gr/Fe/Ir(111),[27] providing essentially the same scenario as DFT calculations done at the PBE level including van der Waals interactions,[42] which only find slightly larger Gr-Fe distances.

To shed light on the interaction mechanism between Gr and the FeCo interface, we show angular resolved photoemission measurements and compare them with the band structure computed using Kohn–Sham DFT. Figure 2(a) shows ARPES results of Gr/FeCo/Ir(111) taken along $\bar{\Gamma}$-$\bar{K}$. The effect of Fe and Co states on the π and σ bands of Gr can be discussed by comparing the system under study with pure Gr/Co and Gr/Fe (either supported on Ir(111) or not), as reported in the literature.[23,27,43–45] At the $\bar{\Gamma}$-point [Fig. 2(a)], the bottom of the π band and the top of the σ bands are shifted to about 10.2 eV and 5.4 eV of binding energy (BE), respectively, in agreement with previous results for pure Fe and Co intercalated systems.[23,27] Moreover, ARPES data extracted along the direction perpendicular to

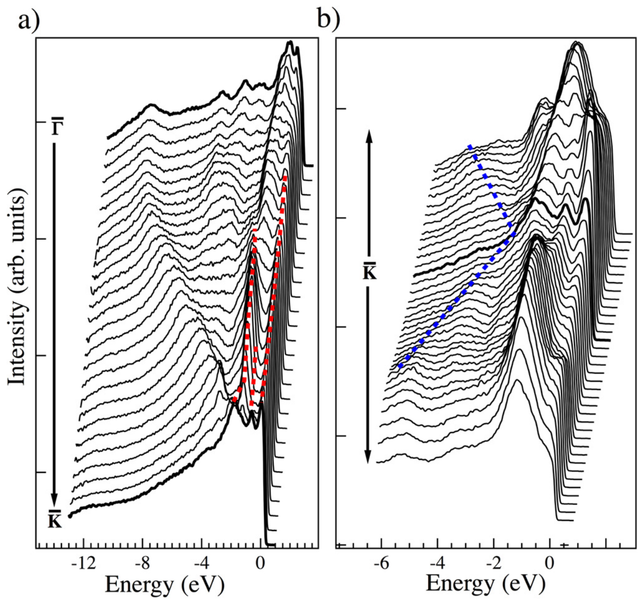

FIG. 2. (a) Selected EDCs of Gr/FeCo/Ir(111), extracted from data of Fig. 3(a), acquired with a photon energy of 86 eV and taken along the $\bar{\Gamma}$-$\bar{K}$ direction. Red dashed lines highlight states originating from the FeCo interface. (b) Selected EDCs taken along the direction perpendicular to $\bar{\Gamma}$-$\bar{K}$. Blue dashed lines highlight the π band of Gr. The $\bar{K}$-point has been extracted at an electron kinetic energy of about 80 eV.

$\bar{\Gamma}$-$\bar{K}$ [Fig. 2(b)] show the maximum of the Gr π band at about 2.1 eV of BE. Other pure Gr/FM systems exhibit a π band maximum between 2.5 and 3.0 eV, depending both on the metal and on the number of intercalated layers.[23,27,43–46] The Gr/Co system, e.g., leads to a crossing point between π bands located at 2.8 eV of BE.[23] For Gr/FeCo/Ir, the lower BE value of the π band maximum suggests a reduced width of the FeCo-d states and thus a reduced hybridization with the π band.

The region in the proximity of the $\bar{K}$-point exhibits several features directly related to the mixed Fe-Co interface with Gr. Specifically, in Fig. 2(a), we highlight with red dashed lines three slightly dispersing states, crossing the $\bar{K}$-point at about −1.8 eV, −0.6 eV, and at the Fermi level (E_F). It is worth noticing that the appearance of these well-defined localized bands within $\sim$2 eV from E_F and their dispersive behavior provide further evidence of a uniform FeCo alloy. The bands at about 4 eV of BE, less dispersive toward the $\bar{K}$ point and resonant with the π band of Gr, can be attributed to the FeCo interlayer. As discussed in the following, these states are due to the majority 3d states of both Co and Fe atoms, while the states close to E_F can be associated with the Fe and Co 3d spin minority bands.

The experimental evidence of narrow bands associated with FeCo in the energy region of E_F and the hybridization of π states of graphene is confirmed by the DFT calculations. The spin-resolved electronic structure of Gr/1ML-FeCo/Ir(111), shown in Figs. 3(b)–3(e), is projected on atomic orbitals of different species and mapped into the 1×1 Gr BZ along the $\bar{\Gamma}$-$\bar{K}$ direction. With respect to free-standing Gr, the main effect on the π and σ bands is a non-rigid shift toward higher BE [Fig. 3(b)], as also found in the literature for pure intercalated systems.[23,27,43–45] In addition, our calculations clearly show a significant interaction of the Gr π-band with the FeCo-d majority states, which is stronger than with the minority bands. This is especially evident in the wide 0–5 eV energy range below E_F [Fig. 3(a)]. The spin-down π band of Gr preserves its linear dispersion up to about −2 eV, where it strongly overlaps with the FeCo minority states [Figs. 3(b)–3(d)], and their interaction pushes the π band maximum down, in agreement with our ARPES measurements. Therefore, in line with a recent paper of Gr grown on a Mn$_5$Ge$_3$ FM interface,[32] the theoretical predictions demonstrate that the interaction of Gr with the FeCo layer gives rise to a downshifted Gr π band, which is mainly minority-spin polarized.

This picture is further confirmed and summarized by the comparison of the total band structure (central panel of Fig. 4), with the spin DOS projected on C, Fe, Co, and Ir atomic orbitals (left-right panels of Fig. 4), computed within DFT for Gr/1ML-FeCo/Ir(111). From the pDOS, we can see that the Fe and Co 3d states, particularly in the majority spin channel, almost coincide (see the supplementary material for a detailed analysis, including the role of DFT+U corrections). The majority spin channel is almost filled, with an intense peak

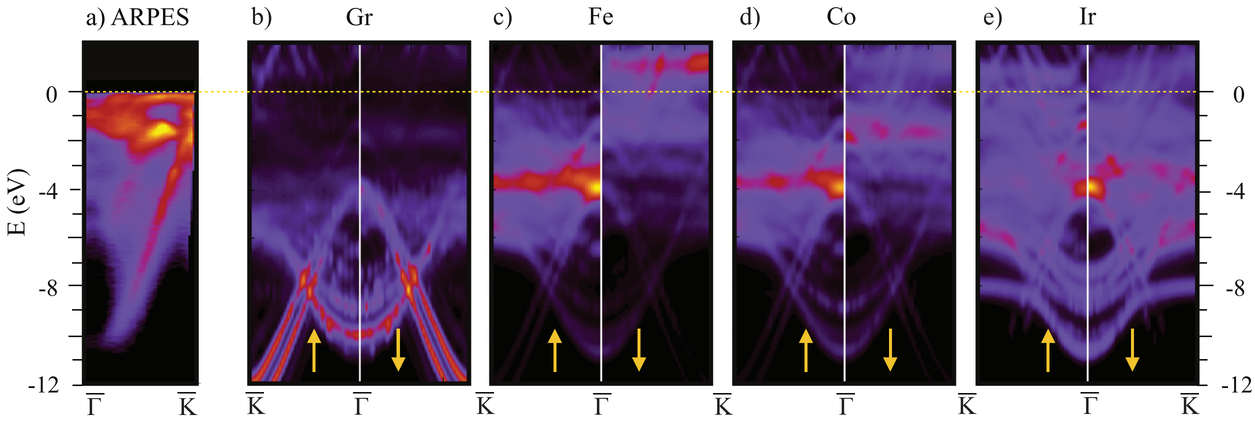

FIG. 3. Comparison between ARPES measurements of Gr/FeCo/Ir(111) taken along the $\bar{\Gamma}$-$\bar{K}$ direction (a) and the band structure computed for the 10×10 supercell of Gr/1ML-FeCo/Ir(111), mapped into the graphene 1×1 BZ and projected into the atomic orbitals of the different atomic species (b)–(e).

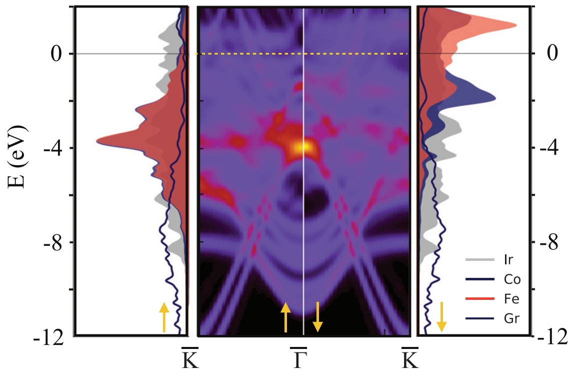

FIG. 4. Central panel: majority and minority spin band structure computed within DFT for Gr/1ML-FeCo/Ir(111). Left (right) panel: majority (minority) spin DOS computed within DFT and projected on C, Fe, Co, and Ir atomic orbitals.

centered at about –4 eV, where the spin-up Dirac cone is strongly hybridized and almost quenched. In the minority spin channel, the main superimposition of Fe and Co pDOS peaks is seen at about –2 eV and at the Fermi level, where, indeed, the transition metal states appear in our ARPES measurements.

The density of states and the spin electronic bands for bulk FeCo alloys have been deeply investigated and discussed in the literature.[4,47,48] The strong hybridization of Fe and Co in the bulk alloy produces an increase in the Fe exchange splitting and a saturation of the magnetic moments.[47,48] More specifically, it has been shown that at about 30% Fe content, the atomic magnetic moments become almost independent of the alloy composition due to a redistribution of 3*d* minority electrons to the 3*d* majority states at the Fe sites. Furthermore, the reduced dimensionality and number of nearest neighbors at the FeCo interface also influence the *d* bandwidth and the spin splitting of the states.[4,47,48]

Despite a number of differences with the Gr/FeCo/Ir interfaces studied here, such as the interaction with Gr or with the Ir surface, some of the features of FeCo alloys subsist. In particular, we observe a larger spin-splitting between majority and minority spin channels and a narrowing bandwidth of the 3*d* states for this confined FeCo layer with respect to bulk Fe and FeCo.[47] A detailed comparison between the Gr/FeCo/Ir(111) interface and the bulk systems is presented in the SI. From the DFT simulations, the spin-resolved DOS of Fe and Co show almost completely filled 3*d*-states in the spin-up channel, with about 4.76(4.70) electrons for Fe(Co), while about 2.08(3.09) electrons are localized in the 3*d* spin-down channel. Though the energy position of the FeCo 3*d* states depends on the values of U chosen for the Hubbard correction, there is always a significant overlap between the Fe and Co states, while the Gr states are almost insensitive to different values of U, as described in the supplementary material.

Therefore, the results shown in Fig. 4 demonstrate that the reduced symmetry and the structural configuration of the intercalated equiatomic FeCo layer induce a clear splitting of Fe 3*d*-up and down bands, with a narrower bandwidth with respect to Fe bulk.

This picture is consistent with previous XMCD measurements on Gr/FeCo/Ir(111), showing a sensible enhancement of the magnetic moments[8] with a strong ferromagnetic coupling between Fe and Co.

In conclusion, within the present study, we characterize the electronic and structural properties of few FeCo layers, embedded between Gr and Ir(111). By means of ARPES, we show that the interaction of the π band of Gr with FeCo-3*d* states pushes the strongly hybridized Dirac cone toward higher BE in analogy with pure intercalated systems. However, in proximity of E_F, we identify dispersive states associated with the FeCo alloy. By means of DFT, we show that the homogeneous intermixing of the two FMs and the artificial structural phase, where the FeCo layer is stretched to the Ir(111) lattice constant, leads to a narrowing and to an enhanced spin splitting of the 3*d* states with respect to pure bulk systems. From an experimental point of view, we have induced such narrowing and enhanced spin splitting within a homogeneous 2D FeCo system. Therefore, our study provides an artificial 2D FeCo system protected from contaminants through the Gr layer, inducing an enhanced magnetic response, which can be further engineered for integration in magnetic devices.

See the supplementary material for selected core level measurements; additional calculations of projected DOS with different values of the Hubbard U parameter; and projected DOS for 10 × 10 Gr/FeCo/Ir(111), 10 × 10 Gr/Fe/Ir(111), and 10 × 10 Gr/Co/Ir(111) and DOS for the corresponding FM bulk systems.

This work was partially supported by the MaX – MAterials design at the eXascale–Centre of Excellence, funded by the European Union program H2020-INFRAEDI-2018-1 (Grant No. 824143), by PRIN FERMAT (No. 2017KFY7XF) from Italian Ministry MIUR, and by Sapienza Ateneo funds. Computational time on the Marconi100 machine at CINECA was provided by the Italian ISCRA program. This work was partly performed in the framework of the nanoscience foundry and fine analysis (NFFA-MIUR Italy Progetti Internazionali) facility. The authors thank A. Vegliante for his contribution to the experiment.

DATA AVAILABILITY

The data that support the findings of this study are available from the corresponding author upon reasonable request.

REFERENCES

[1] P. James, O. Eriksson, B. Johansson, and I. A. Abrikosov, Phys. Rev. B **59**, 419 (1999).
[2] F. Luo, X. L. Fu, A. Winkelmann, and M. Przybylski, Appl. Phys. Lett. **91**, 262512 (2007).
[3] M. Getzlaff, J. Bansmann, F. Bulut, R. Gebhardt, A. Kleibert, and K. Meiwes-Broer, Appl. Phys. A **82**, 95 (2006).
[4] G. Moulas, A. Lehnert, S. Rusponi, J. Zabloudil, C. Etz, S. Ouazi, M. Etzkorn, P. Bencok, P. Gambardella, P. Weinberger, and H. Brune, Phys. Rev. B **78**, 214424 (2008).
[5] P. Gambardella, S. Rusponi, M. Veronese, S. S. Dhesi, C. Grazioli, A. Dallmeyer, I. Cabria, R. Zeller, P. H. Dederichs, K. Kern, C. Carbone, and H. Brune, Science **300**, 1130 (2003).
[6] B. Nonas, I. Cabria, R. Zeller, P. H. Dederichs, T. Huhne, and H. Ebert, Phys. Rev. Lett. **86**, 2146 (2001).
[7] P. Gambardella, A. Dallmeyer, K. Maiti, M. C. Malagoli, W. Eberhardt, K. Kern, and C. Carbone, Nature **416**, 301 (2002).
[8] G. Avvisati, P. Gargiani, D. Lizzit, M. Valvidares, P. Lacovig, C. Petrillo, F. Sacchetti, and M. G. Betti, Appl. Surf. Sci. **527**, 146599 (2020).
[9] N. Sethulakshmi, A. Mishra, P. Ajayan, Y. Kawazoe, A. K. Roy, A. K. Singh, and C. S. Tiwary, Mater. Today **27**, 107 (2019).
[10] B. D. Terris and T. Thomson, J. Phys. D: Appl. Phys. **38**, R199 (2005).

[11] S. Bhatti, R. Sbiaa, A. Hirohata, H. Ohno, S. Fukami, and S. N. Piramanayagam, Mater. Today **20**, 530 (2017).

[12] D. I. Bardos, J. Appl. Phys. **40**, 1371 (1969).

[13] E. D. Fabrizio, G. Mazzone, C. Petrillo, and F. Sacchetti, Phys. Rev. B **40**, 9502 (1989).

[14] C. Paduani and J. C. Krause, J. Appl. Phys. **86**, 578 (1999).

[15] W. Pepperhoff and M. Acet, *Constitution and Magnetism of Iron and Its Alloys* (Springer-Verlag, Berlin/Heidelberg, 2001).

[16] R. S. Sundar and S. C. Deevi, Int. Mater. Rev. **50**, 157 (2005).

[17] T. Hasegawa, S. Kanatani, M. Kazaana, K. Takahashi, K. Kumagai, M. Hirao, and S. Ishio, Sci. Rep. **7**, 13215 (2017).

[18] M. Einax, W. Dieterich, and P. Maass, Rev. Mod. Phys. **85**, 921 (2013).

[19] M. Batzill, Surf. Sci. Rep. **67**, 83 (2012).

[20] M. Weser, E. Voloshina, K. Horn, and Y. Dedkov, Phys. Chem. Chem. Phys. **13**, 7534 (2011).

[21] Y. Dedkov and E. Voloshina, J. Phys.: Condens. Matter **27**, 303002 (2015).

[22] R. Decker, J. Brede, N. Atodiresei, V. Caciuc, S. Blügel, and R. Wiesendanger, Phys. Rev. B **87**, 041403 (2013).

[23] D. Pacilè, S. Lisi, I. D. Bernardo, M. Papagno, L. Ferrari, M. Pisarra, M. Caputo, S. K. Mahatha, P. M. Sheverdyaeva, P. Moras, P. Lacovig, S. Lizzit, A. Baraldi, M. G. Betti, and C. Carbone, Phys. Rev. B **90**, 195446 (2014).

[24] D. Pacilè, P. Leicht, M. Papagno, P. Sheverdyaeva, P. Moras, C. Carbone, K. Krausert, L. Zielke, M. Fonin, Y. Dedkov, F. Mittendorfer, J. Doppler, A. Garhofer, and J. Redinger, Phys. Rev. B **87**, 035420 (2013).

[25] H. Vita, S. Böttcher, P. Leicht, K. Horn, A. B. Shick, and F. Máca, Phys. Rev. B **90**, 165432 (2014).

[26] Y. Dedkov and E. Voloshina, J. Electron. Spectrosc. Relat. Phenom. **219**, 77 (2017).

[27] C. Cardoso, G. Avvisati, P. Gargiani, M. Sbroscia, M. S. Jagadeesh, C. Mariani, D. A. Leon, D. Varsano, A. Ferretti, and M. G. Betti, Phys. Rev. Mater. **5**, 014405 (2021).

[28] G. Avvisati, S. Lisi, P. Gargiani, A. D. Pia, O. De Luca, D. Pacilè, C. Cardoso, D. Varsano, D. Prezzi, A. Ferretti, and M. G. Betti, J. Phys. Chem. C **121**, 1639 (2017).

[29] M. Yang, Y. Liu, T. Fan, and D. Zhang, Prog. Mater. Sci. **110**, 100652 (2020).

[30] R. S. Weatherup, L. D'Arsié, A. Cabrero-Vilatela, S. Caneva, R. Blume, J. Robertson, R. Schloegl, and S. Hofmann, J. Am. Chem. Soc. **137**, 14358 (2015).

[31] M. Bazarnik, R. Decker, J. Brede, and R. Wiesendanger, Surf. Sci. **639**, 70 (2015).

[32] E. Voloshina, B. Paulus, and Y. Dedkov, J. Phys. Chem. Lett. **12**, 19 (2021).

[33] P. Giannozzi, S. Baroni, N. Bonini, M. Calandra, R. Car, C. Cavazzoni, D. Ceresoli, G. L. Chiarotti, M. Cococcioni, I. Dabo *et al.*, J. Phys.: Condens. Matter **21**, 395502 (2009).

[34] P. Giannozzi, O. Andreussi, T. Brumme, O. Bunau, M. Buongiorno Nardelli, M. Calandra, R. Car, C. Cavazzoni, D. Ceresoli, M. Cococcioni, N. Colonna, I. Carnimeo, A. Dal Corso, S. de Gironcoli, P. Delugas, R. A. DiStasio, Jr., A. Ferretti, A. Floris, G. Fratesi, G. Fugallo, R. Gebauer, U. Gerstmann, F. Giustino, T. Gorni, J. Jia, M. Kawamura, H.-Y. Ko, A. Kokalj, E. Küçükbenli, M. Lazzeri, M. Marsili, N. Marzari, F. Mauri, N. L. Nguyen, H.-V. Nguyen, A. O. de-la Roza, L. Paulatto, S. Poncé, D. Rocca, R. Sabatini, B. Santra, M. Schlipf, A. P. Seitsonen, A. Smogunov, I. Timrov, T. Thonhauser, P. Umari, N. Vast, X. Wu, and S. Baroni, J. Phys.: Condens. Matter **29**, 465901 (2017).

[35] J. P. Perdew and A. Zunger, Phys. Rev. B **23**, 5048 (1981).

[36] C. J. Cramer and D. G. Truhlar, Phys. Chem. Chem. Phys. **11**, 10757 (2009).

[37] M. Cococcioni and S. De Gironcoli, Phys. Rev. B **71**, 035105 (2005).

[38] G. Avvisati, C. Cardoso, D. Varsano, A. Ferretti, P. Gargiani, and M. G. Betti, Nano Lett. **18**, 2268 (2018).

[39] A. Calloni, G. Bussetti, G. Avvisati, M. S. Jagadeesh, D. Pacil, A. Ferretti, D. Varsano, C. Cardoso, L. Du, F. Ciccacci, and M. G. Betti, J. Chem. Phys. **153**, 214703 (2020).

[40] V. Popescu and A. Zunger, Phys. Rev. B **85**, 085201 (2012).

[41] P. Bonfà, https://bitbucket.org/bonfus/unfold-x for the sources of the unfold-x code by P. Bonfa.

[42] R. Decker, M. Bazarnik, N. Atodiresei, V. Caciuc, S. Blügel, and R. Wiesendanger, J. Phys.: Condens. Mater. **26**, 394004 (2014).

[43] A. Varykhalov, D. Marchenko, J. Sánchez-Barriga, M. R. Scholz, B. Verberck, B. Trauzettel, T. O. Wehling, C. Carbone, and O. Rader, Phys. Rev. X **2**, 041017 (2012).

[44] J. Brede, J. Sławińska, M. Abadia, C. Rogero, J. E. Ortega, I. Piquero-Zulaica, J. Lobo-Checa, A. Arnau, and J. I. Cerdá, 2D Mater. **4**, 015016 (2016).

[45] D. Usachov, A. Fedorov, M. M. Otrokov, A. Chikina, O. Vilkov, A. Petukhov, A. G. Rybkin, Y. M. Koroteev, E. V. Chulkov, V. K. Adamchuk, A. Grüneis, C. Laubschat, and D. V. Vyalikh, Nano Lett. **15**, 2396 (2015).

[46] L. Massimi, S. Lisi, D. Pacilè, C. Mariani, and M. G. Betti, Beilstein J. Nanotechnol. **5**, 308 (2014).

[47] R. H. Victora, L. M. Falicov, and S. Ishida, Phys. Rev. B **30**, 3896 (1984).

[48] S. Pizzini, A. Fontaine, E. Dartyge, C. Giorgetti, F. Baudelet, J. P. Kappler, P. Boher, and F. Giron, Phys. Rev. B **50**, 3779 (1994).

Narrowing of d bands of FeCo layers intercalated under graphene
Supplemental Material

Daniela Pacilè*,[1] Claudia Cardoso*,[2] Giulia Avvisati,[3] Ivana Vobornik,[4] Carlo Mariani,[3] Dario A. Leon,[5,2] Pietro Bonfà,[6,2] Daniele Varsano,[2] Andrea Ferretti,[2] and Maria Grazia Betti[3]

[1] *Dipartimento di Fisica, Università della Calabria, I-87036 Arcavacata di Rende, (Cs) Italy**
[2] *Centro S3, CNR-Istituto Nanoscienze, I-41125 Modena, Italy*
[3] *Dipartimento di Fisica, Università di Roma "La Sapienza", I-00185 Roma, Italy*
[4] *Istituto Officina dei Materiali (IOM)-CNR, Laboratorio TASC,*
Area Science Park, S.S.14, Km 163.5, 34149 Trieste, Italy
[5] *Università di Modena e Reggio Emilia I-41125 Modena, Italy*
[6] *Università di Parma, Dipartimento di Scienze Matematiche, Fisiche e Informatiche, I-43124 Parma, Italy*

(Dated: March 4, 2021)

I. SELECTED CORE LEVELS

The quality of the equiatomic FeCo layers intercaleted under Gr grown on Ir(111) has been checked by core level spectra and LEED measurements. A challenging step in the preparation procedure is the temperature-induced intercalation of ferromagnetic metals avoiding the alloy formation with the Ir(111) substrate. We have grown a high-quality Gr/FeCo/Ir(111) intercalated system keeping the temperature at about 500K for few minutes. In order to monitor the absence of Fe-Ir and Co-Ir alloying, we have taken Ir $4f$ core level spectra and compare them with those of Gr/Ir(111). Some representative measurements are shown in Fig. S1, where we show the Ir $4f_{7/2}$ peak of Gr/Ir(111) (top) and Gr/FeCo/Ir(111) (bottom), fitted by a Pseudo-Voigt curve to highlight the bulk and surface components. We point out that, upon intercalation, the surface component of the Ir $4f_{7/2}$ peak (green curve) exhibits the expected reduced intensity but any measurable chemical shift. The Ir $4f_{7/2}$ bulk component (blue curve) exhibits a chemical shift of about 50 meV towards lower BE, which is however comparable to the line width enlargement measured going from Gr/Ir(111) (400 meV) to Gr/FeCo/Ir(111) (450 meV). Other representative spectra of Ir $4f$, C$1s$, Co $2p$ and Fe $2p$, together with details on the fitting procedures, are reported in [1]. Therefore, we can conclude that the temperature we have used is high enough to trigger the intercalation process, as shown by LEED and ARPES measurements reported in the main text, but relatively low to avoid a prevalent alloy formation of Co and Fe atoms with the underlaying Ir(111) substrate. In line with present results, previous papers have shown that such alloying occurs on Ir(111) well above 600 K [2, 3].

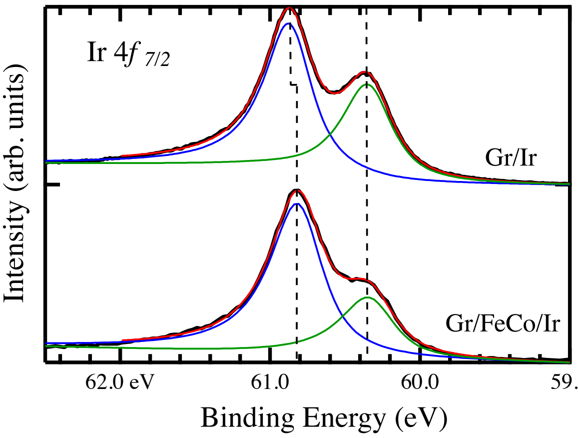

FIG. S1: Core level spectra taken with photon energy of 176 eV, showing the Ir $4f_{7/2}$ peak (black curves) and fitting components (blue and green curves; their sum is the red curve) of Gr/Ir (top) and Gr/FeCo/Ir (bottom).

II. CALCULATION METHODS

A. Structural parameters

The Gr/1ML-FeCo/Ir(111) interface was simulated by means of Density Functional Theory, taking explicitly into account the complete moiré induced periodicity by using a 9×9 supercell of Ir(111), corresponding to a 10×10 supercell of pristine Gr. The lattice parameters were obtained by performing a relaxation of the Ir bulk in the LDA approximation using ultrasoft pseudopotentials (USPP), resulting in a Ir–Ir bond distance of 2.7048 Å (corresponding to a hexagonal cell of 46.001 Bohr radius for the moiré structure). In all the calculations we included four metallic layers (3 Ir plus one FeCo layer). The two sides of the slab were made non-equivalent by adding a layer of H atoms in one of the two sides. Atomic positions were then fully relaxed (except for the two bottom Ir layers and the H saturation layer) until ionic forces were smaller than 0.001 Ry/Bohr. All the self-consistent calculations were performed using a 2×2 **k**-point grid,

---

*Electronic address: *Authors to whom correspondence should to addressed: daniela.pacile@fis.unical.it and claudia-maria.cardosopereira@nano.cnr.it

U	Fe/Ir m(Fe)	Co/Ir m(Co)	Gr/Fe/Ir m(Fe)	Gr/Co/Ir m(Co)
0	2.67	1.74	2.09	1.13
2	2.93	1.88	2.42	1.40
4	3.20	2.01	2.61	2.10
5	3.16	1.86	2.63	1.96
6	3.14	2.26	2.62	2.02

TABLE S1: Magnetic moment per atom in μ_B/atom computed for the 1×1 Fe/Ir, Co/Ir, Gr/Fe/Ir and Gr/Co/Ir interfaces, considering different values of U, given in eV.

USPP to model the electron-ion interaction and a kinetic energy cutoff of 30 and 240 Ry to represent Kohn-Sham wavefunctions and density, respectively.

B. Parameters for the DFT+U scheme

Since LDA is known to underestimate the values of the orbital magnetic moments in transition metals [4], we have adopted a DFT+U scheme [5], with a Hubbard U parameter of 2 eV for Fe and 4 eV for Co in the calculations for the 10×10 Gr/FeCo/Ir(111) supercell.

The U value was chosen after systematic tests done on smaller model systems consisting in 1×1 and 2×2 cells where we kept fixed the LDA Ir lattice parameter. We considered interfaces with and without graphene. In the latter case, the graphene layer was artificially stretched in order to have commensurate interfaces. We begin by computing the Hubbard parameters using linear-response within the framework of density-functional perturbation theory [6] for the Fe/Ir(111) and Co/Ir(111) interfaces, obtaining respectively values of 2.4 and 4.8 eV. Since a similar calculation done on the large 10×10 supercell is forbiddingly heavy from the computational point of view, the choice for the values of U resorted to the analysis of the following data.

The magnetic moments computed for Fe and Co 1×1 interfaces for a set of different U values are reported in Tab. S1. As expected, the inclusion of U increases the magnetic moment of both Fe and Co. For the interfaces without graphene, the maximum magnetic moment is achieved for U=4 eV, whereas for the interfaces with graphene, the magnetic moment increases with U for all the values considered. In any case, the changes are more abrupt for the U values between 0 and 4 eV. We can observe that for all the values of U, the presence of graphene reduces the magnetic moment of both Fe and Co (though the reduction for Fe is significantly larger for $U \leq 4$ eV).

In Fig. S2 we show the the Projected Density Of States (pDOS) computed for a 2×2 Gr/FeCo/Ir supercell with different U parameters. For all the values of U considered we observe a significant hybridization of the Fe an Co states both in the majority and minority spin channels, together with a downshift of the majority spin states which depends on the chosen values of U. On the other hand, the graphene pDOS remains unaltered, being very similar for all the values of U. It is worth noticing that, in the 2×2 supercell considered here, the graphene lattice is stretched and therefore its pDOS differs from the one computed for the larger 10×10 supercell shown in the main text.

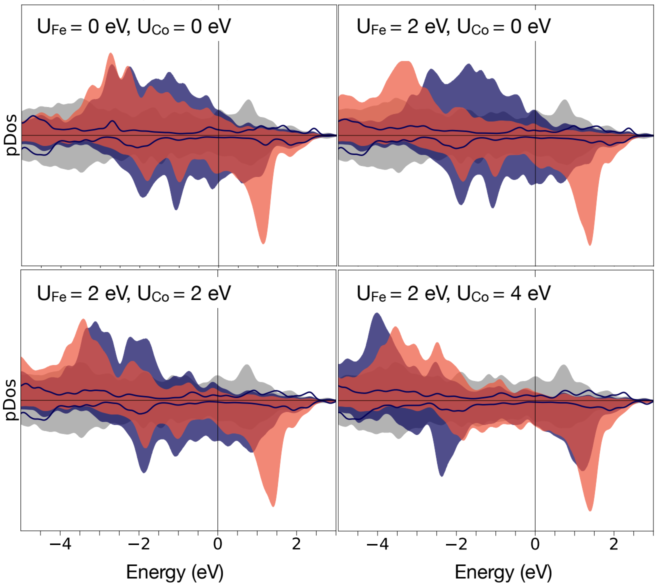

FIG. S2: Projected density of States computed for a 2×2 Gr/FeCo/Ir supercell with different values of U, in eV. In all the panels: Fe states (red area), Co states (blue area), Ir (gray area), Gr (solid line).

The values of U for the 10×10 Gr/FeCo/Ir(111) supercell were chosen by considering all the information described above. We have concluded that it was reasonable to use the values of 2 and 4 eV for Fe and Co respectively. Similar values had been used for Gr/Co/Ir(111) [7] and Gr/Fe/Ir(111) [8]. In the main text we have reported that the majority spin states coincide in energy and the minority spin states also show a large overlap, keeping in mind that this behavior depends critically on the chosen values of U, as demonstrated by the analysis provided in Fig. S2.

III. COMPARISON OF PDOS FOR DIFFERENT TRANSITION METALS

In Figure S3 we present the DOS projected on the $3d$ metal and on graphene, computed within DFT+U for Gr/FeCo/Ir(111) and Gr/Fe/Ir(111) and Gr/Co/Ir(111). The calculations were done considering the complete moiré induced periodicity by using a 9×9 supercell of Ir(111), corresponding to a 10×10 supercell of pristine Gr, similarly to the results presented in the main text. For the reasons explained above, we have adopted a DFT+U scheme [5], with a Hubbard U parameter of 2 eV

	Gr/FeCo/Ir		**Gr/Fe/Ir**		**Gr/Co/Ir**	
	up	**down**	**up**	**down**	**up**	**down**
Fe	4.76	2.08	4.74	2.20	-	-
Co	4.70	3.09	-	-	4.71	3.00
Fe+Co	4.74	2.58	-	-	-	-

TABLE S2: Average occupation per atom and per spin of the valence states, $3d$, computed for the Gr/FeCo/Ir, Gr/Fe/Ir and Gr/Co/Ir interfaces. Values of U=2 eV and U=4 eV have been adopted for Fe and Co atoms, respectively.

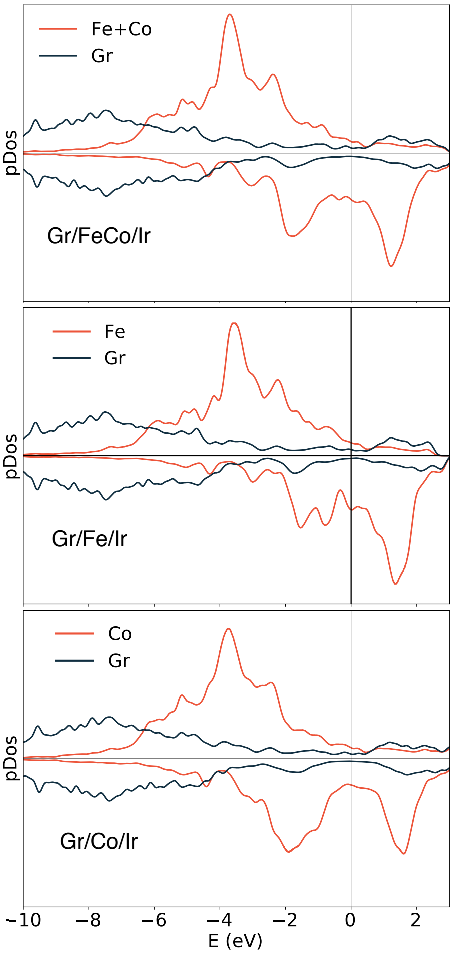

FIG. S3: Density of states projected on the $3d$ metal and on graphene, computed for a 10×10 Gr/FeCo/Ir supercell compared with the pDOS computed for 10×10 Gr/Fe/Ir and 10×10 Gr/Co/Ir. Values of U=2 eV and U=4 eV have been adopted for Fe and Co atoms, respectively.

for Fe and 4 eV for Co, and again we would like to stress the critical dependence of the DOS on the chosen values of U.

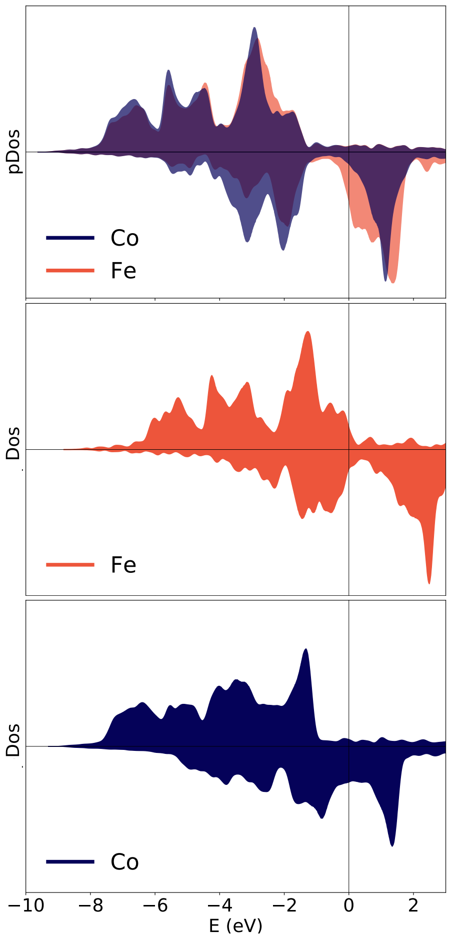

FIG. S4: Density of States computed for the bulk systems bcc FeCo, bcc Fe and hpc Co with the same values of U used for the interfaces: U=2 eV and U=4 eV for Fe and Co atoms, respectively.

The three systems present a large spin split of the $3d$ states, with the majority spin states fully occupied. The main differences are seen in the minority spin states. Despite the fact that all interfaces show two sets of peaks, one below and the other above the Fermi energy, the relative intensity and shape of the peaks is different: for Gr/Co/Ir(111) the set of peaks below Fermi has the same height but is broader than the one above; the opposite happens for Gr/Fe/Ir(111) and Gr/FeCo/Ir(111), that present similar DOS shapes and the unoccupied peak larger than the one below E_F. The values of the occupation averaged for Fe an Co for each spin state are summarized in Table S2. This is reflected in the magnetization. The total magnetization of the interface, including three Ir layers, is respectively 176, 203 and 139 μ_B for Gr/FeCo/Ir(111) and Gr/Fe/Ir(111) and Gr/Co/Ir(111). The average magnetic moment per atom for the $3d$ metals is 2.7 μ_B for Fe and 1.6 μ_B for Co in case of Gr/FeCo/Ir(111). These values are comparable with the ones computed for the pure intercalated layer, for Fe in Gr/Fe/Ir(111), 2.5 μ_B and for Co in Gr/Co/Ir(111), 1.7 μ_B, showing that the spin magnetic moment of Fe and Co does not change much with the relative Fe/Co concentration, as previously reported for $\mathrm{Fe}_x\mathrm{Co}_{1-x}$/Pt(111) [9]. The computed spin moment for $\mathrm{Fe}_x\mathrm{Co}_{1-x}$/Pt(111) are around 3 μ_B for Fe and 2 μ_B for Co, higher then the values reported here but the two model systems show several differences. In the case of $\mathrm{Fe}_x\mathrm{Co}_{1-x}$/Pt(111), the absence of the graphene layer and the fact that the studied geometry considers a commensurate interface, straining the FeCo layer by 10% to match the underlying Pt surface.

In Figure S4 we present the DOS for the Fe, Co and FeCo bulk systems, computed at the same level of theory. For the sake of comparison, we considered the same values of U, even if we expect them to be overestimated in this case. When comparing the pure systems with the league FeCo, we can see that there is a downshift in energy resulting in a coincidence of the Fe and Co states. For the minority spin states, there is a also a redistribution between the Fe and Co states which narrows the occupied minority spin states and results in a larger magnetic moment. In fact, when going from the pure systems to the league, the Fe magnetic moment increases form 2.4 μ_B to 2.9, and the Co moment form 1.5 μ_B to 1.7 μ_B. This increase is larger than what we see for the interfaces, for which, both in the case of the pure systems and Gr/FeCo/Ir(111), the occupied minority spin states are well separated from the occupied, resulting in two narrower sets of peaks.

[1] G. Avvisati, P. Gargiani, D. Lizzit, M. Valvidares, P. Lacovig, C. Petrillo, F. Sacchetti, and M. G. Betti, Appl. Surf. Sci. **527**, 146599 (2020).

[2] J. Brede, J. Sławińska, M. Abadia, C. Rogero, J. E. Ortega, I. Piquero-Zulaica, J. Lobo-Checa, A. Arnau, and J. I. Cerdá, 2D Mater. **4**, 015016 (2016).

[3] M. Bazarnik, R. Decker, J. Brede, and R. Wiesendanger, Surf. Sci. **639**, 70 (2015).

[4] C. J. Cramer and D. G. Truhlar, Phys. Chem. Chem. Phys. **11**, 10757 (2009).

[5] M. Cococcioni and S. De Gironcoli, Phys. Rev. B **71**, 035105 (2005).

[6] I. Timrov, N. Marzari, and M. Cococcioni, Phys. Rev. B **98**, 085127 (2018).

[7] R. Decker, J. Brede, N. Atodiresei, V. Caciuc, S. Blügel, and R. Wiesendanger, Phys. Rev. B **87**, 041403 (2013).

[8] C. Cardoso, G. Avvisati, P. Gargiani, M. Sbroscia, M. S. Jagadeesh, C. Mariani, D. A. Leon, D. Varsano, A. Ferretti, and M. G. Betti, Phys. Rev. Materials **5**, 014405 (2021).

[9] G. Moulas, A. Lehnert, S. Rusponi, J. Zabloudil, C. Etz, S. Ouazi, M. Etzkorn, P. Bencok, P. Gambardella, P. Weinberger, and H. Brune, Phys. Rev. B **78**, 214424 (2008).

PHYSICAL REVIEW B **104**, 115157 (2021)

Frequency dependence in *GW* made simple using a multipole approximation

Dario A. Leon,[1,2,*] Claudia Cardoso,[2] Tommaso Chiarotti,[3] Daniele Varsano,[2]
Elisa Molinari,[1,2] and Andrea Ferretti[2]

[1]*FIM Department, University of Modena & Reggio Emilia, Via Campi 213/a, Modena, Italy*
[2]*S3 Centre, Istituto Nanoscienze, CNR, Via Campi 213/a, Modena, Italy*
[3]*Theory and Simulation of Materials (THEOS), Ecole Polytechnique Fédérale de Lausanne (EPFL), CH-1015 Lausanne, Switzerland*

(Received 3 August 2021; accepted 7 September 2021; published 27 September 2021)

In the GW approximation, the screened interaction W is a nonlocal and dynamical potential that usually has a complex frequency dependence. A full description of such a dependence is possible but often computationally demanding. For this reason, it is still common practice to approximate $W(\omega)$ using a plasmon pole (PP) model. Such an approach, however, may deliver an accuracy limited by its simplistic description of the frequency dependence of the polarizability, i.e., of W. In this work, we explore a multipole approach (MPA) and develop an effective representation of the frequency dependence of W. We show that an appropriate sampling of the polarizability in the frequency complex plane and a multipole interpolation can lead to a level of accuracy comparable with full-frequency methods at a much lower computational cost. Moreover, both accuracy and cost are controllable by the number of poles used in MPA. Eventually, we validate the MPA approach in selected prototype systems, showing that full-frequency quality results can be obtained with a limited number of poles.

DOI: 10.1103/PhysRevB.104.115157

I. INTRODUCTION

In the context of condensed matter physics or quantum chemistry, many body perturbation theory (MBPT) provides accurate methods to study spectroscopic properties of matter from an *ab initio* perspective [1–3]. The calculations often adopt the so-called GW approximation [2,4–7] for the evaluation of the self-energy. As summarized in Sec. II, common single-step G_0W_0 implementations typically make use of one-particle energies and wavefunctions from previous DFT calculations to build the noninteracting one-particle Green's function $G(\omega)$ and the dynamical screened interaction potential $W(\omega)$. Next, the self-energy is evaluated via a frequency convolution of these two quantities that give the name to the approximation. More advanced approaches include, e.g., GW self-consistency treated at different levels [8–13], or the adoption of vertex corrections [10,14–16] and cumulant expansions [17]. A more comprehensive discussion of these aspects can be found, e.g., in Refs. [6,7].

Since its first implementations, the GW approach has been successfully applied to a wide range of systems [6,7] for the description of quasiparticle (QP) energies and bands as measured by ARPES experiments [18–22], including spectral functions [22,23], electronic satellites [17,24,25], and QP lifetimes [26,27]. Importantly, GW quasiparticle energies are also routinely used as input for absorption spectroscopy calculations within the Bethe-Salpeter approach [1,28]. Reflecting its wide adoption, the GW method has been implemented within multiple numerical schemes [29], ranging from localized basis sets [15,30–32], to plane waves and pseudopotentials or PAW [33–37], to all-electron approaches using LAPW [8,9,38,39], also allowing for cross validation and verification [37,40].

Crucial to the deployment of the method, the frequency integration in the evaluation of the GW self-energy has also been addressed in different ways. Common implementations of the GW method make use of the so-called plasmon-pole approximation (PPA) [41–45] where, besides the different technicalities, the frequency-dependency of the polarizability is simplified through an analytical model with a single pole (for positive frequencies, plus its anti-resonant match). The PPA method has the computational advantage of greatly simplifying the self-energy evaluation, but on the other hand its accuracy may be compromised especially for systems displaying a complex frequency structure in the screened potential. A number of alternative methods targeting a more accurate and possibly full frequency description of the self-energy exist [7], including: numerical evaluation of the GW frequency integrals [33,46–49]; full frequency contour-deformation (FF-CD) methods [9,50,51], taking advantage of the analytic properties of G and W; exact integration using the analytical structure of W [31]. While these approaches are typically accurate in terms of integration, they may turn out computationally demanding or somehow limited in accuracy by the analytic continuation (AC) methods [7,40,52–55] required by some of them.

In this work, we further explore the analytic properties of the response function by using a multipole model. The results are then used to implement a new technique, referred here as the multipole approximation (MPA), that allows one to obtain a simplified yet accurate description of W on the frequency real axis and evaluate the GW self-energy in an efficient way. The MPA technique naturally bridges from the PPA to a full-frequency treatment of the GW self-energy. This new approach has been implemented numerically within the YAMBO code [34,56] and tested in different materials.

---

[*] darioalejandro.leonvalido@nano.cnr.it

The work is organized as follows. In Sec. II, we first summarize the basic equations of the *GW* method and present the main ideas of the MPA method, in Sec. III, we describe an optimal frequency sampling strategy to reach a good accuracy with a reduced computational cost, and finally, in Sec. IV, we show the performance of the proposed method for three prototype bulk materials: silicon, hBN, and rutile TiO_2. In Appendix A, we present the mathematical details of the MPA interpolation and in Appendix B, we discuss in detail different plasmon-pole models and their connection.

II. THEORY: FORMULATION

A. Quasiparticle energies within *GW*

Following Hedin's equations [1,4], the *GW* approximation for the electron-electron self-energy Σ is obtained by neglecting vertex contributions beyond the independent-particle level (for both Σ and the irreducible polarizability X_0). This leads to an expression where Σ^{GW} is given in terms of a frequency convolution of the Green's function G with the screened Coulomb potential W,

$$\Sigma^{GW}(\omega) = \frac{i}{2\pi}\int_{-\infty}^{+\infty} d\omega' e^{-i\omega'\eta} G(\omega-\omega')W(\omega'), \qquad (1)$$

which can be seen as the first order in a perturbation expansion involving W instead of the bare interaction v. By expressing the independent particle irreducible polarizability X_0 as

$$X_0(\omega) = -\frac{i}{2\pi}\int_{-\infty}^{+\infty} d\omega' G(\omega+\omega')G(\omega'), \qquad (2)$$

the screened Coulomb interaction W and the dressed polarizability X can be obtained from the following Dyson equation:

$$\begin{aligned} X(\omega) &= X_0(\omega) + X_0(\omega) v X(\omega), \\ W(\omega) &= \varepsilon^{-1}(\omega) v = v + vX(\omega)v. \end{aligned} \qquad (3)$$

In the above expressions, v is the bare Coulomb potential and ε is the dielectric function. Importantly, the frequency dependence of W comes from its correlation term $W_c = W - v = vXv$, in turn leading to the correlation part of the self-energy, Σ_c, according to Eq. (1).

Usually, a noninteracting Green's function G_0, typically the Green's function of the Kohn-Sham (KS) system, is taken as initial guess and the *GW* self-energy is evaluated without performing further self-consistent iterations (one-shot G_0W_0). Treating the self-energy as a first order perturbation to the KS problem, one can then compute the quasiparticle (QP) energies, ϵ_m^{QP}, either by numerically solving the exact QP equation,

$$\epsilon_m^{\mathrm{QP}} = \epsilon_m^{\mathrm{KS}} + \langle \psi_m^{\mathrm{KS}} | \Sigma(\epsilon_m^{\mathrm{QP}}) - v_{xc}^{\mathrm{KS}} | \psi_m^{\mathrm{KS}} \rangle, \qquad (4)$$

or its linearized form:

$$\epsilon_m^{\mathrm{QP}} \approx \epsilon_m^{\mathrm{KS}} + Z_m \langle \psi^{\mathrm{KS}} | \Sigma(\epsilon_m^{\mathrm{KS}}) - v_{xc}^{\mathrm{KS}} | \psi_m^{\mathrm{KS}} \rangle. \qquad (5)$$

In the latter expression, the renormalization factor Z_m is computed from the first term of the Taylor expansion of the self-energy, Σ:

$$Z_m = \left[1 - \langle \psi_m^{\mathrm{KS}} | \frac{\partial \Sigma(\omega)}{\partial \omega}\bigg|_{\omega=\epsilon_m^{\mathrm{KS}}} | \psi_m^{\mathrm{KS}} \rangle \right]^{-1}. \qquad (6)$$

In practice, in order to build the self-energy and compute quasiparticle corrections at the G_0W_0 level, as a first step one needs to construct the polarizability X_0 from the knowledge of G_0 according to Eq. (2). The former is then used for the calculation of W.

The Lehmann representation for the bare Green's function G_0, computed using the KS states is written in a compact form as:

$$G_0(\omega) = \sum_m^{N_B} P_m \left[\frac{f_m}{\omega - E_m - i\eta} + \frac{(1-f_m)}{\omega - E_m + i\eta} \right], \qquad (7)$$

where $|\psi_m\rangle$ and $E_m = \epsilon_m^{\mathrm{KS}}$ are KS eigenpairs, f_m their occupations, $P_m = |\psi_m\rangle\langle\psi_m|$ their projectors, and the sum-over-states is usually truncated at a maximum number of bands N_B. Eventually, the limit $\eta \to 0^+$ is taken. By using G_0 in Eq. (2), the irreducible polarizability can be expressed as

$$X_0(\omega) = \sum_n^{N_T} \frac{2\Omega_n^{\mathrm{KS}} R_n^{\mathrm{KS}}}{\omega^2 - (\Omega_n^{\mathrm{KS}})^2}, \qquad (8)$$

where n runs over single particle transitions, possibly truncated to N_T according to the number of bands included in the calculation. Note, however, that methods avoiding the explicit sums over empty states have been developed and made available [57–59]. In Eq. (8), R_n^{KS} are the transition amplitudes computed from the Kohn-Sham states, while the poles Ω_n^{KS} are defined as

$$\Omega_n^{\mathrm{KS}} = \Delta\epsilon_n^{\mathrm{KS}} - i\delta, \qquad (9)$$

where $\Delta\epsilon_n^{\mathrm{KS}} \geqslant 0$ and $\delta \to 0^+$ is a damping parameter that ensures the time ordering, similarly to η in the case of G_0.

Here, for the sake of simplicity, we have kept all spatial degrees of freedom implicit and have not highlighted quantum numbers such as **k** and **q** deriving from a possible translational symmetry of the system. In this respect, and using a plane-wave basis set of **G** vectors, $X_0(\omega)$ and R_n^{KS} in Eq. (8) would depend on the extra indexes $\mathbf{qGG}'$, while the index n labels transitions between states $\mathbf{k}, i$ and $\mathbf{k}-\mathbf{q}, j$.

B. Frequency integration methods in *GW*

In principle, the screened interaction $W(\omega)$ needs to be computed, as the solution of Eq. (3), for all the frequencies needed to evaluate the *GW* self-energy according to Eq. (1). Nevertheless, the frequency dependence of W may be quite complex, making the evaluation of the correlation part of the *GW* self-energy not straightforward and computationally demanding.

Early approaches [41–45] adopted the so-called plasmon-pole model, originally proposed with explicitly real poles neglecting any spectral broadening. The simplification of the structure of X, and also of W according to Eq. (3), that the model provides is called the plasmon-pole approximation (PPA) [41,60]. The PPA has mainly two variants, one proposed by Godby and Needs (GN) [43], and the other by Hybertsen and Louie (HL) [41] (though more parametrizations and refinements exist [42], for example, the von der Linden-Horsch [44], or Engel-Farid [45] models). The analytic continuation of the polarizability X, within the PPA is written, for each $\mathbf{qGG}'$ (suppressed in the equation) matrix element, as

$$X^{\mathrm{PP}}(z) = \frac{2\Omega^{\mathrm{PP}} R^{\mathrm{PP}}}{z^2 - (\Omega^{\mathrm{PP}})^2}, \tag{10}$$

where Ω^{PP} is defined according to $\mathrm{Re}[\Omega^{\mathrm{PP}}] > 0$ and $\mathrm{Im}[\Omega^{\mathrm{PP}}] = 0^-$. For the sake of the present work, the two approaches are summarized and compared in Appendix B.

In a full frequency real-axis (FF-RA) approach, the polarizability is evaluated considering a dense frequency grid on the real axis and the integral for the self-energy evaluation is then computed numerically [46,47,61]. Such an approach requires the use of a finite damping that broadens the structure of the polarizability [47], and a large number of frequency sampling points is typically required to converge the integral. Other numerical integration techniques for the evaluation of the response function or the *GW* self-energy make use of quadrature rules [48,51], spectral representations of the polarizability [33,49], or resort to Fourier transform to imaginary time to perform frequency convolutions [11,32,52,55].

Other procedures make use of imaginary-path axis integral methods in order to transform the integration on the real axis in the self-energy into an integral over an imaginary axis [9,50,51]. A similar approach resorts to a contour deformation (CD) defined in the first and third quadrants of the complex plane [62], in order to obtain a convenient frequency path that avoids all the poles of W and encompasses only the poles of G. The integration on the real axis is then replaced by a sum of the residues of the poles in the contour plus an integral on the imaginary axis. This integral can be addressed either numerically [63,64] or with the help of multipole forms [53,54] or Padé approximants [7,40]. Taking advantage of the time-reversal symmetry of W, it is possible to reduce the frequency range in which W is evaluated for the self-energy integration, either on the real or the imaginary axis [9,50,51].

Other dedicated approaches are also available. A many-pole model for the self-energy has been developed for the calculation of inelastic losses in x-ray spectroscopy [65,66]. Full-frequency *GW* has also been reformulated as a frequency-independent eigenvalue problem [67]. Similarly, a spectral representation of propagators in the form of a generalized sum-over-poles combined with an algorithmic inversion technique has been recently developed and applied to the homogeneous electron gas [68]. The FF-CD has been recently used jointly with analytic-continuation techniques in an all electrons scheme that adopts a sampling along both, the imaginary axis and parallel to the real axis [64].

C. The multipole scheme

In this work, we develop a multipole approach to represent W and evaluate the *GW* self-energy. Our multipole scheme is based on the Lehmann representation of X [2,69–71], in which the polarizability is written as a sum of poles. It is important to emphasize that, contrarily to standard PPA implementations, we consider complex poles and that the computed poles do not correspond to single-particle transitions (poles of X_0), but are rather intended to represent plasmon excitations. Each plasmonic pole describes the envelope of a set of transitions, with a finite imaginary part corresponding to the width of the excitation.

To represent and exploit the analytic properties of the polarizability X, we define a complex frequency $z \equiv \omega + i\varpi$, and write $X(z)$ as the sum of a finite (and small) number n_p of poles:

$$X^{\mathrm{MP}}(z) = \sum_{n}^{n_p} \frac{2\Omega_n R_n}{z^2 - \Omega_n^2}. \tag{11}$$

As for PPA, X^{MP}, R_n, Ω_n also depend on the spatial indexes $\mathbf{qGG}'$. Then, we determine the parameters Ω_n and R_n by interpolating the polarizability $X(z)$ computed numerically on a number of frequencies that is twice the number of poles (in order to match the unknowns). This leads to a nonlinear system of $2n_p$ equations and variables:

$$\sum_{n=1}^{n_p} \frac{2\Omega_n R_n}{z_j^2 - \Omega_n^2} = X(z_j), \quad j = 1, \ldots, 2n_p. \tag{12}$$

The expression in Eq. (11) is at the core of the MPA approach. In fact, once the solution of the system is known, we obtain an analytical representation of $X(z)$ over the whole complex plane, suitable to evaluate Σ^{GW}. Indeed, by exploiting the Lehmann representation of the Green's function, Eq. (7), and making use of Eq. (11) to evaluate W_c, it is possible to compute the correlation part of the *GW* self-energy as

$$\Sigma_c(\omega) = \sum_{m}^{N_B} \sum_{n}^{n_p} P_m v R_n \left[\frac{f_m}{\omega - E_m + \Omega_n - i\eta} + \frac{(1 - f_m)}{\omega - E_m - \Omega_n + i\eta} \right]. \tag{13}$$

This expression generalizes the PPA solution to the case of a multipole expansion for $X(z)$, and bridges to an exact full-frequency approach when the number of poles in X is increased to convergence.

Concerning the solution of the nonlinear system in Eq. (12), several approaches are possible. While the system can be solved analytically for a small number of poles, in general the exact solution can be accessed numerically either by mapping the nonlinear problem into an equivalent system that is linear with respect to the parameters R_n and Ω_n, or through the Padé/Thiele procedure [72–74]. A detailed description of our implementations of these approaches can be found in Appendix A.

For the one pole case, the analytical solution of the interpolation with 2 complex frequencies is easily obtained:

$$\begin{cases} \Omega^2 = \dfrac{X(z_1) z_1^2 - X(z_2) z_2^2}{X(z_1) - X(z_2)} \\ 2\Omega R = -\left(z_1^2 - z_2^2\right) \dfrac{X(z_1) X(z_2)}{X(z_1) - X(z_2)}. \end{cases} \tag{14}$$

We have also derived the analytical solution for the case of 2 and 3 poles, which are significantly more complex and not reported here, but are nevertheless encoded in the YAMBO solver.

III. THEORY: SAMPLING STRATEGIES

An interpolation in the form of Eq. (11) is independent of the chosen sampling frequencies as far as they are all different, and the number of poles in the model, n_p, equals the total number of poles of the target polarizability, N_T. Nevertheless, in the present approach we intent to describe $X(z)$ using a number of poles much smaller than N_T, and therefore the representation is not unique. We then need to understand the possible choices for the points to be used in the interpolation of X. In the following, we discuss how a shift of the frequency sampling from the real axis affects the structure of the polarizability together with alternative sampling strategies. Eventually we show that the sampling plays a fundamental role in achieving a good approximation of $X(z)$ with a reduced number of poles.

A. The polarizability in the complex plane

According to the Lehmann representation, the poles of the time-ordered dressed polarizability X, are distributed above/below the real axis (at an infinitesimal distance), in an energy range determined by the corresponding transitions. X presents a very complex structure along the real axis, while at increasing distance from the real axis the analytic continuation of X becomes smoother. As discussed in Sec. II B, existing approaches typically sample $X(z)$ at frequencies either along the real or the imaginary axis. As an alternative we have studied samplings with components on both axes.

Let's consider at first a sampling of X along a line parallel to the real axis, but at a distance ϖ. From the point of view of the distance from the poles, this sampling effectively balances the contribution of different poles, in particular those located at large (real) frequencies. Moreover, the constant shift from the real axis smooths out the frequency dependence of the polarizability and can be understood as a filter effect resulting from the convolution between the imaginary part of the polarizability computed on the real axis, $-\text{Im}[X(\omega)]\text{sgn}(\omega)$, and the function $1/\pi(\omega + i\varpi)$ with a pole in the complex frequency plane ($z = \omega + i\varpi$), which is a kind of Hilbert transform:

$$X(z) = -\frac{1}{\pi}\int_{-\infty}^{+\infty} \frac{\text{Im}[X(\omega')]\text{sgn}(\omega')}{z-\omega'}d\omega'. \tag{15}$$

The larger the value of the shift, ϖ, the smoother the function in the convolution and the sampled polarizability $X(z)$, and therefore the fewer the poles required to model it, as also depicted in Fig. 1. It is interesting to note that the FF-RA method described in Sec. II B makes typically use of a finite damping to obtain a similar simplification of the structure of X. In this respect, the multipole interpolation method presented here has the advantage that, once the parameters R_n and Ω_n are obtained, it is then possible to perform a sort of deconvolution towards the real-axis, by evaluating there the polarizability when performing the integral of the self-energy. This allows us to get rid of (or at least reduce) the effect of the artificial smoothing of $X(z)$, which is not possible in the FF-RA scheme.

B. Analysis of one-pole solutions

Before presenting our numerical results for different sampling strategies, we discuss some analytical results useful to guide our analysis.

As shown in Appendix B 1, the two most used versions of the PPA can be mapped into a X interpolated on two different frequency samplings. In fact, in the Godby-Needs (GN) scheme, the parameters of the plasmon pole model (PPM) are obtained by computing $X(z)$ at $z_1 = 0$ and $z_2 = i\varpi_p$, being ϖ_p comparable with the experimental plasma frequency of the material, while the conditions imposed by the Hybertsen-Louie (HL) scheme are shown in Appendix B 1 to be equivalent to sampling X at $z_1 = 0$ and $z_2 = \infty$ (meaning that X and X^{HL} have the same leading order coefficient in the $1/z^2$ term for $z \to \infty$). In practice, the two methods give slightly different results: the HL-PPM tends to overestimate the position of the pole with respect to GN-PPM [60,75], and GN-PPM reproduces better the polarizability with respect to full frequency calculations [60]. Mathematically, this can be understood by considering that the interpolation of a function $X(z)$ with a structure is more effective when the sampling is done in a region of meaningful variation of the function, as done in the GN-PPM case. It is therefore reasonable to expect that the choice of the sampled frequency points affects the interpolated X.

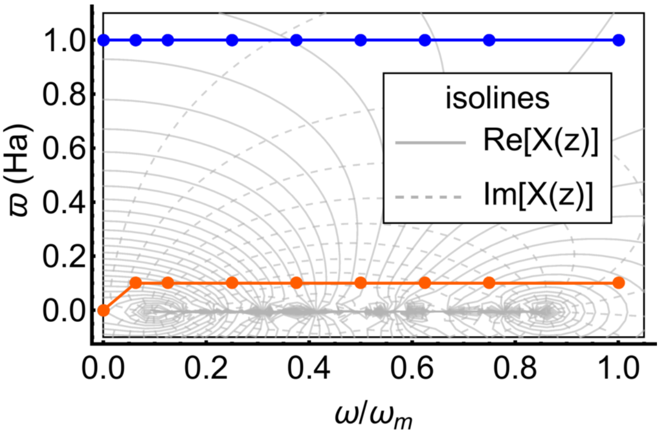

FIG. 1. An illustration of the double parallel sampling with a nine points semihomogeneous grid along the real axis with $\varpi_2 = 1$ Ha, similar to the imaginary frequency used in the GN PPM and $\varpi_1 = 0.1$ Ha, except for the origin of coordinates. The isolines in the background correspond to a toy polarizability function with 200 poles on the real axis.

In Ref. [76], we perform a one-pole fitting, using the solution given by Eq. (14), to a test function (model polarizability) with two poles,

$$X^M(z) = \frac{2\Omega_1 R_1}{z^2 - \Omega_1^2} + \frac{2\Omega_2 R_2}{z^2 - \Omega_2^2}, \tag{16}$$

and compute a series expansions of the fitting parameters, Ω and R, for a perturbation on the reference sampling. This allows us to investigate the dependency of the MPA fit parameters on the sampling. We conclude that it is possible to write equations for Ω and R capturing the behavior of both the GN- and HL-PPM schemes at the same time, and going from one to the other with a continuous function. The same analysis also shows that a sampling close and parallel to the real axis (see Fig. 1, orange line except for the first point) introduces an error in Ω and R that is proportional to the distance from the real axis, when comparing to the solution obtained when performing a sampling on the real axis. This means that, with X sampled parallel and close to the real axis, it is convenient to stay as close to the real axis as possible, as in the case of the FF-RA, where the damping needs to be sufficiently small in order to avoid the introduction of a systematic error. As shown in Sec. III C, this is not the case when using a double parallel sampling.

In Sec. I C of Ref. [76], we define and report the f factors in the expansions of Ω and R, and show that the test function behaves as a one-pole polarizability when $R_2/R_1 \to 0$ (one pole dominates) or $Q_2 \to Q_1$ (the two poles tend to coalesce). In these cases, the solutions do not depend on the sampling, which supports the idea of obtaining a simplified description of the polarizability with a reduced number of poles in cases where some of the poles are close to each other or some of the residues are much larger than others. The sensitivity of the MPA method to the sampling will depend on the ratio of the residues and on the distance between the poles of X. While we have not analytically investigated more complicated test polarizability functions or fitting models (including a larger number of poles), we have performed numerical analyses (e.g., a three pole function fitted on a two pole model) which tend to confirm the findings discussed above.

C. Double parallel sampling

After testing several sampling strategies (samplings parallel to the real axis, tilted with a positive or negative angle with respect to it, etc.), our results led to the choice of a sampling along two lines parallel to the real axis, that we will call double parallel sampling:

$$s^{\mathrm{DP}} = \begin{cases} \mathbf{z}^1\colon z_n^1 = \omega_n + i\varpi_1 \\ \mathbf{z}^2\colon z_n^2 = \omega_n + i\varpi_2, \end{cases} \qquad n = 1, \dots, n_p, \tag{17}$$

where one of the two branches is a line close to the real axis while the other is located further away, e.g., $\varpi_1 < \varpi_2$. The sampling is illustrated in Fig. 1, by the orange and green lines, while in gray we represent the isolines of a toy polarizability function with poles close to the real axis. From the isolines it is possible to see that, at some distance of the real axis, individual poles that are close enough are no longer distinguishable and contribute to a collective excitation. In a simplified view, X sampled along the first line, in orange, preserves some of the structure of X in the region of the poles and X sampled along the second line, in blue, is simple enough to be described with a small number of poles, and accounts for the overall structure of X. The two branches should not be too close in order to avoid numerical instabilities arising from the underdetermination of the resulting system of equations.

This sampling has proved to converge faster with respect to the number of poles and to be less sensitive to the distance of the first line from the real axis (ϖ_1) than the others we tried. This can be understood from the analysis of a small perturbation to $z_1 = 0$ applied to the GN-PPM sampling (at fixed z_2), i.e., to the simplest one-pole double parallel sampling. The linear term in the perturbation of Ω and R (see Eqs. (S5) and (S6) in Ref. [76]) cancels and the first perturbative term is quadratic on ϖ, at variance with perturbations on z_2 where the linear term is present (Eq. (S8) in the Ref. [76]). Moreover, considering different sampling strategies, Ω and R change in the same way, when passing from a real axis sampling to a parallel or tilted sampling ($z_1 = 0$ only in the latter), further stressing that overall behavior is governed by z_2 and that a perturbation to z_1 has negligible impact.

We still have to chose a distribution of the frequencies along the real axis, $\{\omega_n\}$, that again favours the convergence with respect to the number of poles. Differently from the homogeneous grid used in Ref. [64], we propose a partition that simply adds new frequency points when increasing the number of poles, reducing in this way oscillations in the results. Here we write a semi-homogeneous partition in powers of 2:

$$\{\omega_n\} : \begin{cases} (0), n_p = 1 \\ (0, 1) \times \omega_m, n_p = 2 \\ \left(0, \frac{1}{2}, 1\right) \times \omega_m, n_p = 3 \\ \left(0, \frac{1}{4}, \frac{1}{2}, 1\right) \times \omega_m, n_p = 4 \\ \left(0, \frac{1}{8}, \frac{1}{4}, \frac{1}{2}, 1\right) \times \omega_m, n_p = 5 \\ \left(0, \frac{1}{8}, \frac{1}{4}, \frac{1}{2}, \frac{3}{4}, 1\right) \times \omega_m, n_p = 6 \\ \left(0, \frac{1}{8}, \frac{1}{4}, \frac{3}{8}, \frac{1}{2}, \frac{3}{4}, 1\right) \times \omega_m, n_p = 7 \\ \dots \end{cases}, \tag{18}$$

where ω_m is the extreme of the interval. We choose to use a finite value of ω_m since X tends to zero for large enough frequency values, and is enough to describe its tail. Also supporting this option is the fact that the fulfillment of the f-sum rule, the condition used in the HL-PPM that is equivalent to taking $z_2 = \infty$ in the GN-PPM recipe (Appendix B 1), is not critical for obtaining an accurate description of polarizability matrix elements within FF methods [77]. The maximum value of ω_m corresponds to the largest energy transition according to the number of empty states included in the calculation of X. Alternatively, one can simply use a frequency with a sufficiently large real part so that it is located in the tail of the polarizability and use the other sampling points to describe its structure closer to the imaginary axis.

In practice, we use the value ϖ_2 used in the GN approach described in Sec. B, in order to have the same sampling on the imaginary axis when using only one pole and a straightforward extension along the real axis when using more poles. Regarding ϖ_1, in case of one pole we take a null value consistently with PP models, while a (small but) finite value is considered for additional sampling points along the real axis in order to avoid numerical noise. Based on the experience and results obtained using the FF real axis method, and the analytical results discussed above (Eq. (S6) in the Ref. [76]), we increase ϖ_1 up to 0.1 Ha. This is also similar the values proposed for molecules in Ref. [64].

D. Failure condition

Sometimes, when considering only a small number of poles, the interpolation gives rise to poles that are either not physical or not reasonable, posing representability problems. This is usually solved by reassigning the values of the poles. An example is given by the treatment of the so-called "unfulfilled modes" that plays an important role in different PPM schemes [37]. Here we discuss the case of the GN-PPM approach as implemented in YAMBO [34,37,43,62]. The condition used to identify unfulfilled modes in the GN-PPM is the following:

$$\mathrm{Re}\left[\frac{X_{\mathbf{GG}'}(\mathbf{q}, 0)}{X_{\mathbf{GG}'}(\mathbf{q}, i\varpi_p)} - 1\right] < 0 \;\to\; \Omega^{\mathrm{GN}} = 1\ \mathrm{Ha}, \tag{19}$$

where the position of the pole is set to $\Omega^{GN} = 1$ Ha in case of failure. This condition is related to the estimate of Ω^{GN} according to Eq. (B5). For diagonal elements ($\mathbf{G} = \mathbf{G}'$), the polarizability evaluated on the imaginary axis is real, making the term in the square-root of Eq. (B5) also real. Unfulfilled modes are then those for which the radicand is negative and the resulting pole imaginary. The same condition is also used for off-diagonal matrix elements in order to ensure that the pole Ω^{GN}, which is anyway taken real, mainly derives from the real part of the radicand in Eq. (B5).

Setting the pole for unfulfilled modes at $\Omega^{\mathrm{GN}} = 1$ Ha usually works well for semiconductors [37], even if it may have a (usually small) impact on the quasiparticle corrections. However, in more complex systems the reliability of the PPA may be compromised either by the large number of matrix elements for which the pole is corrected or simply by the inadequacy of such a simple model correction.

In the case of MPA, we propose a slightly different strategy. The condition in Eq. (19), used in the PP approach, applies to a sampling on the imaginary axis but can be generalized as:

$$\Omega_n = \begin{cases} \sqrt{\Omega_n^2}, & \mathrm{Re}\big[\Omega_n^2\big] \geqslant 0 \\ \sqrt{-\big(\Omega_n^2\big)^*}, & \mathrm{Re}\big[\Omega_n^2\big] < 0 \end{cases} \tag{20}$$

avoiding in this way, in case of failure, the use of a replacement constant value. The second line in Eq. (20), when applied, is equivalent to exchange the real and imaginary parts of Ω_n. In addition, since we consider complex poles, if needed we also impose time ordering, i.e., while $\mathrm{Re}[\Omega_n] \geqslant 0$ because of Eq. (20), we may force $\mathrm{Im}[\Omega_n] < 0$. Note this procedure is applied to all n_p poles in MPA.

We now analyze the evaluation of the residues when at least one of the poles of the multipole interpolation is modified by the failure condition above. We start by considering a model with a single pole, for which the residue R can be calculated using the information of either the sampling point z_1, first equation in Eq. (B5) within the GN model, or z_2 as

$$R = \frac{X_2\big(z_2^2 - \Omega^2\big)}{2\Omega}. \tag{21}$$

When the pole is not corrected, the computed residue is independent of the choice between z_1 and z_2. However that is not the case if the failure condition is used. In order to improve the representation with respect to considering only one of the given solutions depending on z_1 or z_2, we propose to use Eq. (A23) to fit R. When using more than one pole, in addition to Eq. (20) we have added an extra condition: in case a pole is close to another or its position is out of the sampling range, its residue is replaced by zero and the fit of Eq. (A23) is applied only to the remaining residues.

E. Representability measures

In order to quantify the representability error of the model with respect to the sampled points when correcting the position of the poles with Eqs. (19) and (20), we compute the mean number of corrected matrix elements, $\langle N_F\rangle$, and an average relative standard deviation, $\langle RSD\rangle$. The analysis presented in the following can be done for each $\mathbf{q}$-point, if translational symmetry is present. For one pole, the average number of failures is simply

$$\langle N_F\rangle_{n_p=1} = \frac{1}{N_g}\sum_{g=\mathbf{GG}'}^{N_g} \Theta\big(\Omega^{\mathrm{MP}}_{n=1,g}\big), \tag{22}$$

where Θ is a Heaviside-like step function that verify the condition:

$$\Theta(\Omega) = \begin{cases} 0, & \mathrm{Re}[\Omega^2] \geqslant 0 \\ 1, & \mathrm{Re}[\Omega^2] < 0. \end{cases} \tag{23}$$

Regarding the error measurement, we use a modified version of the relative standard deviation, also known as coefficient of variation, that is then averaged over all the matrix elements. Since we model all the matrix elements with the same number of poles, the average deviation gathers, in a single estimate, the representability error. The estimator was modified by replacing in the normalization factor the mean value of the sampled values of X by their maximum value. Namely, for each matrix element $g = \mathbf{GG}'$ (within a given $\mathbf{q}$ block, not labeled explicitly here), we define

$$M_g = \max_j |X_{\mathbf{GG}'}(z_j)|. \tag{24}$$

This is justified by the fact that X is close to zero for a large region of frequencies, together with its average when it is computed with several points, which may results in an inadequate use of the coefficient of variation. The error estimators then read

$$\langle RSD\rangle_{n_p=1} = \frac{1}{N_g}\sum_{g=\mathbf{GG}'}^{N_g} \frac{1}{M_g}\sqrt{\sum_{j=1}^{2}\big|X^{\mathrm{MP}}_{jg} - X_{jg}\big|^2}, \tag{25}$$

$$\langle RSD\rangle_{\mathrm{PPA}} = \frac{1}{N_g}\sum_{g=\mathbf{GG}'}^{N_g} \frac{\Theta\big(\Omega^{\mathrm{PP}}_{ng}\big)}{M_g}\sqrt{\sum_{j=1}^{2}\big|X^{\mathrm{PP}}_{jg} - X_{jg}\big|^2}. \tag{26}$$

In case of the PPA, we compute the error just for the matrix elements that fail the condition in order to favour the comparison with MPA, since there may be a deviation already due to the fact of discarding the imaginary part of the poles in the PPA (MPA is based on an interpolation, while PPA is not).

In the general multipole case, we define

$$\langle N_F\rangle = \frac{1}{N_g}\sum_{g=\mathbf{GG}'}^{N_g} \frac{\sum_n^{n_p}\Theta\big(\Omega^{\mathrm{MP}}_{ng}\big)\big|R^{\mathrm{MP}}_{ng}\big|}{\sum_n^{n_p}\big|R^{\mathrm{MP}}_{ng}\big|}, \tag{27}$$

$$\langle RSD\rangle = \frac{1}{N_g}\sum_{g=\mathbf{GG}'}^{N_g} \frac{1}{M_g}\sqrt{\frac{1}{2n_p - 1}\sum_{j=1}^{2n_p}\big|X^{\mathrm{MP}}_{jg} - X_{jg}\big|^2}, \tag{28}$$

where we have introduced a normalization by the residues of each pole in the counter of the failure condition $\langle N_F\rangle$, in order to differentiate the contribution of each pole.

IV. RESULTS: MPA PERFORMANCE

We have validated the MPA method in three different bulk materials: Si, a prototype semiconductor, hBN with AA and AA′ staking, and rutile TiO_2, a mid-band-gap semiconductor oxide. We compare the MPA approach described above with PPA and FF calculations and with the existing literature. In

TABLE I. Quasiparticle (QP) transitions computed with the linearized QP Eq. (5) on top of PP, MPA and FF. In case of hBN, FF calculations are performed using a 10 Ry cut-off for the X matrix (results in square brackets) and then extrapolated to 25 Ry, using the MPA results as reference. All other calculations are directly performed with a 25 Ry cutoff.

System	QP(eV)	PPA	MPA	FF
Si	$\Gamma_c \rightarrow \Gamma_v$	3.28	3.30	3.30
	$K_c \rightarrow \Gamma_v$	1.26	1.30	1.30
hBN$_{AA}$	$M_c \rightarrow K_v$	7.35	7.47	7.46 [7.25]
	$K_c \rightarrow K_v$	7.02	7.16	7.16 [6.91]
	$H_c \rightarrow K_v$	5.33	5.50	5.50 [5.23]
	$L_c \rightarrow K_v$	5.26	5.42	5.42 [5.17]
hBN$_{AA'}$	$L_c \rightarrow K_v$	6.21	6.24	6.24 [6.20]
	$K_c \rightarrow K_v$	6.17	6.20	6.20 [6.17]
	$H_c \rightarrow K_v$	6.02	6.05	6.05 [6.01]
	$M_c \rightarrow K_v$	5.93	5.98	5.98 [5.92]
TiO$_2$	$\Gamma_c \rightarrow \Gamma_v$	3.20	3.27	3.26

particular, we compare our results for Si with Refs. [37,78], hBN with Refs. [79,80], and TiO$_2$ with Ref. [37].

DFT calculations were performed using the QUANTUM ESPRESSO package [81,82]. We employed the LDA exchange-correlation functional for Si and hBN, while GGA-PBE for TiO$_2$, with norm-conserving pseudopotentials in all cases. For Si, we use a grid of 12 × 12 × 12 **k**-points, a kinetic energy cutoff of 20 Ry and 300 KS states to perform sums-over-states. In case of hBN, we used **k**-point meshes of 18 × 18 × 9 and 18 × 18 × 6, corresponding to AA and AA$'$ stacking respectively, with an energy cutoff of 60 Ry and 400 KS states. For rutile TiO$_2$, we use a shifted **k**-grid of 4 × 4 × 6 **k** points, a kinetic energy cutoff of 70 Ry for the wave functions, and 600 KS states.

GW calculations were performed with the YAMBO code [34,56]. We use a standard Monte Carlo stochastic scheme called random integration method (RIM) [34,83] to treat integrals over the Brillouin zone with Coulomb divergence. The RIM technique is used in order to accelerate convergences with respect to the **k**-point mesh in case of hBN and TiO$_2$, but not for Si simply to illustrate that the MPA works well independently of this choice. The size of the polarizability matrix is set to 25, 10, and 15 Ry for Si, hBN and TiO$_2$, respectively. In the case of hBN, the value of 10 Ry is not sufficient to converge quasiparticle corrections, and a more suitable value is 25 Ry. Due to the high computational cost of FF real-axis calculations, we decided to perform the comparison of PPA, MPA, and FF methods for hBN with a X matrix cutoff of 10 Ry, while the results obtained with 25 Ry (quasiparticle energies in the case of PPA and MPA) are given in Table I. Regarding the self-energy evaluation, in the bare Green function we use a damping parameter $\eta = 0.1$ eV for all calculations.

A. The polarizability matrix

In Figs. 2, 3, and 4, we plot a set of diagonal and off-diagonal matrix elements of the polarizability for three different bulk materials: Si, hBN, and TiO$_2$ rutile, respectively. Each plot shows the real and imaginary parts of the polarizability computed within MPA using a different number of poles, compared with the corresponding FF real-axis results. The same number of poles is used for all the matrix elements. In fact, on the one hand the multiple peak structures

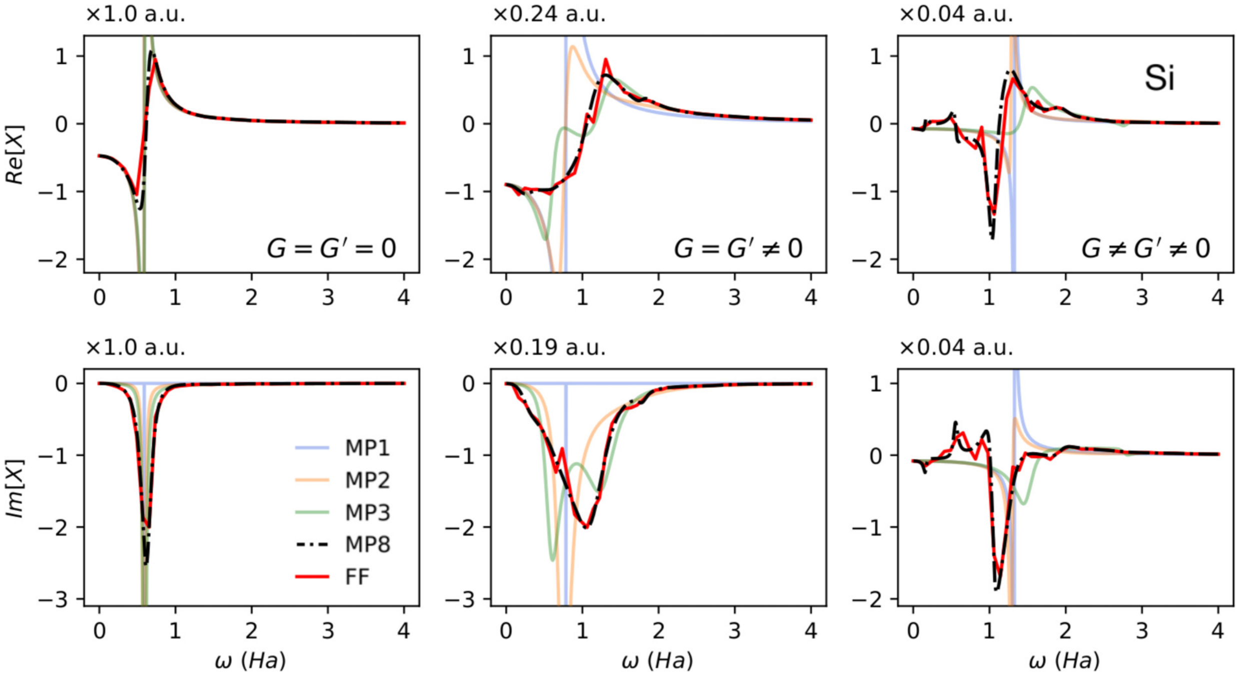

FIG. 2. Selected Si X matrix elements computed within MPA with 1, 2, 3, and 8 poles and compared with the corresponding FF real-axis results. Although the real and imaginary parts of the function are plotted using different arbitrary units, the different matrix elements can be compared since their scale is consistent and indicated in each plot.

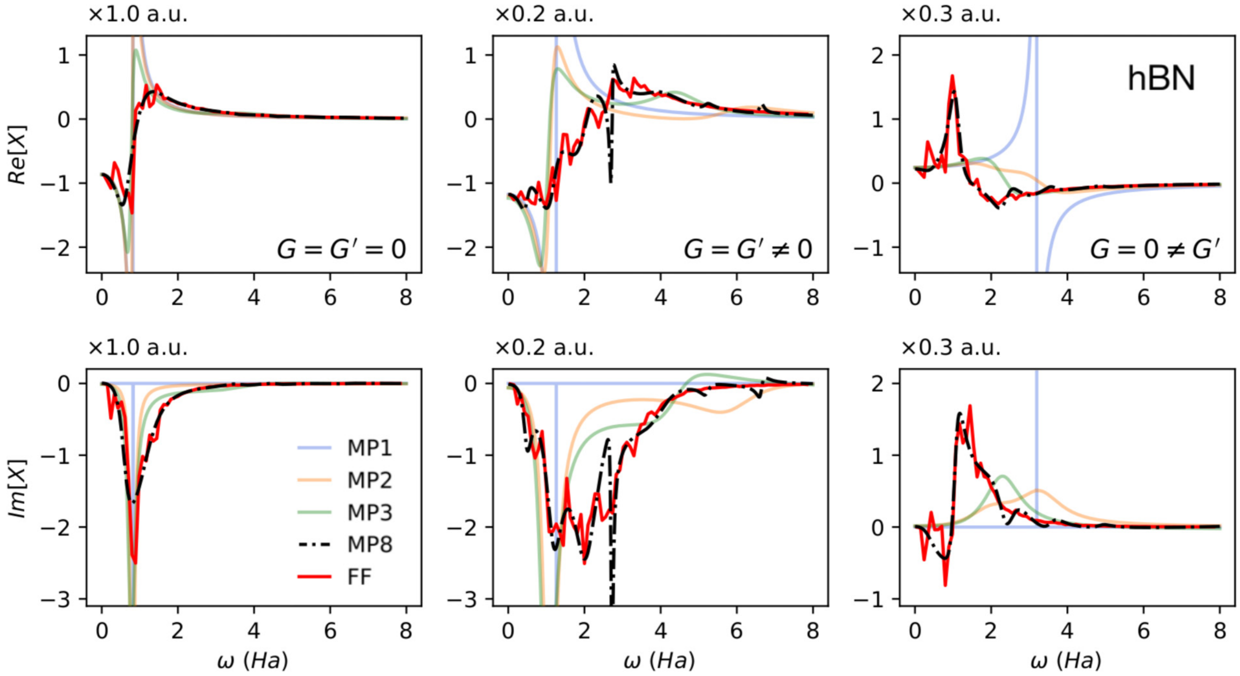

FIG. 3. Selected hBN X matrix elements computed within MPA with 1, 2, 3, and 8 poles and compared with the corresponding FF real-axis results. The same scheme from Fig. 2 is used for the units.

of X is more complex for large **G**-vectors, while on the other hand their maximum amplitude, and therefore their weight in the integration of the self-energy, decreases with **G**. This means that a more simplistic description of the structure of these elements will not affect much the computed Σ. For reasons of computational convenience, besides the number of poles, the array of sampled frequencies is also the same for all the matrix elements. Of course, the complexity of X depends on the material under study. In silicon, for instance, the most important matrix elements have an almost single-peak structure that favours the use of a single pole, while for TiO_2, the first element, $\mathbf{G} = \mathbf{G}' = 0$, already shows several peaks and a slower decay of the maximum amplitude with respect to **G**.

The imaginary part of diagonal elements of X describes the spectral properties of the polarizability, and therefore is always negative with peaks around the real part of the poles

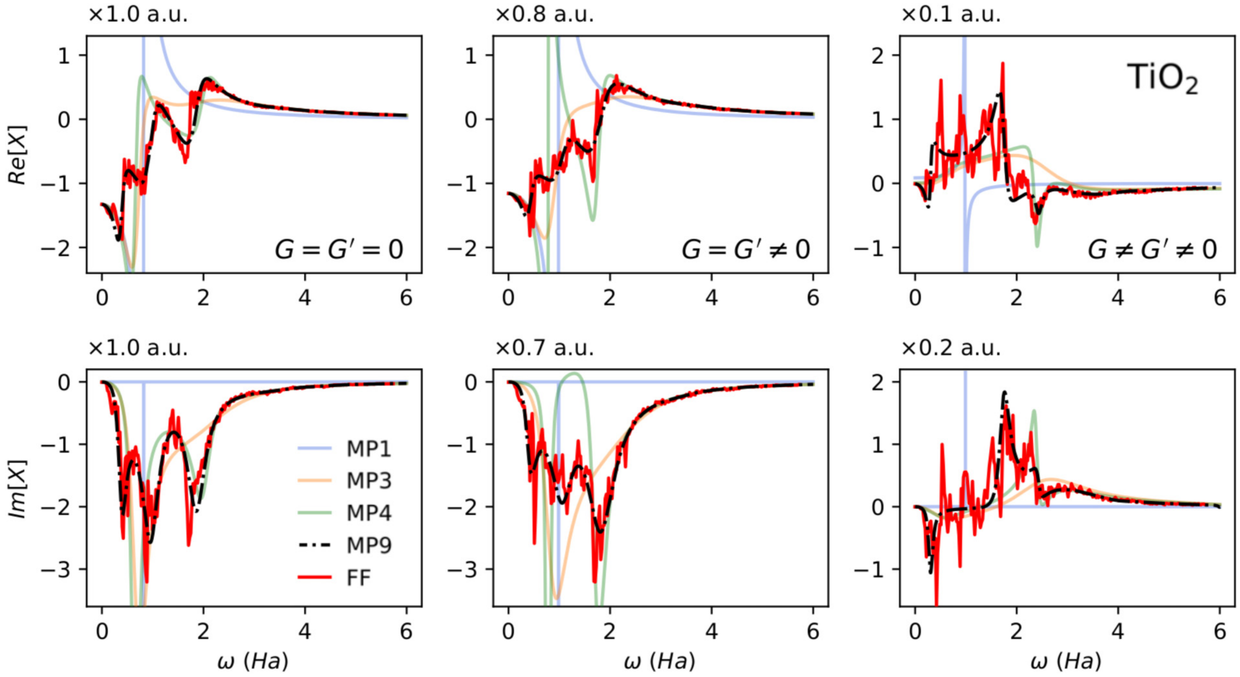

FIG. 4. Selected TiO_2 X matrix elements computed within MPA with 1, 3, 4, and 9 poles and compared with the corresponding FF real-axis results. The same scheme from Fig. 2 is used for the units.

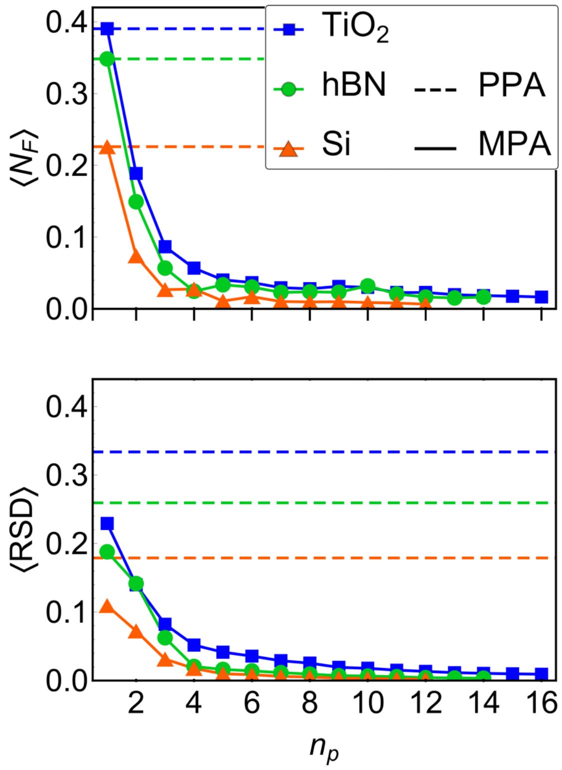

FIG. 5. (Top) $\langle N_F \rangle$, mean number of matrix elements for which the position of the poles was corrected according to Eq. (20) for MPA and Eq. (19) for PPA, and (bottom) $\langle RSD \rangle$, average deviation as defined in Eq. (28), as a function of the number of poles used in the MPA approach. Due to the high computational cost of the FF calculations, in case of hBN the comparison is made with a non fully converged dimension of the polarizability matrix, of 10 Ry. The plots correspond to the AA stacking, but similar values are seen also for the AAAA′ stacking with 10 Ry of X matrix.

and widths given by their imaginary part. A model with a single pole describes approximately the envelop of the real part of diagonal elements, but is unable to describe the width of the main peak, since the small value of the imaginary part of the pole obtained from the interpolation is translated into a delta-like peak. The use of a complex pole is not that different from a real one obtained by neglecting its imaginary part, as in the PPA case. The inclusion of a second pole however, may improve the description of the imaginary part of the diagonal elements of X even if there are no significant improvements in the real part. On the other hand, the off-diagonal matrix elements of X show a mixture of their real and imaginary parts, since the residues of the poles in Eq. (8) have an imaginary part depending on their $\mathbf{G}$ and $\mathbf{G}'$ components. Off-diagonal matrix elements are more likely to fail the PP condition of Eq. (19) and even a single but complex pole and the generalized failure condition of Eq. (20) may lead to considerable improvements on the description of X, as shown in the right panels of Fig. 2.

In general the description of the polarizability improves quickly as the number of poles increases, as demonstrated by the representability measurements $\langle N_F \rangle$ and $\langle RSD \rangle$ plotted in Fig. 5. Already with one pole, the error of the generalized condition is lower than the one obtained with the PPM and then both $\langle N_F \rangle$ and $\langle RSD \rangle$ rapidly decrease with increasing number of poles.

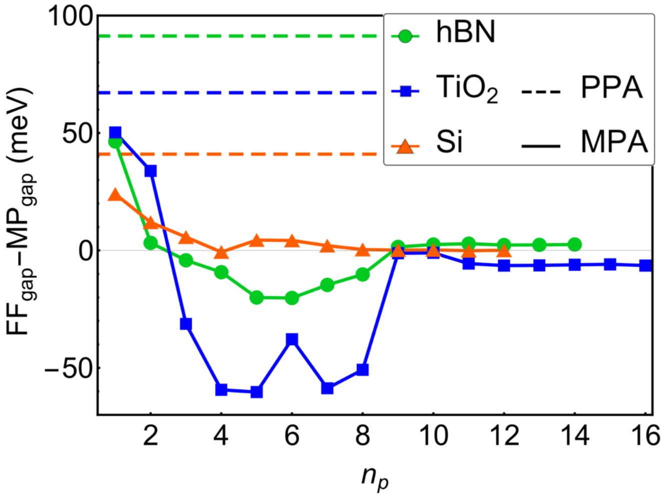

FIG. 6. Deviations of the fundamental gap calculated via the MPA with respect to FF results as a function of number of poles for Si, hBN and TiO$_2$. As in Fig. 5, in case of hBN we use 10 Ry of X matrix and plot only the results of the AA stacking.

B. The *GW* quasiparticle correction

In Fig. 6, we report the convergence of the *GW* correction to the band gap with respect to the number of poles used in the MPA for the three systems under study. The same frequency sampling was used in the three cases, namely a double parallel sampling, Eq. (17) with the grid given by Eq. (18) along the real axis and shifts $\varpi_1 = 0.1$ Ha and $\varpi_2 = 1$ Ha. For TiO$_2$, which has a more structured polarizability, the quasiparticle corrections are more sensitive to the sampling. With a single pole model using different values of ϖ_2 the results can differ by as much as ∼100 meV. In the multipole case the difference decreases to 6 meV when comparing results obtained with $\varpi_2 = 0.5$ and 1.0 Ha. Even if we expect the highest value to lead to a slightly simpler X, the convergence is reached with the same number of poles in both cases.

Interestingly, the same convergence behavior is found for the three systems: between 8 and 11 poles the quasiparticle corrections differ by less than 1 meV from the FF results. The number of poles needed to obtain convergence is much more homogeneous than the number of frequencies in FF real axis calculations (300 for Si, 400 for hBN, and 1500 for TiO2), since the shifts ϖ in the double parallel sampling determine the structure of the polarizability and therefore the number of poles required to model it.

We report our final QP results in Table I. In the case of hBN, the difference between the PPA and FF-RA values changes with respect to the size of the polarizability matrix. At 10 Ry we found similar differences for stacking AA and AA′ with a maximum value of 0.10 eV. At 25 Ry the difference increases up to a maximum value of 0.17 eV for the stacking AA and decreases up to a maximum value of 0.05 eV for the stacking AA′, the plasmon-pole approximation being more accurate in the AA′ configuration.

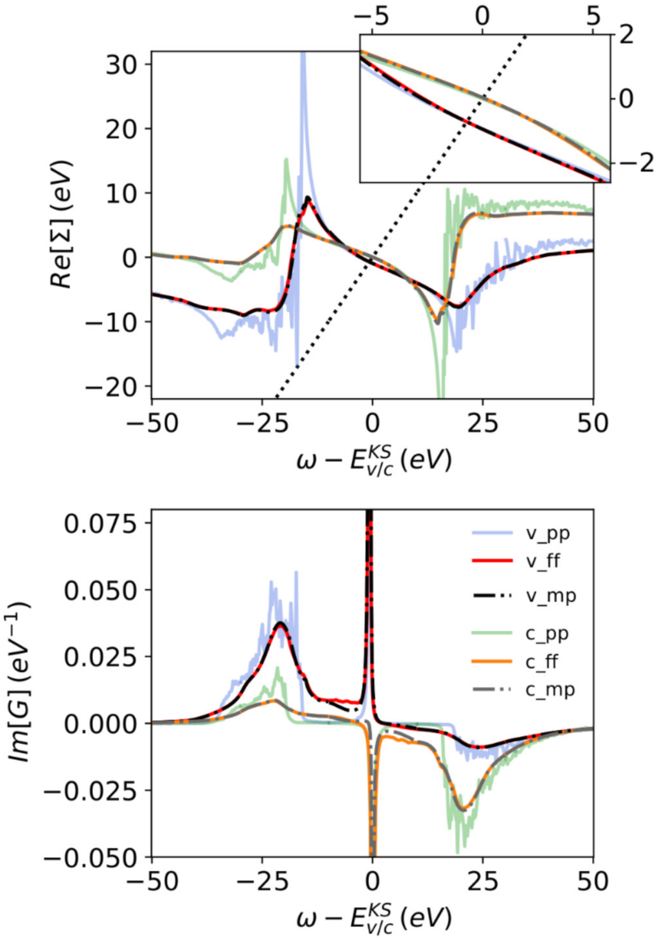

FIG. 7. Frequency dependence of the Si valence (v) and conduction (c) real part of the self-energy (top) and spectral function (bottom) of the quasiparticles involved in the fundamental gap computed with PPA, MPA, and FF.

C. Self-energy and spectral function

The present MPA method targets the dynamical dependence of the dressed polarizability, in turn directly related to W, in order to perform the frequency integral in the self-energy and finally to compute the quasiparticle corrections to the independent particle states. For this purpose, we need a good description of $\Sigma(\omega)$ in a frequency region around the solution of the quasiparticle equation, Eq. (4). However, the description of the self-energy in a larger range of frequencies is interesting by itself, since $\Sigma(\omega)$ contains, besides the quasiparticle energies, information about many-body features like satellites and quasiparticle lifetimes. These properties are computed by solving the corresponding Dyson equation for the Green function, $G = G_0 + G_0\Sigma G$. Through Eq. (13), the MPA method provides a description for the frequency dependence of the self-energy, that we assess in this section.

In Fig. 7, we compare the Si self-energy (top) and spectral function (bottom), obtained as the imaginary part of the dressed Green's function, Im[G], computed within PPA, MPA, and FF-RA. The self-energy presents a typical two-pole structure [52,53] corresponding to the contributions of the empty and occupied states. The picture can be better understood taking Eq. (13) into account: occupied states contribute to the self-energy at energies around the value $-\Omega$ plus their own KS energies (negative), different from the empty states that contribute at $+\Omega$ plus a positive term from the KS energies further separating the two contributions of the main plasmon at $\pm\Omega$.

The PPA gives a good description of the tail of the main peaks, especially including the region around the solution of the quasiparticle equation, and the overall behavior of Σ. However, intrinsic representability problems appear due to the inability of PPA in describing the imaginary part of W. The result is a very noisy Σ, particularly around its peaks, giving rise to noisy satellite peaks in the spectral function. In contrast, the MPA self-energy (computed with eight poles, i.e., the number required to obtained converged quasiparticle energies) reproduces quite well the FF-RA results in the whole energy range. In fact, there is a reversal on the level of complexity of the polarizability with respect to the self-energy: X is smooth when computed within PPA, and very structured in FF-RA and MPA, whereas Σ is very spiky within PPA and smooth for FF-RA and MPA.

This result can be understood by analyzing the effect of the Dyson equation for W, Eq. (3), on the polarizability matrix elements $X_{\mathbf{GG}'}(\mathbf{q},\omega)$. At the independent particle level, X_0 presents a large number of peaks described by Eq. (8). When applying the Dyson equation, the poles from different matrix elements of X_0 are combined, resulting in a dressed polarizability X with broader peaks corresponding to plasmonic excitations, as shown in Figs. 2–4. Thanks to this feature, it is possible to use few (complex) poles in the MPA modeling (then approximated with 1 real pole in PPA) of each matrix element $X_{\mathbf{GG}'}(\mathbf{q},\omega)$. However, there is a further pole superposition of the matrix elements in the integral of the self-energy [Eq. (13)], whose accurate description in a full frequency range needs a proper modeling of the imaginary part of X. This superposition in PPA is partially remedied by the finite η damping of the Green function, while the presence of finite imaginary parts in the MPA poles naturally improves the PPA description. In silicon, the proximity of the several electronic states and the number of additional low-intensity plasmon-excitation result in a noisy behavior of the PPA self-energy around the main peaks. In contrast, the FF and MPA methods properly describe the superposition of all the excitations, and the resulting $\Sigma(\omega)$ function is smooth.

This picture may be different for less screened systems like, e.g., molecules [40,84], where the energy levels are scattered, the plasmonic excitations are far apart, and the plasmon-pole model may lead to a self-energy that presents a simpler structure than a FF treatment. On the other hand, the nonexistence of a gap in metallic systems may lead to a self-energy with a single main peak [85] also noisy within PPA. However, the special cases of metals with small plasmon energies or strongly correlated materials are particularly challenging for simple models like the PPA, since the quasiparticle solutions lie in a zone of multiple plasmonic excitations, as shown in Ref. [86] for SrVO$_3$. The applicability of the PPA on such systems has been discussed in the literature [5,47] and the advantages in using the MPA method for a metallic case are the subjects of a future work.

V. CONCLUSIONS

In this paper, we have introduced and developed a multipole approximation (MPA) to represent the reducible polarizability and to evaluate the correlation self-energy in the *GW* method. The MPA method can be seen as a generalization of the commonly used plasmon-pole approximation (PPA), while increasing the number of poles in the description of X it tends to the exact, full frequency solution. Therefore MPA naturally bridges from PPA to FF *GW*, with controllable accuracy and computational cost. We have provided numerical methods to compute the MPA parameters and investigated in detail the effect of different frequency samplings on the procedure. In doing so, we have also discussed two common formulations of the PPA (Godby-Needs and Hybertsen-Louie PPM's) showing how they can be seen in a unified frame. Eventually, the MPA method has been validated and benchmarked on selected bulk semiconductors (Si, hBN, rutile TiO_2), showing systematic improvement over the PPA, and numerical agreement with FF *GW* already with about 10 poles.

The present MPA approach, in the few poles regime, considerably improves the quasiparticle energies with respect to PPA without a significant increase in the computational cost. When considering more poles, around 10 for the systems studied here, its computational cost is comparable to AC approaches. In this regime, we have shown that MPA reaches an accuracy comparable with standard FF contour deformation methods [7,40], significantly more demanding. Moreover, we believe MPA presents several advantages with respect to this method. In the contour deformation approach, the number of frequencies used in the evaluation of W increases with the distance of the state from the Fermi level due to the increasing number of poles of G entering in the contour [64], whereas within MPA all the quasiparticles have the same computational cost. Another advantage of MPA relies on its analytic form, which allows one to solve analytically the frequency integral of the self-energy that has also a multipole form. Moreover, the frequency structure of the polarizability is meaningful and permits the analysis of the plasmonic interactions. The MPA technique applies irrespectively of the basis set, and can also be straightforwardly extended beyond G_0W_0, e.g., to quasiparticle self-consistent *GW* approaches [8,9].

Overall, our findings show that the multipole approach can be used to obtain a simple and effective representation of response functions. We illustrated how to analyze simple types of sampling in order to understand and design good recipes. We show that the MPA with optimal sampling strategies in the complex plane can lead to a level of accuracy comparable with full-frequency methods at much lower costs, not only for the quasiparticle energies, but also for the whole energy range relevant for the self-energy.

ACKNOWLEDGMENTS

We acknowledge stimulating discussions with Nicola Marzari, Pino D'Amico, Alberto Guandalini, Miki Bonacci, Simone Vacondio and Matteo Zanfrognini. This work was partially supported by the MaX – MAterials design at the eXascale–European Centre of Excellence, funded by the European Union program H2020-INFRAEDI-2018-1 (Grant No. 824143). We also thank SUPER (Supercomputing Unified Platform – Emilia-Romagna) from Emilia-Romagna POR-FESR 2014-2020 regional funds. T.C. also acknowledges support by the Swiss National Science Foundation (Grant No. 200021-179138). Computational time on the Marconi100 machine at CINECA was provided by the Italian ISCRA program.

APPENDIX A: MPA INTERPOLATION

1. Linear solver

The nonlinearity of the system of equations in Eq. (12) depends only on inverse factors involving the variables Ω_n, since the system is otherwise linear in R_n. It is possible to separate these two behaviours by following the procedure described below. We start by splitting the sampled points $\{z_j, X(z_j)\}$ in two sets, for example,

$$\begin{aligned} s_1&: \ j = 1, \dots, n_p, \\ s_2&: \ j = n_p + 1, \dots, 2n_p. \end{aligned} \tag{A1}$$

The first set defines a matrix $\mathbf{A_1}$ and vector $\mathbf{x_1}$ as follows:

$$\begin{aligned} \mathbf{A_1}_{mn} &= \frac{2\Omega_n}{z_m^2 - \Omega_n^2}, \\ \mathbf{x_1}_m &= X(z_m), \quad n, m = 1, \dots, n_p \end{aligned} \tag{A2}$$

such that we can write a linear system for the vector $\mathbf{r} = (R_1, R_2, \dots, R_{n_p})$:

$$\mathbf{A_1}\mathbf{r} = \mathbf{x_1}. \tag{A3}$$

We can do the same with the other half of the data, by defining the matrix $\mathbf{A_2}$ and the vector $\mathbf{x_2}$ as

$$\begin{aligned} \mathbf{A_2}_{mn} &= \frac{2\Omega_n}{z_{n_p+m}^2 - \Omega_n^2}, \\ \mathbf{x_2}_m &= X(z_{n_p+m}), \quad n, m = 1, \dots, n_p \end{aligned} \tag{A4}$$

leading to

$$\mathbf{A_2}\mathbf{r} = \mathbf{x_2}. \tag{A5}$$

Either Eq. (A3) or (A5) can be used to compute the residues if the positions of the poles are known. Furthermore, from these two equations it is possible to obtain a complete set of n_p equations for Ω_n:

$$\mathbf{r} = (\mathbf{A_1})^{-1}\mathbf{x_1} = (\mathbf{A_2})^{-1}\mathbf{x_2}. \tag{A6}$$

Here we explore in depth this idea using a different formulation that maps the problem into an equivalent linear system that can be easily solved with standard linear algebra tools.

Within the multipole model, $X(z)$ can be written in the form of a particular Padé approximant, i.e., as a fraction of two polynomials $N(z^2)$ and $D(z^2)$ of degree $n_p - 1$ and n_p, respectively:

$$\begin{aligned} X(z) &= \frac{N_{n_p-1}(z^2)}{D_{n_p}(z^2)} \\ &= \frac{a_1 + a_2 z^2 + \cdots + a_{n_p} z^{2(n_p-1)}}{b_1 + b_2 z^2 + \cdots + b_{n_p} z^{2(n_p-1)} + z^{2n_p}}, \end{aligned} \tag{A7}$$

where the factorization of $D_{np}(z^2)$ gives the position of all the poles:

$$D_{n_p}(z^2) = \prod_{n=1}^{n_p} \left(z^2 - \Omega_n^2\right). \tag{A8}$$

On the other hand, the coefficients a_n in the numerator involve combinations of poles and residues. From the point of view of the system of equations, we are changing the unknown variables $\{R_n, \Omega_n\}$ into $\{a_n, b_n\}$. If we consider a vector constructed from the progression of powers of z: $\mathbf{Z}(z) = (1, z^2, \dots, z^{2(n_p-1)})$, and vectors $\mathbf{a}$ and $\mathbf{b}$ constructed from the coefficients of $N(z^2)$ and $D(z^2)$: $\mathbf{a} = (a_1, a_2, \dots, a_{n_p})$ and $\mathbf{b} = (b_1, b_2, \dots, b_{n_p})$, we can write Eq. (A7) in a more compact way and then make it linear with respect to the new variables:

$$X(z) = \frac{\mathbf{Z}(z) \cdot \mathbf{a}}{\mathbf{Z}(z) \cdot \mathbf{b} + z^{2n_p}}. \tag{A9}$$

$$X(z) z^{2n_p} + X(z)\,\mathbf{Z}(z) \cdot \mathbf{b} = \mathbf{Z}(z) \cdot \mathbf{a}. \tag{A10}$$

By using the first set of points of Eq. (A1), we can define the following vector and matrices:

$$\mathbf{v_1} = \begin{bmatrix} X(z_1) z_1^{2n_p} \\ X(z_2) z_2^{2n_p} \\ \vdots \\ X(z_{n_p}) z_{n_p}{}^{2n_p} \end{bmatrix}, \tag{A11}$$

$$\mathbf{Z_1} = \begin{bmatrix} 1 & z_1^2 & \dots & z_1^{2(n_p-1)} \\ 1 & z_2^2 & \dots & z_2^{2(n_p-1)} \\ \vdots & \vdots & & \vdots \\ 1 & z_{n_p}^2 & \dots & z_{n_p}^{2(n_p-1)} \end{bmatrix}, \tag{A12}$$

$$\mathbf{M_1} = \begin{bmatrix} X(z_1) & X(z_1) z_1^2 & \dots & X(z_1) z_1^{2(n_p-1)} \\ X(z_2) & X(z_2) z_2^2 & \dots & X(z_2) z_2^{2(n_p-1)} \\ \vdots & \vdots & & \vdots \\ X(z_{n_p}) & X(z_{n_p}) z_{n_p}^2 & \dots & X(z_{n_p}) z_{n_p}^{2(n_p-1)} \end{bmatrix}. \tag{A13}$$

$\mathbf{Z_1}$ is known as a square Vandermonde matrix [87] and is always invertible as far as all the sampling points are different [88]. Then we can write Eq. (A10) in matrix form:

$$\mathbf{v_1} + \mathbf{M_1 b} = \mathbf{Z_1 a}, \tag{A14}$$

while an analog equation is obtained with the second set of points:

$$\mathbf{v_2} + \mathbf{M_2 b} = \mathbf{Z_2 a}. \tag{A15}$$

By combining Eqs. (A14) and (A15) to remove vector $\mathbf{a}$ we obtain a linear system for $\mathbf{b}$:

$$\mathbf{Mb} = \mathbf{v}, \tag{A16}$$

$$\begin{aligned} \mathbf{M} &= \mathbf{Z_1}^{-1}\mathbf{M_1} - \mathbf{Z_2}^{-1}\mathbf{M_2}, \\ \mathbf{v} &= -\mathbf{Z_1}^{-1}\mathbf{v_1} + \mathbf{Z_2}^{-1}\mathbf{v_2}. \end{aligned} \tag{A17}$$

In terms of the number of matrix inversions to be performed, Eqs. (A16) and (A17) can be recast into the following more practical form:

$$\left[\mathbf{Z_2}\mathbf{Z_1}^{-1}\mathbf{M_1} - \mathbf{M_2}\right]\mathbf{b} = -\mathbf{Z_2}\mathbf{Z_1}^{-1}\mathbf{v_1} + \mathbf{v_2}. \tag{A18}$$

Before we proceed, in order to the reduce numerical instabilities of the algorithm, it is convenient to carry out a normalization

$$\begin{aligned} z_j &= y_j z_{\max}, \\ z_{\max} &= \max(|z_n|), \quad n = 1, \dots, n_p, \end{aligned} \tag{A19}$$

where, i.e., $z_{\max}$ is the largest frequency modulus in the sampling set involved with the matrix we need to invert, $\mathbf{Z_1}$.

The proposed normalization balances the large differences among the matrix elements that emerge when increasing the number of poles, due to the range of the sampling and the increasing powers. Rescaled unknowns can then be defined as

$$\begin{aligned} a_n' &= a_n (z_{\max})^{n-1} \\ b_n' &= b_n (z_{\max})^{n-1} \end{aligned} \;. \tag{A20}$$

Likewise, we also define the $\mathbf{Y_{1,2}}$ and $\mathbf{M}'_{\mathbf{1,2}}$ matrices similarly to $\mathbf{Z_{1,2}}$ and $\mathbf{M_{1,2}}$, Eqs. (A12) and (A13) respectively, by using y_n instead of z_n. Eventually, Eqs. (A16)-(A17) can be rewritten as a linear system for $\mathbf{b}'$:

$$[\mathbf{Y_2}\mathbf{Y_1}^{-1}\mathbf{M}'_\mathbf{1} - \mathbf{M}'_\mathbf{2}]\mathbf{b}' = -\mathbf{Y_2}\mathbf{Y_1}^{-1}\mathbf{v_1} + \mathbf{v_2}. \tag{A21}$$

Once we have computed $\mathbf{b}'$, and in turn $\mathbf{b}$ via Eq. (A20), we need to obtain the poles Ω_n, which are the variables with physical meaning and those required in the evaluation of the self-energy integral. As mentioned above, this is equivalent to find the zeros of the polynomial $D_{n_p}(z^2)$ in Eq. (A8), and a powerful method to perform this task is the diagonalization of the corresponding companion matrix:

$$\mathbf{C} = \begin{bmatrix} 0 & 0 & \dots & 0 & -b_1 \\ 1 & 0 & \dots & 0 & -b_2 \\ 0 & 1 & \dots & 0 & -b_3 \\ \vdots & \vdots & \ddots & \vdots & \vdots \\ 0 & 0 & \dots & 1 & -b_{n_p} \end{bmatrix}. \tag{A22}$$

The eigenvalues of $\mathbf{C}$ correspond to the squares of the position of the poles, Ω_n^2.

As mentioned before, in case all the poles are different, the residues may be computed with either Eq. (A3) or (A5). Alternatively we can use all the $2n_p$ points to fit R_n with a linear least squares method:

$$\min_{\mathbf{r}} ||\mathbf{Ar} - \mathbf{x}||, \tag{A23}$$

where, for each $n = 1, \dots, n_p$ and $j = 1, \dots, 2n_p$, one has

$$\mathbf{A}_{jn} = \frac{2\Omega_n}{z_j^2 - \Omega_n^2}, \quad \mathbf{x}_j = X(z_j). \tag{A24}$$

A similar least-square approach was also recently adopted in the definition of the sum-over-poles approach [68], and applied to the case of the homogeneous electron gas.

2. Padé/Thiele solver

An alternative way to the method described above consists in solving at the same time both polynomials N and D in the

Padé interpolant in Eq. (A7) by means of the Thiele's interpolation formula, witch expresses the interpolant as a continued fraction of the reciprocal differences [72]. The number of required steps corresponds to the number of points to be interpolated, that is $2n_p$ in our case:

$$\frac{N(z^2)}{D(z^2)} = \frac{c_1}{1+}\,\frac{c_2\big(z^2-z_1^2\big)}{1+}\cdots\frac{c_{2n_p}\big(z^2-z^2_{2n_p-1}\big)}{1+\big(z^2-z^2_{2n_p-1}\big)g_{2n_p}(z)}, \tag{A25}$$

where the coefficients c_s and functions $g_s(z)$ are given by the following recursion relations:

$$c_s = g_s(z_s), \tag{A26}$$

$$g_s(z) = \begin{cases} X(z_s), & s=1 \\ \dfrac{g_{s-1}(z_{s-1})-g_{s-1}(z)}{(z-z_{s-1})g_{s-1}(z)}, & s \geqslant 2 \end{cases}, \tag{A27}$$

where index $s = 1, \dots, 2n_p$ represents both the iteration step and the index of the corresponding point in the given set. The polynomials $N(z^2)$ and $D(z^2)$ and their coefficients can then be computed recursively. Notice that in Thiele's relation the definition of each polynomial differs from the one in Eq. (A7) by a multiplicative constant that, however, does not affect the zeros of the polynomials, and moreover cancels out in the fraction.

As in the case of the linear solver, with Thiele's procedure we are interested in computing only the monomial coefficients of the denominator, since we can always obtain the residues by means of Eqs. (A3) or (A23). The recipe [72] for the polynomial in the denominator is:

$$D_s(z) = \begin{cases} 1, & s=0,1 \\ D_{s-1}(z) - c_s(z-z_{s-1})D_{s-2}(z), & s \geqslant 2 \end{cases}. \tag{A28}$$

The desired polynomial of degree n_p is obtained in the last step, $s = 2n_p$. Notice that in this notation the index s does not reflect anymore the degree of the polynomial. In each iteration the degree of the polynomial $D_s(z)$ is $(s-1)/2$ for odd integers and $s/2$ for even numbers. We can write a vector of the coefficients of the final polynomial, $\mathbf{d} = (d_1, \dots, d_{n_p}, d_{n_p+1})$. It has an extra dimension comparing to vector $\mathbf{b}$ in Eq. (A10) due to the multiplicative constant mentioned before that goes to the higher order monomial of D in Eq. (A7). The recursion of the polynomial in Eq. (A28) can be easily translated into a recursion of the vector $\mathbf{d}$:

$$\mathbf{d}^s = \begin{cases} (1, 0, \dots, 0), & s=0,1 \\ d_i^s = d_i^{s-1} + c_s z_s d_{i+1}^{s-2} - c_s z_{s-1} d_i^{s-2}, & s \geqslant 2, \end{cases} \tag{A29}$$

where the second term of the sum in the rhs of Eq. (A29) is computed just for $i = 1, \dots, n_p$, while the other two include also the last dimension, $i = n_p + 1$.

The recursion of the c_s coefficients can also be recast in vectorial form, by considering in each iteration, s, a $2n_p$ dimensional vector, $\mathbf{c}$:

$$\mathbf{c}^s : \begin{cases} (X(z_1), \dots, X(z_{2n_p})), & s=1 \\ c_j^s = \dfrac{c_{j-1}^{s-1} - c_j^{s-1}}{(z_j - z_{j-1})c_j^{s-1}}, & s \geqslant 2 \end{cases}, \tag{A30}$$

where now the iterations are represented by index s in the upper position, and the vector coordinates and point identifiers are represented by index j in the lower position. Notice however that only one particular component of vector $\mathbf{c}^s$ enters in Eq. (A29) at each iteration, i.e., $c_s \equiv c_s^s$, other components are worth only to update the vector. Once computed $\mathbf{d}$, the relation with the coefficient of vector $\mathbf{b}$ is as simple as $b_n = d_n/d_{n+1}$, that recovers the unitary coefficient accompanying the higher order monomial of the polynomial. The position of the poles can then be computed with the companion matrix, Eq. (A22), likewise in the case of the linear solver.

APPENDIX B: PLASMON POLE MODELS

As stated in Sec. II B, there are several flavours of the plasmon-pole model (PPM), that are compared for instance in Refs. [60,89], but two of them are more commonly used, one due to Hybertsen and Louie [41] (HL), and the other due to Godby and Needs [50] (GN). In the Hybertsen and Louie (HL) approach, two physical constraints are imposed: (1) compliance with the Kramers-Kronig relations in the limit of small frequencies, and (2) compliance with the f-sum rule. The Kramers-Kronig relations for X^{HL} provide

$$\begin{aligned} X^{\mathrm{HL}}(0) &= \frac{2}{\pi}\mathcal{P}\int_0^\infty d\omega\,\omega^{-1}\mathrm{Im}[X^{\mathrm{HL}}(\omega)] \\ &= \frac{2}{\pi}\mathcal{P}\int_0^\infty d\omega\,\omega^{-1}\mathrm{Im}[X(\omega)] = X(0), \end{aligned} \tag{B1}$$

whereas the f-sum rule is enforced by the condition:

$$\frac{2}{\pi}\int_0^\infty d\omega\,\omega\,\mathrm{Im}[X^{\mathrm{HL}}(\omega)] = \frac{2}{\pi}\int_0^\infty d\omega\,\omega\,\mathrm{Im}[X(\omega)] = S, \tag{B2}$$

where X is the computed dressed polarizability. In the above equation, the result of the integral (S) can be expressed in terms of some of the components of the electronic density and Coulomb interaction. On a plane-wave basis, it reads

$$\begin{aligned} S_{\mathbf{G}\mathbf{G}'}(\mathbf{q}) &= -\frac{\omega_p^2}{v(\mathbf{q}+\mathbf{G})}\,\frac{\rho(\mathbf{G}-\mathbf{G}')}{\rho(0)}\,\frac{(\mathbf{q}+\mathbf{G})\cdot(\mathbf{q}+\mathbf{G}')}{|\mathbf{q}+\mathbf{G}|^2} \\ &= \rho(\mathbf{G}-\mathbf{G}')\,[(\mathbf{q}+\mathbf{G})\cdot(\mathbf{q}+\mathbf{G}')], \end{aligned} \tag{B3}$$

where ρ is the electronic density and the plasma frequency, ω_p, is computed as $\omega_p = \sqrt{4\pi\rho(0)}$.

In the Godby and Needs (GN) approach, the polarizability is evaluated at two different frequencies located along the imaginary axis of the frequency plane: $z = 0$ and $z = i\varpi_p$, being ϖ_p comparable with the plasma frequency of the material.

$$(R^{\mathrm{GN}}, \Omega^{\mathrm{GN}}) : \begin{cases} X^{\mathrm{GN}}(0) = X(0) \\ X^{\mathrm{GN}}(i\varpi_p) = X(i\varpi_p) \end{cases}. \tag{B4}$$

Other versions of the PPA are based on the above recipes aiming at improving the description of the off-diagonal matrix elements of the polarizability [44,45,90]. We will now take a closer look at the GN and HL approaches, from the point of view of the multipole approximation.

1. Connecting the GN- and HL-PPM schemes

The idea of interpolating the two parameters (R^{PP}, Ω^{PP}) of the plasmon-pole model starting from X evaluated at two different frequencies, used by the GN-PPM, is very flexible, and multiple sampling options can be adopted. Nevertheless, using different pairs of sampling frequencies typically leads to different parametrization of the resulting PPM. With this in mind, we search for the pair of frequency points to be used in Eq. (14) that would correspond to the conditions imposed by the HL scheme. The equations for the GN-PPM are

$$X(0) = -\frac{2R^{\mathrm{GN}}}{\Omega^{\mathrm{GN}}},$$
$$\Omega^{\mathrm{GN}} = \varpi_p \,\mathrm{Re}\left[\frac{X(i\varpi_p)}{X(0) - X(i\varpi_p)}\right]^{\frac{1}{2}}, \tag{B5}$$

while those for the HL-PPM are

$$X(0) = -\frac{2R^{\mathrm{HL}}}{\Omega^{\mathrm{HL}}}, \quad 2\Omega^{\mathrm{HL}}R^{\mathrm{HL}} = S. \tag{B6}$$

We note that Eq. (B1) in the HL formulation, connected to the Kramers-Kronig relation, implies the first condition (equality of X and X^{HL} at $\omega = 0$) imposed in the GN recipe, Eq. (B4), as also evident in comparing Eqs. (B6) and (B5).

If we consider the exact polarizability X, written in the Lehmann representation similar to the multipole model given in Eq. (11), but with all the N_T addends and with $\mathrm{Im}[\Omega_n] \to 0^-$, and solve the integral in the f-sum rule, we get

$$\frac{2}{\pi}\int_0^\infty d\omega\, \omega\, \mathrm{Im}[X(\omega)] = 2\sum_n \Omega_n R_n. \tag{B7}$$

Then, the condition imposed by HL in the plasmon-pole model is

$$2\Omega^{\mathrm{HL}}R^{\mathrm{HL}} = 2\sum_n \Omega_n R_n. \tag{B8}$$

This relation imposes the equality of the $1/z^2$ coefficient (leading order) of the asymptotic behavior of the polarizabilities, making explicit the known fact that sum rules describe properties at infinity [91]:

$$\lim_{\omega\to\infty} X^{\mathrm{HL}}(\omega)/X(\omega) = 1. \tag{B9}$$

This means that in the long frequency range, $\omega \gg \max_n |\Omega_n|$, X behaves as a one-pole function with the exact same asymptotic decay of X^{HL}. Thus we can think of the HL representation as a limiting case of GN-PPM recipe when the second frequency goes to infinity:

$$(R^{\mathrm{HL}}, \Omega^{\mathrm{HL}}) : \begin{cases} X^{\mathrm{HL}}(0) = X(0) \\ X^{\mathrm{HL}}(\infty) = X(\infty) \end{cases}, \tag{B10}$$

where the evaluation of the infinite frequency in the second equation is taken as the limit of the X^{HL}/X ratio, according to Eq. (B9).

[1] G. Onida, L. Reining, and A. Rubio, Rev. Mod. Phys. **74**, 601 (2002).

[2] R. M. Martin, L. Reining, and D. M. Ceperley, *Interacting Electrons* (Cambridge University Press, Cambridge, 2016).

[3] N. Marzari, A. Ferretti, and C. Wolverton, Nat. Mater. **20**, 736 (2021).

[4] L. Hedin, Phys. Rev. **139**, A796 (1965).

[5] F. Aryasetiawan and O. Gunnarsson, Rep. Prog. Phys. **61**, 237 (1998).

[6] L. Reining, WIREs Comput. Molecular Sci. **8**, e1344 (2018).

[7] D. Golze, M. Dvorak, and P. Rinke, Front. Chem. **7**, 377 (2019).

[8] M. van Schilfgaarde, T. Kotani, and S. Faleev, Phys. Rev. Lett. **96**, 226402 (2006).

[9] T. Kotani, M. van Schilfgaarde, and S. V. Faleev, Phys. Rev. B **76**, 165106 (2007).

[10] M. Shishkin, M. Marsman, and G. Kresse, Phys. Rev. Lett. **99**, 246403 (2007).

[11] A. Kutepov, K. Haule, S. Y. Savrasov, and G. Kotliar, Phys. Rev. B **85**, 155129 (2012).

[12] A. Kutepov, V. Oudovenko, and G. Kotliar, Comput. Phys. Commun. **219**, 407 (2017).

[13] M. Grumet, P. Liu, M. Kaltak, J. c. v. Klimeš, and G. Kresse, Phys. Rev. B **98**, 155143 (2018).

[14] W. Chen and A. Pasquarello, Phys. Rev. B **92**, 041115(R) (2015).

[15] X. Ren, N. Marom, F. Caruso, M. Scheffler, and P. Rinke, Phys. Rev. B **92**, 081104(R) (2015).

[16] E. Maggio and G. Kresse, J. Chem. Theory Comput. **13**, 4765 (2017).

[17] M. Guzzo, G. Lani, F. Sottile, P. Romaniello, M. Gatti, J. J. Kas, J. J. Rehr, M. G. Silly, F. Sirotti, and L. Reining, Phys. Rev. Lett. **107**, 166401 (2011).

[18] A. Damascelli, Z. Hussain, and Z.-X. Shen, Rev. Mod. Phys. **75**, 473 (2003).

[19] L. Hedin, J. Michiels, and J. Inglesfield, Phys. Rev. B **58**, 15565 (1998).

[20] Q. Yan, P. Rinke, M. Winkelnkemper, A. Qteish, D. Bimberg, M. Scheffler, and C. G. V. de Walle, Semicond. Sci. Technol. **26**, 014037 (2010).

[21] M. Dauth, M. Wiessner, V. Feyer, A. Schöll, P. Puschnig, F. Reinert, and S. Kümmel, New J. Phys. **16**, 103005 (2014).

[22] J. S. Zhou, L. Reining, A. Nicolaou, A. Bendounan, K. Ruotsalainen, M. Vanzini, J. J. Kas, J. J. Rehr, M. Muntwiler, V. N. Strocov, F. Sirotti, and M. Gatti, Proc. Nat. Ac. Sci. **117**, 28596 (2020).

[23] F. Bechstedt, M. Fiedler, C. Kress, and R. Del Sole, Phys. Rev. B **49**, 7357 (1994).

[24] U. von Barth and B. Holm, Phys. Rev. B **54**, 8411 (1996).

[25] F. Caruso, C. Verdi, S. Poncé, and F. Giustino, Phys. Rev. B **97**, 165113 (2018).

[26] A. Marini, R. Del Sole, A. Rubio, and G. Onida, Phys. Rev. B **66**, 161104(R) (2002).

[27] M. Palummo, M. Bernardi, and J. C. Grossman, Nano Lett. **15**, 2794 (2015).

[28] S. Albrecht, L. Reining, R. Del Sole, and G. Onida, Phys. Rev. Lett. **80**, 4510 (1998).

[29] A comprehensive list of common electronic structure codes can be found, e.g., in L. M. Ghiringhelli, C. Carbogno, S. Levchenko, F. Mohamed, G. Huhs, M. Lüders, M. Oliveira, and M. Scheffler, NPJ Comput. Materials **3**, 46 (2017); or in L. Talirz, L. Ghiringhelli, and B. Smit, arXiv:2108.12350v1.

[30] X. Blase, C. Attaccalite, and V. Olevano, Phys. Rev. B **83**, 115103 (2011).

[31] F. Bruneval, T. Rangel, S. M. Hamed, M. Shao, C. Yang, and J. B. Neaton, Comput. Phys. Commun. **208**, 149 (2016).

[32] J. Wilhelm, D. Golze, L. Talirz, J. Hutter, and C. A. Pignedoli, J. Phys. Chem. Lett. **9**, 306 (2018).

[33] M. Shishkin and G. Kresse, Phys. Rev. B **74**, 035101 (2006).

[34] A. Marini, C. Hogan, M. Grüning, and D. Varsano, Comput. Phys. Commun. **180**, 1392 (2009).

[35] X. Gonze, B. Amadon, P.-M. Anglade, J.-M. Beuken, F. Bottin, P. Boulanger, F. Bruneval, D. Caliste, R. Caracas, M. Côté, T. Deutsch, L. Genovese, P. Ghosez, M. Giantomassi, S. Goedecker, D. Hamann, P. Hermet, F. Jollet, G. Jomard, S. Leroux *et al.*, Comput. Phys. Commun. **180**, 2582 (2009).

[36] J. Deslippe, G. Samsonidze, D. A. Strubbe, M. Jain, M. L. Cohen, and S. G. Louie, Comput. Phys. Commun. **183**, 1269 (2012).

[37] T. Rangel, M. Del Ben, D. Varsano, G. Antonius, F. Bruneval, F. H. da Jornada, M. J. van Setten, O. K. Orhan, D. D. O'Regan, A. Canning, A. Ferretti, A. Marini, G.-M. Rignanese, J. Deslippe, S. G. Louie, and J. B. Neaton, Comput. Phys. Commun. **255**, 107242 (2020).

[38] C. Friedrich, S. Blügel, and A. Schindlmayr, Phys. Rev. B **81**, 125102 (2010).

[39] H. Jiang and P. Blaha, Phys. Rev. B **93**, 115203 (2016).

[40] M. J. van Setten, F. Caruso, S. Sharifzadeh, X. Ren, M. Scheffler, F. Liu, J. Lischner, L. Lin, J. R. Deslippe, S. G. L. C. Yang, F. Weigend, J. B. Neaton, F. Evers, and P. Rinke, J. Chem. Theory Comput. **11**, 5665 (2015).

[41] M. S. Hybertsen and S. G. Louie, Phys. Rev. B **34**, 5390 (1986).

[42] S. B. Zhang, D. Tománek, M. L. Cohen, S. G. Louie, and M. S. Hybertsen, Phys. Rev. B **40**, 3162 (1989).

[43] R. W. Godby and R. J. Needs, Phys. Rev. Lett. **62**, 1169 (1989).

[44] W. von der Linden and P. Horsch, Phys. Rev. B **37**, 8351 (1988).

[45] G. E. Engel and B. Farid, Phys. Rev. B **47**, 15931 (1993).

[46] K.-H. Lee and K. J. Chang, Phys. Rev. B **49**, 2362 (1994).

[47] A. Marini, G. Onida, and R. D. Sole, Phys. Rev. Lett. **88**, 016403 (2001).

[48] F. Liu, L. Lin, D. Vigil-Fowler, J. Lischner, A. F. Kemper, S. Sharifzadeh, F. H. da Jornada, J. Deslippe, C. Yang, J. B. Neaton, and S. G. Louie, J. Comput. Phys. **286**, 1 (2015).

[49] T. Miyake and F. Aryasetiawan, Phys. Rev. B **61**, 7172 (2000).

[50] R. W. Godby, M. Schlüter, and L. J. Sham, Phys. Rev. B **37**, 10159 (1988).

[51] F. Aryasetiawan in, *Strong Coulomb Correlations in Electronic Structure Calculations*, 1st ed. (CRC Press, London, 2000), p. 96.

[52] H. N. Rojas, R. W. Godby, and R. J. Needs, Phys. Rev. Lett. **74**, 1827 (1995).

[53] M. M. Riegera, L. Steinbeck, I. D. White, H. N. Rojas, and R. W. Godby, Comput. Phys. Commun. **117**, 211 (1999).

[54] J. A. Soininen, J. J. Rehr, and E. L. Shirley, J. Phys.: Condens. Matter **15**, 2573 (2003).

[55] P. Liu, M. Kaltak, J. Klineš, and G. Kresse, Phys. Rev. B **94**, 165109 (2016).

[56] D. Sangalli, A. Ferretti, H. Miranda, C. Attaccalite, I. Marri, E. Cannuccia, P. Melo, M. Marsili, F. Paleari, A. Marrazzo, G. Prandini, P. Bonfà, M. O. Atambo, F. Affinito, M. Palummo, A. Molina-Sánchez, C. Hogan, M. Grüning, D. Varsano, and A. Marini, J. Phys.: Condens. Matter **31**, 325902 (2019).

[57] P. Umari, G. Stenuit, and S. Baroni, Phys. Rev. B **81**, 115104 (2010).

[58] F. Giustino, M. L. Cohen, and S. G. Louie, Phys. Rev. B **81**, 115105 (2010).

[59] M. Govoni and G. Galli, J. Chem. Theory Comput. **11**, 2680 (2015).

[60] P. Larson, M. Dvorak, and Z. Wu, Phys. Rev. B **88**, 125205 (2013).

[61] G. Lehmann and M. Taut, Phys. Status Solidi (b) **54**, 469 (1972).

[62] A. Oschlies, R. W. Godby, and R. J. Needs, Phys. Rev. B **51**, 1527 (1995).

[63] C. Friedrich, Phys. Rev. B **100**, 075142 (2019).

[64] I. Duchemin and X. Blase, J. Chem. Theory Comput. **16**, 1742 (2020).

[65] J. J. Kas, A. P. Sorini, M. P. Prange, L. W. Cambell, J. A. Soininen, and J. J. Rehr, Phys. Rev. B **76**, 195116 (2007).

[66] J. J. Kas, J. Vinson, N. Trcera, D. Cabaret, E. L. Shirley, and J. J. Rehr, J. Phys.: Conf. Ser. **190**, 012009 (2009).

[67] S. J. Bintrim and T. C. Berkelbach, J. Chem. Phys. **154**, 041101 (2021).

[68] T. Chiarotti, N. Marzari, and A. Ferretti, arXiv:2109.07972.

[69] A. L. Fetter and J. D. Walecka, *Quantum Theory of Many-Particle Systems* (McGraw-Hill, New York, 1971).

[70] J. A. Soininen, J. J. Rehr, and E. L. Shirley, Phys. Scr. **2005**, 243 (2005).

[71] S. Ismail-Beigi, Phys. Rev. B **81**, 195126 (2010).

[72] H. J. Vidberg and J. W. Serene, J. Low Temp. Phys. **29**, 179 (1977).

[73] K.-H. Lee and K. J. Chang, Phys. Rev. B **54**, R8285 (1996).

[74] Y.-G. Jin and K. J. Chang, Phys. Rev. B **59**, 14841 (1999).

[75] M. Stankovski, G. Antonius, D. Waroquiers, A. Miglio, H. Dixit, K. Sankaran, M. Giantomassi, X. Gonze, M. Côté, and G.-M. Rignanese, Phys. Rev. B **84**, 241201(R) (2011).

[76] See Supplemental Material http://link.aps.org/supplemental/10.1103/PhysRevB.104.115157 for a detailed description of one and two pole models.

[77] A. Miglio, D. Waroquiers, G. Antonius, M. Giantomassi, M. Stankovski, M. Côté, X. Gonze, and G.-M. Rignanesee, Eur. Phys. J. B **85**, 322 (2012).

[78] A. Kutepov, S. Y. Savrasov, and G. Kotliar, Phys. Rev. B **80**, 041103(R) (2009).

[79] D. Wickramaratne, L. Weston, and C. G. Van de Walle, J. Phys. Chem. C **122**, 25524 (2018).

[80] K. A. Mengle and E. Kioupakisa, APL Mater. **7**, 021106 (2019).

[81] P. Giannozzi, S. Baroni, N. Bonini, M. Calandra, R. Car, C. Cavazzoni, D. Ceresoli, G. L. Chiarotti, M. Cococcioni, I. Dabo, A. D. Corso, S. de Gironcoli, S. Fabris, G. Fratesi, R. Gebauer, U. Gerstmann, C. Gougoussis, A. Kokalj, M. Lazzeri, L. Martin-Samos *et al.*, J. Phys.: Condens. Matter **21**, 395502 (2009).

[82] P. Giannozzi, O. Andreussi, T. Brumme, O. Bunau, M. B. Nardelli, M. Calandra, R. Car, C. Cavazzoni, D. Ceresoli, M. Cococcioni, N. Colonna, I. Carnimeo, A. D. Corso, S. de Gironcoli, P. Delugas, R. A. DiStasio, A. Ferretti, A. Floris, G. Fratesi, G. Fugallo *et al.*, J. Phys.: Condens. Matter **29**, 465901 (2017).

[83] C. A. Rozzi, D. Varsano, A. Marini, E. K. U. Gross, and A. Rubio, Phys. Rev. B **73**, 205119 (2006).

[84] J. Lischner, S. Sharifzadeh, J. Deslippe, J. B. Neaton, and S. G. Louie, Phys. Rev. B **90**, 115130 (2014).

[85] M. Cazzaniga, Phys. Rev. B **86**, 035120 (2012).

[86] T. Miyake, C. Martins, R. Sakuma, and F. Aryasetiawan, Phys. Rev. B **87**, 115110 (2013).

[87] B. Ycart, arXiv:1204.4716.

[88] N. Macon and A. Spitzbart., Amer. Math. Monthly **65**, 95 (1958).

[89] R. Shaltaf, G.-M. Rignanese, X. Gonze, F. Giustino, and A. Pasquarello, Phys. Rev. Lett. **100**, 186401 (2008).

[90] M. Giantomassi, M. Stankovski, R. Shaltaf, M. Grüning, F. Bruneval, P. Rinke, and G. Rignanese, Phys. Status Solidi (b) **248**, 275 (2011).

[91] B. B. Crowley, arXiv:1508.05606.

Frequency dependence in GW made simple using a multipole approximation: Supplemental Material

Dario A. Leon[1,2], Claudia Cardoso[2], Tommaso Chiarotti[3], Daniele Varsano[2], Elisa Molinari[1,2], and Andrea Ferretti[2]
[1] *FIM Department, University of Modena & Reggio Emilia, Via Campi 213/a, Modena (Italy)*
[2] *S3 Centre, Istituto Nanoscienze, CNR, Via Campi 213/a, Modena (Italy) and*
[3] *Theory and Simulation of Materials (THEOS), Ecole Polytechnique*
Fédérale de Lausanne (EPFL), CH-1015 Lausanne (Switzerland)

I. ANALYSIS OF DIFFERENT SAMPLINGS

In the following, we consider the following test function (modelling a polarizability with two pairs of poles)

$$X^M(z) = x_1(z) + x_2(z) \equiv \frac{2\Omega_1 R_1}{z^2 - \Omega_1^2} + \frac{2\Omega_2 R_2}{z^2 - \Omega_2^2}, \tag{S1}$$

and study how different sampling options affect the solution of the fitting procedure when using one pole.

A. Perturbing the GN-PPM sampling

Let us define the reference GN sampling with an imaginary frequency of modulus ϖ_0:

$$s^{GN} : \begin{cases} z_1 = 0 \\ z_2 = i\varpi_0, \end{cases} \tag{S2}$$

and those we want to compare with, starting with a perturbation on z_1:

$$s^0 : \begin{cases} z_1 = \omega \\ z_2 = i\varpi_0, \end{cases} \tag{S3}$$

$$s^{i0} : \begin{cases} z_1 = i\varpi \\ z_2 = i\varpi_0, \end{cases} \tag{S4}$$

where $\varpi < \varpi_0$. When ω and ϖ are small, we have a similar behaviour with the same parameters:

$$\begin{cases} \Omega^0 = \Omega^{GN}\left(1 - \frac{f_1^0}{\varpi_0^2}\omega^2 + O[\omega^3]\right) \\ R^0 = R^{GN}\left(1 - \frac{c_1^0 f_1^0}{\varpi_0^2}\omega^2 + O[\omega^3]\right), \end{cases} \tag{S5}$$

$$\begin{cases} \Omega^{i0} = \Omega^{GN}\left(1 + \frac{f_1^0}{\varpi_0^2}\varpi^2 + O[\varpi^3]\right) \\ R^{i0} = R^{GN}\left(1 + \frac{c_1^0 f_1^0}{\varpi_0^2}\varpi^2 + O[\varpi^3]\right). \end{cases} \tag{S6}$$

We also consider a perturbation on z_2 as:

$$s^{\varpi_0} : \begin{cases} z_1 = 0 \\ z_2 = i(\varpi_0 + \varpi). \end{cases} \tag{S7}$$

When ϖ is small in this case, we have:

$$\begin{cases} \Omega^{\varpi_0} = \Omega^{GN}\left(1 + \frac{f_0^{\varpi_0}}{\varpi_0}\varpi + O[\varpi^2]\right) \\ R^{\varpi_0} = R^{GN}\left(1 + \frac{f_0^{\varpi_0}}{\varpi_0}\varpi + O[\varpi^2]\right). \end{cases} \tag{S8}$$

When $\varpi \gg \varpi_0$ in Eq. (S7), we have:

$$\begin{cases} \Omega^{\varpi_0} = \Omega^{GN} L_{\varpi_0}\left(1 - \frac{f_\infty^{\varpi_0}\varpi_0^2}{\varpi^2} + O[\varpi^{-3}]\right) \\ R^{\varpi_0} = R^{GN} L_{\varpi_0}\left(1 - \frac{f_\infty^{\varpi_0}\varpi_0^2}{\varpi^2} + O[\varpi^{-3}]\right). \end{cases} \tag{S9}$$

The HL approach can be included in this regime and from this equation we can understand why the HL solution overestimates Ω and R with respect to GN, since it is given by the asymptotes:

$$\begin{cases} \Omega^{HL} = \Omega^{GN} L_{\varpi_0} \\ R^{HL} = R^{GN} L_{\varpi_0}. \end{cases} \tag{S10}$$

Moreover, it is possible to merge both behaviours of Eq. (S8) and (S9) into a single a function that goes continuously from one solution to the other:

$$\begin{cases} \Omega^{\varpi_0}(\varpi) = \frac{\Omega^{GN}\varpi_0^2 + \Omega^{HL}\varpi^2}{\varpi_0^2 + \varpi^2} - \frac{\varpi\varpi_0^2}{\frac{\varpi^3}{\Omega^{HL} f_\infty^{\varpi_0}} - \frac{\varpi_0^3}{\Omega^{GN} f_0^{\varpi_0}}} \\ R^{\varpi_0}(\varpi) = \frac{R^{GN}\varpi_0^2 + R^{HL}\varpi^2}{\varpi_0^2 + \varpi^2} - \frac{\varpi\varpi_0^2}{\frac{\varpi^3}{R^{HL} f_\infty^{\varpi_0}} - \frac{\varpi_0^3}{R^{GN} f_0^{\varpi_0}}}. \end{cases} \tag{S11}$$

B. Samplings along the real axis

Lets start by defining samplings, for now still with two frequencies, but that represent samplings along a line either parallel P or tilted, with a positive A^+ or negative A^- angle, with respect to the real axis (RA).

$$s^{RA} : \begin{cases} z_1 = 0 \\ z_2 = \omega_0, \end{cases} \tag{S12}$$

$$s^{P} : \begin{cases} z_1 = i\varpi \\ z_2 = \omega_0 + i\varpi, \end{cases} \tag{S13}$$

$$s^{A+}:\begin{cases} z_1 = 0 \\ z_2 = \omega_0 + i\varpi, \end{cases} \tag{S14}$$

$$s^{A-}:\begin{cases} z_1 = i\varpi \\ z_2 = \omega_0. \end{cases} \tag{S15}$$

When ϖ is small, we have:

$$\begin{cases} \Omega^P = \Omega^{A+} = \Omega^{RA}\left(1 - i\dfrac{f_0^{\omega_0}}{\omega_0}\varpi + O[\varpi^2]\right) \\ R^P = R^{A+} = R^{RA}\left(1 - i\dfrac{f_0^{\omega_0}}{\omega_0}\varpi + O[\varpi^2]\right), \end{cases} \tag{S16}$$

which shows that a parallel sampling close to the real axis affects the parameters by a quantity that is proportional to the shift ϖ.

When ϖ is large, we have:

$$\begin{cases} \Omega^{A+} = \Omega^{HL}\left(1 - \dfrac{f_\infty^{\omega_0}\omega_0^2}{\varpi^2} + O[\varpi^{-3}]\right) \\ R^{A+} = R^{HL}\left(1 - \dfrac{f_\infty^{\omega_0}\omega_0^2}{\varpi^2} + O[\varpi^{-3}]\right). \end{cases} \tag{S17}$$

C. Form of the f-factors

In order to get a general picture from the coefficients of the series expansions presented in the previous sections, we write them in a compact way by defining simply recognizable averaged quantities that may be weighted by particular elements. We use a notation, $\overline{\Omega^e}_w$, in which Ω represent the average quantity, the position of a pole in this case, while e is an exponent and w the weighting function:

$$f_\infty^{\omega_0} = \frac{1}{2\omega_0^2}\frac{(\Omega_1^2 - \Omega_2^2)^2}{\overline{\Omega}_R\overline{\Omega}_{R^{-1}}}, \tag{S18}$$

$$f_\infty^{\varpi_0} = \frac{1}{2\varpi_0^2}\frac{(\Omega_1^2 - \Omega_2^2)^2}{\overline{\Omega}_R\overline{\Omega}_{R^{-1}}}, \tag{S19}$$

$$f_1^0 = \frac{(\Omega_1^2 - \Omega_2^2)^2}{2\Omega_1^2\Omega_2^2}\frac{\varpi_0^2}{\overline{\Omega^2}_{x^{-1}}(i\varpi_0)}, \tag{S20}$$

$$f_0^{\varpi_0} = \frac{(\Omega_1^2 - \Omega_2^2)^2}{(\varpi_0^2 + \Omega_1^2)(\varpi_0^2 + \Omega_2^2)}\frac{\varpi_0^2}{\overline{\Omega^2}_{x^{-1}}(i\varpi_0)}, \tag{S21}$$

$$f_0^{\omega_0} = \frac{(\Omega_1^2 - \Omega_2^2)^2}{(\omega_0^2 - \Omega_1^2)(\omega_0^2 - \Omega_2^2)}\frac{\omega_0^2}{\overline{\Omega^2}_{x^{-1}}(\omega_0)}, \tag{S22}$$

$$L_{\varpi_0} = \frac{\sqrt{\overline{\Omega^{-2}}_x(i\varpi_0)}}{\overline{\Omega^{-1}}_R}, \tag{S23}$$

$$\begin{cases} R_{HL} = R_1 + R_2 \\ \Omega_{HL} = \dfrac{1}{\overline{\Omega^{-1}}_R}, \end{cases} \tag{S24}$$

$$c_1^0 = -\overline{x(\varpi_0)/x(i\varpi_0)}_{R/\Omega}; \tag{S25}$$

where:

$$\overline{\Omega}_R \equiv \frac{R_1\Omega_1 + R_2\Omega_2}{R_1 + R_2}, \tag{S26}$$

$$\overline{\Omega}_{R^{-1}} \equiv \left(\frac{\Omega_1}{R_1} + \frac{\Omega_2}{R_2}\right)(R_1 + R_2), \tag{S27}$$

$$\overline{\Omega^{-1}}_R \equiv \frac{R_1\Omega_1^{-1} + R_2\Omega_2^{-1}}{R_1 + R_2}, \tag{S28}$$

$$\overline{\Omega^{-2}}_x(i\varpi_0) \equiv \frac{\Omega_1^{-2}x_1(i\varpi_0) + \Omega_2^{-2}x_2(i\varpi_0)}{X^M(i\varpi_0)}, \tag{S29}$$

$$\overline{\Omega^2}_{x^{-1}}(\omega_0) \equiv X^M(\omega_0)[\Omega_1^2 x_1^{-1}(\omega_0) + \Omega_2^2 x_2^{-1}(\omega_0)], \tag{S30}$$

$$\overline{x(\varpi_0)/x(i\varpi_0)}_{R/\Omega} \equiv \frac{\frac{R_1}{\Omega_1}\frac{x_1(\varpi_0)}{x_1(i\varpi_0)} + \frac{R_2}{\Omega_2}\frac{x_2(\varpi_0)}{x_2(i\varpi_0)}}{\frac{R_1}{\Omega_1} + \frac{R_2}{\Omega_2}}. \tag{S31}$$